JACOBS
UNIVERSITY

Ion Transport Through Bacterial Outer Membrane Porins: A Computational Study

by

Niraj Hasmukhbhai Modi

A thesis submitted in partial fulfillment
of the requirements for the degree of

Doctor of Philosophy
in Biochemical Engineering

Approved Dissertation Committee:

Prof. Dr. Ulrich Kleinekathöfer
(Jacobs University Bremen, Germany)

Prof. Dr. Roland Benz
(Jacobs University Bremen, Germany)

Dr. Syma Khalid
(University of Southampton, UK)

Date of Defense: 16th December 2013

School of Engineering and Science, Jacobs University Bremen

Abstract

Ion transport through membrane proteins and nanopores is a process of significant importance which has implications ranging from controlling various biological processes to applications in the field of nanoanalytics and stochastic sensing. Therefore it is imperative to probe the behavior and dynamics of ions in nanoscale confinements provided by membrane proteins. The research work reported in this thesis is aimed at understanding ion transport processes, namely ion selectivity and ion conductance, through bacterial outer membrane porins using molecular dynamics simulations.

The major focus of this thesis is to probe the phosphate selectivity of the OprP porin from the bacterium *Pseudomonas aeruginosa*. The protein OprP is induced in the outer membrane of bacteria under conditions of phosphate starvation and is responsible for the high-affinity uptake of phosphate ions under such circumstances. Free-energy molecular dynamics simulations revealed atomic details leading to the phosphate selectivity of the channel. To further understand the phosphate selectivity of OprP and underlying structure-function relationships, several important residues of OprP have been mutated. Such studies on the mutant OprP channels have enabled us to probe the relative contributions of the residues and their properties, namely charge, size, the ability to desolvate the permeating ion etc., in assigning the phosphate selectivity to OprP. Moreover, the findings obtained for the phosphate selectivity of OprP were further extended to probe the diphosphate selectivity of OprO, a homologous porin of OprP with a high sequence and structural similarity. *In silico* double mutants of OprP and OprO demonstrated a trend to interchange the phosphate selectivity of OprP and the diphosphate selectivity of OprO.

The other focus of the thesis is to decipher the ion conductance properties through the OmpF and NanC porins from *Escherichia coli*. A particular kind of bulky ions, i.e., ionic liquids have been investigated with respect to their temperature-dependent pore conductance properties through OmpF. Such ionic liquids can improve the time-resolution of electrophysiological measurements and may be useful in various biosensing applications. Applied-field simulations revealed the importance of a particular orientation of the permeating ion to be able to pass through the pore. In case of NanC, an asymmetric distribution of charged residues inside the pore was found to be responsible for an asymmetric conductance property and a weak anion selectivity of the porin. In addition, mutants

of OmpF and NanC have been generated to modify ion conductance properties of these porins.

The findings presented in this thesis enhance the atomistic and functional understanding of ion transport processes through bacterial outer membrane porins in particular and various other membrane proteins in general. Molecular details obtained from such studies can be further exploited to engineer the ion transport properties through nanopores to achieve diverse possible applications, e.g., the design of ion-specific sieves and sensing of biological agents.

Acknowledgment

Working on the PhD has been a memorable experience. This dissertation would not have been possible without the help and support of many people. I take this opportunity to thank all of them.

First and foremost, I express my deepest gratitude to my supervisor Prof. Dr. Ulrich Kleinekathöfer for providing me an opportunity to work in his research group and for his excellent guidance and constant support. He guided me through the details of this interesting research topic and at the same time provided me an opportunity to explore new ideas. His door was always open for discussions. I sincerely thank him for his help and motivation. Furthermore, I would like to sincerely thank Dr. Syma Khalid and Prof. Dr. Roland Benz for being in my thesis committee and for their precious time to examine the thesis.

My deepest gratitude goes to Prof. Dr. Roland Benz and Prof. Dr. Mathias Winterhalter for the excellent experimental collaborations and useful guidance that helped me to understand experimental details in a better way. I sincerely thank Prof. Winterhalter for his constant support and excellent encouragement. I would also like to thank Prof. Dr. R.E.W. Hancock, University of British Columbia, for his valuable suggestions that led to new ideas. I am thankful to Prof. Dr. Bert van den Berg, Newcastle University, for providing the unpublished crystal structure for OprO.

I thank all group members of my group - Karunakar, Surya, Meisam, Bogdan, Jing, Jignesh, Carlos - for interesting discussions and help. My special thanks to former group members of my group, Dr. Robert Schulz and Dr. Carsten Olbrich, for their help (not just work related) during the initial stage of my stay in Bremen. I also thank Dr. Kozhinjampara R. Mahendran for providing useful suggestions and encouragement. I thank all group members of the Winterhalter group and the Benz group, particularly Pratik, Ivan, Usha, Sonali, Harsha, for interesting discussions regarding the experimental work. Special thanks to Dr. Ivan Bárcena-Uribarri and Pratik Raj Singh for providing experimental data. I am thankful to Karunakar for proofreading my thesis.

I am thankful to Jacobs University Bremen and Chemnitz University of Technology for providing the computational resources. I would like to thank Dr. Achim Gelessus for

an excellent technical support with the CLAMV facilities.

It is a pleasure to thank those who balanced my life beyond research. I am grateful to my friends, Dr. Jignesh Mungalpara and Hitesh Patel for their support and help. Those interesting skype discussions and Christmas vacations were very refreshing from a routine research work. I thank all friends from the Jacobs-Indian community, Susruta, Rohan, Sunil, Tripti, Mahesh, Sagar, Shubham, Rakesh, Rajesh, Naveen, DJ, Binit, Rajni, Abhishek, Prasad, Karunakar, Jignesh, Sandeep, Vikas, Sujit, Bala for their help and providing a social life here in Bremen.

I am forever indebted to my parents for their support, blessings and care. I do not have adequate words to thank them. Moreoevr, I am thankful to all my family members and friends whose good wishes have always kept me going. Last but not least, I am grateful to my wife, Krishna, for her unconditional love, care and infinite patience.

Funding

The research leading to these results has received support from the Innovative Medicines Joint Undertaking under Grant Agreement No. 115525, resources which are composed of financial contribution from the European Union's seventh framework programme (FP7/2007-2013) and EFPIA companies in kind contribution. In addition, financial support from the NANOFUN Research Center, Jacobs University Bremen, and the Deutsche Forschungsgemeinschaft (DFG) is duly acknowledged.

Contents

1. Introduction

Reproduced in part from the feature article by Modi, N.; Winterhalter, M; and Kleinekathöfer, U., "Computational modeling of ion transport through nanopores", *Nanoscale*, **2012**, 4(20), pp 6166-6180 (DOI: 10.1039/C2NR31024D) - by permission of The Royal Society of Chemistry.
See Appendix E for the published version of the feature article.

1.1. Ion transport

Transport of ions through biological membranes is a process of fundamental importance in cell biology. Such transport functions are facilitated by membrane proteins which collectively regulate diverse biological functions by virtue of maintaining the necessary electrochemical gradients across the cell membrane that is essential to a survival of the cell [1]. Membrane channels establish such gradients by controlling the influx and outflux of ions across cellular membranes *via* their high selectivity combined with specific conductivity and through gating mechanisms. Depending on the type of energy sources involved in ion transport processes, it can be broadly divided into passive and active transport. Passive transport does not require any external energy sources and the transport is driven by membrane potentials that exist across biological membranes. Active transport, on the contrary, requires external energy sources to facilitate ion transport across the membrane against the concentration gradient. The most prominent examples of active transport are ion pumps, e.g., sodium potassium pump, that utilize energy obtained from ATP hydrolysis to allow ion transport against the concentration gradient across the membrane [2]. The focus of this thesis is passive transport of ions across the bacterial outer membrane proteins.

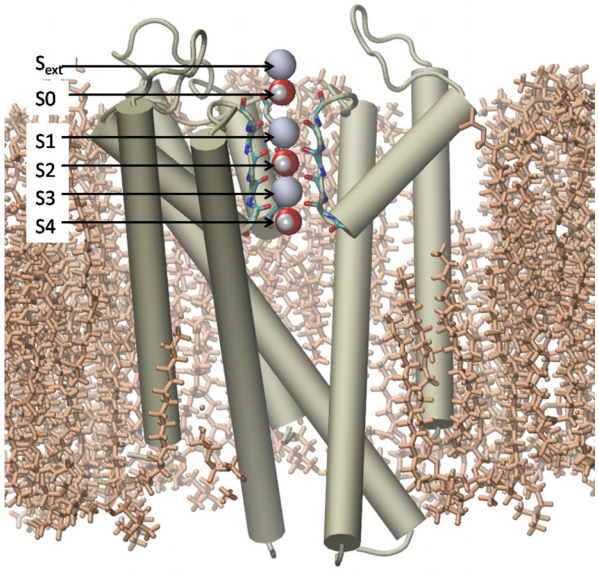

Figure 1.1.: A potassium ion selective KcsA channel embedded in a lipid membrane. The binding sites S0 to S4 and S_{ext} are shown to be occupied by K^+ ions (blue spheres) and water (red and white sphere) in an alternative manner. Backbone residues of the 'selectivity filter' region are shown in stick representation. One of the four monomers of KcsA is not shown for the sake of clear visualization of the binding sites. The figure is adapted from Ref. 3 with permission from The Royal Society of Chemistry.

.

In living organisms, ion transport processes are mainly facilitated by ion channels and they regulate various biological functions, e.g., cell signaling, muscle contraction, osmotic stress response etc.[1]. Such functions are monitored by selective permeability of ion channels to specific ions. One such K^+ selective channel, the KcsA channel from *Streptomyces lividans*, is shown in Figure 1.1. Dysfunction of ion channels lead to various diseases, such as cystic fibrosis, osteoporosis, muscular dystrophy [4] and about 15% of marketed drugs utilize ion channels as a drug target [5]. Hence understanding the functions of ion channels is necessary to enable development new drugs. A detailed knowledge of ion transport processes through membrane proteins also allows to design biomimetic channels which have potential applications ranging from water desalination to fuel cells [6].

Other than biology, knowledge of ion transport through nanochannels is essential in the field of nano-analytics and stochastic sensing. Here ion current measurements are used as a probe to detect the transport of substrates through nanopores. A membrane containing a single nanochannel separates an electrolyte solution into two compartments which are connected only via the transmembrane pore of the nanochannel. A transmembrane voltage is applied, producing a steady ionic current through an open pore. If a solute is passing through the pore, it leads to a transient reduction of the ionic current in time-dependent electrophysiological measurements. One such schematic setup is shown in Figure 1.2. The ratio of the interior surface to the volume is very high for nanochannels due to their small diameter and that makes them ideal candidates in this kind of stochastic sensing applications. One of the very prominent applications of nanopores in stochastic sensing

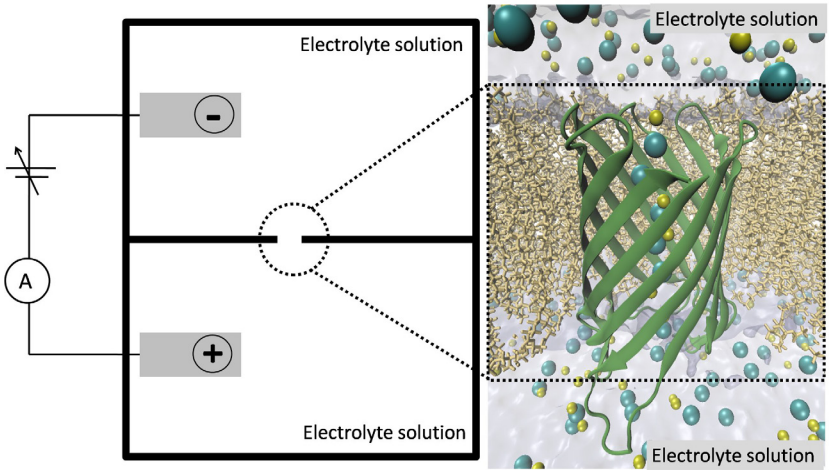

Figure 1.2.: Schematic experimental setup of ion transport measurements through nanopores together with a corresponding all-atom model being used in molecular dynamics simulations. The figure is adapted from Ref. 3 with permission from The Royal Society of Chemistry.

is DNA sequencing [7–10]. This thesis includes investigations on ion transport through different bacterial outer membrane porins utilizing molecular dynamics simulations that have implications mainly in understanding biological processes and possible applications in the field of nano-analytics utilizing the OmpF porin.

1.2. Typical questions of interest concerning ion transport

Ion transport through membrane proteins consists of multiple complex processes including ion selectivity, ion conductance and gating of the channel. Although all of them may be considered as an integral part of the ion transport mechanism, computationally they can be probed separately partly due to different time scales associated with such processes and different methods which can be applied to study them.

1.2.1. Ion selectivity

Experimental studies indicating the presence of Na^+ and K^+ selective channels dates back to as early as 1960. The solved crystal structure of the K^+ selective KcsA channel [11] from *Streptomyces lividans* provided the basis to probe this channel using computer simulations. The structure of KcsA [11, 12] revealed that the extracellular side of the pore is very narrow and exclusively lined by backbone carbonylic oxygen atoms (Figure 1.1) [11]. This region of the pore acts as "selectivity filter". The intracellular part of the pore is wider with a cavity radius of around 8 Å [11].

The issue of ion selectivity in potassium channels is still a matter of debate with three different working hypotheses. The "snug-fit hypothesis", attributes the selectivity to the slightly different atomic size of the K^+ and Na^+ ions [11, 13]. Due to atomic fluctuation in the binding site which are larger than the difference in ionic radii, this hypothesis is questionable [14]. The "field-strength hypothesis" suggests that the number and/or physical properties of the ligands coordinating the bound ions determine the ion selectivity [14, 15]. The third variant, the "over-coordination hypotheses", proposes that it is the number of coordinating ligands to the bound ion and not their physical properties which largely decides the selectivity [16, 17]. Sansom and coworkers compared all three hypotheses for the selective K^+ channel KcsA and the non-selective NaK channel using MD simulations [18]. According to this study, using the snug-fit hypothesis one could not differentiate between the selectivity of the KcsA channel and the non-selectivity of the NaK channel while the over-coordination hypothesis was able to justify the selectivity.

Results regarding the field-strength hypothesis were inconclusive in the above study while some other recent studies supported the hypothesis [15, 19]. In addition, quantum mechanics/molecular mechanics (QM/MM) Car-Parrinello simulations were performed to shed light on the processes underlying the selectivity filter [20] though also this methods has its own problems [21].

Similarly other channels such as an anion-selective ClC channel and a cation-selective nicotinic acetylcholine receptor (nAchR) were computationally investigated to understand their selectivity mechanisms [22–24]. Omp32, an anion-selective porin from *Delftia acidovorans*, was studied to investigate its selectivity using free-energy molecular dynamics simulations. In this thesis, we have investigated in detail the phosphate selectivity of the OprP porin from *Pseudomonas aeruginosa*. We have also investigated the poly-phosphate selectivity of OprO, a homologous porins of OprP from *P. aeruginosa*.

1.2.2. Ion conductance

Ion conductance is an important property which is routinely measured in electrophysiological bilayer experiments to characterize the channel for various properties, e.g., size of the pore, asymmetric properties of channel depending on the direction of the applied voltage, etc. The MD simulation study by Aksimentiev and coworkers first demonstrated that applied-field simulations can be used to calculate channel conductances with quantitative accuracy [25]. In that study, simulations at different applied voltage biases revealed an asymmetric current-voltage curve indicating an ion current rectification (ICR) [25]. This feature arose due to the dependence of the current value on the polarity of the applied bias. It was recently shown that the magnitude of the rectification also depends on the type of the cation by investigating different alkali chloride solutions for current-voltage relationships [26]. In addition, it was reported that the ion conductance was severely affected by the protonation state of an individual residue suggesting its possible role in pH assisted gating of the pore [25].

Pezeshki and coworkers studied ion conductances of two structurally similar *E. coli* porins, OmpF and OmpC, with respect to their dependence on temperature and KCl concentrations [27–29]. Excellent agreement between theory and experiments was obtained at around room temperature and at lower salt concentrations up to 1 M. Another studies with divalent ions conductance, e.g., Mg^{2+}, Ca^{2+}, through OmpF revealed anion selectivity of the porin while the porin was slightly cation-selective for the KCl conductance [30, 31]. VDAC, a mitochondrial porin, was investigated to understand concentration-dependent ion conductance using both MD [32, 33] and brownian dynamics (BD) [34]

simulations.

Ion conductance MD simulations through very narrow porins or ion channels can be computationally very expensive. Due to small currents of narrow channels, long simulation times are required to get statistically meaningful ion permeation events. For example, applied-field MD simulation for the Kv1.2 channel was carried out on the microsecond time scale [35]. Such long time scale simulations verified the K^+ permeation mechanism as suggested by potential of mean force (PMF) calculations where it was shown that configurations with two or three K^+ ions alternatively occupy the binding sites and K^+ ions are separated by one water molecule each in between (see Figure 1.1) [12, 36].

In this thesis, ion conductance simulations of different porins, namely OmpF, OprP, OprO and NanC, are presented.

1.2.3. Gating of channels

Regulation of cellular functions requires that ions be released at certain times but not at other times, and this variable ion conductance can be achieved by a process called gating. It is computationally challenging to model such gating processes due to the long time scales involved with them. Nevertheless, several channels were studied computationally to understand their gating mechanisms. Crystal structures of KcsA in low and high salt concentrations revealed different structural arrangements in the selectivity filter (see Figure 1.1) region [37]. This finding suggests a possible role of the filter region in the gating mechanism, the so called C-type inactivation, which was also explored by several computational studies [38–40] targeted molecular dynamics (TMD) study suggested the transition between closed and open states to occur in a 'zipper-like' fashion [41]. Recent studies with a series of KcsA crystal structures in fully open and partially open forms investigated the structural mechanism of C-type inactivation and proposed a possible contribution of allosteric couplings between different regions of the channel in the inactivation process [42]. Moreover, the movement of the inner gate on the intracellular side of the channel and its influence on the inactivation process by inducing conformational changes in the filter region was investigated by a combined experimental and computational study [43].

Mechanosensitive channels (MSCs) undergo large structural changes to maintain mechanical tensions within cells and to prevent lysis of cells due to osmotic stress. Mechanosensitive channels from *E. coli* were investigated to understand transition from closed to open conformation by different simulation techniques, like targeted molecular dynamics (TMD) [44] and steered molecular dynamics (SMD) [45] simulations.

Small porins like OmpA from *E. coli* and OprF from *P. aeruginosa* showed gating behavior and were investigated by MD simulations [46, 47]. Electrophysiological experiments on OccK family of porins had revealed multiple sub-states of some of the channels [48] with different conductances which need corresponding simulations to characterize them atomistically.

1.3. Computational methods to study ion transport

Various theories have been developed to determine the ion transport through nanopores. In general there is a trade-off between the computational resources needed and the details as well as the accuracy which can be extracted from the respective method. The methods discussed below can be used individually or, to some extent, in a combination with each other. Such a combination of methods can help to portray a better picture of ion transport by overcoming the limitations associated with a particular method. Especially one has to keep in mind the large spatial and temporal scales over which the calculations need to be performed in a converged manner [49].

1.3.1. Continuum models

The main idea in continuum models is to approximate all components of the simulated system i.e., water, ions, proteins, etc. via a continuum. Instead of a large number of individual atoms, a system with a few continuous elements is achieved. The most well-known continuum theory for ion transport is certainly the Poisson- Nernst-Planck (PNP) scheme [50–54] which combines the Nernst-Planck and the Poisson equations. The Nernst-Planck continuum electro-diffusion theory describes the flux density $\mathbf{J}_\alpha$ of ion type α at position $\mathbf{R}$ in terms of its concentration C_α and the corresponding potential gradients [55–58]

$$\mathbf{J}_\alpha(\mathbf{R}) = -D_\alpha(\mathbf{R})\left(\nabla C_\alpha(\mathbf{R}) + \frac{C_\alpha(\mathbf{R})}{k_B T}\nabla V_\alpha^{\text{eff}}(\mathbf{R})\right) \tag{1.1}$$

with the diffusion coefficient $D_\alpha(\mathbf{R})$ and the effective potential V_α^{eff}. The potential, $V_\alpha^{\text{eff}}(\mathbf{R})$, at each position $\mathbf{R}$ is the sum of potentials excluding ions from the interior of the pore or membrane and an electrostatic potential $\phi(\mathbf{R})$. The later one is determined by solving the Poisson equation

$$\nabla\Big[\epsilon(\mathbf{R})\nabla\phi(\mathbf{R})\Big] = -4\pi\left(\rho_P(\mathbf{R}) + \sum_\alpha C_\alpha(\mathbf{R})\right) \tag{1.2}$$

where $\epsilon(\mathbf{R})$ denotes the position-dependent dielectric constant and $\rho_P(\mathbf{R})$ the charge density of the pore. Solving these two coupled differential equations, the Nernst-Planck equation, Eq. (1.1), and the Poisson equation, Eq. (1.2), in a self-consistent manner yields the electrostatic potential, the concentration, and the flux of the ions. The parameters for the PNP calculations are often obtained empirically but in some cases have been, at least partially, extracted from atomistic simulations [57, 59]. While ions and water molecules are always treated as continuous, the channel is sometimes approximated to various extends in its form and charge distribution. To give some examples, the PNP method was applied to study the ion transport through the outer membrane protein F (OmpF) [57, 60–62], the voltage-dependent anion channel (VDAC) [59], a calcium channel [63], the gramicidin channel [51, 64], the protegrin transmembrane pore [65] and also synthetic nanopores [66–69].

However, a simplistic representation as in the PNP approach has several limitations and various questions regarding the applicability of continuum based method in the nanoscale systems have already been raised [52, 70]. The PNP theory works best for wide aqueous pores and may cause problems for regions of constricted volume. Furthermore, the finite volume of the ions which becomes important for narrow nanopores is neglected [71]. Additionally, exclusion of non-electrostatic interactions between ions, overestimation of the shielding effect by counterions inside a pore [72, 73] and lack of the description of dielectric boundary effects are a few shortcomings associated with the method. Nevertheless, the PNP method has shown its usefulness to study ion transport at a relatively small computational cost [74].

In addition, a large number of extensions of the PNP approach has been developed over the years. One of them is the density functional theory-PNP method in which the ions are described as charged, hard spheres with excess chemical potentials computed from equilibrium density functional theory [63, 75, 76]. Its efficiency has been tested especially for the ryanodine receptor calcium channel to study the energetics of Ca^{2+}-binding selectivity over the monovalent cations [63]. Another theory, the Energetic Variational Analysis (EnVarA), has been developed by Eisenberg and coworkers [77]. This variational model was developed to deal with complex fluids including flowing interacting subelements which can be more complex than hard sphere ions. Furthermore, in yet another complementary approach one aims at determining structural features of nanopores from measurements of its function, namely current voltage curves in different solutions. From a mathematical point of view, this is an inverse problem [78, 79]. At the same time one can employ this approach to design channels with desirable properties

such as a particular selectivity [79].

1.3.2. Brownian dynamics

The Brownian dynamics (BD) method lies in between the dichotomy of detailed all-atom MD simulations and continuum-based approaches. In the BD scheme, the ions and nanopores are treated explicitly while the solvent molecules are described implicitly. The interactions of the solvent molecules with the rest of the system are modeled via frictional and stochastic forces. These two latter forces are not independent from each other but interrelated via the fluctuation-dissipation theorem [80]. The equation of motion is given by a Langevin equation [53, 54, 81, 82]

$$m_i \frac{d^2}{dt^2}\mathbf{R}_i(t) = \mathbf{F}_i(t,\mathbf{R}) - m_i\gamma_i\dot{\mathbf{R}}_i(t) - \xi_i(t) \tag{1.3}$$

where ξ_i denotes the stochastic forces and $\mathbf{F_i}$ the systematic forces. The term $m_i\gamma_i\dot{\mathbf{R}}_i$ denotes the frictional forces with m_i being the mass, γ_i being the reciprocal of the relaxation time and $\dot{\mathbf{R}}_i$ the velocity of ith particle. The systematic force $\mathbf{F}_i$ accounts for electrostatic forces due to the interactions between the charged particles and with a possible external potential.

Several biological pores such as OmpF [57, 83, 84], potassium channels [85, 86], α-hemolysin [87], the VDAC [34], and synthetic nanopores [88] have been investigated utilizing BD simulations. Using this method, one can obtain current-voltage and conductance-concentration curves at reasonable computational cost. Furthermore, those results can be compared to experimental measurements directly which provides the basis for the validation of this kind of simulations. On the other hand, limitations associated with the representation of the rigid protein-water interface and the continuum solvent should be considered carefully. Generally, constant dielectric fields are used throughout the system to represent the water implicitly. In reality, the local dielectric constant of water may vary considerably depending on the environment. For example, water molecules present in the pore may have altered dielectric constants due to a charges and confinements. In such cases, environment-dependent dielectric constants can correctly account for electrostatic screening effects. As a possible extension, one might extract local dielectric constants from MD simulations and subsequently employ them in BD calculations [34, 57].

As a promising augmentation, an atomic-resolution BD method has recently been developed [89, 90]. For this scheme one needs to determine the three-dimensional

potential of mean force (PMF) maps at high resolution from all-atom MD simulations. This approach has been applied to measure ion currents during DNA translocation [90]. It has been shown that the atomic-resolution BD method produces results with orders of magnitude less computational effort than all-atom MD. At the same time, the ion distributions and ion currents predicted by both methods are in agreement [90]. Though the numerical effort for the 3D PMF maps is very large, the speedup is tremendous if viewed in connection with the obtained accuracy. This approach seems to be very promising and will most likely be applied to other systems in the near future as well.

As an alternative to the BD approach one might view the dynamic Monte Carlo scheme [91], an extension of the equilibrium Monte Carlo theory. In this approach a randomly-chosen ion from the ionic solution is moved to a new random position within a maximum displacement of its previous position. The paths followed by the ions constructed in such a manner resemble those of MD or BD ion trajectories [91].

1.3.3. Molecular dynamics

Molecular Dynamics (MD) simulations have become a very valuable tool for biophysical and biochemical analysis as well as prediction over the last years. In this approach, all atoms in the system are treated as classical particles moving under the influence of the Newton's classical equations of motion [92–94]

$$m_i \frac{d^2}{dt^2}\mathbf{R}_i(t) = \mathbf{F}_i(t) = -\nabla V(\mathbf{R}_i(t), \ldots, \mathbf{R}_N(t)) \tag{1.4}$$

where $\mathbf{R}_i$ and m_i denote the position and mass of atom i, respectively, and N the total number of atoms in the system. To solve the equation Eq. 1.4, several algorithms exist. Some of the most important ones are the *leap-frog* algorithm and the *velocity Verlet* algorithm [93].

The force $\mathbf{F}_i$ acts on atom i and is determined as the gradient of the potential energy, $V(\mathbf{R}(t))$, of the system. The empirical force fields describe the potential energy of the system in terms of the interactions between the atoms. In its functional form, the potential energy function has two kind of parameters, bonded and non-bonded ones

$$V(\mathbf{R}_{1,\ldots,N}) = V^{\text{bonded}}(\mathbf{R}_{1,\ldots,N}) + V^{\text{nonbonded}}(\mathbf{R}_{1,\ldots,N}) \tag{1.5}$$

The bonded part describes the interaction of atoms with their covalently-bonded

neighbor atoms

$$V^{\text{bonded}}(\mathbf{R}_{1,\dots,N}) = \sum_{\text{bonds}} \frac{k_l}{2}(l-l_0)^2 + \sum_{\text{angles}} \frac{k_\Theta}{2}(\Theta-\Theta_0)^2 + \sum_{\text{impr.}} \frac{k_\omega}{2}(\omega-\omega_0)^2 + \sum_{\text{torsion}} \frac{k_\varphi}{2}(1+\cos(n\varphi+\delta). \tag{1.6}$$

where l_0, Θ_0, ω_0 represent equilibrium bond length, bond angle and improper dihedral angle respectively. Torsion angle is represented by cosine function. Force constants are denoted by k_α with $\alpha = \{l, \Theta, \omega, \varphi\}$.

The non-bonded part of the potential includes electrostatic and *van der Waals* interactions

$$V^{\text{nonbonded}}(\mathbf{R}_{1,\dots,N}) = \sum_{j=1}^{N}\sum_{i>j}^{N}\left(\frac{q_i q_j}{4\pi\epsilon_0 r_{ij}} + 4\epsilon_{ij}\left[\left(\frac{\sigma_{ij}}{r_{ij}}\right)^{12} - \left(\frac{\sigma_{ij}}{r_{ij}}\right)^{6}\right]\right) \tag{1.7}$$

with the charges q_i and q_j, the vacuum permittivity ϵ_0, the *Lennard Jones* parameters σ_{ij} and ϵ_{ij} and the distance r_{ij} of the particles i and j. Because of the long-range behavior of the electrostatic interaction, this term is treated with approximations to reduce the computational costs and one of the most widely used techniques which allows such approximations is the *particle mesh Ewald* (PME) method [93]. The parameters for the force fields are obtained via quantum-mechanical calculations which can be further improved by fitting to experimental data. Among the force field sets commonly used in MD simulation of biomolecules are CHARMM [95], AMBER [96], GROMOS [97] and OPLS [98]. The various force field sets may differ in the functional form of individual terms and especially in the parametrization procedures for the large number of parameters involved.

One of the biggest advantages of the MD technique is the readily available time-dependent atomic detail of the molecular system making an analysis of the structure-function relationship feasible. Unfortunately this advantage comes at a large computational cost. Moreover, one has to keep in mind that various biological processes occur at time scales ranging from femtoseconds over milliseconds to seconds with, e.g., protein folding, being on the slower side of this spectrum. This has to be seen in connection to the usual MD time step in the femtoseconds range to account for fast vibrational modes such as hydrogen bond vibrations. With the present computational resources, simulations in the range of a few hundreds of nanoseconds are the common practice [99] which may

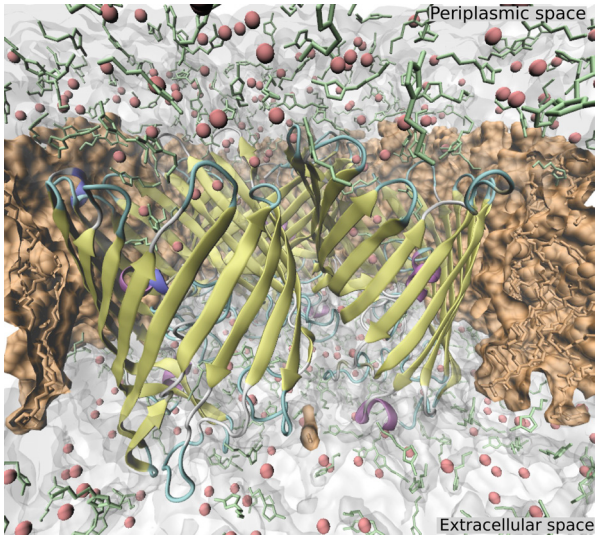

Figure 1.3.: Typical MD simulation setup for ion transport through nanopores. The OmpF nanopore is shown in a yellow cartoon representation and water as a gray surface. Moreover, the $BMIM^+$ ions are displayed using a green stick delineation and the Cl^- ions as pink spheres. The figure is adapted from Ref. 3 with permission from The Royal Society of Chemistry.

be extended up to several microseconds [35, 100].

Although MD simulations have been very successful providing microscopic details of biological processes, several limitations associated with the method have to be taken into account. Standard force fields used in biomolecular simulations account for electrostatic interactions in terms of fixed, usually atom-centered, charges and the corresponding interactions are often based on a simple pairwise-additive models. However, real physical systems undergo substantial polarization when placed into a medium with an high dielectric constant such as a water or in the presence of an external applied electric field. Polarizable force fields are available to explicitly account for many-body induced polarization effects but they are computationally more expensive [101, 102]. Modeling a pH value is another challenge in MD simulations. Regularly, the effect of a certain pH value is indirectly incorporated into the system setup by calculating the pKa of ionizable residues [103]. The protonation states of these residues are fixed according to the pKa results and usually not changed during a MD simulation. Recent extensions address this issue such as the λ dynamics in which the titration coordinate λ is driven by generalized forces between the protonated and deprotonated states [104, 105].

Generation of a membrane potential in MD simulations

Ion transport through nanopores is normally driven by a potential difference across the membrane. In living cells, such potential differences across membranes are gen-

erated by ionic concentration gradients maintained by ion channels and transporters. In electrophysiological measurements, artificial potential gradients are generated using an electrode-based experimental setup. Therefore the question arises how to apply an electrostatic potential difference across the membrane in MD simulations. The generation of an ionic concentration gradient across the membrane and in turn a potential difference is not a straightforward task considering the periodic boundary conditions used in the simulation. These boundary conditions are regularly applied to avoid finite-size effects.

One method to address this problem is to build a system comprising of two parallel lipid membranes, the so-called twin-bilayer approach, to generate two separate bulk phases [106, 107]. An electrostatic potential difference in such a system setup can be generated by different ionic concentrations in the two separate bulk phases. This kind of approach increases the system size considerably and hence the computational cost. Alternatively, a slightly less expensive approach can be used in which the second membrane is replaced by a vacuum slab separating the two bulk phases [108]. In both above approaches, it is troublesome to maintain an uniform transmembrane potential over a finite simulation time as even one permeating ion can change the electrostatic potential considerably [108]. In practice, one has to continuously monitor the potential difference across the membrane and adjust charge imbalances to avoid any large deviations in the transmembrane potential. Recently this problem has been tackled by several schemes in MD simulations. In one of the approaches. the ion concentration in each compartment and thus the electrostatic potential is regulated by exchange of ions and water molecules between different compartments [109]. This approach has been applied in BD simulations earlier [110]. In the second approach, a small transition region of a particular thickness is defined at each of the edges of the periodic box, over which a dynamically adjusted external force directed along the z axis acts on all the ions to maintain the necessary concentration gradient between two compartments [111].

An alternative approach is to apply an homogeneous electric field E throughout the entire system sometimes called the tinfoil approach [112–114]. In this scheme one effectively applies an additional force $q_i \cdot E$ to all charged atoms with charge q_i as if they would be subject to an homogeneous electric field E. This field E is usually applied perpendicular to the membrane plane (z direction) and is proportional to the applied voltage V, i.e., $E = V/L_z$, with the system length L_z in z direction. Subsequently the ionic current can be determined by summing up the movement of the charges projected onto

the z direction via [25, 112]

$$I(t) = \frac{1}{L_z} \sum_{i=1}^{N} q_i \frac{z_i(t + \Delta t) - z_i(t)}{\Delta t} \,. \tag{1.8}$$

The conductance is then defined as the ratio of computed current and applied voltage. In the field of MD simulations for membrane proteins, this approach was first used by Aksimentiev and Schulten [25] to quantitatively study the ion transport through an α-hemolysin nanopore. Subsequently, this scheme has been successfully employed to study ion transport in diverse systems [27–29, 35, 115–119]. Furthermore, the validity of this approach has recently been tested for several examples [114, 120]. In this thesis, we have applied the same approach to investigate ion conductance properties of different porins. Since ion currents through nanopores are usually in the sub-nA to nA range only a limited number of charges permeate through the nanopore in a simulation time of a nanosecond. To obtain statistically meaningful numbers of ion permeation events, the applied voltage in simulations is often in the range of 1 V and therefore a few times larger than the usually applied 50-150 mV in biological nanopore experiments.

Free energy calculations

MD simulations can be utilized to generate an ensemble of configurations, from which thermodynamic quantities like free energy differences, ΔA, can be computed. Particularly of our interest is the change in free energy of the system along one or several chosen degrees of freedom, often called as “reaction coordinates”. The change of free energy of the system with respect to such chosen degree(s) of freedom is known as a potential of mean force (PMF). Such PMF calculations are widely applied to understand ion transport through nanopores [22, 23, 121–127]. However, a challenging task is to achieve uniform sampling along the chosen degree of freedom. Considering the Boltzmann sampling of phase space, it is difficult to overcome the high free energy barriers that separate the thermodynamic states of interest within the time scale accessible by MD simulations. To overcome the sampling problems associated with the high energy regions of the phase space, several approaches have been developed to enhance the sampling along the chosen degree of freedom.

One such widely used approach to achieve a uniform sampling along the reaction coordinate is the Umbrella Sampling (US) method. In this method, an additional harmonic bias potential is applied to achieve a uniform sampling along the reaction coordinate. The weighted histogram analysis method (WHAM) can be subsequently used to combine the

probability distributions from multiple biased simulations along the reaction coordinate and to convert them to a single unbiased probability profile, from which a free energy profile along a reaction coordinate can be obtained.

Another approach called thermodynamic integration (TI) relies on calculating and subsequently integrating the derivatives of the free energy with respect to a chosen degree of freedom, ξ [128]. Within the TI approach, there are two ways to overcome sampling difficulties associated with high energy barriers. The first one, called the method of constraints, consists of imposing a constraint force on the system such that ξ is constant. The interval of interest $[\xi_0, \xi_1]$ can be discretized into a number of quadrature points. At each point, the derivative $dA/d\xi$ can be computed by running a constraint simulation. A quadrature can subsequently be used to estimate $\Delta A = \int_{\xi_0}^{\xi_1} dA/d\xi \, d\xi$. The second method, called adaptive biasing force (ABF) is based on the continuous application of a biasing force which is dynamically adapted to compensate the current estimate of the free energy and thereby virtually erasing the roughness of the free energy surface as the system progresses along ξ. To achieve this objective, the average force acting on ξ, $\langle F_\xi \rangle_\xi$, is calculated from an unconstrained MD simulation

$$dA(\xi)/d\xi = \langle \partial V(\mathbf{x})/d\xi \rangle_\xi - 1/\beta \langle \partial ln|J|/d\xi \rangle_\xi = -\langle F_\xi \rangle_\xi \tag{1.9}$$

where $|J|$ is the determinant of the Jacobian for the transformation from Cartesian to generalized coordinates. The first term of the ensemble average in Eq. 1.9 accounts for physical forces exerted on the system, obtained from the potential energy function V($\mathbf{x}$). The second term in Eq. 1.9 is a purely geometric correction to account for the difference in phase space availability as ξ varies. Contrary to the instantaneous component of force, F_ξ, only the average force $\langle F_\xi \rangle_\xi$ is physically meaningful.

In the framework of the ABF approach, F_ξ is accumulated in small bins of finite size, $\delta\xi$ and thereby giving an estimate of the derivative $dA(\xi)/d\xi$ using Eq. 1.9. The so-called adaptive biasing force applied along the chosen degree of freedom to overcome the free energy barrier can be defined as

$$\mathbf{F}^{ABF} = -\langle F_\xi \rangle_\xi \boldsymbol{\nabla}_x \xi \tag{1.10}$$

As the simulation progresses and the sampling of the phase space proceeds, the estimate $dA(\xi)/d\xi$ is progressively refined. The application of the biasing force, $\mathbf{F}^{ABF}$, introduced in the equations of motions ensures that the force acting along the reaction coordinate ξ averages to zero over time. As a result, progression of the system along

ξ is determined mainly by self-diffusion properties and uniform sampling along ξ can be achieved. We have used the ABF method to obtain the free energy profiles for the transport of different ions through OprP and OprO porins as well as their mutants.

One of the other approaches to achieve an accelerated sampling along the chosen degree of freedom is Metadynamics [129, 130]. In this approach, an external history-dependent bias potential which is a function of the reaction coordinate is added to the Hamiltonian of the system. This potential can be written as a sum of Gaussians deposited along the system trajectory in the reaction coordinate space to discourage the system from revisiting configurations that have already been sampled.

It is also possible to derive equilibrium properties like free energy differences from nonequilibrium simulations by applying a method suggested by Jarzynski and further developed by Crooks [128, 131]. According to the second law of thermodynamics, the average work $\langle W \rangle$ performed via a nonequilibrium process that alters a parameter λ of a system from λ_0 at time zero to λ_t at time t is greater than or equal to the equilibrium free energy difference between the two states

$$\Delta A = A(\lambda_t) - A(\lambda_0) \leq \langle W \rangle \tag{1.11}$$

where the equality is true only if the process is quasi-static. Jarzynski proposed an equality that persists irrespective of the speed of the process:

$$e^{-\beta \Delta A} = \langle e^{-\beta W} \rangle \tag{1.12}$$

where $\beta = (k_B T)^{-1}$. However being a nonequilibrium process, a large number of simulations are required to derive reliable free energy profiles.

1.4. Porins

Porins are channel-forming proteins present in the outer membrane of Gram-negative bacteria and some Gram-positive bacteria of the Mycolata group, the mitochondria and the chloroplast [132, 133]. Structurally they have a β-barrel architecture and can either be in a trimeric or a monomeric form [134]. The β-barrel structure is formed by varying number of β-sheets that are connected to each other via long extracellular loops and small periplasmic turns (Figure 1.4). Some of the loops fold inside the lumen of the pore and form constriction regions. Porins function as molecular sieves that mediate passive diffusion of diverse substrates into the periplasm of bacteria. They can be functionally

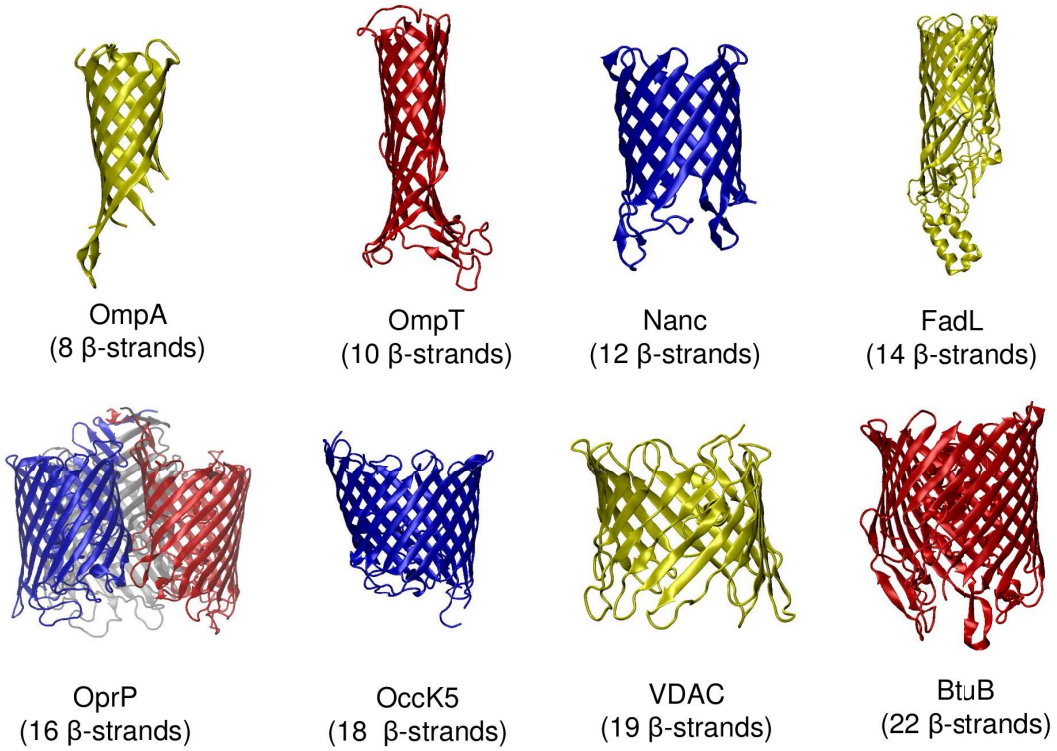

Figure 1.4.: Porins with different sizes ranging from 8 β-strands to 22 β-strands.

classified as either non-specific porins or substrate-specific porins [133]. Non-specific porins allow passive diffusion of small solutes down their electrochemical gradient without having a defined preference for particular solutes. Examples of non-specific porins are OmpF, OmpC, and PhoE of *E. coli*. Specific porins, however, have a clear preference for the particular solutes. Such specificity is generally obtained by the presence of the defined affinity sites inside the pore for the particular solute. Examples of specific porins are the carbohydrates transporting porins LamB and ScrY of *E. coli*, the phosphate and polyphosphate selective porins OprP and OprO from *P. aeruginosa*, as well as the nucleoside specific Tsx porin of *E. coli*.

Porins exhibit a range of features which make them suitable candidate to understand various biological processes of membrane proteins and for applications in biosensing. They are available in different sizes (Figure 1.4) and provide a range of ion and substrate selectivities. They can act as model systems to test computational models of ion transport. For example OmpF was a testbed system for the development of the Grand Canonical Monte Carlo/Brownian Dynamics (GCMC/BD) method [135, 136]. Porins have a stable β-barrel structure. Hence they can easily be engineered to achieve specific transport properties while maintaining the overall structural stability, which makes them ideal candidates for biosensing applications. For example, OmpG was engineered to make it a “silent” pore, i.e., a pore devoid of any intrinsic gating activity, which is essential

for biosensing applications [137]. Similarly OmpF was engineered with respect to its conductance and selectivity properties [60, 61, 138].

Porins are very crucial to allow the passage of antibiotics through bacterial outer membrane porins [139–141]. One of the reasons for the antimicrobial resistance by bacteria is the low outer membrane permeability of antibiotics. The design of antibiotics with the improved bacterial outer membrane permeability is the active area of research. Both electrophysiology experiments and computer simulations are carried out to understand the translocation of antibiotics through porins [139, 142–149].

1.5. Aims and outline of the thesis

The aims of this thesis can be summarized in the following points:

a) To decipher phosphate and poly-phosphate selectivity of the OprP and OprO porins in detail and to the understand ion selectivity of porins and channels in general

b) To investigate ion conductance properties through bacterial outer membrane porins having different structures and range of selectivities

c) To engineer porins to alter their ion selectivity and ion conductance properties

d) To complement electrophysiological experiments to provide an atomistic picture of ion transport through porins

e) To understand ion transport processes through bacterial outer membrane porins and underlying structure-function relationships

The aforementioned points have been addressed in this thesis in the following chapters:

Chapter 2 explains the phosphate selectivity of OprP porin from *P. aeruginosa*. Free-energy molecular dynamics simulations have been carried out to obtain energetics of permeation of different ions through OprP. Molecular factors responsible for the selectivity of OprP are described and the ion selectivity of different channels and porins are discussed.

In **Chapter 3**, one of the very important central arginine residue of OprP, R133, is investigated to understand its relative contribution towards the phosphate selectivity of OprP. Such investigations on mutant channels are aimed to achieve the structure-function relationship of the porin. Free-energy molecular dynamics simulations complemented electrophysiological bilayer measurements and highlighted the importance of the residue

R133 in conferring the phosphate selectivity to OprP. The particular role of the charge of the R133 residue and its ability to alter the solvation behavior of permeating ions are explained.

In **Chapter 4**, another important residue of OprP, D94, is investigated via both molecular simulations and electrophysiological bilayer measurements. The significance of a negatively charged aspartate residue in an anion-biding site of an anion-selective porin OprP and its possible implications in transport of phosphate through OprP are discussed.

Chapter 5 investigates the diphosphate selectivity of OprO from *P. aeruginosa*, a homologous porin of OprP. Diphosphate selectivity of OprO *versus* phosphate selectivity of OprP are probed utilizing free-energy molecular dynamics simulations. Going one step further, the OprP and OprO porins are engineered *via* generating double mutants to swap their respective selectivities. In addition, applied-field molecular dynamics simulations are carried out to understand KCl transport properties through wildtype OprP and OprO as well as engineered porins.

Chapter 6 describes ion conductance properties of bulky ions, i.e., ionic liquid 1-butyl-3-methyl-imidazolium chloride (BMIM-Cl), through OmpF. Such special kind of ions are used in electrophysiology experiments to improve the time-resolution of measurements which is important in biosensing. Temperature-dependent conductance of BMIM-Cl ions through OmpF are calculated using applied-field MD simulations and compared with experimental measurements. Molecular interactions of BMIM-Cl ions with the porin are investigated and the significance of the particular orientation of $BMIM^+$ ions to permeate through the pore is presented.

In **Chapter 7**, concentration-dependent applied-field as well as equilibrium MD simulations for the ion conductance through the NanC channel - a 12 β-strand porin from *E. coli* - are carried out to investigate the asymmetric conductance property and weak anion selectivity of the porin. Additionally, *in silico* NanC mutants are generated to engineer the channel with respect to its asymmetric conductance property and anion selectivity.

Finally, in **Chapter 8**, the major findings and possible future directions are summarized. Supporting information for Chapters 2, 3, 4 and 6 are put in Appendices A, B, C and D, respectively. In Appendix E, a published feature article regarding modeling ion transport through nanopores is reprinted. Appendix F contains a publication on a channel from *Nocardia farcinica* where a homology model of this hetero-oligomeric channel was constructed to interpret the electrophysiology data regarding the peptide translocation

through the channel.

2. Modeling the Ion Selectivity of the Phosphate Specific Channel OprP

Abstract

Ion selectivity of transport systems is an essential property of membranes from living organisms. These entities are used to regulate multifarious biological processes by virtue of selective participation of specific ions in transport processes. To understand this process, the phosphate selectivity of the OprP porin from *Pseudomonas aeruginosa* was studied using all-atom free energy molecular dynamics simulations. These calculations were performed to define the energetics of phosphate, sulfate, chloride, and potassium ion transport through OprP. Atomic-level analysis revealed that the overall electrostatic environment of the channel was responsible for the anion selectivity of the channel, while the particular balance of interactions between the permeating ions and water as well as channel residues drove the selectivity between different anions. The selectivity of OprP is discussed in the light of well-studied ion channels that are highly selective for potassium or chloride.

Reproduced with permission from the article by Modi, N.; Benz, R; Hancock, R. E. W; and Kleinekathöfer, U., "Modeling the Ion Selectivity of the Phosphate Specific Channel OprP", *J. Phys. Chem. Lett.*, **2012**, 3(23), pp 3639-3645 (DOI: 10.1021/jz301637d). Copyright [2012] American Chemical Society.

2.1. Introduction

Many biological processes involve the participation of specific ions. The differentiation between ions and ion types is critically important for the functions of biological units. For example, potassium channels selectively and rapidly facilitate the movement of K^+ ions out of the cell and at the same time prevent the entry of Na^+ ions, thus maintaining the necessary electrochemical gradient across the cell membrane which is essential for the survival of the cell [1]. Likewise, ions contribute significantly towards the structure and function of many proteins and enzymes. Binding of the wrong ion type can disrupt the activity of such molecules [150]. High selectivity is achieved by specific membrane proteins that collectively regulate the appropriate ionic concentration gradients across the different compartments of biological systems and the majority of them belong to the family of ion channels [1]. The ability to discriminate between different ions with a high efficiency is fundamental to their functions. Understanding the structure-function relationship of such ion channels is therefore critical due to their biological importance, e.g., as drug targets to treat diseases [5] and to design ion-selective man-made nanopores for various applications, such as water desalination [151]. It is believed that such ion-selectivity is the result of a fine-tuned balance of a variety of interactions between ions, proteins, water molecules and the membrane environment. Although quantifying such interactions is not trivial, molecular dynamics (MD) free energy simulations provide important tools to identify and quantify microscopic factors responsible for selectivity and complement experimental studies.

Several ion-selective channels and membrane proteins like the KcsA channel [14–18, 152, 153], the ClC channel [154], the NaK channel [18, 155], the nicotinic acetylcholine receptor (nAchR) [23] and others have been investigated using MD simulations and free energy calculations. In addition, non-selective porins like OmpF were also probed to understand the energetics of various antibiotics transport and modulation of binding sites in the presence of other ions [144, 147]. Amongst the ion-selective channels, the potassium channel KcsA has been thoroughly studied to address the issue of selectivity and in many cases serves as a benchmark system as to how to probe selectivity in other channels. Amongst the different mechanisms suggested for the selectivity of this channel, the first one was the “snug-fit hypothesis” which attributed the selectivity to the slight difference in atomic sizes of Na^+ and K^+ [11]. This hypothesis was subsequently ruled out when considering the atomic fluctuations in the binding site, which are larger than the differences in ionic radii [14]. The alternative “field-strength hypothesis” attributes the selectivity to the number and/or physical properties of the ligands coordinating the

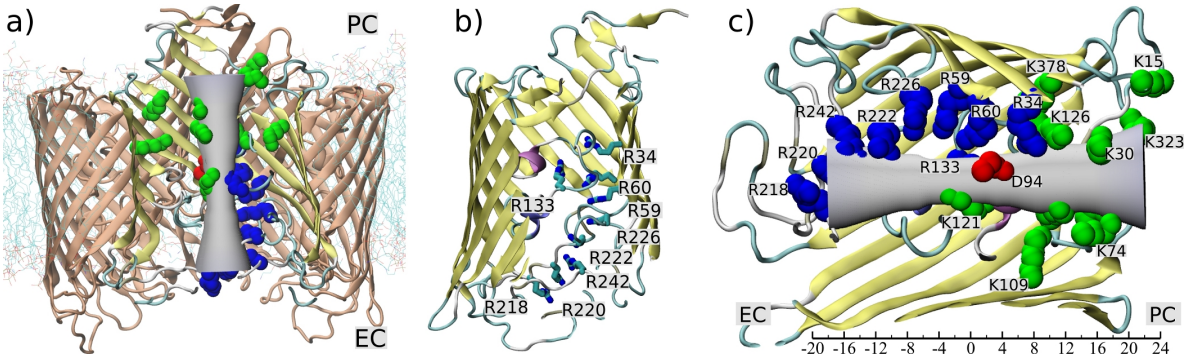

Figure 2.1.: OprP structural features. a) OprP trimer embedded in lipid membrane. The pore of the one of the monomers is shown with a grey hourglass shape to indicate the approximate relative radius of the pore in different regions and to guide the eye to the possible pathway for ion permeation. Important charged residues are shown as spheres (Arg-blue, Lys-green, Asp-red).b) Residues of the Arginine-ladder shown as sticks. c) Important charged residues are labeled and mapped to their position along z axis.

permeating ions [14, 15], while the "over-coordination hypothesis" assigns the selectivity to the number of coordinating ligands only and not their physical properties [16, 17].

Amongst the various membrane proteins, outer membrane of Gram-negative bacteria contain a special class of proteins called porins [133]. These porins have a β-barrel architecture and most of them are relatively non-specific general diffusion channels (e.g., OmpF and OmpC of enteric bacteria). Exceptions are the porins that selectively transport carbohydrates (ScrY and LamB), nucleosides (Tsx) and phosphate ions (OprP). In particular, the high phosphate-selectivity of OprP represents an interesting ion selectivity property that is not common to the porin class of proteins. OprP is integral outer membrane protein of *Pseudomonas aeruginosa* and is involved in high-affinity uptake of phosphate under phosphate starvation conditions [156]. Under such circumstances, phosphate permeation is ∼20 times higher than the Cl^- transport as indicated by electrophysiological experiments [157–159]. This is largely due to the 100-500 times higher binding affinity of OprP for phosphate compared to chloride [157–159].

The crystal structure of OprP revealed its trimeric architecture in which each monomer is formed by 16 β strands having extracellular and periplasmic loops (Fig. 2.1) [160]. Loops L3, L5 and T7 (Appendix A, Fig. A1) play an important role in channel formation. Some of the important structural features which drive the anion-selectivity of the channel are the so-called arginine ladder including R218, R220, R242, R222, R226, R59, R60, R34 that extends from the extracellular side down the channel to the middle of the pore, the central phsophate binding site (D94, Y62, S124, S1235, K121, K126, R34, R133) and a lysine cluster (K13, K15, K25, K30, K74, K109, K313, K323, K378) on the periplasmic

side of the channel (Fig. 2.1). Positively charged Arg and Lys residues are also present in non-specific porins like OmpF where they help to facilitate the transport of negatively charged antibiotics with caroboxylic groups [144].

An initial MD simulation study with OprP suggested permeation mechanisms for phosphate and chloride ions [121]. The selectivity of phosphate over chloride was attributed to the differential hydration properties of these two ions on the periplasmic side of the channel due to their different sizes. Apart from unequal sizes of the permeating ions, there seems to be other factors which may also contribute significantly towards the high phosphate selectivity of the pore. For example, OprP also has ∼20 times higher affinity for phosphate binding than for sulfate even though phosphate and sulfate ions are similar in size [157]. Hence differential selectivity within anions (binding affinities are in the order of phosphate, sulfate and chloride, from high to low) as obtained by electrophysiological measurements of OprP [157] need to be further analyzed at the atomic scale. Furthermore it is interesting to investigate factors responsible for the selectivity of this relatively wide porin channel compared to well-studied and relatively narrow, inflexible ion channels. Due to flexible side chains, OprP can be called a "brush-like" nanopore. To achieve detailed understanding of the selectivity in OprP, we employed full atomistic free-energy MD simulations to obtain the energetics of phosphate, chloride and sulfate ion transport through OprP. As an extreme case, we also studied the energetics of cation transport with potassium as example. Applied-field simulations as for previously performed for α-hemolysin [25], MscS [118], OmpF [27, 161] and OmpC [28] and reviewed in Ref. 3 were not preferred for OprP due to the small ion currents within a limited simulation time.

2.2. Results and Discussion

Details about the system setup and MD simulations are given in Supporting Information (see Appendix A). In our study, we have considered the monovalent form of phosphate ($H_2PO_4^-$, different from the one in Ref. 121) and divalent sulfate (SO_4^{2-}) anion, as they are the most common protonation states around the physiological pH of 7. To determine the effective free energy profiles for the transport of different ions through OprP, the adaptive biasing force (ABF) [162, 163] method as implemented in the *collective variable* module of NAMD 2.8 program [131] was utilized. The principal axis of the channel was aligned parallel to the z axis and the reaction coordinate was defined as the z position of the ion

The individual one-dimensional Potential of Mean Force (PMFs) for the transport of

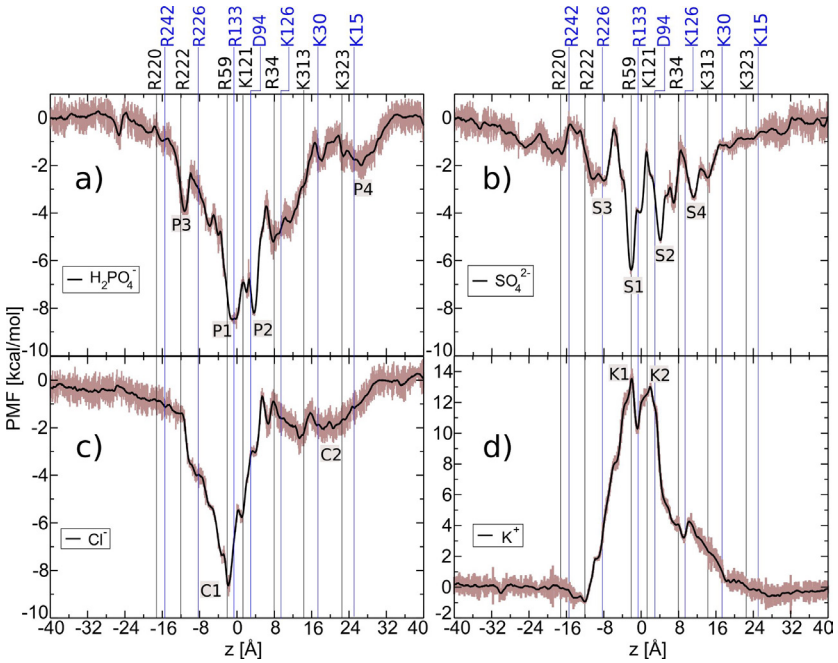

Figure 2.2.: PMF profiles for the permeation of a) $H_2PO_4^-$, b) SO_4^{2-}, c) Cl^- and d) K^+ ions through OprP. Important residues of OprP along the ion permeation pathway are mapped onto the PMF profiles with respect to their positions along the z axis. Important binding site regions/barriers are also labeled. The error bars are shown in brown.

each of four ions, $H_2PO_4^-$, SO_4^{2-}, Cl^- and K^+, through OprP are shown in Fig. 2.2. All four ions had characteristically different PMF profiles with the generalization that the three anions have energetically favorable binding regions while the cation has a high permeation barrier. Some of the important residues were mapped onto the PMF profiles based on their approximate positions along the z axis. The PMF for the phosphate ion revealed two central binding sites, P1 and P2, and two additional minor binding sites, P3 and P4 (Fig.2.2a). The central binding sites, P1 and P2, were energetically very favorable with well depth of ∼9 kcal/mol. These two sites were spatially ∼5 Å apart along the z axis and with an energy barrier of ∼2 kcal/mol between them. The presence of the two central binding sites was in agreement with the crystal structure data [160] and the previous simulation study [121]. It is important to note here that the values of the free energy changes observed in our simulations were different from those Ref. 121. This may be due to the different protonation state of the phosphate ion, $H_2PO_4^-$, that we used in our study (compared to PO_4^{3-} which is unlikely to found at physiological pH); the use of different force fields [127] and simulation protocols or cooperative effect of ions (in Ref. 121 three ions, one in each channel, are treated simultaneously). One also needs to keep in mind that PMF calculations for membrane proteins are also reported to be sensitive to simulation details like finite system size and use of non-polarizable force

fields especially for lipid hydrocarbons of the membrane [127]. Nevertheless, the form of the PMF profile was rather similar. Binding site P1 corresponded to the residues R59, R60, K121, and R133 while site P2 is formed by residues R34, R60, D94, S125, and R133 (Fig. 2.3). Furthermore, the minor binding site, P3, on the extracellular side was composed of residues from the arginine ladder, namely R222, R226 and R242 (Fig. 2.3), and had a well-depth of ∼2 kcal/mol. Multiple ions can also be included near site P3 due to the large size of the pore in this region. Site P3 along with the other residues of the arginine ladder may act as an entrance funnel to OprP which increases the local concentration of anions while electrostatically repels the cations. Another minor binding site, P4, was located on the periplasmic side with contributions from residues of the lysine cluster, K15 and K323. It is worth noting that the overall PMF profile with the existence of prominent central binding sites is different from that of ion channels such as KcsA where the free energy landscapes are quite flat with minor local binding sites along the permeation pathway.

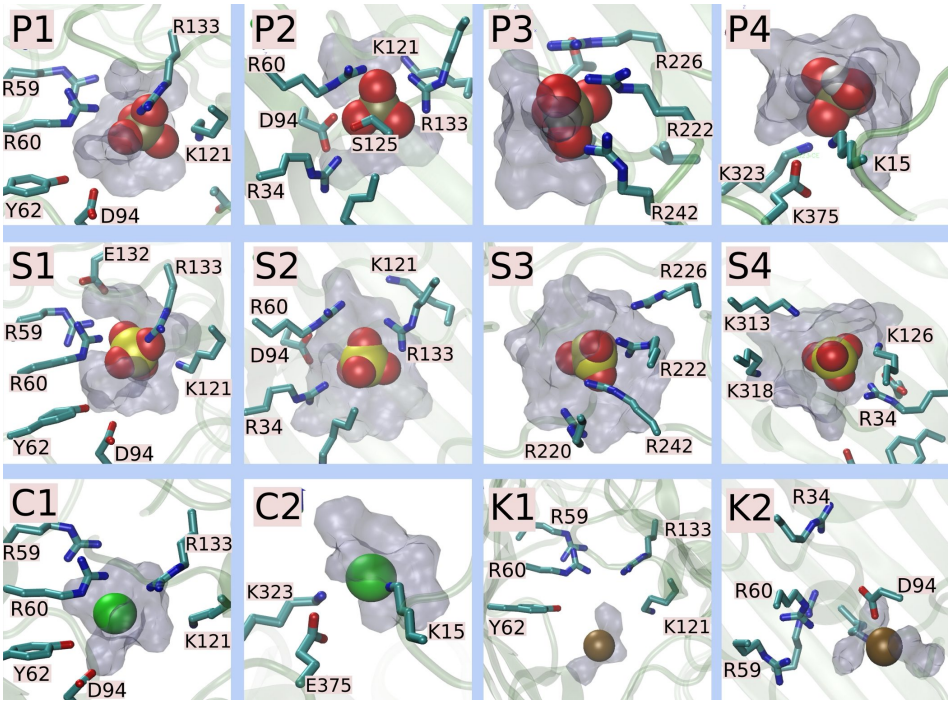

Figure 2.3.: Representative snapshots of important binding site (for anions) and barrier (for K^+) regions. Ions are shown as van der Waals spheres, the amino acid residues as sticks and water molecules as grey surface. In accordance with the PMF profiles, P1, P2, P3 and P4 denote the binding sites for $H_2PO_4^-$; S1, S2, S3 and S4 for SO_4^{2-}; C1 and C2 for Cl^-. K1 and K2 the barrier regions for K^+.

The free energy landscape for sulfate ion transport again showed two central binding sites, S1 and S2 (corresponds to site P1 and P2 for phosphate) and additional local stabilization regions, S3 (corresponding to P3 for phosphate) and S4 (Fig.2.2b). The

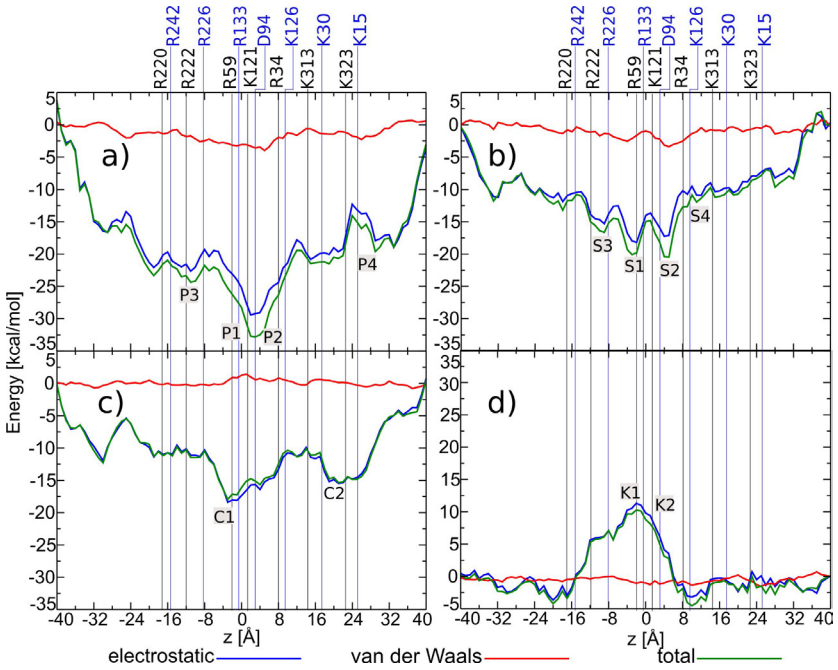

Figure 2.4.: The electrostatic and van der Waals interaction energy components for the permeation of a) $H_2PO_4^-$, b) SO_4^{2-}, c) Cl^-, and d) K^+ ions through OprP. Important residues of OprP along the ion permeation pathway are mapped with respect to their position along the z axis. Regions of binding sites/barriers are also labeled as per identified in PMF profiles. All energy values denote relative interaction energies assuming zero interaction energies in the bulk.

depth of the central binding region is ∼7 kcal/mol with an energy barrier of ∼4 kcal/mol between binding sites S1 and S2. In contrast, the PMF for the small mono-atomic Cl^- ion showed only one central binding site (corresponds to site P1 for phosphate) with an energy well-depth similar to that of phosphate (Fig.2.2c). Similar positions of the energy wells for phosphate and chloride ions were also reported in Ref. 121. Additional minor local stabilization regions could be observed around the residues of the lysine cluster (site C2). The different PMF profiles for the anions, especially the variations in the magnitude of the energetic stabilization in the binding regions and the overall pore attractive volume, were consistent with the selectivity between anions as observed in electrophysiological experiments [157]. As expected, the free energy profile for the K^+ ion had huge energetic barriers (K1 and K2, corresponds to P1 and P2 for phosphate) of 13 kcal/mol, making the channel practically impermeable for this ion type (Fig.2.2d). No significant local stabilization regions are found for K^+ along the entire length of the pore. The calculated dissociation constants (Kd) based on PMF profiles (see SI for details) are found to be 0.23 μM, 0.72 μM, 23.3 μM and 14.9 mM for $H_2PO_4^-$, Cl^-, SO_4^{2-} and K^+, respectively.

To further investigate the contributions of individual interaction components towards the selectivity of OprP, namely electrostatic and van der Waals, the interaction energies

were calculated for each permeating ion in the different regions of the pore (Fig. 2.4). For this purpose the pore was divided into bins of 1 Å in size and the energies were averaged in each bin. Such an analysis revealed that the electrostatic component of the energy was the major contributor towards determining the overall transport properties of ions through OprP, with very minor contributions from van der Waals interactions. Phosphate ion experienced very favorable electrostatic interaction energies compared to bulk indicating an overall positive electrostatic potential inside the pore formed by the presence of the positively charged arginine and lysine residues. The binding sites/barrier regions deduced from the PMF profiles are denoted in Fig. 2.4 for the sake of comparison. The phosphate ion had a strong electrostatic interaction with the central binding site regions, P1 and P2, and also more favorable local interaction energies in minor binding sites (Fig. 2.4a). This indicates role of the electrostatic energy component in the formation of binding sites.

Similarly the two other anions, sulfate and chloride, experienced favorable electrostatic interactions inside the pore with stronger interactions in the binding site regions (Fig. 2.4b, c). Although the magnitudes of the electrostatic interaction energies were different for each anion, these difference could not be interpreted directly in terms of selectivity as it is necessary to take into account a loss of configurational entropy upon the binding of ions inside the pore which would lead to a penalty in the overall binding affinity [164]. These types of entropic penalties are the results of motional restrictions of the ions in the confined environment inside the channel and in particular in binding sites (see Fig. S5). The larger ions, $H_2PO_4^-$ and SO_4^{2-}, tended to have higher entropic penalties compared to small ions like Cl^-. In contrast to the anions, K^+ ions had unfavorable electrostatic energies, particularly in the central region of the pore where diameter was quite narrow (Fig. 2.4d). Based on these findings, it could be concluded that the overall electrostatic environment of the OprP channel conferred its anion selectivity.

To further understand the selectivity between different anions, a more detailed analysis of the interactions between permeating ions, water, channel and their interplay is required. For example, in the case of the KcsA channel, the selectivity for K^+ was suggested to be predominantly affected by the type of the ligands coordinating with the permeating ions (carbonyl oxygen of the channel versus water oxygen) in agreement with the so called "field-strength hypothesis" [15]. The main idea behind this hypothesis is that different type of coordinating ligands have varying intrinsic physical and electrostatic properties. Hence a change in their relative contribution may confer selectivity to a particular ion. We examined the coordination properties of the permeating ions through OprP. The first hydration shell for each of the four ions was determined based on their radial distribution

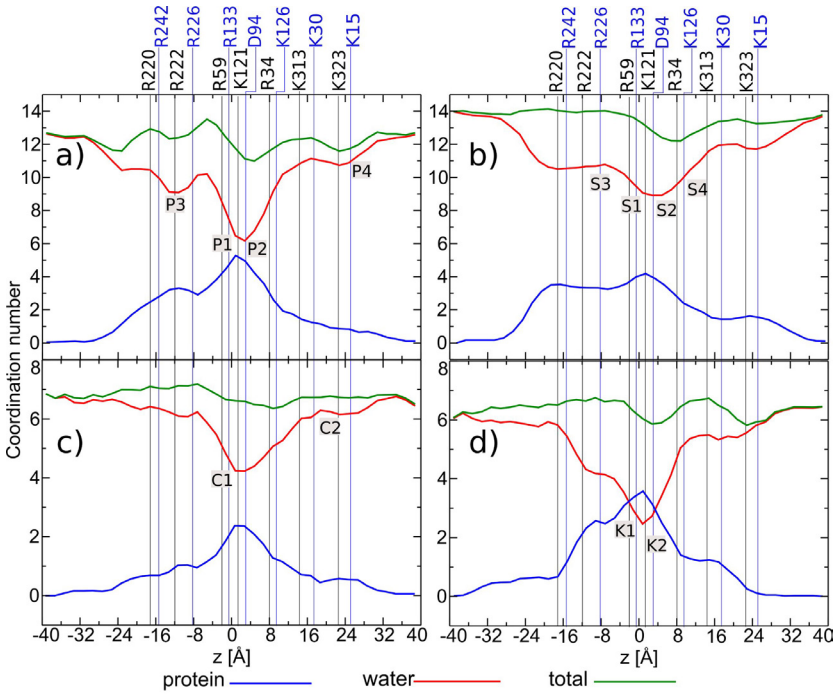

Figure 2.5.: Coordination numbers (protein and water contacts) for the permeation of a) $H_2PO_4^-$, b) SO_4^{2-}, c) Cl^-, and d) K^+ ions through OprP. The regions of binding sites/barriers are also labeled as per definition in the PMF profiles.

functions in the bulk region (see Appendix A, Fig. A3). Fig. 2.5 shows the coordination number profiles for each of the permeating ions along the length of the pore and extended towards bulk regions on both sides of the pore. The binding sites/barriers identified in the PMF profiles were also labeled here for the sake of comparison. The oxygen atoms of the water molecules versus the nitrogen atoms of the channel walls were considered as coordinating ligands for the three anions while in the case of K^+, oxygen atoms of the channel were considered instead of nitrogen atoms.

The average number of coordinating water molecules decreased as the permeating ions move from the bulk phase to the channel interior which was compensated by a higher number of protein contacts with the channel (Fig. 2.5). The total number of coordinating ligands (water versus protein) remained almost constant throughout the channel with minor fluctuations. It is also worth noting that there are pronounced similarities in the changes in water coordination and the corresponding PMFs shown in Fig. 2.2. As a general trend, ions tended to remove more water molecules from the hydration shell in the binding site/barrier regions which is compensated by a high number of protein contacts. For example, in the case of $H_2PO_4^-$, the largest number of water molecules was removed in the central binding site regions (P1 and P2) leading to a maximum protein contacts in this regions. Even changes in the number of water molecules were reflected in

similar changes in the PMF profiles as seen for P3 and P4.

In the context of suggested hypotheses of ion selectivity, the "over-coordination hypothesis" justified the selectivity for $H_2PO_4^-$ (coordination number: 13) and SO_4^{2-} (coordination number: 14) over Cl^- (coordination number: 7) but could not explain the selectivity of $H_2PO_4^-$ over SO_4^{2-}. In terms of the "field-strength hypothesis", the relative contribution from the type of coordinating ligands (water oxygen versus protein nitrogen) was different for both ions types indicating possible mechanisms for selectivity. The most prominent differences were in the central binding site regions (P1, P2 and S1, S2 for $H_2PO_4^-$ and SO_4^{2-}, respectively) where relative to SO_4^{2-}, $H_2PO_4^-$ had more contributions from the protein towards the coordinating ligands.

One interesting aspect of the anion-selective channels, particularly Cl^- channels, is that selectivity tends to follow the Hofmeister (lyotropic) series, i.e., weakly hydrated anions show higher permeability than those binding water molecules more strongly [165–167]. This indicates that the hydration energy is the limiting factor in determining the transport properties of Cl^- channels. In our study with the three studied anions, the Hofmeister series can be written as SO_4^{2-}>$H_2PO_4^-$>Cl^-. Sulfate has the strongest hydration and chloride the weakest. With OprP being a wider porin, the transport of smaller anions, e.g., Cl^-, might not always correspond to the removal of water molecules from the hydration shell, thus making the contribution of the lyotropic sequence towards the selectivity of small ions somewhat less important. However for larger anions, the selectivity of $H_2PO_4^-$ over SO_4^{2-} could well be explained in terms of this effect. It is energetically more costly to remove water molecules from the hydration shell of sulfate than from phosphate [168]. Furthermore, a larger amount of work is required to dehydrate an anion than a cation of similar size [169]. In this context, K^+ can shed its hydration shell water molecules more easily than Cl^-. This is reflected in Fig. 2.5d where K^+ stripped more water molecules compared to Cl^-, even though the overall electrostatic environment was not favorable for a positively charged ion. This led to a large energetic barrier for K^+ permeation through the channel (Fig. 2.2).

To this point, we have limited our discussion of ion selectivity of OprP to thermodynamic equilibrium factors which essentially drive ion-binding selectivity. However these channels are designed to allow the flow of ions. Hence kinetic factors play a role in determining the overall transport processes [15]. In particular we were interested to analyze the transitions of $H_2PO_4^-$ or SO_4^{2-} ions between the two central binding sites. The role of the residue K121 in the transfer of phosphate from site P1 to P2 has been previously discussed [121, 160]. In addition to K121, the role of D94 also needs to be investigated

in such transition processes as this aspartate side chain can form hydrogen bonds with the permeating phosphate ion in its monobasic form. The strategically important position of D94 closer to site P2 in OprP (2.1c) also provides an opportunity to help phosphate ions to be knocked out of binding site P2 in addition to assisting their transition between the two central binding sites. A similar kind of interaction was not possible in the case of SO_4^{2-} due to the absence of any hydrogen bond donor.

As expected, we observed a positive correlation between the z positions of K121 and $H_2PO_4^-/SO_4^{2-}$ (Fig. 2.6. It indicated that the dynamics of K121 was coupled to the permeating ions and established its role in transferring these two ions from one central binding site to the other (see Appendix A for details). A similar analysis with the D94 residue showed a positive correlation for $H_2PO_4^-$ but a lack of any correlation with SO_4^{2-} (Fig. 2.6). Correlated movements between D94-$H_2PO_4^-$ (one-sample t(26)=2.98, p=0.006), K121-$H_2PO_4^-$ (one-sample t(26)=2.26, p=0.032), K121-SO_4^{2-} (one-sample t(27)=2.05, p=0.049) were found to be statistically significant while non-significant in the case of D94-SO_4^{2-} (one-sample t(27)=0.80, p=0.428). These findings indicate a possible additional contribution of D94, in conjunction with K121, to transit $H_2PO_4^-$ between two central binding sites. This observation was also reflected in the PMF profiles where SO_4^{2-} had an energetic barrier of ∼4 kcal/mol (from S1 to S2) compared to the smaller energetic barrier of ∼2 kcal/mol (from P1 to P2) for $H_2PO_4^-$. Hence the presence or absence of H-bond donors for the permeating ion can influence the energetic costs for

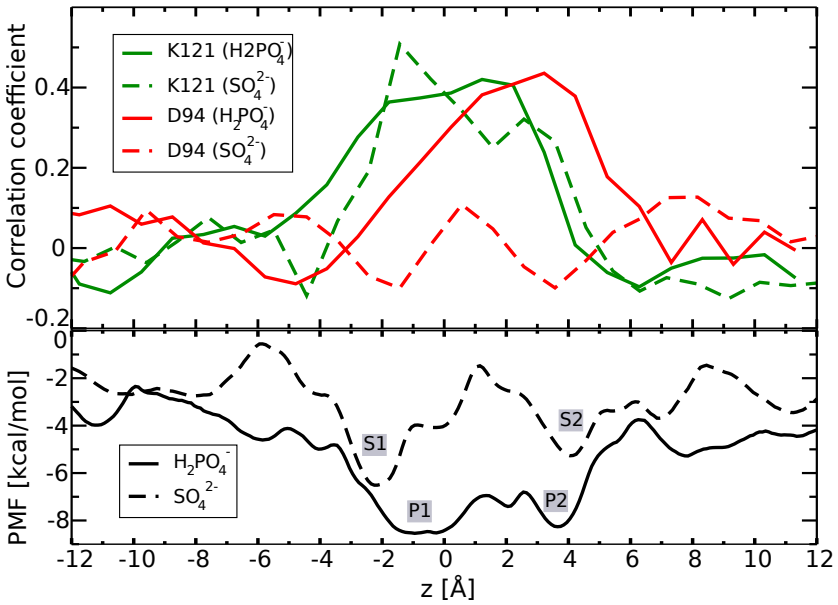

Figure 2.6.: Correlated movement of permeating $H_2PO_4^-$ and SO_4^{2-} ions with K121 and D94. Respective PMFs for both ions in central bindings sites regions are also shown for the sake of comparison.

ion transfer between the two central binding sites via interactions with D94 and thereby may alter the permeation rates. The functional importance of D94 is also reflected in the evolutionary process as it is conserved among the orthologs of OprP in different Pseudomonas species (see Appendix A, Fig. A5).

2.3. Conclusions

In conclusion, we have probed the selectivity of OprP using full atomistic free-energy MD simulation studies. PMF profiles for the permeation of four different ions were obtained. The selectivity of OprP was discussed in the context of well-studied ion channels, especially the K^+ channel KcsA and anion-selective Cl^- channels. The generalized mechanisms of selectivity for OprP can be summarized as a coarse-to-fine scheme in the following order:

1. Although OprP is lined by flexible amino acid side chains ("brush-like" nanopore), the first level of selectivity can be explained based on the "size-exclusion" principle which is also the case for non-selective porins like OmpF.
2. Discrimination between cations and anions is conferred by the overall electrostatic environment of the channel.
3. The selectivity between ion types of the same charge (cations or anions) results from a fine-tuned balance of interactions between permeating ions and water as well as protein atoms and their corresponding interaction strengths.

In addition, kinetics factors are also important in determining the overall transport properties of ions through a channel. Future studies can be directed towards investigating the role of individual important amino acid residues, e.g., those from binding site regions or the arginine ladder, in determining the selectivity and transport properties of OprP. This kind of study might help to delineate detailed structure-function relationship of this porin in particular and broaden our present understanding of ion selectivity of different channels in general.

Acknowledgments

This work has been supported by grants KL 1299/6-1 and BE 865/16-1 of the Deutsche Forschungsgemeinschaft (DFG).

Supporting Information

Details regarding system setup, simulation parameters and analysis of the results are given in Appendix A.

3. Role of the Central Arginine R133 of OprP: Effects of Charge and Solvation

Abstract

The outer membrane porin OprP of *Pseudomonas aeruginosa* forms a highly specific phosphate selective channel. This channel is responsible for the high-affinity uptake of phosphate ions into the periplasmic space of the bacteria. A detailed investigation of the structure-function relationship of OprP is inevitable to decipher the anion and phosphate selectivity of this porin in particular and to broaden the present understanding of the ion selectivity of different channels. To this end we investigated the role of the central arginine of OprP, R133, in terms of its effects in selectivity and ion transport properties of the pore. Electrophysiological bilayer measurements and free-energy molecular dynamics simulations were carried out to probe the transport of different ions through various R133 mutants. For these mutants the change in phosphate binding specificity, ion conduction and anion selectivity was determined and compared to previous molecular dynamic calculations and electrophysiological measurements with wild-type OprP. Molecular analysis revealed a rather particular role of arginine 133 and its charge, while at the same time this residue together with the network of other residues, namely D94 and Y114, has the ability to dehydrate the permeating ion. These very specific features govern the ion selectivity of OprP.

Reproduced with permission from the article by Modi, N.; Bárcena-Uribarri, I.; Bains, M; Benz, R; Hancock, R. E. W; and Kleinekathöfer, U., "Role of the Central Arginine R133 toward the Ion Selectivity of the Phosphate Specific Channel OprP: Effects of Charge and Solvation", *Biochemistry*, **2013**, 52(33), pp 5522-5532 (DOI: 10.1021/bi400522b). Copyright [2013] American Chemical Society.

The experimental work presented in this chapter has been performed by Ivan Bárcena-Uribarri and Manjeet Bains in the groups of Prof. Dr. Roland Benz, Jacobs University Bremen, and Prof. Dr. R.E.W. Hancock, University of British Columbia.

3.1. Introduction

The outer membranes of Gram negative bacteria act as molecular filters. The filter function is mainly due to the presence of a certain class of membrane proteins called porins [133]. Porins have a β-barrel architecture and form water-filled, membrane-spanning channels that permit the passage of charged and neutral solutes including ions across the bacterial outer membrane into the periplasmic space. Most porins form relatively nonspecific general diffusion pores (e.g., OmpF and OmpC of *E. coli*) whereas some act as substrate-specific channels such as those selectively transporting carbohydrates (LamB and ScrY of *E. coli*, OprB of *P. putida*), nucleosides (Tsx of *E. coli*) or phosphate ions (OprP of *P. aeruginosa*)[133]. A molecular analysis of the substrate specificity of these porins is inevitable in order to understand the corresponding structure-function relationship as this has major implications that go far beyond biological systems, e.g., in the design of substrate-specific synthetic nanopores with diverse functions [8, 170]. Electrophysiological experiments complemented by all-atom molecular dynamics simulations provide an excellent platform to investigate the functions and selectivity of these porins and to understand, for example, ion [3, 25, 27, 28, 161, 171] or antibiotics transport [143, 144, 146, 147].

Under phosphate limitation or starvation condition *Pseudomonas aeruginosa* induces the protein OprP in its outer membrane for high-affinity uptake of phosphate ions [156]. The selectivity of OprP for phosphate represents an interesting example of substrate specificity for which various details are still unknown. The OprP channel is an exception among the substrate-specific porins because of its anion selectivity and in particular because of its a high phosphate selectivity. The OprP crystal structure reveals a trimeric form of the porin in which each monomer consists of 16 β-strands and extracellular, as well as periplasmic, loops [160]. In particular, the loops L3, L5,and T7 fold into the lumen of the pore and are responsible for the constriction regions inside the pore (Fig. 3.1a). Important structural features that determine the anion selectivity of the channel are the so-called arginine ladder including residues R218, R220, R242, R222, R226, R59, R60 and R34 that extends from the extracellular side down the channel to the middle of the pore and a lysine cluster including residues K13, K15, K25, K30, K74, K109, K313, K323, K378 on the periplasmic side of the channel (see Fig. 3.1). Two central phosphate binding sites are formed by residues D94, Y62, S124, S1235, K121, K126, R34, and R133 [160].

Our previous electrophysiological experiments suggested that phosphate permeation is ∼20 higher than the chloride transport [157–159]. This was largely attributed to an

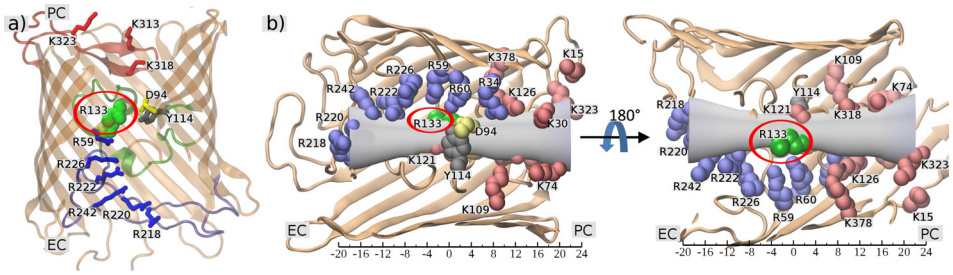

Figure 3.1.: Structural features of OprP. a) An OprP monomer is shown with loops L3 (green), L5 (blue) and T7 (red) which lead to a narrow pore. Important residues along the pathway of the pore are shown as sticks (Arg - blue, Lys - red, Asp - yellow, Tyr - gray) and Arg133 as green colored spheres. EC and PC denote the extracellular and periplasmic sides of the pore, respectively. b) The monomer pore is shown together with a gray hourglass shape to demonstrate the approximate radius of the pore in the different regions and to indicate a possible ion permeation pathway. Important residues, including Arg133, are labeled and mapped to their position along the z axis.

100-500 fold higher binding affinity of OprP for phosphate compared to chloride. Recently, we also probed the ion selectivity of wild-type OprP utilizing all-atom molecular dynamics free-energy calculations [172]. In that study the transport properties of various ions was compared by determining the potential of mean force (PMF) profiles. Molecular details for the selectivity of OprP were revealed and also discussed in the context of well-studied ion channels like potassium or chloride selective channels. The porin OprP and especially its selectivity was also investigated by Sansom and coworkers using molecular dynamics simulations [121] and employed as a template for possible artificial nanopores [173].

To enable further understanding of the structure-function relationships of this specific porin, the contributions of individual residues, that are likely to be relevant to the selectivity of OprP, need to be investigated. To this end, we investigated the role of one of the most important residues of the central binding sites, arginine 133 (R133), towards the selectivity of OprP. R133 is strategically located in the central region of the pore (see Fig. 3.1) and is reported to form interactions with the phosphate ion in both central binding sites [160]. Its positive charge, large side chain and H-bond donor capacity makes it probably one of the most influential residues for controlling the selectivity and governing the corresponding molecular interactions. In addition, its functional importance is also evident in the evolutionary process as R133 is conserved among the orthologs of OprP in different Pseudomonas species (see Appendix B, Fig. B1). Three mutants of OprP were generated as listed in Table 3.1: R133E (charge inversion - positive to negative charge), R133Q (positive to neutral charge, large side-chain compared to alanine) and R133A (positive to neutral charge, small side chain) where the letters R, E, Q, and A represent the amino acids arginine, glutamate, glutamine and alanine, respectively.

Electrophysiological experiments with planar lipid bilayer were performed to understand the transport of different ions through OprP and to obtain binding constants for phosphate-mediated inhibition of chloride transport. These experiments were complemented by free-energy molecular dynamics simulations to probe the molecular details. The findings were compared with results for wild-type (WT) OprP to understand the contribution of R133 towards the selectivity of OprP.

3.2. Materials amd Methods

3.2.1. Experimental details

Bacterial strains and growth conditions

Escherichia coli strain DH5α (Invitrogen, CA, United States) was used as a host for clones containing the OprP expression plasmid pAS27 [174] and the various plasmids containing an OprP single mutations. *E. coli* CE1248 [175] - which lacks the major porins OmpC, OmpF and PhoE - was used in all expression studies to facilitate the purification of the OprP mutants. *E. coli* CD1248 cells harboring the various plasmids were inoculated from Luria-Bertani agar plates (Fisher Scientific, Canada) containing 100 μg/ml ampicillin (Sigma, Canada) directly into 1.0 liter of Luria-Bertani broth supplemented with 100 μg/ml ampicillin and 0.4 % glucose to impede the expression of LamB. The cells expressing the different OprP mutants were induced once they reached an OD600 of 0.5-0.8 with 0.8 mM of IPTG and further cultivated overnight. Afterwards, the cells were harvested by centrifugation at 8,000 x g for 10 min.

Site-directed mutagenesis and sequencing of OprP mutants

OprP	Codon	5′-3′ Primer	Protein side chain
R133 (WT)	CGC	not mutated	-CH2-CH2-CH2-NH-C(NH2)-NH
R133E	GAG	CCGCGCTGGAG**GAG** AACCTCACCTACG	-CH2-CH2-COOH
R133Q	CAG	CACCGCGCTGGAG**CAG** AACCTCACCTAC	-CH2-CH2-CO-NH2
R133A	GCC	CCGCGCTGGAG**GCC** AACCTCACCTACG	-CH3

Table 3.1.: Mutants designed to study the role of the amino acid R133 in ion selectivity and phosphate substrate specificity. The codons of the wild type and mutants are indicated as well as the primers used to mutate them. The side chains of the different amino acids are also shown.

The pAS27 plasmid was individually mutated using the Quick-Change® mutagenesis kit (Stratagene, USA) following the manufacturer instructions. The primers used to perform the single mutations are described in Table 3.1. For each amino acid substitution two complimentary primers containing the desired mutation were designed according to guidelines in the QuikChange XL Site-directed Mutagenesis manual, and synthesized by AlphaDNA (Montreal, Canada). Mutagenic codons containing mismatches that corresponded to the substitution mutation in the encoded amino acid sequence of OprP are also listed in Table 3.1. Each of the mutagenized OprP constructs was sequenced by the Nucleic Acid Protein Service Unit (University of British Columbia, Vancouver, Canada) to ensure they had the correct mutant sequence and no additional mutations.

Protein extraction and purification

The *E. coli* CE1248 pellets obtained after cultivation were resuspended in 10mM Tris-HCl pH 8.0 containing 20% sucrose and 50 μg/ml DNase 1. The resuspended cells were incubated at 23 °C for 10 min and then placed on ice and lyzed two times by passage through a French pressure cell at 15,000 psi; unbroken cells were removed by centrifugation at 5,000 x g for 10 min at 4 °C. The supernatants were layered onto a 2-step sucrose gradient (50% and 70%) and centrifuged in a SW28 swinging bucket rotor at 23,000 rpm for 18 hours at 4 °C. Once the fraction containing the outer membranes was collected, the concentration of sucrose was diluted to below 20% with distilled water and the membranes were pelleted in an ultracentrifuge at 41,000 rpm at 4 °C for 1 hour. The outer membranes were then washed once with water. The proteins present in the outer membranes were solubilized first with a buffer containing 10mM Tris HCl pH 8.0 and 3% tetraoxyethylene n-octyl ether (C8E4) (Bachem Inc., USA), followed by this buffer with the addition of 10 mM EDTA, pH 8.0 and then with added 1.0 M NaCl. The solubilized fractions were analyzed by SDS-PAGE and OprP was predominantly found in the fraction solubilized with 10mM Tris-HCl pH 8.0, 3% C8E4 and 10mM EDTA. The selected fraction was then diluted to obtain a final C8E4 concentration of 0.6%. Subsequently, the OprP native and mutant proteins were purified using a NaCl gradient applied to a MonoQ column on a FPLC system (Pharmacia, United States). The OprP protein eluted at a salt concentration of 250-300 mM NaCl. The presence of the protein was checked using SDS-PAGE and Western immunoblotting.

Sodium dodecyl sulfate-polyacrylamide gel electrophoresis (SDS-Page) and Western immunoblotting (WB)

To check the expression of the OprP mutants and its purification, whole cell lysates of *E. coli* CE1248 or the FPLC fractions were loaded onto a 12% SDS polyacrylamide gel and electrophoresed. The gels were stained with Coomassie blue or transferred to polyvinylidene fluoride (PVDF) membranes and incubated with monomer-specific anti-OprP rabbit serum as previously described [174]. *E. coli* CE1248 harboring pAS27 was used as a positive control and *E. coli* CE1248 harboring the vector plasmid pTZ19U (Pharmacia, USA) was used as a negative control.

Black lipid bilayer: single channel conductance, zero current measurements and phosphate titration

The black lipid bilayer assay has been previously described [176]. An artificial membrane was spread over a 0.5 mm^2 hole dividing two compartments of a Teflon cuvette. The artificial membranes were formed using a solution of 1 % diphytanoylphosphatidylcholine (DiPhPC) in n-decane (Avanti Polar Lipids, Alabaster, AL). Both compartments are filled with a salt solution (0.1M KCl). Two Ag/AgCl electrodes with salt bridges switched in series were immersed in each compartment of the the membrane cell. One of the electrodes was connected to a home-made voltage source and the other to a home-made amplifier/filter based on a Burr-Brown operational amplifier. The output signal of the amplifier was monitored with a digital oscilloscope and a strip chart recorder (Rikadenki Electronics, Germany). For single channel conductance and titration experiments, a +50 mV voltage was applied to the electrode connected to the voltage source.

Measurements to study inhibition of chloride conductance mediated by phosphate binding to the binding sites were performed for OprP and the R133 mutants as previously described [177, 178]. The aqueous phase contained 0.1M KCl, 10 mM MES at pH 6 in these experiments. The protein was added to the membrane cell under stirring conditions The membrane conductance increased for about 30 minutes due to reconstitution of OprP and its mutants. Once the conductance was stable and did not increase further, at that time small amounts of concentrated phosphate solutions (pH 6) were added to both sides to study inhibition of chloride conductance by binding of phosphate to the binding site. This could be detected by the reduction of the membrane conductance. After progressive increments of the phosphate concentration under stirring, the half saturation constant for chloride conductance through OprP and its mutants as mediated by phosphate binding was calculated using the Michaelis-Menten equation [177, 179].

Zero current measurements to study the ion selectivity were performed as described elsewhere [176, 180]. An electrochemical gradient was progressively established by adding a 0.5M KCl, LiCl or KAc solution to the cis-side and 0.1 M of the same salt to the trans-side of the membrane cell. The aqueous salt solutions were buffered with 10 mM HEPES, pH 6, if not indicated otherwise, T=20°. The generated potentials were measured with a high-impedance electrometer (Keithley 617) connected to the trans-side electrode under zero current conditions.

3.2.2. Computational details

Molecular dynamics system setup

A trimer of OprP (PDB code 2O4V) [160] was embedded into a palmitoyloleoyl-glycero-phosphathidyl ethanolamine (POPE) lipid bilayer that was constructed from pre-equilibrated patches using VMD [181]. Subsequently, the system was solvated using TIP3P water molecules. The R133 residues in each of the monomers were mutated to glutamate (E), glutamine (Q) or alanine (A) to generate the three mutant systems R133E, R133Q, and R133A, respectively. Each of the three systems was subjected to 5000 steps of energy minimization to remove unfavorable sterical contacts followed by a ∼5 ns equilibration run. One of the three studied ions (phosphate, chloride and potassium), was subsequently placed at the mouth of the one of the monomers on the extracellular side for each of the mutants (9 different systems systems considering the different combinations between three ions and three mutants). As already done in our WT OprP study [172], the monovalent form of the phosphate ion, $H_2PO_4^-$, was chosen since phosphate is predominantly monobasic at pH 6 of experimental measurements. All nine systems were neutralized by addition of potassium ions and each system contained ∼120,000 atoms.

Molecular dynamics simulation parameters

The simulations were performed in the NPT ensemble with the program NAMD 2.8 [131] and the CHARMM27 force field [95] along with additional force field parameters for $H_2PO_4^-$ [182]. The temperature of 310 K and the pressure of 1 atm were maintained in all the simulations using Langevin dynamics along with a Langevin piston algorithm. Periodic boundary conditions were used in the simulations. Short-range nonbonded interactions were calculated using a cutoff of 12 Å and a switching distance of 10 Å. The long-range electrostatic interactions were accounted for using the particle mesh Ewald method [183]. Bonded interaction were evaluated every 1 fs. Short-range nonbonded and long-range electrostatic interactions were evaluated at every 2 fs and 4 fs respectively using the

r-RESPA multiple time step method [184]. Bond constraints were applied to all water hydrogen atoms with the SHAKE algorithm [185] .

Free energy calculations

The adaptive biasing force (ABF) approach [162, 163, 186] as implemented in the *collective variable* module of the NAMD 2.8 program [131] was applied to determine the effective free energy profiles for the transport of different ions through OprP mutants. The principal axis of the channel was aligned parallel to the z axis and the reaction coordinate was assigned to be the z position of the ion. Moreover; the change in free energy was determined with respect to the bulk value. The full reaction coordinate with a length of ∼84 Å along the z axis was subdivided into 21 windows with a length of 4 Å each to enhance the sampling efficiency. This range of reaction coordinate along the z axis also consisted of extended bulk regions on both sides of the channel. The initial starting conformations of the system for each window were retrieved by constant velocity steered molecular dynamics (SMD) simulations wherein each studied ion was dragged through the channel along the z axis. In the ABF method, the average force acting on the respective ion was accumulated in 0.1 Å sized bins within each window. In addition, the application of the adaptive bias was initiated only after 800 samples were accumulated in the individual bins to address the issue of the fluctuations of the instantaneous forces and to calculate a reasonable starting estimation of the biasing forces. Later on, the resulting data were integrated to generate the potential of mean force (PMF) profiles. Production runs in each window were carried out for at least 6 ns while considerably extended runs were performed for about 15-20 ns in the central binding site windows (-10 to 10 Å). This lead to production runs of ∼160 ns for each ion and a total simulation time of ∼1.4 µs for all nine systems in total (three ions and three mutants).

3.3. Results and Discussion

As shown in Table 3.2, electrophysiological bilayer experiments showed that the single channel conductance (G) of the OprP channel suffered an extreme reduction for all of the three mutants. The channel conductance went down from 160 pS in 0.1 M KCl measured for the wildtype (WT) protein to a conductance of between 5 and 12 pS for the three R133 mutants. Furthermore, a drastic increase of the apparent dissociation constant (half saturation constant, 1/K) was observed when the OprP mutants were used to study the inhibition of chloride conductance by adding phosphate to the membrane cell (Table 3.2). Charge inversion mutation, R133E, and the mutation of arginine to

OprP	**G (pS)** (KCl)	Half saturation constants of chloride conductance inhibition by phosphate (1/K) (10^{-3}M)	Stability constants of chloride conductance inhibition by phosphate (K) (1/M)
R133 (WT)	160	1.2	820±160
R133E	8	45	22±1.8
R133Q	5	33	30±2.2
R133A	12	50	20±1.9

Table 3.2.: Single channel conductance and half saturation constants of chloride conductance inhibition by phosphate binding for WT OprP and mutants. The single channel conductance was obtained in 0.1 M KCl, 10 mM MES, pH 6, T=20 °C and applying 50 mV voltage. The stability constant for chloride conductance inhibition by phosphate was obtained from titration experiments with the OprP WT and mutant channels mediated conductance, using the Michaelis-Menten equation described elsewhere [177]. The phosphate solution had a pH of 6. Mean value of at least three individual titration experiments are shown.

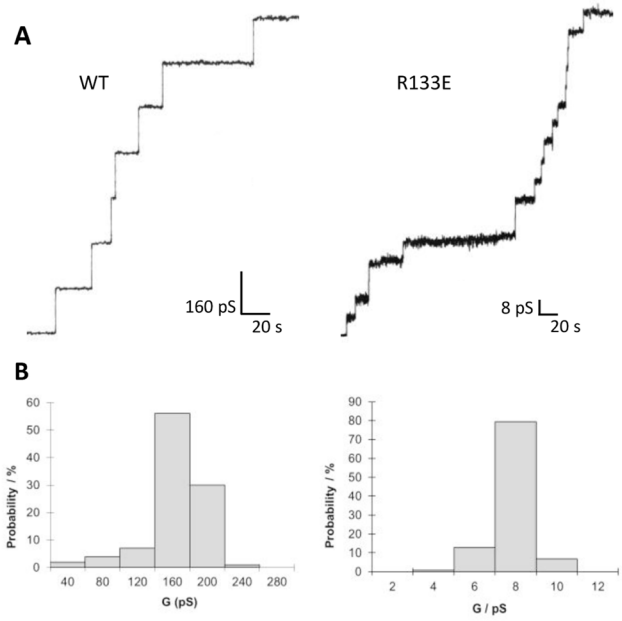

Figure 3.2.: Single channel activity of OprP wildtype (WT) and the R133E mutant. A) Step-wise increase in conductance produced by individual insertions in a DiPhPC membrane. Time and conductance for each measurement are shown by the scale. Different scales were used to optimize the resolution of the single channel conductance for each sample. B) Histograms summarizing the conductance (G) in picosiemens (pS) of the single channel events observed for WT OprP (left) and R133E mutant (right). The measurements were performed in 0.1 M KCl, 10mM MES, pH 6, 20 °C with an applied voltage of 50 mV.

neutral alanine with a small side chain, R133A, led to to the weakest inhibition of chloride conductance by phosphate with ∼40 increase of the half saturation constant as compared to WT (Table 3.2). The other mutation, R133Q, in which positively charged arginine was replaced by the neutral glutamine with a large side chain, also resulted in a weaker binding of phosphate with an increase of the half saturation constant by a factor of about 30 (Table 3.2). This findings indicate the critical importance of the positive charge at this particular position of OprP in assigning the high phosphate specificity to the pore. If the length of the side chain had any effect on phosphate binding is difficult to say because electrostatic effects seem to play an extremely high role in the phosphate binding process. It is also difficult to say if there exists a significant difference in half saturation constants between all three R133 mutants.

	Permeability ratios P_a/P_c (V_m [mV])			
Electrolyte	**R133**	**R133E**	**R133Q**	**R133A**
KCl	>70 [159]	28 (-37.3 ± 0.9)	17 (-35.1 ± 3.6)	29 (-37.4 ± 2.4)
LiCl	>100	22 (-36.3 ± 0.6)	25 (-36.9 ± 1.9)	15 (-34.3 ± 1.0)
KAc (pH 7)	>100	6 (-27.0 ± 0.3)	62 (-39.4 ± 0.4)	32 (-37.7 ± 1.3)

Table 3.3.: Zero-current measurements to study the ion selectivity of OprP and the R133 mutants. The experiments were carried out for five-fold gradients (0.1 M *versus* 0.5 M) of three different salts. The ratio of anions to cations permeability, (P_a/P_c) was calculated using the Goldmann-Hodgin-Katz equation [176] from at least three individual experiments. The zero-current membrane potential, V_m, is defined as the difference between the potential at the dilute side and the concentrated side of salt solutions.

Additionally zero current measurements were carried out to study possible changes in the ion selectivity of the R133 mutants compared to the WT. After establishing a 5-fold concentration gradient across the membrane, the electrical potential difference was measured using an electrometer. In previous studies [159], the WT OprP protein displayed an anion to cation permeability ratio, P_a/P_c, of greater than 70 in KCl (Table 3.3). Hydrated K^+ and Cl^- have approximately the same hydrodynamic radius and therefore a similar size. This permeability ratio indicates a clear preference of the OprP channel for anions. In a similar manner, the ion selectivity in KCl was also analyzed for the R133 mutants in this study. R133E/Q/A mutants retained the overall anion selectivity of the channel. However, the mutants showed a decrease in anion selectivity with the permeability ratio, P_a/P_c, dropping from >70 for the WT to about 20-30 for the different mutants as listed in Table 3.3. The decrease of selectivity between OprP wildtype and the three R133 mutants is significant. However, the diffusion potentials (V_m) observed with all three mutants are in a range where small errors in the potential measurements results

in large changes of permeability ratio. This means that difference of permeability ratio between the three R133 mutants is presumably not significant. To support the results obtained for KCl, the measurements were repeated using lithium chloride (LiCl) and potassium acetate (KAc). Also for these salts, the R133 mutants showed a decrease in the anion selectivity of the channel compared to WT.

To further probe the molecular factors behind the influence of R133 on the phosphate binding, all-atom free-energy molecular dynamics simulations were performed. One-dimensional potential of mean force (PMF) profiles were calculated (see Materials and methods for details) to quantify the changes in the free energy associated with the transport of the different ions through the OprP mutants R133E/Q/A. In a previous study we had already derived similar profiles for the transport of ions through WT OprP [172]. Here we compare our new results obtained with mutants to the WT data to enable discussion of the relative contribution of R133 towards the ion selectivity of OprP. The PMF profile for the transport of $H_2PO_4^-$ through WT OprP had revealed two energetically favorable central binding site regions with an energy well depth of $\sim$ 8 kcal/mol (see Fig. 3.3a) [172]. Contrary to the WT results, the $H_2PO_4^-$ transport through the R133E mutant indicated a complete inversion of the PMF profile in which the energetically favorable central binding site region was replaced by a central barrier with a height of $\sim$7 kcal/mol as shown in Fig. 3.3a. R133E is a charge inversion mutation in which the positive charge of arginine was replaced by the negative charge of glutamate. This numerical finding already demonstrates the importance of residue R133 in making phosphate transport through the OprP channel energetically favorable.

Subsequently R133 was mutated to the neutral glutamine (Q) with a relatively large side chain and the similarly neutral alanine (A) but with a very small side chain to further understand the effect of charge and size of the residue. The R133Q and R133A mutants also showed a barrier to $H_2PO_4^-$ transport, albeit the barrier heights were smaller, i.e., 4 kcal/mol and 3 kcal/mol for R133Q and R133A, respectively, cf. that of R133E showing a 7 kcal/mol barrier (see Fig. 3.3a). Changes in the charge of a residue at position 133 from positive (R) to neutral (Q or A) to negative (E) and the associated large changes in the PMF profiles for the $H_2PO_4^-$ transport are a strong indication of the importance of specific charges towards the ion selectivity at this particular position of OprP. Moreover, the barrier height for R133Q was $\sim$1 kcal/mol higher than that for R133A which indicates the influence, on ion-selectivity and transport, of the size of the side chain and consequently steric factors, albeit that the effect was small compared to the charge effects. In addition, based on the PMF profiles, we calculated the dissociation constants ($1/K$) for the $H_2PO_4^-$

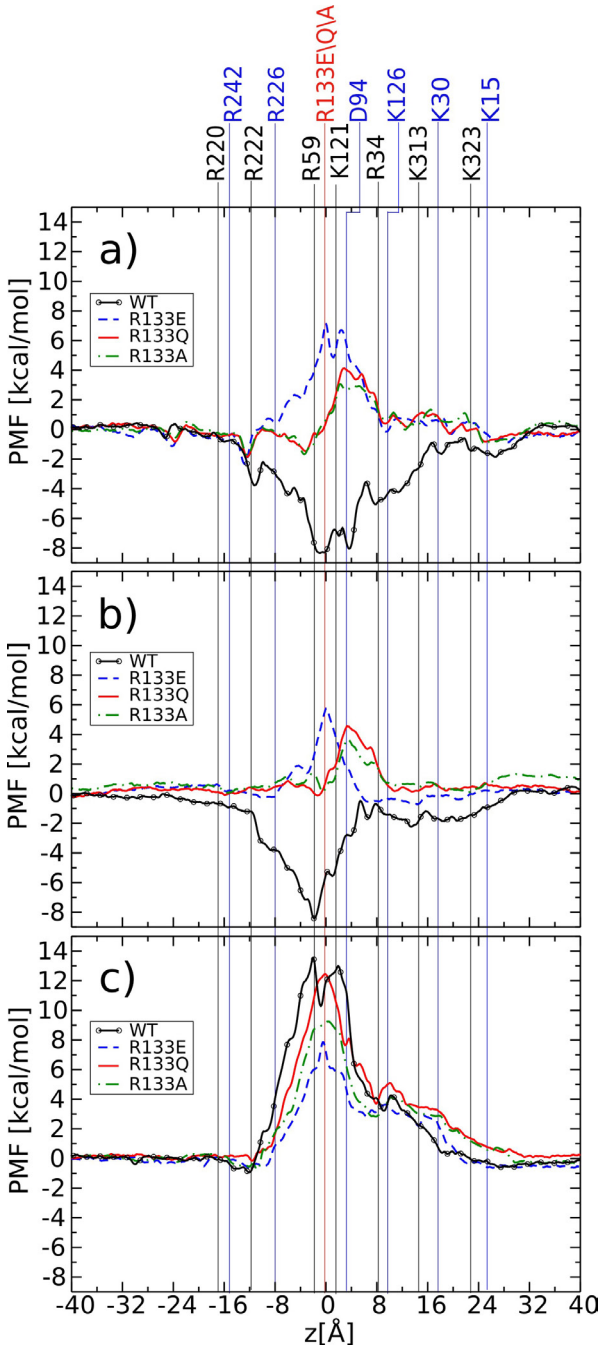

Figure 3.3.: PMF profiles for the permeation of a) $H_2PO_4^-$, b) Cl^-, and c) K^+ ions through the OprP mutants R133E, R133Q, and R133A. Th PMFs for the WT channel are shown for comparison [172]. Important residues of OprP along the ion permeation pathway are mapped onto the PMF profiles with respect to their positions along the z axis.

transport through OprP mutants to compare with experiments. To this end, the same method discussed in Ref. 172 was used to calculated the dissociation constants. The calculated dissociation constants were found to be 8.6 mM, 3.82 mM, 5.4 mM, and 0.23 μM for R133E, R133Q, R133A ,and WT OprP, respectively. While these values were not in quantitative agreement with the experimentally determined half saturation constants, qualitatively they showed a similar trend. For example, in simulations we observed a drastic reduction in phosphate binding affinity from WT OprP to all R133 mutants as was the case with experiments (Table 3.2). In addition, difference between the binding affinity of phosphate to the three R133 mutants is not significant in simulations which is in agreement with the experiments (Table 3.2).

Cl^- transport through the R133E mutant (Fig. 3.3b) also showed an inversion of the PMF with a barrier height of $\sim$ 6 kcal/mol. The WT OprP channel had a single central binding site with a well depth of $\sim$ 8 kcal/mol [172]. In contrast, the R133Q and R133A mutations resulted in barrier heights of approximately 4 kcal/mol and 3 kcal/mol for Cl^-, respectively. The qualitative rank order of the barrier heights among the studied mutants for the Cl^- transport was consistent with that assessed for the $H_2PO_4^-$ ion. The R133E mutant has the highest barrier height and the R133A variant the lowest. These Cl^- transport findings can be interpreted in a manner similar to that for the $H_2PO_4^-$ transport, indicating the effects of charge and steric factors on the PMF profiles. Here we would like to point out that PMF calculations for membrane proteins are also reported to be affected by simulation details such as the finite system size and the use of non-polarizable force fields especially for the lipid hydrocarbons of the membrane [127]. Sometimes these shortcomings might lead to over-estimation of barrier heights. Since we are focusing on relative comparisons of PMF profiles, these problems will be much less severe in the present case. The PMF profiles for the $H_2PO_4^-$ and the Cl^- transport through R133 mutants consistently proved that any change in this particular residue led to a channel that was devoid of anion-binding capacity. This finding is also reinforced by the drastic reduction in experimental phosphate stability constants as listed in Table 3.2 for the R133 mutants.

Such drastic changes in PMF profiles for anions transport through the R133 mutants, particularly R133E, makes the transport of the cation, K^+, very intriguing. In our previous study of the WT pore [172], K^+ had to overcome a huge energetic barrier of $\sim$13 kcal/mol as seen in Fig. 3.3c. It is interesting to examine if the R133E mutant can experience a similar PMF inversion for a cation as is observed for anions. As shown in Fig. 3.3c, the PMF profile for K^+ transport through the R133E mutant revealed a reduction in the barrier height from 13 kcal/mol to 7 kcal/mol but not a complete PMF inversion. Based on these

findings, it can be stated that the R133E mutation might be required to make the OprP channel cation selective but is not by itself sufficient. In the case of R133Q, the barrier height for K^+ transport was similar to that of the WT and has a value of 9 kcal/mol for the R133A mutant.

The PMF profiles for K^+ and Cl^- transport through R133 mutants also explained a drastic reduction in the KCl conductance from 160 pS for WT to 5-12 pS for mutants in electrophysiological experiments (see Table 3.2). Both K^+ and Cl^- ions have to pass energetic barriers in order to travel through the mutant pores which make their transport less favorable leading to a reduced conductance. While in the case of the WT channel, Cl^- had an energetically favorable binding site region within the pore, as depicted in Fig. 3.3b, and a major part of the conductance is contributed by chloride ions. Moreover, the PMF profiles obtained are consistent with the ion selectivity measurements reported in Table 3.3 . The electrophysiological measurements indicated that the R133 mutants maintain a preferences for anions but this property is less pronounced than observed in the WT. The preference for anions of the respective mutant channels was supported by the PMF profiles whereby for all the R133 mutants, K^+ ions had a higher energetic barrier to pass than did the Cl^- ions (see Figs. 3.3b,c). The reduced preference for anions by R133 mutants compared to WT OprP could be explained by the fact that in the WT channel, a large difference exists between PMFs of Cl^- and K^+ while in the case of mutants, these differences are less pronounced (Figs. 3.3b,c))

In addition to the PMF profiles, the contribution of individual energy components, namely the electrostatic and the van der Waals interactions, to the differential selectivity and binding of ions between various R133 mutants was determined. For this purpose, the pore was divided into 1 Å bins and average energies between the permeating ion and the channel were calculated, with a cutoff distance of 12 Å using the NAMDenergy plugin. A similar analysis in our previous study with respect to the WT pore showed that the electrostatic components of the energy are the major factor in determining the anion selectivity of the channel, with minor contributions from the van der Waals interactions [172]. For the mutants also, the electrostatic interactions turned out to be the most dominating factor that impacted on the differential binding and selectivity of ions for the different mutants. The van der Waals interaction energies were very small (data not shown). In the case of $H_2PO_4^-$ transport through the R133E channel, the ion experienced unfavorable electrostatic interactions in the central region of the pore, in contrast to the very favorable energies obtained for the WT case as shown in Fig. 3.4a. For R133Q/A, the electrostatic energy components were similar to the bulk region, but

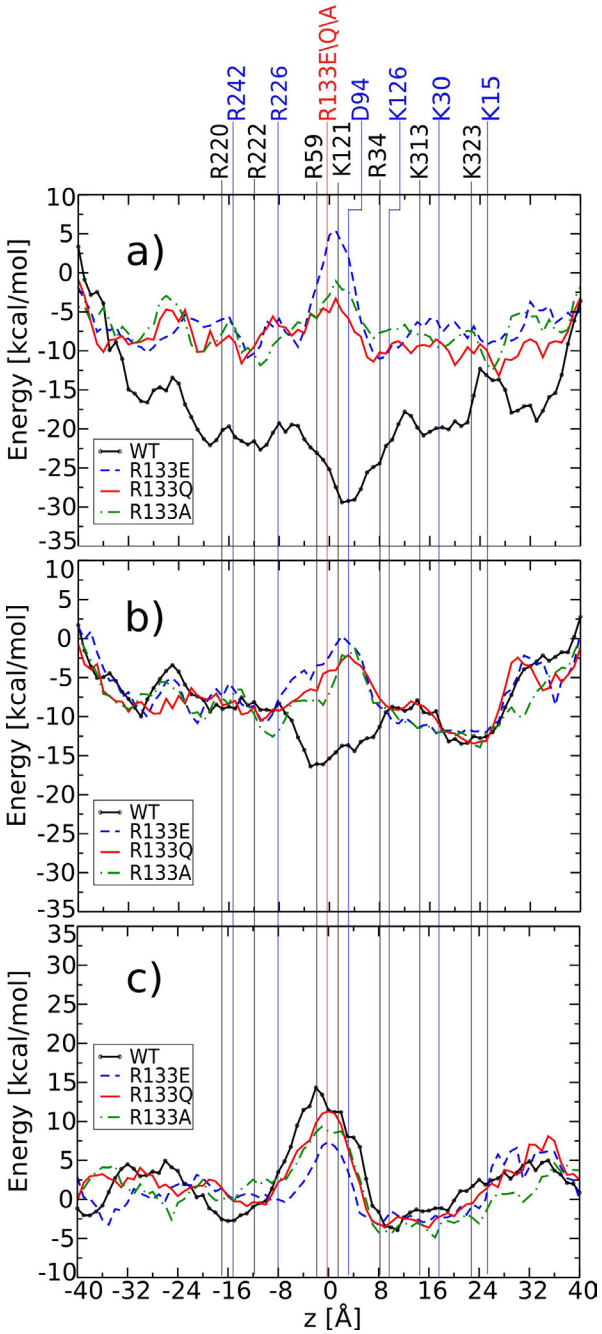

Figure 3.4.: Electrostatic interaction energy for the a) $H_2PO_4^-$, b) Cl^-, and c) K^+ ions passing through the OprP mutants R133E, R133Q, and R133A. For comparison the electrostatic energy for the WT channel is also shown [172]. Important residues of OprP along the ion permeation pathway are mapped with respect to their position along the z axis. All energy values denote relative interaction energies assuming zero interaction energies in the bulk phase.

the $H_2PO_4^-$ ion certainly lost its energetic advantages demonstrated for the WT case (see Fig. 3.4a). As shown in Fig. 3.4b for Cl^- ions, similar trends could be observed in terms of electrostatic interactions between the ion and the channels of R133 mutants. In addition to electrostatic factors, entropic penalties associated with the confinement of ions and particularly for larger ions such as $H_2PO_4^-$ molecular ions [164], as well as penalties due to dehydrating the ion may also contribute towards the overall barriers observed in the PMF profiles. The results for K^+ ions are displayed in Fig. 3.4c. These ions experienced less unfavorable electrostatic interactions in the mutants compared to the WT channel but a barrier nevertheless was evident as also reflected in the PMF profile.

One of the very interesting aspects of ion-selective channels from the perspective of an atomic analysis is the coordination number. It yields clues about the interactions and interplay between the permeating ions, surrounding water molecules, and the channel. Such analysis are widely exploited to derive a couple of hypotheses addressing the issue of ion-selectivity, particularly in the K^+ selective KcsA channel. One of these hypotheses is the so-called "field-strength hypothesis" which suggests that selectivity is determined by the type and the relative contribution of the coordinating ligand (e.g., protein versus water) [14, 15]. The idea behind this hypothesis is that different kinds of coordinating ligands will have differences in their intrinsic physical and electrostatic properties. Hence the change in their relative contribution may result in a selectivity towards a particular ion. The "over-coordination hypothesis" attributes selectivity to the total number of coordinating ligands only and not their physical properties [16, 17]. To perform a coordination number analysis, we followed the same procedure as reported previously for our WT simulations [172] (also see Appendix B, Fig. B2).

As a general trend and consistent with our previous results for WT OprP, the average number of coordinating water molecules decreased from the bulk phase as the ion moved inside the pore, which were compensated for by a higher number of protein contacts (Fig. 3.5). The total number of coordinating ligands (water and protein contacts) remained almost constant throughout the pore. Considering the above discussed ion-selectivity hypotheses, the "over-coordination hypothesis" could not explain the selectivity of each of the ions for the WT OprP and different R133 mutants. Each ion had the same number of coordinating ligands among the WT OprP and different mutants, for example, $H_2PO_4^-$ had a coordination number of 13 for WT and R133E/Q/A. In contrast, the relative contributions (water *versus* protein contacts) varied for each ion among the WT and different mutants (Fig. 3.5). For example, a phosphate ion (Fig. 3.5a) has different ratio of water *versus* protein contacts in the cases of WT OprP and the R133 mutants. The

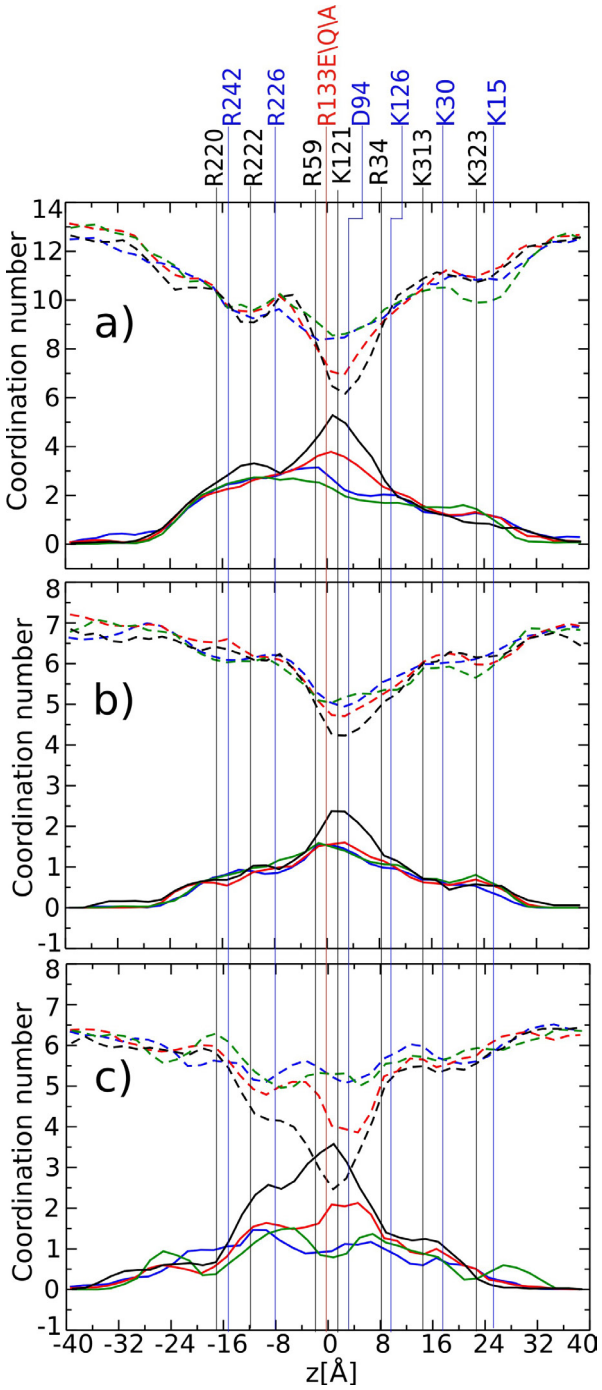

Figure 3.5.: The coordination number, i.e., the water (dash line) and protein (solid line) contacts, for the different ions, a) $H_2PO_4^-$, b) Cl^-, and c) K^+, through the OprP mutants channels R133E (blue), R133Q (red), and R133A (green). For comparison the coordination numbers for the WT channel (black) are also shown [172]. Important residues of OprP along the ion permeation pathway are mapped with respect to their position along the z axis.

highest number of protein contacts is present in WT OprP. Hence more water contacts are replaced by energetically favorable protein contacts in wildtype protein. This could explain the selectivity and higher binding affinity of phosphate for WT OprP compared to the R133 mutants and this line of argument is in agreement with the "field-strength hypothesis".

In the central bindings sites the $H_2PO_4^-$ ion transport through the WT pore indicated the removal of seven water molecules compared to the bulk phase which was compensated for by a higher number of protein contacts. As shown in Fig. 3.5a, and different from the situation with WT OprP, the $H_2PO_4^-$ ions stripped six and four water molecules to enable passage through the R133Q and R133E/R133A pores, respectively. As a general trend, less water molecules were removed for all R133 mutants compared to the WT pore. R133 remained in contact with the $H_2PO_4^-$ ions in the entire central region in WT OprP simulations. A possible explanation for the removal of only four water molecules in case of R133E might be the electrostatic repulsion between the negatively charged glutamate and the phosphate ion which in turn would lead to a loss of contacts between them. A closer contact between the R133 residue in WT channel and the negative ion would otherwise force water molecules to leave the phosphate hydration shell. A similar effect in R133A could be attributed to steric factors due to the small size of the alanine side chain. Figure 3.5b shows that the Cl^- transport through the R133 mutants revealed similar but somewhat more muted trends where less, i.e., two instead of three water molecules, were stripped compared to the WT channel.

The K^+ transport through the R133E mutant unfolded somewhat surprising results in terms of the coordination number. K^+ ions, being positively charged, were expected to strip more water molecules in the case of the R133E mutant compared to WT, due to the possible attractive electrostatic interactions between the ion and negatively charged glutamate (E). The same attractive interactions were responsible for stripping off more water molecules from $H_2PO_4^-$ in the WT pores due to favorable electrostatic interactions between the positively charge arginine and the negatively charged phosphate. Contrary to intuition, in the case of the cations also, the WT OprP removed more water molecules from the hydration shell than the R133E mutant. Indeed, R133E mutants stripped at maximum one water molecule compared to four in the WT case as seen in Fig. 3.5c. As a general result, we observed that irrespective of the ion type (cation or anion), WT OprP could remove more water molecules from the hydration shell of the permeating ion than any of the studied R133 mutants.

Possible reasons for the unexpected behavior of the K^+ permeation through the R133E

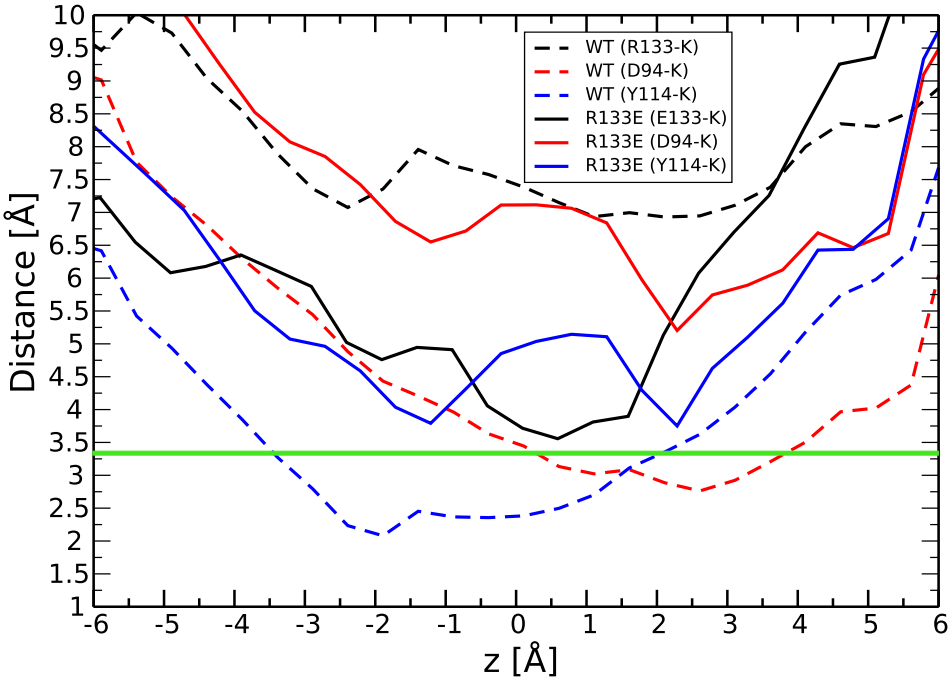

Figure 3.6.: Average distances between a K^+ ion and terminal side chain atoms of residues R133/E133, D94 and Y114 from WT as well as the R133E mutant in the central regions of the OprP pore. The horizontal green line indicates the first hydration shell radius for K^+ ions. Average distances are measured with a bin width of 0.5 Å.

mutants in terms of coordination numbers were analyzed in further detail. The average distances were measured between the permeating K^+ ion and various residues of the WT as well as the R133E pore in the central region of the pore, i.e., between -6 Å to 6 Å. In the case of the WT channel, R133 and K^+ ions maintained very large distances between them and they could not come closer than 7 Å (Fig. 3.6). For the R133E mutant, E133 and K^+ came as close as 3.7 Å to each other but this is not close enough to facilitate the removal of the majority number of water molecules from the first hydration shell since K^+ has a first hydration shell radius of 3.3 Å as indicated in Fig. 3.6.

A detailed analysis of the binding site residues revealed that two residues, D94 (aspartate) and Y114 (tyrosine), were present at the wall opposite to R133/E133 (see Fig. 3.1). For the WT channel, the strong electrostatic repulsion between R133 and the K^+ ion - having the closest distance of 7 Å - pushed the ion onto the wall at the opposite side and into close contact with D94 and Y114. The average distances between the permeating K^+ ions and these two residues are shown in Fig. 3.6. The distances between the ions and D94/Y114 were small enough, i.e., as low as 2 Å, to facilitate removal of a first hydration shell water molecule from the K^+ ions. Different to WT results, in the case of the R133E mutant, D94/Y114 and the K^+ ions are at distances larger than the first

hydration shell radius of the ion (see Fig. 3.6). This might be due to the absence of any electrostatic repulsion between E133 residue in the mutant and K^+, contrary to the case for WT OprP. Furthermore, E133 and the K^+ ions did not experience strong enough attractive electrostatic interactions - having a closest distance of 3.7 Å - to facilitate removal of the large number of first hydration shell water of the ion. One of the possible reasons for the lack of such a strong attractive interaction between the K^+ ions and E133 could be the formation of a salt bridge between K121 (lysine) and E133, as observed in our simulations. Such a salt bridge is not possible between K121 and R133 in the case of the WT channel as they electrostatically repel each other.

The above analysis revealed one of the most important characteristics of the R133 residue of OprP in its ability to alter the solvation properties of permeating ions, and thereby indirectly regulate the selectivity and the ion transport properties of the pore. In the WT OprP, R133 has a clear preference to dehydrate the permeating ions, i.e., "drying out" effect, compared to the other residues in the mutants at this particular position. Taking advantage of its strategic position in OprP, its positive charge and large size, R133 has a tendency to "dry out" the permeating ions, both cations as well as anions. Thereby the R133 residue makes the ion more vulnerable to the channel environment in terms of various interactions. In the case of anions, it enforces "drying out" effects by an attractive electrostatic interactions, while in the case of cations it modifies their interactions with other residues (here D94 and Y114) via a strong electrostatic repulsion between the permeating cation and R133. Ion dehydration is an important property for the transport of ions through narrow channels [187]. Particularly for anion selective channels, e.g., Cl^- channels, the hydration energy of the permeating ions was reported to be the rate-limiting process in the ion transport [165–167]. In such a scenario, the importance of the R133 residue, due to its ability to dehydrate the ions becomes even more evident in the anion-selective channel OprP. Consistent with this, previous single channel studies for OprP with anions of different sizes demonstrated small increase in single channel conductance going from F^- to Cl^- and the subsequent linear decrease in the series Cl^-, Br^- and I^- indicating that the hydration shell and size of the anions are important factors for the ion permeation through the channel[188].

3.4. Conclusions

In our quest to achieve a detailed understanding of the structure-function relationship of OprP, and in continuation with our previous work on the WT pore, we have probed the ion selectivity of the OprP channel with a focus on an important central residue, R133. In

this study, both electrophysiological measurements and free-energy MD simulations were carried out to investigate the role of R133 in determining phosphate binding specificity, ion selectivity and ion transport properties. To achieve this goal, three mutants were generated - namely R133E, R133Q and R133A - to understand the effect of charge and steric factors at this particular position of OprP. Electrophysiological measurements showed that any change in the R133 residue leads to a drastic reduction in the stability constant for phosphate binding. In qualitative agreement with experiments, PMF profiles obtained via MD simulations also indicated a change in the PMF profiles concerning the transport of phosphate from energetically favorable binding site regions for WT OprP to energetically unfavorable barrier regions for R133E/Q/A mutants. Furthermore, bilayer experiments revealed an extreme reduction in the pore KCl conductance and a reduced anion selectivity for all three R133 mutants compared to WT. The corresponding PMF profiles for K^+ and Cl^- transport through R133 mutants explained these observations from the experiments. In addition, taking advantage of the atomic details provided by the MD simulations, we observed the important characteristic of the R133 residue in OprP to alter the solvation property of the permeating ion via its ability to dehydrate the ion and thereby controlling the molecular interactions of the ions with the pore. Our study reveals the role of the R133 residue - particularly its charge and ability to change the solvation behavior of the permeating ion - in the structure-function relationship of OprP. These kind of detailed information can be further exploited to understand the ion selectivity of other pores and nanochannels and to enable the design of ion-selective artificial nanopores as e.g. proposed in Ref. 173.

Funding

The research leading to these results has received support from the Innovative Medicines Joint Undertaking under Grant Agreement n°115525, resources which are composed of financial contribution from the European Union's seventh framework programme (FP7/2007-2013) and EFPIA companies in kind contribution. This work has also been supported by grants KL 1299/6-1 and BE 865/16-1 of the Deutsche Forschungsgemeinschaft (DFG) and a Canadian Institutes for Health Research grant to REWH who also has a Canada Research Chair in Health and Genomics.

Acknowledgments

The authors would like to thank Que-Tien Tran for her contribution at the early stage of this study.

Supporting information

Supporting information are avialable in Appnedix B. Multiple sequence alignment among OprP orthologs in different Pseudomonas species, RDF profiles for ion hydration number and PMF profiles with error bars are presented.

4. Significance of a Negatively Charged Residue D94 of OprP in the Phosphate Binding and Permeation

Abstract

OprP is the phosphate-selective porin induced in the outer membrane of Gram-negative bacteria *P. aeruginosa* under conditions of phosphate starvation. Under such circumstances, a high-affinity uptake of phosphate ions from a dilute environment is enabled by presence of the defined binding sites for phosphate in OprP. However, presence of the negatively charged aspartate residue D94 in a binding site of the negatively charged phosphate is intriguing in terms of the electrostatic interactions. Therefore, we investigated the role of the D94 residue of OprP in the phosphate binding and permeation by generating the mutant channels. In electrophysiological measurements, mutations of the negatively charged D94 to positively charged residues, particularly lysine led to a drastic increase in the binding affinity of phosphate to the mutant channels. Free-energy molecular dynamics simulations revealed a very deep potential well for phosphate in the D94K mutant compared to the wildtype OprP in agreement with electrophysiological experiments. A possible significance of the negatively charged D94 residue in imparting the appropriate binding affinity to phosphate for OprP and in turn to regulate an efficient and a unidirectional transport of phosphate across the outer membrane of bacteria is presented. The presence and conservation of a negatively charged residue in the anion binding sites of anion-selective porins of the β-proteobacteria group of bacteria further demonstrated a significance of the negatively charged residue in the binding sites of anion-selective porins.

The material in this chapter is so far unpublished. The unpublished experimental work presented in this chapter has been performed by Ivan Bárcena-Uribarri and Manjeet Bains in the groups of Prof. Dr. Roland Benz, Jacobs University Bremen, and Prof. Dr. R.E.W. Hancock, University of British Columbia.

4.1. Introduction

Molecular recognition is a fundamental process underlying all of the critical processes in biology. Enzyme catalysis, cellular signaling, protein-protein association, the regulation of transcription and translation as well as the fidelity of DNA replication, to name a few, rely on recognition between two or more molecular binding partners [189]. It is of key importance to understand how these molecules recognize each other and to investigate underlying forces which govern these processes. The idea of molecular recognition started from the shape-complementarity based "lock-and-key" model as proposed by Fischer to understand enzyme catalysis [190]. Subsequently Pauling and Delbrück postulated in 1940 that intermolecular electrostatic interactions, van der Waals interactions and hydrogen bonds dictate the molecular recognition processes [191]. Since then such intermolecular forces are investigated not only to understand molecular recognition processes but to engineer such processes for various applications, e.g., to optimize intermolecular interactions between the protein and the ligand to rationally design drug molecules or to change ion selectivity properties of channels and porins.

Ion selectivity of membrane proteins represents a prime example of molecular recognition processes. For example, the ability of potassium channels to selectively recognize K^+ over Na^+ is intriguing [1]. Similarly, the ability of a phosphate selective channel to differentiate between two tetrahedral-shaped oxyanions, i.e., phosphate and sulphate, is another example of a high-level specificity observed in molecular recognition processes. Compared to globular proteins, molecular recognitions in membrane proteins and channels have additional dimensions that need to be considered. Apart from a selective permeability towards particular ions or substrates, membrane channels are generally responsible for an efficient and a unidirectional permeation of ions and substrates across the cellular membrane to regulate various biological processes. An efficient permeation, in terms of a rate of substrates transport across the membrane, requires an appropriate binding affinity of the permeating substrates to the channel since too strong binding may lead to a very slow permeation. An unidirectional permeation sometimes involves various additional components of the respective transport systems in addition to a transmembrane channel which act concertedly to achieve an uptake of substrates in one particular direction. For example, an involvement of the periplasmic phosphate binding protein (PBP) to unidirectionally transport phosphate ions through OprP in Pseudomonas aeruginosa [192]. Phosphate ions first bind to the binding sites within OprP and subsequently to the periplasmic PBP to enable an uptake of phosphate ions across the bacterial outer membrane. Such multiple binding partners require appropriate affinities of phosphate

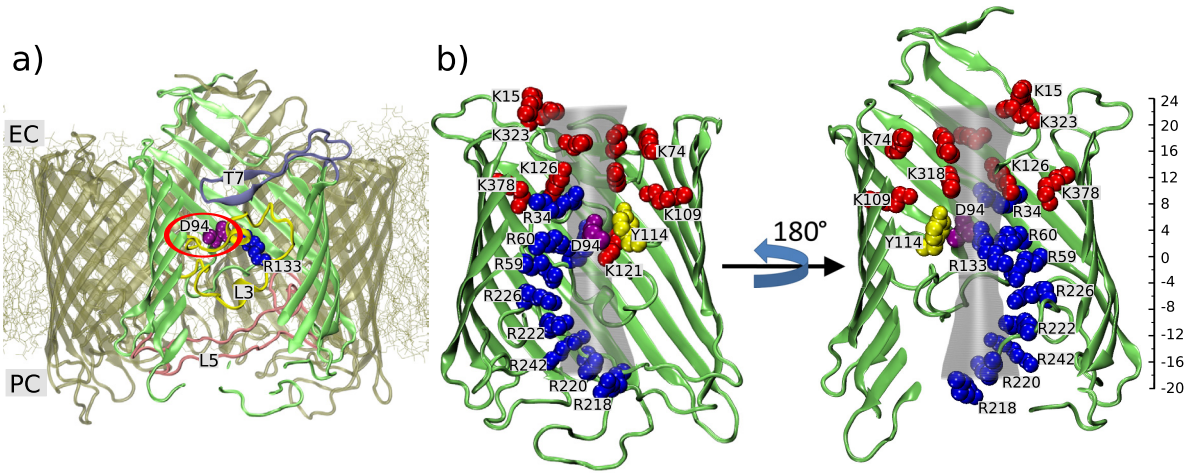

Figure 4.1.: Structural features of OprP. a) An OprP trimer is shown embedded in a membrane. Important loops - L3, L5 and T7 - which are responsible for the formation of narrow regions inside the pore are shown. EC and PC denote the extracellular and periplasmic sides of the pore respectively. b) The monomer pore is shown together with a gray hourglass shape to demonstrate the approximate radius of the pore in the different regions and to indicate a possible ion permeation pathway. Important residues, including Asp94 (purple), are labeled and mapped to their position along the z axis.

to OprP. To achieve such an "appropriate" affinity, a fine-tuning of interactions between the permeating ion and the channel is anticipated. In this study, we are focusing on the role of the negatively charged aspartate residue of OprP, D94, in regulating such delicate molecular recognition processes in OprP. Electrophysiological bilayer measurements complemented by free energy molecular dynamics simulations provide an ideal platform to probe ion-selective membrane proteins. For example, the KcsA channel[14–18, 152, 153], the NaK channel [18, 155], the ClC channel [154] and the nicotinic acetylcholine receptor [23] have been investigated in a similar manner to understand their ion selectivities.

OprP is a phosphate-selective porin and is induced in the outer membrane of *P. aeruginosa* under phosphate starvation conditions. It is responsible for the high-affinity uptake of phosphate inside the bacteria under such circumstances [156]. Our previous electrophysiological measurements suggest that the phosphate binds to OprP with an 100-500 higher binding affinity compared to chloride [157–159]. Even more interesting is the twenty times higher affinity of phosphate for OprP compared to the oxyanion sulfate [157]. Previously and in addition to the electrophysiological measurements we have investigated the phosphate selectivity of OprP using free-energy molecular dynamics simulation and explained the possible molecular reasons responsible for the selectivity of the channel [172]. Sansom and co-workers also probed the selectivity of OprP using molecular dynamics simulations [121] and designed biomimetic nanopores [173].

The crystal structural of OprP demonstrates the trimeric organization of the porin in which each monomer is formed by 16 β-strands that are connected to each other via extracellular and periplasmic loops (Figure 4.1a) [160]. Important are the loops L3, L5 and T7 that fold inside the lumen of the pore and form constriction regions inside the channel (Figure 4.1a). Important structural features that confer anion selectivity to the channel are the so-called arginine ladder - formed by residues R218, R220, R242, R222, R226, R59, R60 and R34 - that extends from the extracellular side down the channel to the middle of the pore (Figure 4.1b). Another is the lysine cluster - consists of residues K13, K15, K25, K30, K74, K109, K313, K323, K378 - on the periplasmic side of the channel (Figure 4.1b). Two central phosphate binding sites are formed by residues D94, Y62, S124, S1235, K121, K126, R34, and R133 [160, 172].

Recently we have shown the importance of the positively charged arginine residue, R133, in the central bindings sites towards the phosphate binding affinity of the channel [193]. Both electrophysiological measurements and free-energy molecular dynamics simulation revealed a drastic decrease in binding affinity of phosphate for OprP if R133 was mutated to any other neutral or negatively charged residues. This kind of mutant studies help to understand the relative contribution of each residue in determining the phosphate selectivity of OprP in particular and to understand the structure-function relationship of porins in general. Out of the conserved residues among the orthologs of OprP in *Pseudomonas* species, most of the residues are positively charged Arg and Lys residues. Conservation of important positively charged residues in the anion selective channel with defined binding sites for anions is not very surprising if one considers the complementary nature of the electrostatic interactions between the two binding partners as commonly perceived in molecular recognition. However, particularly intriguing is the presence of a negatively charged aspartate residue, D94, in one of the central phosphate binding sites. The phosphate ion has two affinity sites in the central region of the pore and D94 is part of one of these sites as suggested by both the crystal structure and MD simulations [160, 172]. Presence of a negatively charged residue in the binding site of the negatively charged phosphate is surprising considering the unfavorable electrostatic interactions between them. Such electrostatic interactions are believed to be very dominant and playing a major role in molecular recognition. For example, in the case of aquaporin channels, the substrate specificities between different subfamilies of aquaporins can be justified based only on electrostatic profiles of the channels [194]. The functional significance of D94 is also evident in the evolutionary process as this residue is conserved among OprP orthologs (see Appendix C, Fig. C1).

Considering above observations, it is imperative to probe the importance of the negatively charged residue D94 in the binding and permeation of the phosphate in OprP. Different mutants of D94 are generated and investigated concerning the change in phosphate binding affinity in electrophysiological bilayer measurements. Free-energy molecular dynamics simulations are aimed at obtaining the molecular reasons behind the experimental observations. The goal of the present study is to understand the possible significance of a negatively charged residue in achieving the "model" anion binding site for anion-selective porins.

4.2. Materials and Methods

4.2.1. Experimental details

Bacterial strains and growth conditions

Escherichia coli strain DH5α (Invitrogen, CA, United States) was utilized to host clones containing the OprP expression plasmid pAS27 [174] and the various plasmids containing an OprP single mutations. *E. coli* CE1248 [175] - which does not have the major porins OmpF, OmpC and PhoE - was utilized in all expression studies to enable the purification of the OprP mutants. *E. coli* CD1248 cells harboring the different plasmids were inoculated from Luria-Bertani agar plates (Fisher Scientific, Canada) containing 100 μg/ml ampicillin (Sigma, Canada) directly into 1.0 liter of Luria-Bertani broth supplemented with 100 μg/ml ampicillin and 0.4 % glucose to impede the expression of LamB. The cells expressing the different OprP mutants were induced once they reached an OD_600 of 0.5-0.8 with 0.8 mM of IPTG and further cultivated overnight. Subsequently the cells were harvested by centrifugation at 8,000 x g for 10 min.

Site-directed mutagenesis and sequencing of OprP mutants

The pAS27 plasmid was individually mutated with the help of the Quick-Change® mutagenesis kit (Stratagene, USA) following the manufacturer instructions. The primers that are used to carry out the single mutations are mentioned in Table 4.1. For each amino acid substitution two complimentary primers containing the desired mutation were designed as per the guidelines in the QuikChange XL Site-directed Mutagenesis manual, and synthesized by AlphaDNA (Montreal, Canada). Each of the mutagenized OprP constructs was sequenced by the Nucleic Acid Protein Service Unit (University of British Columbia, Vancouver, Canada) to ensure they had the correct mutant sequence and no additional mutations. Mutagenic codons containing mismatches that corresponded to

the substitution mutation in the encoded amino acid sequence of OprP are also described in Table 4.1.

Protein extraction and purification

The *E. coli* CE1248 pellets received after cultivation were resuspended in 10mM Tris-HCl pH 8.0 containing 20% sucrose and 50 µg/ml DNase 1. The resuspended cells were incubated at 23 °C for 10 min and subsequently placed on ice and lyzed two times by passage through a French pressure cell at 15,000 psi; unbroken cells were discarded by centrifugation at 5,000 x g for 10 min at 4 °C. The supernatants were layered onto a 2-step sucrose gradient (50% and 70%) and centrifuged in a SW28 swinging bucket rotor at 150000 g for 18 hours at 4 °C. Once the fraction that had the outer membranes was collected, the concentration of sucrose was diluted to below 20% with distilled water and the membranes were pelleted in an ultracentrifuge at 41,000 rpm at 4 °C for 1 hour. The outer membranes were then washed once with water. The proteins present in the outer membranes were solubilized first with a buffer containing 10mM Tris HCl pH 8.0 and 3% tetraoxyethylene n-octyl ether (C8E4) (Bachem Inc., USA), followed by this buffer with the addition of 10 mM EDTA, pH 8.0 and subsequently with added 1.0 M NaCl. The solubilized fractions were analyzed by SDS-PAGE and OprP was predominantly found in the fraction solubilized with 10mM Tris-HCl pH 8.0, 3% C8E4 and 10mM EDTA. The selected fraction was subsequently diluted to obtain a final C8E4 concentration of 0.6%. The OprP native and mutant proteins were purified using a NaCl gradient applied to a MonoQ column on a FPLC system (Pharmacia, United States). The OprP protein eluted at a salt concentration of 250-300 mM NaCl. The presence of the protein was ensured using SDS-PAGE and Western immunoblotting.

Sodium dodecyl sulfate-polyacrylamide gel electrophoresis (SDS-Page) and Western immunoblotting (WB)

To ensure the expression of the OprP mutants and its purification, whole cell lysates of *E. coli* CE1248 or the FPLC fractions were loaded onto a 12% SDS polyacrylamide gel and electrophoresed. The gels were stained with Coomassie blue or transferred to polyvinylidene fluoride (PVDF) membranes and incubated with monomer-specific anti-OprP rabbit serum as previously described [174]. *E. coli* CE1248 harboring pAS27-OprP (wildtype) was utilized as a positive control and *E. coli* CE1248 harboring the vector plasmid pTZ19U (Pharmacia, USA) was utilized as a negative control.

OprP	Codon	5′-3′ Primer	Protein side chain
D94 (WT)	GAC	not mutated	-CH2-COOH
D94K	AAG	GCGCCGGCTACTTT**AAG** GAAGCTTCGGTCAC	-CH2-CH2-CH2-CH2-NH2
D94R	CGC	GCGCCGGCTACTTT**CGC** GAAGCTTCGGTCAC	-CH2-CH2-CH2-NH- C(NH2)-NH
D94N	AAC	GCGCCGGCTACTTT**AAC** GAAGCTTCGGTCAC	-CH2-CO-NH2
D94Q	CAG	GCGCCGGCTACTTT**CAG** GAAGCTTCGGTCAC	-CH2-CH2-CO-NH2
D94A	GCC	GCGCCGGCTACTTT**GCC** GAAGCTTCGGTCAC	-CH3

Table 4.1.: Mutants designed to study the role of the amino acid D94 in ion selectivity and phosphate substrate specificity. The codons of the wild type and mutants are indicated as well as the primers used to mutate them. The side chains of the different amino acids are also shown.

Black lipid bilayer: single channel conductance, zero current measurements and phosphate titration

The black lipid bilayer assay has been described previously elsewhere [176]. An artificial membrane was spread over a 0.5 mm^2 hole dividing two compartments of a Teflon cuvette. The artificial membranes were formed using a solution of 1 % diphytanoylphosphatidylcholine (DiPhPC) in n-decane (Avanti Polar Lipids, Alabaster, AL). Both compartments are filled with a salt solution (0.1M KCl). Two Ag/AgCl electrodes with salt bridges switched in series were immersed in each compartment of the the Teflon cuvette. One of the electrodes was connected to a home-made voltage source whereas the other to a home-made amplifier/filter based on a Burr-Brown operational amplifier. The output signal of the amplifier was monitored with a digital oscilloscope and a strip chart recorder (Rikadenki Electronics, Germany). A +50 mV voltage was applied for single channel conductance and titration experiments.

Measurements to probe inhibition of chloride conductance due to phosphate binding to the binding sites were done for OprP and D94 mutants as previously described [177, 178]. The aqueous phase contained 0.1M KCl, 10 mM MES at pH 6 in these experiments. The protein was added to the cuvette under stirring conditions The membrane conductance increased for about 30 minutes due to reconstitution of OprP and its mutants. Once the conductance was stable and did not increase further, small amounts of concentrated phosphate solutions (pH 6) were added to both sides to study inhibition of chloride conductance by interaction of phosphate to the binding site. This could be detected by the reduction of the membrane conductance. After progressive increase of the phosphate

concentration under stirring, the half saturation constant for chloride conductance through OprP and its mutants as mediated by phosphate binding was calculated with the help of the Michaelis-Menten equation [177, 179].

Zero current measurements to probe the ion selectivity were carried out as described elsewhere [176, 180]. An electrochemical gradient was progressively established by adding a 0.5M KCl solution to the cis-side and 0.1 M of the same salt to the trans-side of the membrane cell. The generated potentials were measured with a high-impedance electrometer (Keithley 617) connected to the trans-side electrode under zero current conditions.

4.2.2. Computational details

Molecular dynamics system setup

A trimer of OprP (PDB code 2O4V) [160] was embedded into a palmitoyloleoyl-glycero-phosphathidyl ethanolamine (POPE) lipid bilayer. The bilayer was constructed from pre-equilibrated patches utilizing VMD [181]. The system was solvated using TIP3P water molecules. The D94 residue in each monomer was mutated to lysine (K) to generate the D94K mutant. The system was subjected to 5000 steps of energy minimization to remove any unfavorable sterical contacts. Subsequently a ∼5 ns equilibration run was performed. In addition, one of the three studied ions (phosphate, chloride and potassium), was placed at the mouth of the one of the monomers on the extracellular side of the mutant. As already done in our WT OprP and R133 mutant studies [172, 193], the monovalent form of the phosphate ion, $H_2PO_4^-$, was chosen since phosphate is predominantly monobasic at pH 6 of experimental measurements. All three systems were neutralized by addition of potassium ions and each system consisted of ∼120,000 atoms.

Molecular dynamics simulation parameters

The simulations were carried out in the NPT ensemble using the program NAMD 2.9 [131] and the CHARMM27 force field [95] as well as additional force field parameters for $H_2PO_4^-$ [182]. The temperature of 310 K and the pressure of 1 atm were maintained in all the simulations utilizing Langevin dynamics along with a Langevin piston algorithm. Periodic boundary conditions were applied in the simulations. Furthermore, the short-range nonbonded interactions were determined using a cutoff of 12 Å and a switching distance of 10 Å. The long-range electrostatic interactions were calculated using the particle mesh Ewald method [183]. Bonded interaction were calculated every 1 fs.

In addition, the short-range nonbonded and long-range electrostatic interactions were calculated every 2 fs and 4 fs, respectively, utilizing‘ the r-RESPA multiple time step method [184]. Moreover, bond constraints were applied to all water hydrogen atoms utilizing the SHAKE algorithm [185] .

Free energy calculations

The adaptive biasing force (ABF) method [162, 163, 186] as implemented in the *collective variable* module of the NAMD 2.9 program [131] was utilized to obtain the effective free energy profiles for the transport of different ions through OprP mutants. The principal axis of the channel was aligned parallel to the z axis and the z position of the ion was considered the as reaction coordinate. Moreover, the change in free energy was calculated with respect to the bulk value. To this end, the full reaction coordinate with a length of ∼84 Å along the z axis was subdivided into 21 windows with a length of 4 Å each to improve the sampling efficiency. This spatial range of the reaction coordinate along the z axis also contains extended bulk regions on both sides of the channel. The initial starting conformations of the system for each window were obtained by constant velocity steered molecular dynamics (SMD) simulations wherein each studied ion was pulled through the channel along the z axis. In the ABF method, the average force acting on the respective ion was accumulated in 0.1 Å-sized bins within each window. In addition, the application of the adaptive bias was initiated only after 800 samples were accumulated in the individual bins to obtain a reasonable starting estimation of the biasing forces. Subsequently the resulting data were integrated to generate the potential of mean force (PMF) profiles. Production runs in each window were performed for at least 6 ns while considerably extended runs were carried out for about 15-20 ns in the central binding site windows (-10 to 10 Å).

4.3. Results

Our goal is to understand the relative contribution of the residue D94 in determining the binding affinity of the phosphate towards OprP. To achieve the same, we have mutated the negatively charged D94 residue of OprP to positively charged residues K (small side chain compared to R) and R (large side chain compared to K), as well as neutral residues, N (polar, small side chain compared to Q), Q (polar, large side chain compared to N) and A (non-polar, very small side chain). D, K, R, N, Q and A denote amino acids aspartate, lysine, arginine, aspargine, glutamine and alanine respectively. These kind of mutations with amino acids having different physicochemical properties help to probe the effect of

OprP	**G (pS)** (KCl)	Half saturation constants of chloride conductance inhibition by phosphate (1/K) (10^{-3}M)	Stability constants of chloride conductance inhibition by phosphate (K) (1/M)
D94 (WT)	160	1.2	820±160
D94K	180	0.06	16701
D94R	160	0.73	1363
D94N	280	0.11	9120
D94Q	160	1.46	686
D94A	200	0.33	3071

Table 4.2.: Single channel conductance and half saturation constants of chloride conductance inhibition by phosphate binding for WT OprP and D94 mutants. The single channel conductance was obtained in 0.1 M KCl, 10 mM MES, pH 6, T=20 °C and applying 50 mV voltage. The stability constant for chloride conductance inhibition by phosphate was obtained from titration experiments with the OprP WT and mutant channels mediated conductance, using the Michaelis-Menten equation described elsewhere [177]. The phosphate solution had a pH of 6. Mean value of at least three individual titration experiments are shown.

charge and size of residues at the particular position inside the channel in conferring the selectivity and ion transport properties to the channel. Through out the discussion in this paper, we will compare results obtained in the present study with D94 mutant channels with that of our previous studies with the wild-type channel [172] and the R133E mutant channel [193] to enable broader discussion on importance of the residue D94 in OprP. R133 is a very important residue in central binding sites and any mutation of this residue led to the drastic decrease in binding affinity of phosphate in OprP [193].

As shown in Table 4.2, the changes in the phosphate dissociation constant or half saturation constant (1/K) were observed for D94 mutants and such changes were dependent on the type of the residue - in terms of charge, size and polarity - present in the mutant channels. The largest change in dissociation constant was observed with the charge inversion mutant, D94K, where 20 times increase in phosphate binding affinity was realized compared to the WT channel. The other charge inversion mutant, D94R, also experienced increase in phosphate binding affinity compared to WT. However, only two-fold increase in binding affinity for D94R mutant may be attributed to the large size of the arginine compared to the lysine and in turn indicates the importance of size and steric factors, in addition to the charge, at this particular position of OprP in governing the phosphate binding. Mutation to a neutral residue, D94N, resulted in a ∼10 times increase in the phosphate binding affinity. Stronger binding of the phosphate to the D94N compared to the D94Q mutant can again be attributed to the steric factors. Changes of

the charge of the residue at the position 94 from negative (D) to neutral (N) to positive (K) and the associated significant changes in phosphate binding affinity, approximately 10-fold increase at each step, indicates the importance of the charge at this particular position in OprP. Single channel KCl conductance (G) of D94 mutants did not result in very significant changes in comparison with the R133 mutants [193].

	Permeability ratios P_a/P_c (V_m [mV])					
Electrolyte	**D94**	**D94K**	**D94R**	**D94N**	**D94Q**	**D94A**
KCl	>70 [159]	25 (-37.3)	10 (-31.4)	50 (-39.5)	2 (-9.1)	33 (-38)

Table 4.3.: Zero-current measurements to study the ion selectivity of OprP and the D94 mutants. The experiments were carried out for five-fold gradients (0.1 M *versus* 0.5 M) of three different salts. The ratio of anions to cations permeability, (P_a/P_c) was calculated using the Goldmann-Hodgin-Katz equation [176] from at least three individual experiments. The zero-current membrane potential, V_m, is defined as the difference between the potential at the dilute side and the concentrated side of salt solutions.

In addition, we also carried out zero current measurements to investigate changes in the ion selectivity of the D94 mutants compared to WT OprP. As a general trend, we observed that all D94 mutants retained anion selectivity (Table 4.3). However, a decrease in the anion selectivity has been observed for all D94 mutants compared to the WT channel. The decrease in the anion selectivity may be attributed to a stronger binding of Cl^- ions to the mutant proteins which may lead to the slower permeation of Cl^- ions in the mutant channels compared to WT. Presumably, a stronger binding of Cl^- may be due to the absence of the negatively charged residue D94 in a central binding site which otherwise electrostatically repel binding of Cl^- to the WT channel.

To further probe the importance of the D94 residue of OprP, we carried out free-energy molecular dynamics simulations to understand the energetics of phosphate, chloride and potassium ion permeation through D94K mutant channels. As discussed above, a charge inversion mutation, D94K, resulted in the strongest binding of the phosphate ion to the channel in electrophysiological measurements. The D94K mutant, in which a negatively charged residue is mutated into a positive one, provides the opportunity to probe the role of negatively charged residues in the anion binding site for anion-selective channels when compared to the WT channel. Hence we calculated one-dimensional potential of mean force (PMF) profiles for the transport of different ions through the D94K mutant (Figure 4.2). To facilitate comparisons, PMF profiles from our previous studies with the WT [172] and the R133E [193] channels are also shown.

The PMF profile for the transport of $H_2PO_4^-$ through the D94K channel reveals

two energetically favorable and very deep central binding sites with well depths as high as 16 kcal/mol (Fig. 4.2a). The WT OprP channel includes two similar central phosphate binding sites but with a well depth of only 8 kcal/mol (Fig. 4.2a). Such a large increase in binding depth from WT OprP to the D94K mutant indicates a very strong binding of the phosphate in the mutant channel. This is well supported by the 20-fold increase in the phosphate binding affinity for the D94K mutant compared to WT in the electrophysiological experiments. A large increase in phosphate binding affinity of the D94K mutant compared to WT is contrary to previously studied R133E mutant where a large decrease, approximately 40 times, in phosphate binding affinity was observed both in experiments and simulations [193]. The PMF profiles along with the experimental observations clearly demonstrates the role of the negative charge belonging to the D94 residue in regulating the binding affinity of phosphate to OprP. The D94 residue in OprP, even with its negative charge, maintains energetically favorable phosphate binding sites in the central region of the channel and at the same time prevents too strong binding of phosphate. The biological importance of achieving such an appropriate binding affinity for the phosphate in OprP and other possible implications of the negative charge in the binding site of OprP will be detailed in the *Discussion* section below.

The PMF profiles for the another anion, Cl^-, also revealed a stronger binding of chloride to the D94K channel compared to the WT pore (Fig. 4.2b). The energetic depth of the binding site increased from 8 kcal/mol for the WT channel to 13 kcal/mol for the D94K mutant. This further confirmed the role of the D94 residue in regulating the appropriate binding affinity of anions in OprP. Furthermore, a decrease in the anion-to-cation permeability ratio, P_a/P_c, for KCl electrolyte solution for D94K compared to WT (Tab. 4.3) might be a result of a slower permeation of Cl^- ions through the mutant channel, due to the stronger binding of anions to the mutant as suggested by the PMF profiles (Fig. 4.2b). The K^+ ion transport through the D94K mutant results in an increase in a barrier height when compared to the WT channel (Fig. 4.2c).

Such large changes in the PMF profiles and in turn associated binding affinities for the permeating phosphate in response to point mutants of OprP is intriguing. To further understand them, we calculated electrostatic potential maps of the WT channel and D94K as well as R133 mutant channels of OprP. Potential maps were calculated using the PMEPlot plug-in of VMD [25, 181] and were averaged over the equilibrium simulation length of 25 ns. As shown in Figure 4.3, the electrostatic potential maps show large changes with respect to point mutations particularly in the central region of the pore. Compared to WT OprP, the D94K mutant displays a very strong electropositive region at

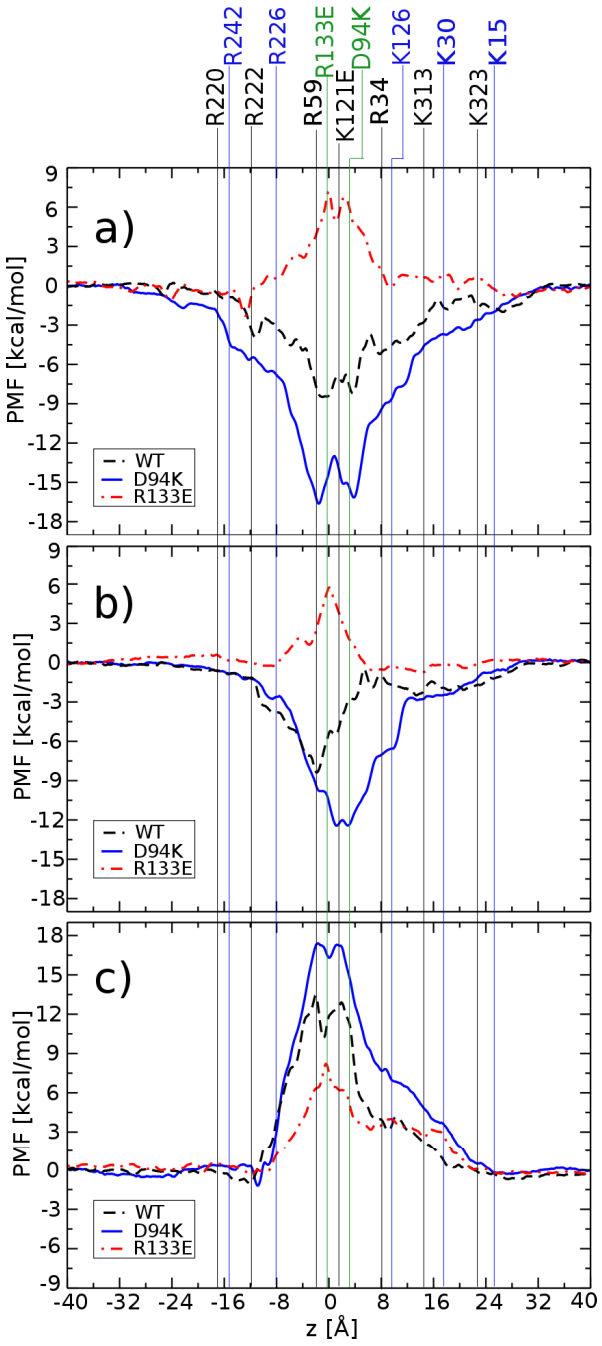

Figure 4.2.: PMF profiles for the permeation of a) $H_2PO_4^-$, b) Cl^-, and c) K^+ ions through the OprP mutant D94K. Data for PMFs for the WT and R133E mutant channels are shown for comparison (see Refs. 172 and 193). Important residues of OprP along the ion permeation pathway are mapped onto the PMF profiles with respect to their positions along the z axis.

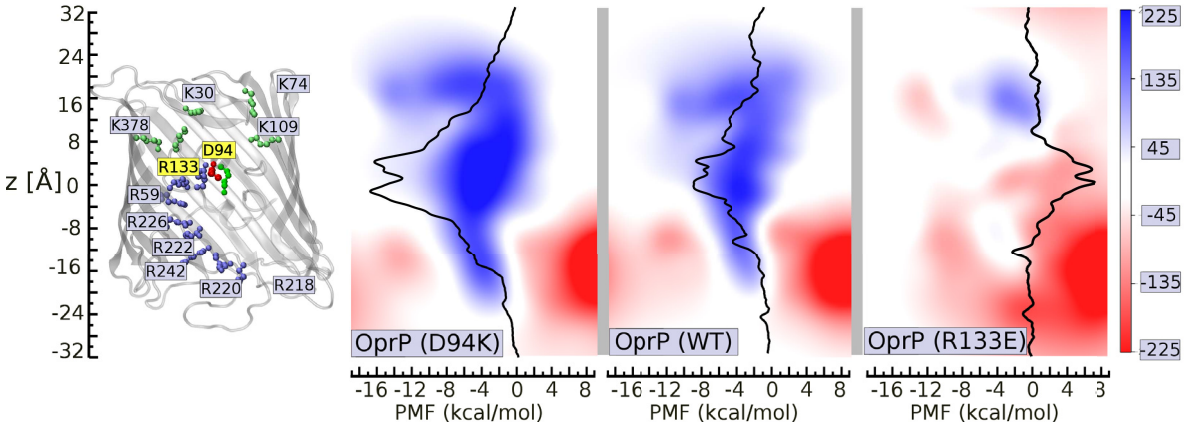

Figure 4.3.: Electrostatic potential maps for the WT OprP and mutants, D94K and R133E. The OprP channel together with important residues are mapped along the potential maps to enable identification of possible residues which are responsible for particular features of potential maps. In addition, PMF profiles for the $H_2PO_4^-$ ion permeation through the WT and mutant channels are mapped onto the respective potential maps to show the correlation between the energetics of the $H_2PO_4^-$ transport and the electrostatic potential profiles. The potential maps are in the $y-z$ plane at an x position corresponding to the middle of the one of the three pores and are generated using the PMEPlot plug-in for VMD [25, 181].

the center of the channel (Fig. 4.3) and provides a strong hint for the very strong binding of the negatively charged phosphate or chloride in the D94K mutant. Conversely, the R133E mutant shows not such an electropositive region at the center of the channel in the potential map (Fig. 4.3) and this justifies the PMF profile for phosphate ion which is void of any energetically favorable affinity region for this particular mutant. Furthermore, we have mapped the respective PMF profiles for the $H_2PO_4^-$ permeation through each of the channel to enable comparisons (Fig. 4.3). A clear correlation between the electropositive and electronegative features of the electrostatic potential maps and the PMF profiles is visible. It is also interesting to observe such "global" effects on the electrostatic potential maps of OprP in response to single point mutants which is due to the long-range nature of the electrostatic interactions.

In a further analysis step, we calculated the electrostatic interaction energies between the permeating ions and the channel in the different regions of the pore (Figure 4.4). For this purpose, the pore was divided into 1 Å bins and the interaction energies were calculated, with a cutoff distance of 12 Å using the NAMDenergy plugin. Compared to the WT, the $H_2PO_4^-$ ions experience more favorable electrostatic interaction energies at the central region of the pore for the D94K mutant (Fig. 4.4a). This finding is in accordance with the PMF profiles (Fig. 4.2a) and electrostatic potential maps of the WT and the D94K channels (Figure 4.3) as discussed above. Similarly, Cl^- ions show more favorable electrostatic interaction energies in the central region of the pore for the D94K mutant

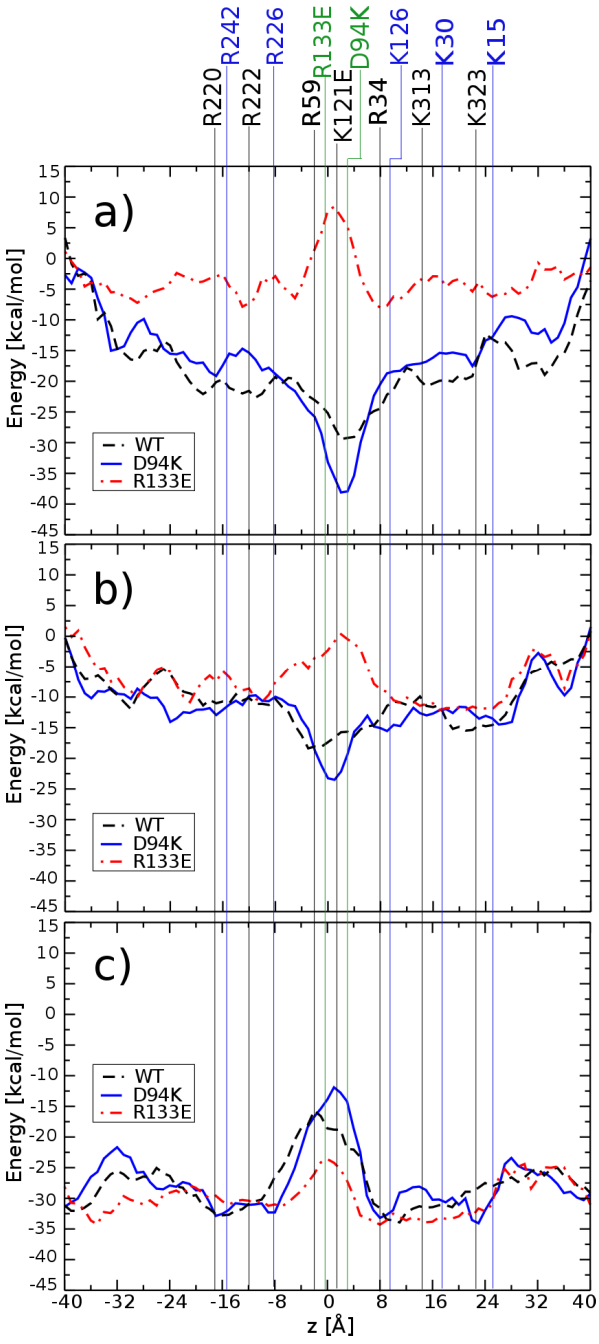

Figure 4.4.: Electrostatic interaction energy for the a) $H_2PO_4^-$, b) Cl^-, and c) K^+ ions passing through the OprP mutant D94K. Data for the electrostatic energy for the WT and R133E mutant channels are shown for comparison (see Refs. 172 and 193). All energy values denote relative interaction energies assuming zero interaction energies in the bulk phase.

when compared to the WT channel (Figure 4.4b). On the contrary, due to the very strong electropositive potential of the D94K mutant, the K^+ ions are subject to very unfavorable electrostatic interaction energies for this particular mutant (Figure 4.4c). This phenomena is also reflected in the PMF profile with an energetic barrier of as high as 17 kcal/mol for the permeation of K^+ ions through the D94K mutant.

Up to this point, we have focused on the electrostatic component of the energy between the permeating ion and the channel which indeed largely determines the stronger binding of phosphate in the D94K channel compared to WT. However, water molecules play an important role in regulating the interactions between the permeating ions and the channel. To interact with the channel, the permeating ion has to remove at least part of the water molecules belonging to the hydration shell, particularly in the narrowest central region of the pore where the channel radius is smaller than the hydrodynamic radius of the permeating ion. Ion selectivity and ion transport properties of the channel are believed to be determined by the interactions and interplay between permeating ion, surrounding water molecules and the channel. For example, we have already shown the importance of the residue R133 of OprP in governing the phosphate binding affinity by its ability to dehydrate the permeating ion along with the network of other residues in OprP [193]. Particularly for anion selective channels, the hydration energy of the permeating ions was reported to be the rate limiting step in determining ion transport processes [165–167].

To understand the effect of the hydration shell, we carried out a coordination number analysis for permeating ions in different regions of the pore for the D94K mutant. A detailed procedure to calculate the coordination number is given elsewhere [172, 193]. As the permeating ions move inside the channel, a part of the water molecules are removed from the respective hydration shell which are compensated by protein contacts. As shown in Fig 4.5a, the $H_2PO_4^-$ ions strip off eight water molecules in the central region of the pore to enable passage through the D94K mutant. Compared to this, $H_2PO_4^-$ ions have to remove seven and four water molecules while permeating through the WT and the R133E channel, respectively. Surprisingly, a clear correlation is seen between the number of water molecules removed from the hydration shell of the permeating phosphate ion and the binding affinity of phosphate in the respective channel. Removal of more water molecules from the hydration shell while passage through a channel, e.g., the D94K channel, results in a stronger affinity of phosphate to that particular channel (Fig. 4.5a). Conversely, stripping of less water molecules, e.g., in the R133E channel, leads to a weaker binding of the phosphate in the respective channel. For the other studied anion, Cl^-, a similar correlation between the removal of water molecules from the hydration shell and

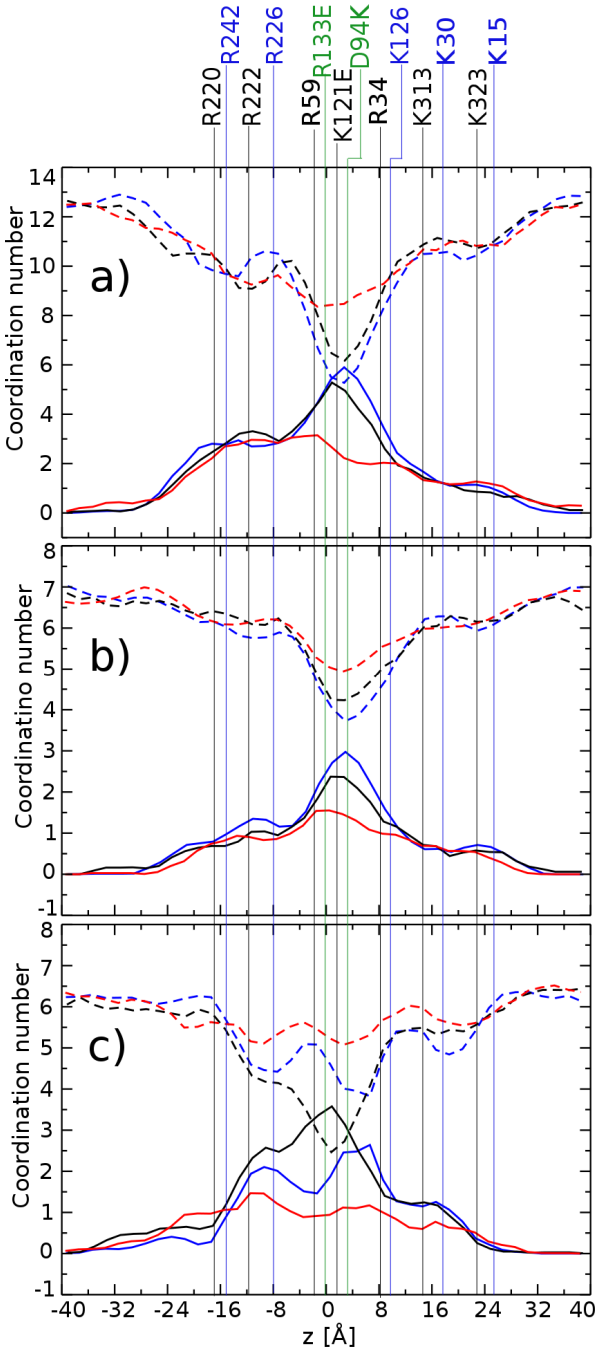

Figure 4.5.: The coordination numbers, i.e., the water (dash line) and protein (solid line) contacts, for the different ions a) $H_2PO_4^-$, b) Cl^-, and c) K^+, through the OprP mutants channels D94K (blue), WT (black), and R133E (red). Data for the WT and R133E mutant channels are shown for the comparison (see Refs. 172 and 193).

the binding affinity was observed (Fig. 4.5b). In the case of D94K, the replacement of hydration shell water by more favorable - in terms of binding affinity to channel- protein contacts results in a stronger binding of anions to this particular mutant. One possible reason for the removal of one more water molecules from the D94K channel compared to the WT is the slightly smaller size of the D94K pore in the central region as indicated by the average radius profile of the channel (see Appendix C, Fig. C2).

4.4. Discussion

With the help of electrophysiological bilayer measurements, it has been shown how the phosphate binding affinity varies with mutating the D94 residues to other amino acids. Of particularl interest is the 20-fold increase in the binding affinity of the phosphate ion to the D94K mutant. Free-energy MD simulations provide a possible molecular picture of such strong affinities of the phosphate to the D94K mutant. The presence of a negatively charged D94 residue in the affinity site prevents very strong binding of the phosphate in the WT OprP. The strong affinity was observed in the D94K channel, where a negatively charged Asp was mutated to a positively charged Lys. The biological significance of achieving an appropriate binding affinity of phosphate to OprP is further discussed below.

In nature, channels and porins are designed to allow permeation of ions and substrates through impermeable membranes. On one hand, some kind of binding for the permeating ions or substrates inside the channel helps to assign substrate specificity and selectivity to channels which are essential to their functions. In particular for channels like OprP, which are induced under phosphate-limiting conditions with growth-limiting phosphate concentrations to induce OprP being as low as 0.15 mM [156], the presence of defined binding sites with affinity for the channel enhance the efficiency of phosphate uptake from dilute environments. However, on the other hand, a very strong binding of the phosphate inside the channel may lead to an inefficient and slow permeation. Hence, to achieve an appropriate binding affinity of phosphate which is essentially a trade-off between the "tight binding" *versus* "permeation efficiency" is necessary to the function of OprP.

One additional and important dimension to the significance of achieving the appropriate binding affinity for phosphate in OprP is given by the presence of the periplasmic phosphate-binding protein (PBP) as a part of the phosphate transport system (PTS) in *P. aeruginosa* [192]. Since the phosphate movement *in vivo* must be unidirectional from the extracellular to periplasmic side in order to meet the cellular nutritional requirements

of the bacteria, an additional high-affinity component in the form of the periplasmic phosphate-binding protein facilitates unidirectional uptake across the outer membrane. The presence of the periplasmic phosphate-binding protein was confirmed by the observed biphasic kinetics of the phosphate transport in *P. aeruginosa*. Moreover, it was shown that the high-affinity component was formed by the phosphate-binding protein [195, 196]. The role of the periplasmic binding protein in the transport through the bacterial outer membrane was also previously established as part of the maltose/maltodextrin uptake system of *E. coli* [197, 198]. Hence, *in vivo* phosphate first binds to the affinity sites within OprP and subsequently binds to the periplasmic phosphate-binding protein to enable passage of phosphate through the outer membrane. However, of critical importance is an "appropriate" interaction strength of the phosphate ions towards OprP to attract phosphate from the dilute extracellular environment and then to allow the phosphate ions to dissociate from the channel to enable its association with the phosphate-binding protein. The presence of the negatively charged D94 in OprP seems to be important in achieving such an appropriate binding affinity for the phosphate.

One further important aspect of the phosphate selectivity of OprP is to discriminate phosphate from a very similar, tetrahedral-shaped oxyanion, i.e., sulfate. At this point we would like to point out that at around the physiological pH 7, phosphate is predominantly monobasic ($H_2PO_4^-$), with some percentage also in dibasic form (HPO_4^{2-}), while sulfate is in its fully ionized divalent (SO_4^{2-}) form. In nature, a precedent for the molecular recognition which allows discrimination between the phosphate and the sulfate can be realized based on the examples of the phosphate-binding protein (PBP) and the sulfate-binding protein (SBP). The ability of the PBP and the SBP to exquisitely discriminate between the phosphate and the sulfate was attributed to the presence of an Asp residue in the binding site of the PBP and the corresponding absence of the Asp residue in the binding site of the SBP [199–202]. Phosphate, in its physiologically available protonation states, can act as a H-bond donor and can specifically interact with a H-bond acceptor carboxylic group of the Asp side chain. However sulfate, in the absence of any H-bond donor, cannot form such specific interactions with the Asp residue and is subject to charge repulsion. OprP, being a phosphate-selective porin, can achieve exquisite specificity for phosphate over sulfate via the presence of the D94 residue in the binding site. Earlier we have already reported the role of D94 in the transition of phosphates between two central binding sites of OprP [172]. A high-energy barrier of 4 kcal/mol, compared to 2 kcal/mol for WT OprP, for the transition of phosphate between the two central binding sites in D94K further reinforces the role of the D94 residue in such transition processes (Fig. 4.2a).

In addition, the presence of the D94 residue in OprP may also help to stabilize the protonation states and in turn the positive charges of the cluster of the three consecutive arginine residues, namely R34, R59 and R60 (see Figure 4.1a), in the narrowest regions of the pore by forming the salt-bridges with them. The positive charges of these arginine residues are very important to maintain the phosphate binding affinity of OprP. It was reported for OmpF and PhoE channels that the close proximity of three adjoining arginine side chains may confer unusual ionization behavior leading to deprotonated forms of these arginines [203]. For the anion-selective porin Omp32 from *Delftia acidovorans*, the protonation states and positive charges of arginines from the arginine cluster was indicated to be stabilized by the formation of salt-bridges with the glutamate (E58) residue [204].

In biology, the functional importance of an amino acid can usually be justified based on its evolutionary conservation. We have already shown the evolutionary conservation of the D94 residue of OprP from *P. aeruginosa* between different OprP orthologs in *Pseudomonas* species (Appendix C, Fig. C1). However, a similar conservation of a negatively charged residue in other anion-selective porins may yield a general building principle of negatively charged residue - in terms of various points as we have discussed above - in anion binding sites of anion-selective porins. Amongst the few reported strongly anion-selective porins, the crystal structure of Omp32 porin from *Delftia acidovorans* is available. The Omp32 porin is a strongly anion-selective porin [205] and has a negatively charged residue, E58, in its anion binding site as also demonstrated by the corresponding PMF profile [206]. *Delftia acidovorans* belongs to the group of β-proteobacteria [207] and the sequence of Omp32 is similar to other reported anion-selective porins from the same group, namely porins from *Bordetella pertussis* [208], *Neisseria gonorrhoeae* [209], *Neisseria meningitidis* [210], and *Acidovorax delafieldii* [211]. Most important is the conservation of the residue E58 in the anion-selective porins of all these bacteria from the β-proteobacteria group supporting the importance of a negatively charged residue in the anion binding site (Appendix C, Fig. C3).

In conclusion, we have shown the importance of the residue D94 of OprP in conferring the appropriate binding affinity of phosphate towards OprP. The mutation of the negatively charged residue at position 94 to a positively charged residue, particularly lysine (K), led to a stronger binding of phosphate in OprP, both in electrophysiological bilayer measurements and free-energy MD simulations. Furthermore, we discussed the possible relevance of attaining the appropriate binding affinity of phosphate towards OprP to achieve an efficient and a unidirectional transport of phosphate across the outer membrane of *P. aeruginosa*.

Other than that, the importance of the D94 residue in conferring the phosphate selectivity to OprP over the sulfate and the possible role of D94 in stabilizing the protonation states and charges of arginine clusters are also described. The presence of a similar negatively charged residue in the anion-selective porins of the β-proteobacteria group of bacteria further reinforces the importance of negatively charged residues in anion binding sites of anion-selective porins. Molecular insights presented here can be useful to design a "model" anion binding site for biomimetic anion-selective porins and channels.

Acknowledgments

The authors would like to thank Que-Tien Tran for her contribution at the early stage of this study. The research leading to these results was conducted as part of the Translocation consortium (www.translocation.eu) and has received support from the Innovative Medicines Joint Undertaking under Grant Agreement n°115525, resources which are composed of financial contribution from the European Union's seventh framework programme (FP7/2007-2013) and EFPIA companies in kind contribution. This work has also been supported by grants KL 1299/6-1 and BE 865/16-1 of the Deutsche Forschungsgemeinschaft (DFG) and a Canadian Institutes for Health Research grant to REWH who also has a Canada Research Chair in Health and Genomics.

5. OprO *versus* OprP: Structure, Dynamics, Ion Selectivity and Ion Conductance

Abstract

OprP and OprO are the homologous porins from *P. aeruginosa* with a high sequence and structural similarity. Despite their similarities, OprP was reported as the phosphate-selective channel whereas OprO as the diphosphate-selective channel in electrophysiological experiments. To this end, we have investigated the phosphate selectivity of OprP and the diphosphate selectivity of of OprO utilizing free-energy molecular dynamics simulations. The potential of mean force profiles revealed a deeper potential well for phosphate in OprP than OprO whereas presence of an additional binding site for diphosphate in OprO compared to OprP. Thus simulations suggested possible reasons for the different selectivities of both porins. Structural analysis of OprP and OprO showed that OprP has two tyrosine residues, Y62 and Y114, in the central narrowest region of the channel whereas the corresponding residues in OprO are the phenylalanine F62 and the aspartate D114. To probe the importance of these two residues in assigning the different selectivities to OprP and OprO, *in silico* double mutants of each porin were generated by swapping their respective residues, i.e., the Y62F Y114D double mutant of OprP and the F62Y D114Y double mutant of OprO. These double mutant channels showed a trend to interchange the phosphate and diphosphate selectivity of OprP and OprO. In addition, applied-field MD simulations with the KCl electrolytes revealed a trend to swap the ion selectivity of the double mutant channels. The findings presented in this study with the double mutant channels of OprP and OprO will be experimentally validated.

The material in this chapter is so far unpublished. The unpublished crystal structure of OprO used in this study has been provided by Prof. Bert van den Berg, New Castle University.

5.1. Introduction

The outer membrane of Gram-negative bacteria acts as a molecular sieve due to the presence of a class of channel-forming proteins called porins [133]. Porins can be divided into two categories: the non-specific porins (e.g., OmpF, OmpC) form channels to allow general diffusion of hydrophilic molecules below a certain size based on the size-exclusion principle, while the substrate-specific porins permit the facilitated diffusion of specific substrates by virtue of having a defined substrate-binding site in their channel. Among the substrate specif porins, the OprP and OprO channels of *Pseudomonas aeruginosa* present interesting examples due to their reported phosphate and polyphosphate selectivity respectively in bilayer electrophysiological measurements [157–159, 212, 213]. Recently we probed the phosphate-selectivity of OprP using all-atom free-energy molecular dynamics (MD) simulations to understand the molecular factors responsible for the selectivity [172]. We also discussed the phosphate-selectivity of OprP in the context of ion-selective channels like K^+-selective or Cl^--selective ion channels. In the present study, we have investigated the molecular details behind the phosphate selectivity of OprP *versus* the diphosphate selectivity of OprO as observed in bilayer experiments. Going one step further, we have engineered OprP and OprO porins via generating *in silico* double mutants of porins to see if the selectivities of OprP and OprO can be swapped.

Double mutants of OprP and OprO suggested based on computational studies will be generated experimentally by the groups of Prof. Bert van den Berg , New Castle University and, Prof. Roland Benz, Jacobs University Bremen. Electrophysiological measurements concerning their selectivities will be performed by the group of Prof. Roland Benz. The so far unpublished crystal structure of OprO used in this study has been provided by Prof. Bert van den Berg, New Castle University.

5.2. Results and Discussion

Sequence and structure comparison between OprP and OprO

In a first step we investigated the sequence and the structural differences between OprP and OprO. The sequences of OprP and OprO have been aligned using Emobss Needle pairwise protein sequence alignment web-service (Fig. 5.1) [214]. OprP and OprO demonstrated 74% sequence identity and 86% sequence similarity between them and only three single amino acid gaps in the OprP sequence need to be introduced in their alignment (Fig. 5.1). This comparison indicates a very high sequence and in turn

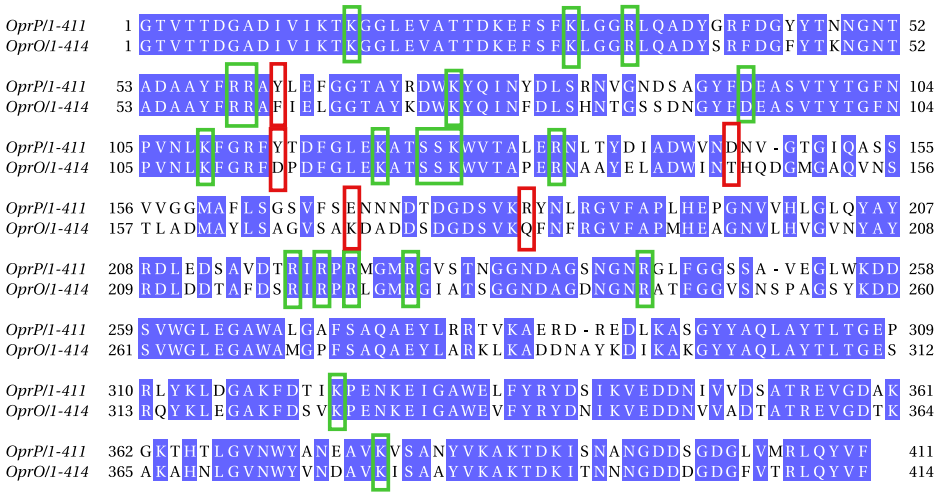

Figure 5.1.: Sequence alignment of OprP and OprO from *Pseudomonas aeruginosa*. Some of the important conserved residues in OprP and OprO which are a part of the arginine ladder, the lysine clusters and the phosphate binding sites are highlighted using green colored boxes. Several non-conserved residues which might be important in assigning phosphate *versus* diphosphate selectivity of OprP and OprO are highlighted using red colored boxes. The figure has been generated using Jalview [215].

structural similarity between the porins OprP and OprO. A closer look at the sequence alignment in Fig. 5.1, particularly those positions highlighted with green boxes, shows that residues which are crucial in assigning the phosphate selectivity to OprP, i.e., residues of central phosphate binding sites, the arginine ladder and the lysine clusters, are all conserved between OprP and OprO. This makes the differential selectivity of OprP and OprO for phosphate and diphosphate even more intriguing.

To understand the structure and dynamics of both porins, OprP and OprO were embedded in POPE lipid bilayers and solvated using TIP3P water molecules. Equilibrium MD simulations of 25 ns each for OprP and OprO were performed in an NPT ensemble using the NAMD 2.9 program [131] and the CHARMM27 force field [95]. Simulations have been performed at a temperature of 310 K and the pressure of 1 atm. Periodic boundary conditions have been utilized and short-range nonbonded interactions were calculated using a cutoff of 12 Å and a switching distance of 10 Å while the long-range electrostatic interactions have been treated using the particle mesh Ewald method [183]. Using the r-RESPA multiple time step method [184], bonded interaction were evaluated every 1 fs while short-range nonbonded and long-range electrostatic interactions at every 2 fs and 4 fs, respectively. Bond constraints are applied to all water hydrogen atoms using the SHAKE algorithm [185].

From the snapshots of equilibrium MD simulations for OprP and OprO, the pore

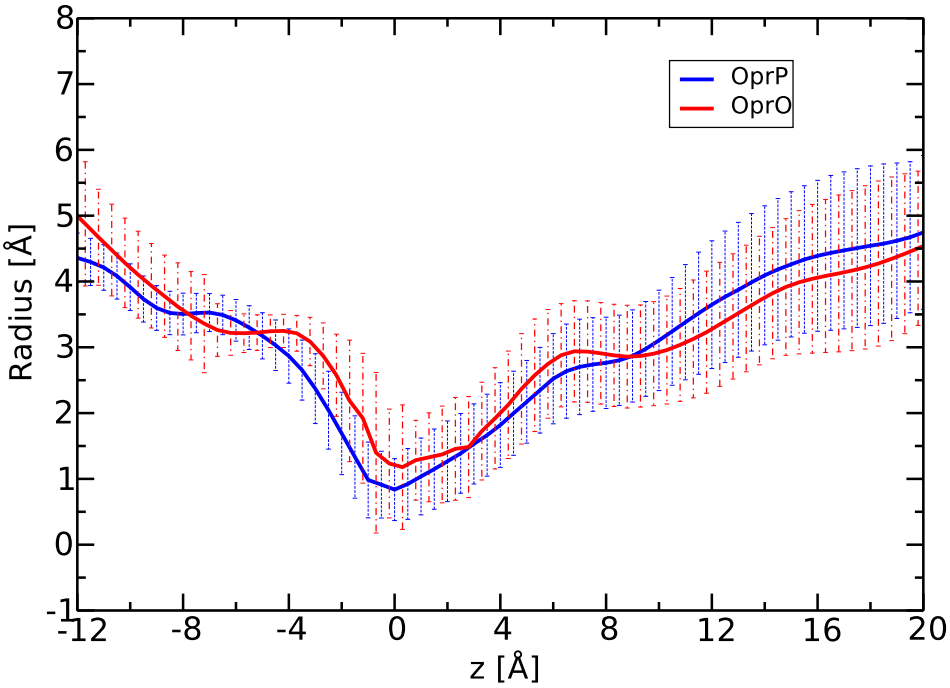

Figure 5.2.: Average radius of the OprP and OprO porins along with the corresponding standard deviation derived from unbiased MD simulations. The pore radius have been determined using the HOLE program [216].

lumen radius have been determined for each snapshot using the HOLE program [216]. The average pore radius and the dynamics of the pores, as denoted by standard deviations, are reported in Fig. 5.2. The most notable differences in radius were found at the central region of the pores, from -4 Å to 2 Å, where OprO has a higher average radius compared to OprP. In addition, OprO has higher fluctuations in the pore radius compared to OprP, as denoted by larger error bars particularly around 0 Å and hence more flexibility in this region (Fig. 5.2).

In a subsequent step, a detailed structural analysis was carried out to further decode the differences in structure and dynamics of OprP and OprO. The structural analysis pointed out two highly important residual differences between OprP and OprO in the central narrowest region of the pore (Fig. 5.3). Two tyrosine residues, Y62 and Y114, in OprP are replaced by F62 (phenylalanine) and D114 (aspartate) in OprO. Fig. 5.3 shows the average diameter surface of the OprP and OprO pore lumen generated using the HOLE program [216] and color-coded according to the radius in the different regions of the pore. The presence of two tyrosines and in particular an aromatic and a bulkier Y114 residue in OprP compared to D114 in OprO makes the OprP pore radius very narrow in this particular region as also visible by the red colored surface, i.e. an average radius below 1 Å (Fig. 5.3a). Other than these two residues, the presence of bulky residues in the central region of OprP (from -4 Å to 2 Å) - namely L135 (A135), T136 (A136),

S166 (G167), N382 (A385), Q204 (N205), Y79 (F79), Y183 (F184) - may contribute to the smaller radius of OprP in this region. The residues in parenthesis indicate the corresponding residues in OprO. Furthermore, the dynamics of the pore can be analyzed by looking at H-bonds and salt-bridges networks between the different residues in the particular region. A salt-bridge is present between the residues D145 and R182 in OprP throughout the complete unbiased MD simulation. The corresponding residues in OprO, i.e., T145 and Q183, cannot form such salt bridges. In addition, the side chains of residues Y62 (F62), Y79 (F79), Y183 (F184), T136 (A136), S166 (G167), N382 (A385) have the ability to form H-bonds due to the presence of H-bond donor/acceptor groups in the side chains of these amino acids while the side chains of the corresponding residues in OprO, as mentioned in parenthesis, lack this ability. These facts may explain the larger variances of the OprO radius in the central region compared OprP as reported in Fig. 5.2. The finding of a larger average radius of OprO is also reinforced by the experimental fact that for a 1 M KCl electrolyte solution the conductance is ∼2 times higher for OprO compared to OprP [158, 213].

Phosphate selectivity of OprP *versus* Diphosphate selectivity of OprO

To understand the selectivity of OprP and OprO, free-energy molecular dynamics simulations have been carried out to determine the energetics of phosphate and diphosphate ion transport through OprP as well as OprO utilizing the same methodology as employed to probe the phosphate selectivity of OprP in our previous studies [172, 193]. The adaptive biasing force (ABF) approach [162, 163] as implemented in the *collective variable* module of the NAMD 2.9 program [131] has been applied to determine the effective free energy profiles for the transport of different ions. The principal axis of the channel is aligned parallel to the z axis and the reaction coordinate is assigned to be the z position of the ion. Moreover, the change in free energy is determined with respect to the bulk value. The monovalent form of the phosphate ion, $H_2PO_4^-$ has been investigated also in consistence with our previous study while the divalent form of the diphosphate ion, $H_2P_2O_7^{2-}$, has been considered as the most probable protonation state at the pH of 6. Force field parameters for $H_2P_2O_7^{2-}$ were obtained with the help of the ParamChem webserver which performs an assignment of parameters and charges using analogy principles [217, 218]. Potential of mean force (PMF) profiles have been determined using a total simulation time of ∼200 ns for the sampling of the phosphate ion in each pore and a total simulation time of ∼300 ns to efficiently sample the PMF of the diphosphate ion. PMF profile for the phosphate ion transport through OprP has already been obtained in our previous study [172].

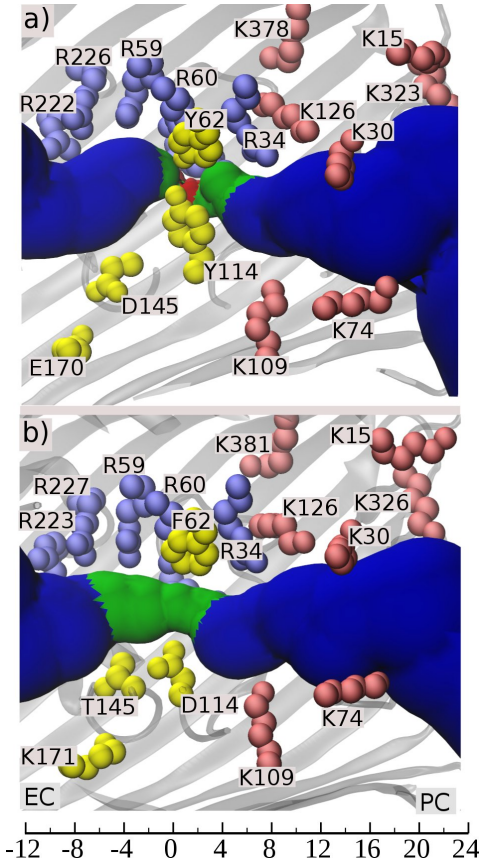

Figure 5.3.: Structural features of a) OprP and b) OprO. Approximate relative radii of both pores are indicated by a solid surface presentation. The different regions are color-coded according to an average radius in the respective regions (blue: radius above 3 Å, green: between 1 to 3 Å, red: below 1 Å). Important residues along the ion permeation pathway are labeled and mapped to their position along the z axis. The yellow colored residues are non-conserved between OprP and OprO and might be important leading to the different ion selectivities of OprP and OprO.

The PMF profiles for the monophosphate transport through OprP and OprO are shown in Fig. 5.4a. Electrophysiological bilayer measurements suggest that phosphate binds ∼4 times stronger to OprP than to OprO (I_{50}= 0.5 mM for OprP and 2.0 mM for OprO) [213]. Our previous study concerning the phosphate transport through OprP demonstrated two central binding sites, P1 and P2, for phosphate with the well-depth of ∼9 kcal/mol (Fig. 5.4a) [172]. These two binding sites are spatially apart by ∼5 Å along the z axis with an energy barrier of ∼2 kcal/mol between them [172]. In the present study, the PMF profile for the phosphate transport through OprO reveals a very similar profile in terms of the overall shape (Fig. 5.4a). Indeed, phosphate ions have two central binding sites in OprO as well and at the same positions as in OprP. The overall similar shape of the PMF profiles for OprP and OprO are not very surprising considering the fact that both proteins share 74% sequence identity and, moreover, the residues which are

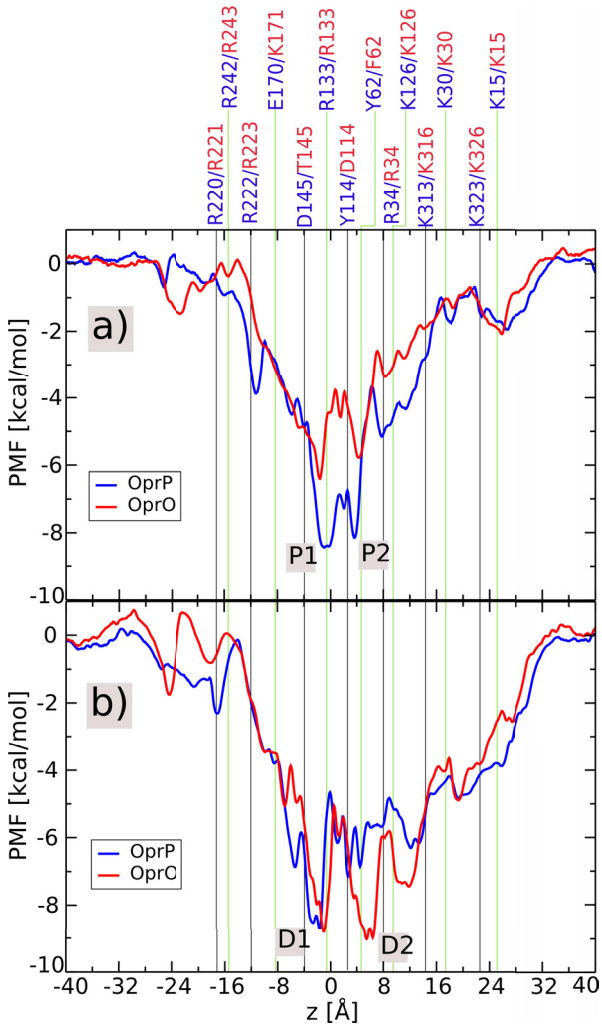

Figure 5.4.: PMF profiles for the transport of a) $H_2PO_4^-$ and b) $H_2P_2O_7^{2-}$ through OprP and OprO. Important residues of OprP and OprO along the ion permeation pathway are mapped onto the PMF profiles with respect to their positions along the z axis and labeled at the top of the figure (blue label: OprP, red labels: the corresponding residues in OprO).

considered to be important in the phosphate transport are all conserved between OprP and OprO (Fig. 5.1). Nevertheless the major difference between the two porins in terms of phosphate transport is the depth of the binding sites for phosphate. Phosphate had a binding well-depth of ∼7 kcal/mol in OprO compared to ∼9 kcal/mol in OprP (Fig. 5.4a). The deeper potential well in OprP leads to a stronger binding of monophosphate in OprP than in OprO. We also calculated the dissociate constant of the phosphate for OprO from the PMF profile using the same method as we have utilized in Ref. 172. The calculated dissociation constants from the PMF profiles for phosphate are found to be 0.23 μM [172] and 7.37 μM for OprP and OprO, respectively. Therefore, our calculation also suggests a stronger binding of phosphate, ∼32 times, in OprP than in OprO which is in qualitative

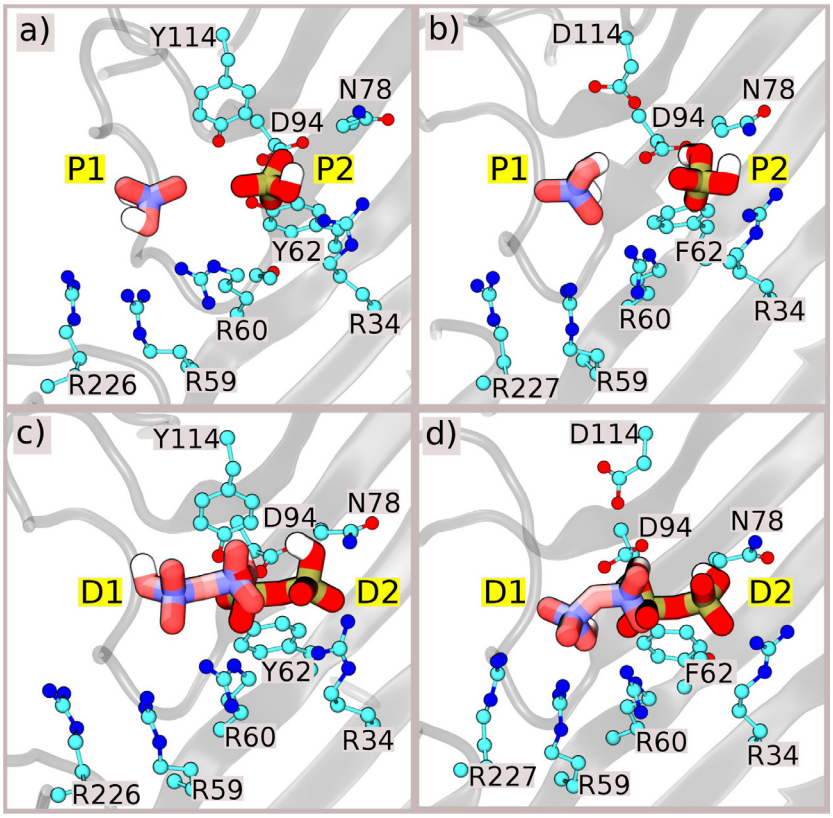

Figure 5.5.: Representative snapshots of $H_2PO_4^-$ in the binding sites P1 and P2 of a) OprP and b) OprO. Similar snapshots of $H_2P_2O_7^{2-}$ in the binding sites D1 and D2 of c) OprP and d) OprO. Phosphate and diphosphate are shown using a stick representation while some of the interacting residues of the channels are shown using a ball-and-stick representation. Two phosphates or diphosphates are shown to demonstrate the relative positions of the binding sites though there is no experimental evidence for a double occupancy of the channel. The PMF calculations have been performed with single phosphate or diphosphate ions.

agreement with experimental ratio of ∼4. Representative snapshots of the phosphate ion in the binding sites P1 and P2 for OprP (Fig. 5.5a) and OprO (Fig. 5.5b) are shown. In OprP the binding site P1 is formed by residues R59, R60, K121 and R133 while binding site P2 is formed by residues R34, Y62 (F62), D94, S124, S125 and R133. The same residues are involved in the formation of the binding sites P1 and P2 for phosphate in OprO unless stated otherwise in parenthesis.

Next we probed the diphosphate ion transport through OprP and OprO. In bilayer experiments ∼16 times stronger binding of diphosphate to OprO compared to OprP was observed and therefore a poly-phosphate selectivity of OprO was reported (I_{50}= 0.3 mM for OprO, and 4.9 mM for OprP) [213]. PMF profiles for the diphosphate transport through OprP and OprO are displayed in Fig. 5.4b. In diphosphate transport through OprO two central binding sites, D1 and D2, with the energy well-depth of ∼9 kcal/mol can be seen.

These two sites, D1 and D2, are separated by a barrier of ∼5 kcal/mol and are spatially ∼5-6 Å apart from each other (Fig. 5.4b). In the case of OprP, the overall PMF profile is quite similar to the one observed for OprO except for the fact that diphosphate experiences only one central binding site in OprP, i.e., D1, and site D2 is missing (Fig. 5.4b). It may be concluded that the higher affinity of OprO for diphosphate is due to the presence of two central binding sites compared to only one site in OprP. Two defined central binding sites for diphosphate in OprO increase the overall pore attractive volume for diphosphate at the center of the channel. The substrate may also hop from one site to the other, contributing to a stronger binding affinity of diphosphate for OprO compared to OprP. The calculated dissociation constant from PMF profiles for diphosphate with OprO and OprP are found to be 0.089 μM and 0.38 μM, respectively. Furthermore, our calculations suggest a stronger binding of diphosphate, ∼4 to 5 times, for OprO compared to OprP, in qualitative agreement with experiment.

Representative snapshots of the diphosphate ion in the sites D1 and D2 for OprP and OprO are shown in Figs. 5.5c and 5.5d, respectively. In OprP the diphosphate binding site D2 is absent. However, we have shown the diphosphate ion in OprP at the same position as that of the site D2 in OprO for comparison. As we have discussed before and can be seen in Fig. 5.5, the presence of the bulky residue Y114 in OprP compared to D114 in OprO makes the OprP pore lumen very narrow in that particular region. The other residue which is different between OprP and OprO in the binding site region is Y62 in OprP while the corresponding residue in OprO is F62. In OprO the binding site D1 is formed by the residues R59, R60, D94, D114, K121 and R133 while the binding site D2 is formed by the residues R34, F62, N78, D94, D114, S124, S125 and R133.

Moreover, we analyzed the simulation data to determine the molecular factors behind the observed differences in PMF profiles for phosphate and diphosphate ions between OprP and OprO. We suspect that the selectivity for phosphate and diphosphate of either of the two porins can be a result of the geometrical factors, such as a pore size, or the different distributions of the charged amino acids between the two porins or a combination of both. From the geometrical point of view, the average pore diameter is smaller for OprP compared to OprO especially in the narrowest part of the pore (Fig. 5.2 and 5.3). As we have also discussed before, the presence of two bulky aromatic tyrosine residues (Y114 and Y62) in OprP generates the narrowest part in the pore. At that position, the pore diameter is larger for OprO due to the presence of less bulky residues, i.e., D114 and F62 (Fig. 5.3). From the charge distribution point of view also, D114 in OprO is most likely important for the diphosphate selectivity as the corresponding residue in OprP, Y114, is

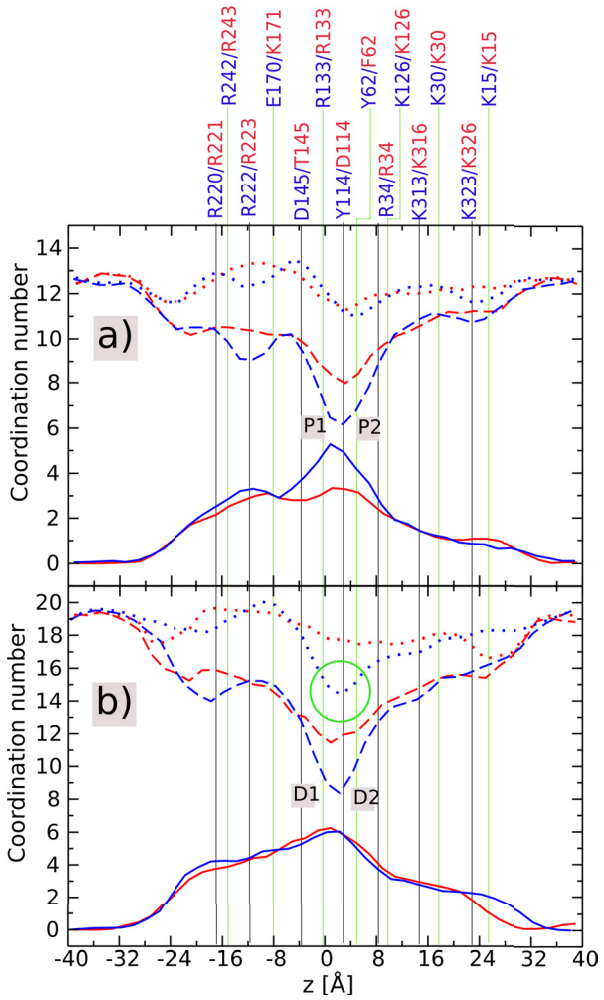

Figure 5.6.: Coordination numbers, i.e., protein (solid line), water (dash line) and total (dot line) contacts, for the permeation of a) $H_2PO_4^-$ and b) $H_2P_2O_7^-$ through OprP (blue) and OprO (red). Important residues of OprP and OprO along the ion permeation pathway are mapped with respect to their positions along the z axis and labeled at the top of the figure (blue labels: OprP, red labels: the corresponding residues in OprO).

neutral.

To further understand the effects of such factors, a coordination number analysis for the permeating ions through OprP and OprO has been carried out. The average number of protein or water contacts within the specified cut-off distance from the permeating ion in the different regions of the pore are termed as “coordination number”. Ion dehydration is one of the most important factors for the passage of ions through narrow pores [187] and can be the rate-limiting step in ion transport as particularly reported for anion-selective channels [165–167]. Removal of water molecules from ion hydration shells is an energetically unfavorable process which needs to be compensated by favorable protein contacts inside the pore. Considering all these factors, the coordination analysis

can give important clues about the interaction between the permeating ions, waters, the protein and their interplay in the different regions of the pore. Such an analysis has been exploited to decipher the K^+-selectivity of potassium channels [15]. Amongst the various suggested hypothesis for ion selectivity based on coordination number, most interesting is the "field-strength hypothesis" [15]. In this hypothesis one assumes that the ion selectivity is a property of the type of the coordinating ligand (water *versus* protein contacts) and their relative contributions with the permeating ion. Different types of coordination ligands have varying intrinsic physical and electrostatic properties and hence change in their relative contribution may assign the selectivity of a particular ion over an other one. In our previous study, the "field-strength hypothesis" was able to explain the selectivity of OprP for phosphate when compared to sulfate or chloride ions [172].

In a similar way as reported in Ref. 172, we carried out a "coordination number" analysis for phosphate and diphosphate ions. As presented in Fig. 5.6a, phosphate ions strip off a maximum of seven water molecules in the central region of OprP which are compensated by the protein contacts. The total number of contacts, i.e., the sum of water and protein contacts, remains almost constant through out the length of the pore. Different to OprP, in OprO phosphate ion strips off a maximum of only five water molecules. As one can see in Fig. 5.6a, the relative contribution of water *versus* protein contacts are different for phosphate in OprP and OprO which is consistent with the selectivity of OprP for phosphate in agreement with the "field-strength hypothesis". Compared to OprO, due to the small average diameter of OprP in the central region and also due to the smaller fluctuation in diameters (Fig. 5.2, 5.3, 5.5), more water molecules are stripped off from the permeating phosphate ions in OprP and are replaced with more suitable - in terms of binding to a channel - protein contacts as coordination ligands. This may lead to the stronger binding of phosphate in OprP.

In the case of diphosphate transport (Fig. 5.6b) through OprO, the diphosphate ion strip off at maximum seven water molecules in the central region of the pore which are compensated by an almost equivalent number and more favorable protein contacts. This fact is also reflected in the PMF profiles by the presence of the two energetically favorable central binding sites, D1 and D2, in OprO. The total number of contacts for the diphosphate remains almost constant through the length of OprO. However, during the diphosphate transport through OprP more water molecules are stripped away, i.e., ten water molecules in OprP compared to seven in OprO (Fig. 5.6b). But contrary to OprO, not all lost water contacts are compensated by favorable protein contacts as highlighted in Fig. 5.6b via the green circle, where the total number of contacts for diphosphate in

OprP dropped significantly, from average 19 contacts throughout the length of the pore to only 14 contacts, near the binding site D2. As the ion dehydration - which is energetically not favorable - is not completely compensated for by favorable protein contacts, this leads to an energetic penalty for diphosphate transport and in turn diminishes the binding site D2 for diphosphate in OprP.

Swapping the phosphate and diphosphate selectivities of OprP and OprO

The PMF profiles for the phosphate and diphosphate transport indicate presumably two very important non-conserved residues between OprP and OprO that are located in the central region of the channels, namely Y114 and Y62 in OprP while the corresponding residues in OprO are D114 and F62. These residues may be crucial in determining the particular ion selectivity of the corresponding channel. It can be hypothesized that by swapping these two residues of OprP and OprO at these two particular positions, i.e., residue 62 and 114, that the phosphate selectivity of OprP and the diphosphate selectivity of OprO can be interchanged. To further understand the effects these residue on the ion selectivity of OprP and OprO, double mutants of each of the porins are generated *in silico*. Residues Y62 and Y114 of OprP are mutated to the corresponding residue of OprO, i.e, phenylalanine (F) and aspartate (D), respectively. We denote the double mutant Y62F Y114D of OprP as the P→O mutant for the sake of clarity in our discussion. Conversely the double mutant F62Y D114Y of OprO is denoted as the O→P mutant. The PMF profiles for the transport of phosphate and diphosphate through the P→O and the O→P mutants have been calculated and are compared with the wildtype OprP and OprO channels in Fig. 5.7.

The PMFs for the phosphate permeation through the wildtype channels contained energetic wells of ∼9 kcal/mol for OprP and ∼7 kcal/mol for OprO (Fig. 5.4a). This leads to a stronger binding of phosphate in OprP compared to OprO and provided a possible reason for the phosphate selectivity of OprP. To swap the phosphate selectivity of OprP and OprO using double mutant proteins, phosphate should have a stronger binding in the O→P mutant (F62Y D114Y) of OprO compared to the P→O mutant (Y62F Y114D) of OprP. Indeed the O→P mutant of OprO revealed a binding depth of ∼8 kcal/mol for phosphate (Fig. 5.7a) while the P→O mutant of OprP had a binding depth of ∼6 kcal/mol for phosphate (Fig. 5.7b). Hence the PMF profiles suggested that with the help of double mutants, i.e., Y62F Y114D of OprP and F62Y D114Y of OprO, the phosphate selectivity of OprP and OprO may be swapped.

The major difference which may be attributed to the diphosphate selectivity of OprO over OprP is the presence of the additional binding site D2 for diphosphate in OprO and

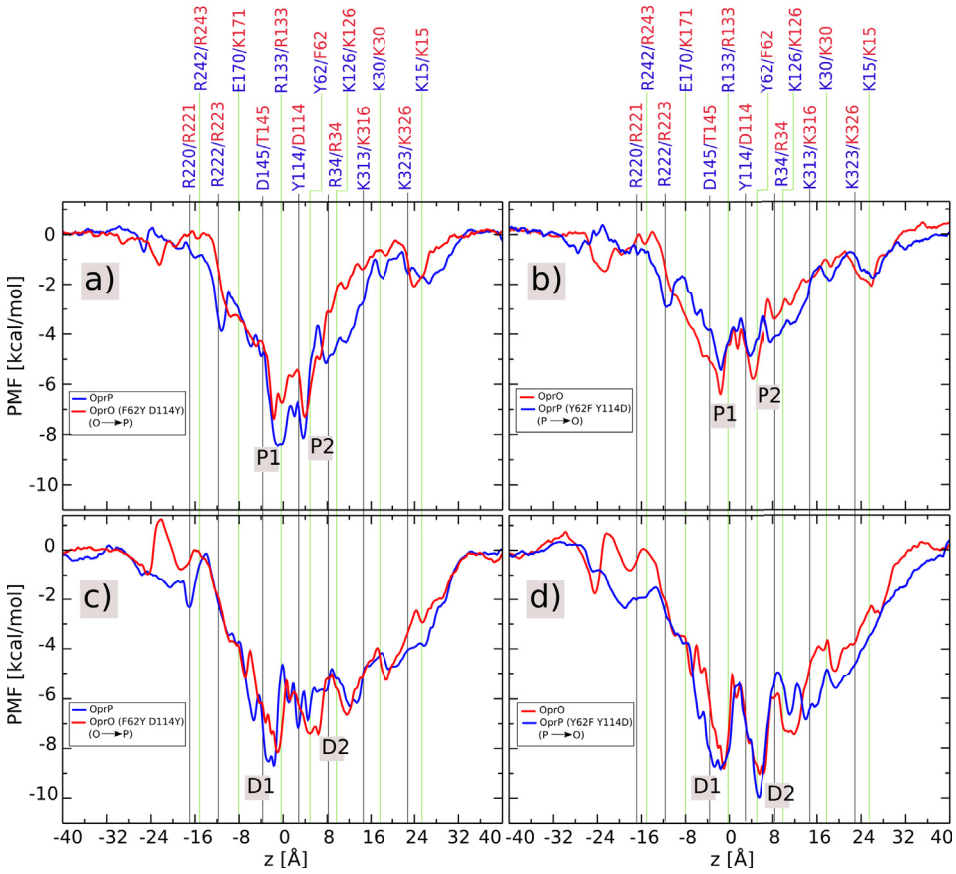

Figure 5.7.: PMF profiles for the transport $H_2PO_4^-$ in panels a) and b) and for $H_2P_2O_7^{2-}$ through the double mutant channels in panels c) and d). At the same time, panels a) and c) show PMF profiles for the O→P (F62Y D114Y) mutant of OprO while panels b) and d) PMF profiles for the P→O (Y62F Y14D) mutant of OprP. For comparisons, the PMF profiles for the phosphate and diphosphate permeation through wildtype OprP and OprO are also shown. Important residues of OprP and OprO along the ion permeation pathway are mapped onto the PMF profiles with respect to their positions along the z axis and labeled at the top of the figure (blue labels: OprP, red labels: the corresponding residues in OprO).

the corresponding absence of the site D2 in OprP (Fig. 5.4b). To swap the diphosphate selectivity of the OprO and OprP double mutants, diphosphate should experience an additional binding site D2 in the P→O mutant (Y62F Y114D) of OprP and the absence of the same site in the O→P mutant (F62Y D114Y) of OprO as can be seen in Fig. 5.4b. PMF profiles for the diphosphate permeation through double mutants reveal the presence of the site D2 in the P→O mutant of OprP (Fig. 5.7d). The O→P mutant of OprO also contains the D2 binding site but with a well-depth that is 2 kcal/mol smaller than that of the wildtype OprO (Fig. 5.7c). Therefore the O→P mutant of OprO starts to loose the binding site D2. Hence with the suggested double mutants, the diphosphate selectivity of OprP and OprO may be swapped which needs further experimental validation.

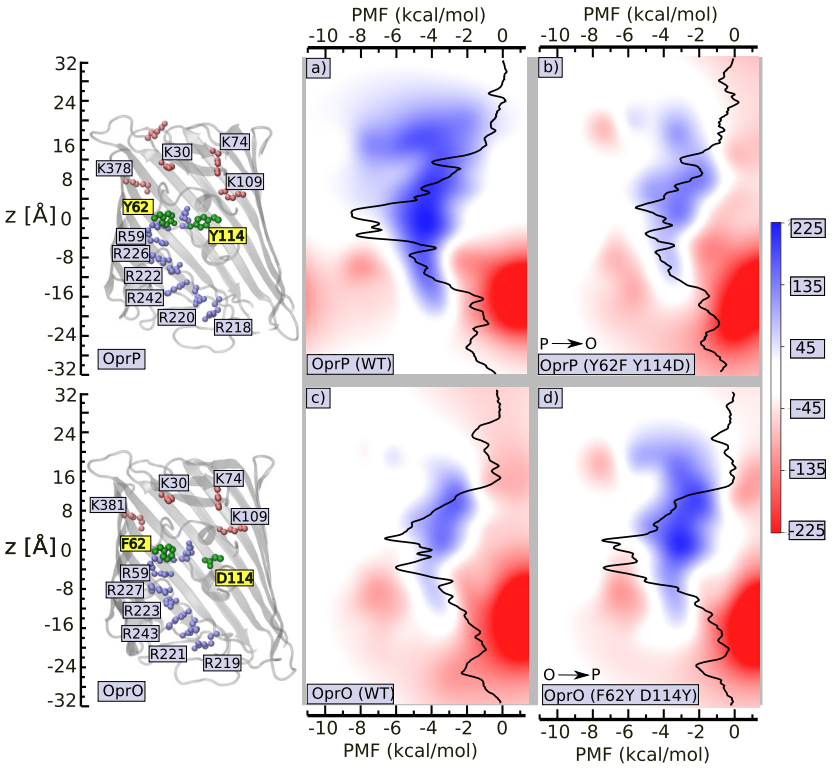

Figure 5.8.: Electrostatic potential maps for a) wildtype OprP, b) P→O mutant(Y62F Y114D) of OprP, c) wildtype OprO, and d) O→P mutant (F62Y D114Y) of OprO. The OprP and OprO channels together with important residues are mapped along the potential maps to enable identification of possible residues which are responsible for particular features of the potential maps. In addition, PMF profiles for the $H_2PO_4^-$ ion permeation through each of the channels are mapped onto the respective potential maps to show the correlation between the energetics of the $H_2PO_4^-$ transport and the electrostatic potential profiles. The potential maps are in the $y-z$ plane at an x position corresponding to the middle of the one of the three pores and are generated using the PMEPlot plug-in for VMD [25, 181].

To further understand the changes in PMF profiles with mutant channels, we calculated electrostatic potential maps of the wildtype OprP and OprO channels as well as their double mutants (Fig. 5.8). Such electrostatic potential maps which essentially drive the electrostatic interactions with the permeating ions can play a key role in assigning selectivities to the channel. For example, in the case of aquaporin channels, the substrate specificities between different subfamilies of aquaporins can be rationalized based only on the electrostatic profiles of the channels [194]. The potential maps are computed using the PMEPlot plug-in of VMD [25, 181] and are averaged over the unbiased simulation length of 25 ns. The potential map for the wildtype OprP (Fig. 5.8a) has a stronger electropositive region at the central region of the channel (indicated by blue color) compared to the wildtype OprO (Fig. 5.8c). This provides a possible hint for the stronger binding of phosphate in OprP compared to OprO. However, in the case of the double mutants,

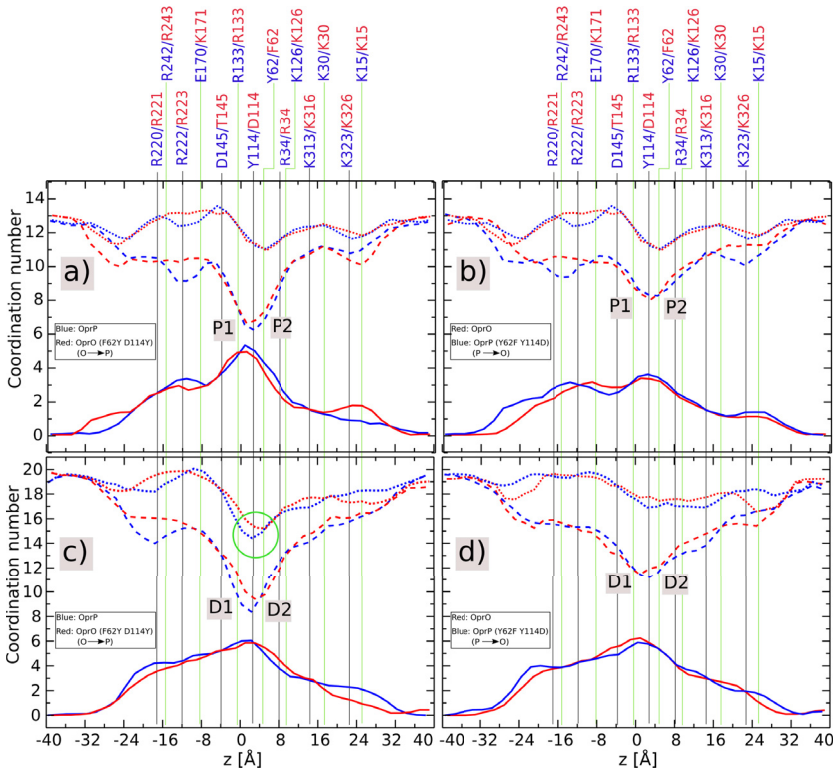

Figure 5.9.: Coordination numbers, i.e., protein (solid line), water (dash line) and total (dot line) contacts for the permeation $H_2PO_4^-$ in panels a) and b) as well as of $H_2P_2O_7^{2-}$ in panels c) and d) through the double mutant channels. At the same time, panels a) and c) display the coordination numbers for the O→P (F62Y D114Y) mutant of OprO while panels b) and d) show the same quantity for the P→O (Y62F Y114D) mutant of OprP. The coordination numbers for the phosphate and diphosphate permeation through wildtype OprP and wildtype OprO are shown as well for comparison. Important residues of OprP and OprO along the ion permeation pathway are mapped with respect to their positions along the z axis and labeled at the top of the figure (blue labels: OprP, red labels: the corresponding residues in OprO).

phosphate has a stronger binding to the O→P mutant (F62Y D114Y) of OprO than to the P→O mutant (Y62F Y114D) of OprP as suggested by the PMF profiles (Fig. 5.4a). We also observed the corresponding changes in the potential maps of the mutant proteins. The O→P double mutant of OprO has a stronger electropositive region (Fig. 5.8d) in the central region of the channel compared to the P→O double mutant of OprP (Fig. 5.8b). In fact, the P→O double mutant of OprP of has an electrostatic potential map very similar to the wildtype OprO potential map (Fig. 5.8b and c). Conversely, the O→P double mutant of OprO has the electrostatic potential map, particularly the strong electropositive region at the center of the channel, which is comparable to the potential map of the wildtype OprP (Fig. 5.8a and d).

The coordination number analysis revealed important clues in rationalizing the

phosphate and diphosphate selectivities of wildtype OprP and OprO, respectively, as shown in Fig. 5.6. In the case of phosphate, stronger binding of phosphate to the wildtype OprP compared to the wildtype OprO is attributed to the removal of more water molecules from the hydration shell of the permeating phosphate in the wildtype OprP (Fig. 5.6a). However, the O→P mutant (F62Y D114Y) of OprO strips more water molecules from the permeating phosphate, almost same in number as the wildtype OprP (Fig. 5.9a), than the P→O mutant (Y62F Y114D) of OprP (Fig. 5.9b). This finding hints a possible clue for the stronger binding of phosphate in the O→P mutant compared to the P→O mutant. In the case of diphosphate, more water molecules are stripped from the permeating ion in the wildtype OprP than the wildtype OprO (Fig. 5.6b). On the contrary, the OprO double mutant F62Y D114Y (O→P) removes more water molecules from the hydration shell of diphosphate ions which is almost same in number as the wildtype OprP (Fig. 5.9c). However, as observed for the wildtype OprP, the removed water contacts are not compensated for by an equivalent number of protein contacts. This leads to a drastic decrease in total contacts near the site D2, as shown by the green-colored circle in Fig. 5.9c, for the O→P mutant of OprO and in turn demonstrates a tendency towards the removal of binding the site D2. These interchanged water-protein contacts profiles for phosphate and diphosphate between wildtype and double mutant channels (Fig. 5.9) explain the observed changes in PMF profiles.

Applied-field simulations of the KCl electrolytes

In addition, we carried out applied-field MD simulations to understand the KCl conductance properties through the OprP and OprO wildtype channels as well as the mutant channels. Two important properties which can be obtained from such simulations will be the conductance and the selectivity of the channel. For the applied field simulations, a homogeneous external electric field E is applied in the z direction proportional to the voltage V, $E = V/L_z$ where L_z is the system length in z direction normal to the membrane [114]. The applied-field simulations have been performed in an NVT ensemble with an applied voltage of 0.5 V in z direction. The detailed procedures to perform such simulations as well as to calculate current and pore conductance are given elsewhere [27]. It was shown by Im and Roux for the OmpF porin that the ratio of individual currents can be approximately equivalent to the permeability ratio if a free energy barrier for the passage of ions is located approximately at the center of the channel[57]. In case of OprP and OprO, a constriction region of the channels is located roughly at the center of the channel (Fig. 5.3) and a free energy barrier/binding region for the K^+ and Cl^- ions are also located at the center of the channel [172]. Therefore, we assume that the selectivity,

Porins	Simulations		Experiments	
	Conductance [pS]	Current ratio [I_a/I_c]	Conductance [pS]	Selectivity [P_a/P_c]
OprP (WT)	350±111	27.6±1.9	260 [158]	>70 [159]
OprO (WT)	717±130	10.1±3.1	610 [213]	-
OprP (Y62F Y114D)	696±17	4.5±1.7	-	-
OprO (F62Y D114Y)	712±80	21.2±3.8	-	-

Table 5.1.: 1 M KCl pore conductance for the wildtype (WT) OprP and OprO as well as double mutant channels. Simulation data reported are the average values of three separate simulations while each of them is 100 ns long.

in terms of anion to cation permeability ratio P_a/P_c, can be proportional to the ratio of individual currents I_a/I_c obtained from Cl^- and K^+ ions for OprP and OprO.

The applied-field simulations results for the KCl transport through the wildtype and the double mutant channels are given in Table 5.1. In bilayer experiments, OprO has an approximately 2 times higher conductance than OprP. In simulations also, the conductance of OprO is ∼2 times higher than that of OprP in agreement with experiments (Table 5.1). The absolute values of simulated conductances for both OprP and OprO are higher than experimental ones. This is probably due to the higher diffusion coefficients of the TIP3P water models used in our simulations [161, 219]. From the simulated current ratio, I_a/I_c, the OprP channels is found to be more anion selective than OprO which needs further experimental validation. The simulated current ratio for OprP is lower than the experimental permeability data which may be attributed to the higher applied voltage in simulations.

It will be interesting to probe if the KCl conductance and selectivity properties of the OprP and OprO channels can be swapped with the double mutant channels. On one hand, the P→O mutant (Y62F Y114D) of OprP demonstrated the conductance and selectivity properties which is close to the wildtype OprO channel (Table 5.1). On the other hand, the O→P mutant (F62Y D114Y) of OprO has a selectivity in a range close to OprP but the conductance is still more like OprO (Table 5.1). Hence the P→O and the O→P mutants shows a clear tendency to swap the KCl selectivity of OprP and OprO. However, the KCl conductance property can only be changed with the P→O mutant which can almost reproduce the conductance of OprO.

5.3. Conclusions

We have carried out free-energy MD simulations to understand the phosphate selectivity of the OprP porin and the diphosphate selectivity of the OprO porin from *P. aeruginosa*.

OprP and OprO are homologous porins having a very high sequence identity and similarity between them. The radius profiles of the channels indicate a slightly larger radius of OprO in the central regions of the channel compared to OprP. The PMF profiles rationalized the specific selectivities of each channel. Phosphate ions have ∼2 kcal/mol deeper central binding pockets in OprP compared to OprO leading to stronger binding of phosphate in OprP. Diphosphate ions experience two central binding sites in OprO and only one central binding site in OprP. Hence the diphosphate selectivity of OprO can be assigned to the presence of one additional binding site, D2, in OprO when compared to OprP. A coordination number analysis reveals the molecular basis for the observed PMF profiles. In case of phosphate, OprP strips off two more water molecules from the permeating phosphate compared to OprO and replaces the water contacts with protein contacts which are favorable for binding of the phosphate to the channel. In the case of diphosphate as well, OprP strips off three more water molecules from the permeating diphosphate ion than OprO. However, not all lost water contacts are replaced by protein contacts, particular near site D2, which leads to the absence of binding site D2 for diphosphate ions in OprP.

Based on the PMF profiles and structural analysis between OprP and OprO, two very important non-conserved residues are found in the central regions of the channels. These residues are Y62 and Y114 in OprP while the corresponding residues are F62 and D114 in OprO. To understand the role of such residues in the phosphate and diphosphate selectivities of OprP and OprO, *in silico* double mutants have been generated. The Y62 and Y114 residues of OprP are mutated to the corresponding residues of OprO and vice versa. Both the P→O mutant (Y62F Y114D) of OprP and the O→P mutant (F62Y D114Y) of OprO resulted in changes in the PMF profiles for the permeation of phosphate and diphosphate ions. The mutants reveal a clear tendency to swap the phosphate selectivity of OprP and the diphosphate selectivity of OprO. The suggested double mutants from computational study will be experimentally validated. The group of Prof. Bert van den Berg, New Castle University, and the group of Prof. Roland Benz, Jacobs University Bremen, will provide the double mutant proteins of OprP and OprO and they will subsequently be measured using electrophysiology for their selectivities by the group of Prof. Roland Benz.

In addition, applied-field MD simulations are carried out to understand the KCl conductance and the selectivity properties through the wildtype OprP and OprO as well as the double mutant channels. For the wildtype OprP and OprO we obtained simulated conductances which are in a reasonable agreement with experiments. Both the P→O mutant (Y62F Y114D) of OprP and the the O→P mutant (F62Y D114Y) of OprO showed a

shift to interchange the KCl selectivity between OprP and OprO. However, in terms of the conductance, only the P→O mutant of OprP changed the KCl conductance to almost that of OprO.

The findings presented in this study provide a molecular basis to understand the ion selectivity of two structurally homologous porins, OprP and OprO, as well as to engineer the selectivity properties of these channels. The findings obtained here can be exploited to change or to fine-tune the selectivity of different channels and porins.

6. Transport of Ionic Liquids in Aqueous Solutions Through OmpF

Abstract

The temperature-dependent transport of the ionic liquid 1-butyl-3-methyl-imidazolium chloride (BMIM-Cl) in aqueous solution is studied theoretically and experimentally in bulk as well as through a biological nanopore, i.e., OmpF and its mutant D113A. This investigation is motivated by the observation that aqueous solutions of BMIM-Cl drastically increase the translocation time of DNA or antibiotics through nanopores in electrophysiological measurements. This makes BMIM-Cl an interesting alternative salt to improve the time resolution. Ion conductance measurements are complemented by applied-field all-atom molecular dynamics simulations. In line with previous investigations on simple salts, the size of the ions and their orientation adds another important degree of freedom to the ion transport. The transport of these bulky ions through nanopores is considerably slower than that of smaller ions. An excellent agreement between theory and conductance measurements is obtained for wild-type OmpF and a reasonable agreement for the mutant. Moreover, all-atom simulations allow an atomistic analysis revealing molecular details of the rate-limiting ion interactions with the channel.

Reproduced with permission from the article by Modi, N.; Singh, P. R.; Mahendran, K. R.; Schulz, R; Winterhalter, M; and Kleinekathöfer, U., "Probing the transport of ionic liquids in aqueous solution through nanopores", *J. Phys. Chem. Lett.*, **2011**, 2(18), pp 2331-2336 (DOI: 10.1021/jz201006b).

6.1. Introduction

Pure ionic liquids (ILs), usually molten salts with a melting point lower than 100 °C, have become subject of intense studies in recent years. ILs are characterized by a high ion conductivity, thermal and chemical stability as well as favorable solvation properties. These characteristics of ILs generated enormous interest and they can be applied to a large number of useful applications including organic synthesis, catalysis, separation and electrochemical studies [220–224]. Moreover, mixtures of water and ILs, i.e., ILs in aqueous solution, have been investigated recently [225, 226], which are actually the subject of our study.

Ion and substrate transport through nanopores is currently an active field of research with exciting biological applications [7, 227]. Concerning the ion transport, most studies, especially including the effect of temperature, have been restricted to simple ions such as KCl, NaCl or $MgCl_2$ (see, e.g., Refs. 25, 27–29, 228–232). Concerning substrate transport, one investigates, e.g., the translocation of antibiotics [139], DNA [7] and peptides [233] through nanopores. The translocation of these substrates is experimentally studied using electrophysiology, i.e., the use of ion-current measurements as indirect probe. One of the potential applications of IL solutions is slowing down the kinetics of fast permeation events through nanopores. To this end, de Zoysa et al. [234] successfully used a 1 M 1-butyl-3-methyl-imidazolium chloride (BMIM-Cl) solution to slow down the DNA translocation in a nanopore. This reduction in speed might help in DNA sequencing by increasing the residence time of DNA in the pore [234]. Furthermore, we have recently shown that a 1 M BMIM-Cl solution increases the residence time of ampicillin in the outer membrane porin F (OmpF) pore by a factor of three compared to a KCl solution of the same concentration [235]. Again, this increase in residence time improved the time resolution to catch fast events of antibiotic translocation through the pore which is otherwise hard to detect or even undetectable. In the same study, it was found that BMIM-Cl compared to KCl leads to a roughly twofold reduction in bulk conductivity while the respective OmpF conductance decreases by about a factor of seven [235]. This study is devoted to understand the underlying interactions of ionic liquids with the nanopore walls.

The investigated nanopore is the general diffusion porin OmpF, i.e., a pore in the outer membrane of the *E. coli* bacterium (see Fig. 6.1c). High resolution crystal structures of OmpF reveal their trimeric organization [236, 237]. The constriction zone contains three positively charged arginine residues R42, R82 and R132 on the one side and two negatively charged residues, namely aspartic acid D113 and glutamic acid E117, on the

other side (see Appendix D, Fig. D1). This spatial arrangement of positively and negatively charged residues is responsible for a strong transversal electric field inside the pore leading to particular orientations of molecules in this region [238–240]. The inner loop L3 is a part of the constriction zone and has a large influence on the translocation properties of the pore.

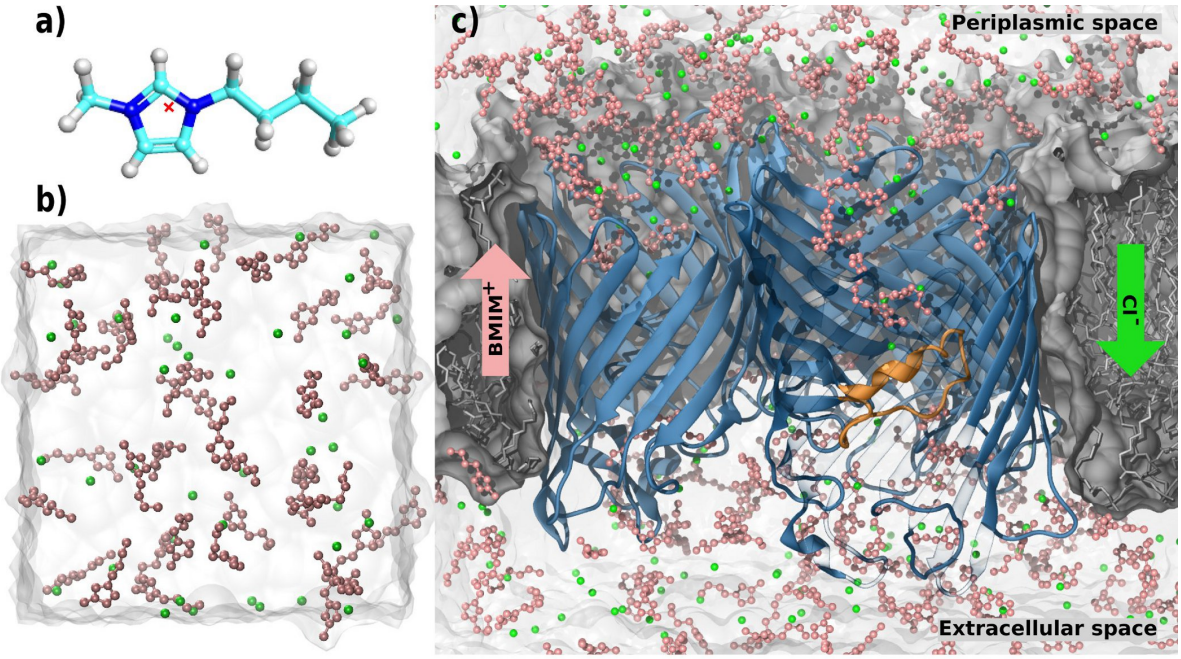

Figure 6.1.: (a) Structure of $BMIM^+$ (atom colors: C-cyan, N-blue and H-white) including the center of charge indicated by a red cross; (b) Simulation box for the bulk simulations. The Cl^- ions are shown as green spheres and the $BMIM^+$ ions as pink ball-stick structures; (c) Simulation setup for the pore simulations including OmpF (blue secondary structure, orange-loop L3) and the membrane (gray surface and stick representation). The arrows indicate the direction of the movement of ions under the effect of a positive applied field. For the sake of visualization, part of the monomer in front has been removed. The figures were generated using VMD [181].

In this study, we investigated molecular details of BMIM-Cl transport through OmpF. Especially the behavior and orientation of the bulky ions within the channel and the constriction region are of interest. To this end, we performed applied field MD simulations to model the ion flow of BMIM-Cl through OmpF and to compare the calculated conductance to experimental data.

6.2. Results and Discussion

As a first step in the molecular modeling of BMIM-Cl in water, we performed with a comparison of bulk conductivity between theory and experiment. The simulations were

performed using NAMD2.7 [131] together with the CHARMM27 force field [95], $BMIM^+$ force field parameters [241] and different water models, e.g., TIP3P [242], TIP4P [243], TIP4P-Ew [244] and TIP4P/2005 [245]. Details are given in the Supporting Information (see Appendix D).

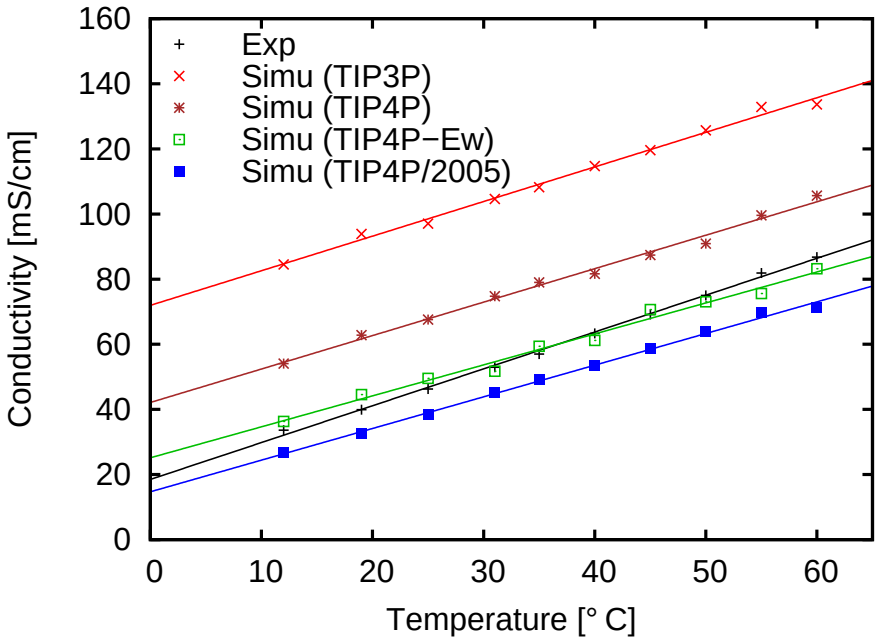

Figure 6.2.: Bulk conductivity versus temperature for different water models compared to experiments.

Dataset	Self Diffusion [10^{-5} cm^2/s]	Bulk Conductivity [mS/cm]
Experimental	2.27 [246]	46.26
TIP3P	5.06 [247]	97.07
TIP4P	3.29 [247]	67.57
TIP4P-Ew	2.4 [244]	49.51
TIP4P/2005	2.08 [245]	38.46

Table 6.1.: Self-diffusion coefficient and bulk conductivity for different water models together with experimental values.

The temperature-dependent bulk conductivity of 1 M BMIM-Cl was calculated for temperatures ranging from 10 °C to 60 °C using the approach of Aksimentiev and Schulten [25] (also see supporting information in Appendix D). As a control of the underlying interactions between ions and water, the temperature dependence of the calculated conductivities are compared to the experimental values (see Fig. 6.2). As in previous simulations for KCl conductivity, we initially employed the TIP3P water model [27, 28]. Though the slope of the simulation data with the TIP3P water model is very similar to the experimental results, a considerable parallel shift is visible. Surprisingly, the ratio

between the calculated conductivity at room temperature and its experimental counterpart is almost equal to that of the corresponding self-diffusion constants of water as listed in Table 6.1. Motivated by the possible connection between conductivity and self diffusion, different water models were probed with self-diffusion constant in decreasing order (see Table 6.1). In conclusion, we found that the conductivity of 1 M BMIM-Cl solution is strongly correlated with the self-diffusion constant of the water model and that the best results are obtained for the TIP4P-Ew water model (see Table 6.1, Fig. 6.2). This is not too surprising since both quantities, the conductivity of BMIM-Cl and the self-diffusion constant of water, involve the process of moving a molecule, i.e., either a $BMIM^+$ ion or a water molecule, through the surrounding water.

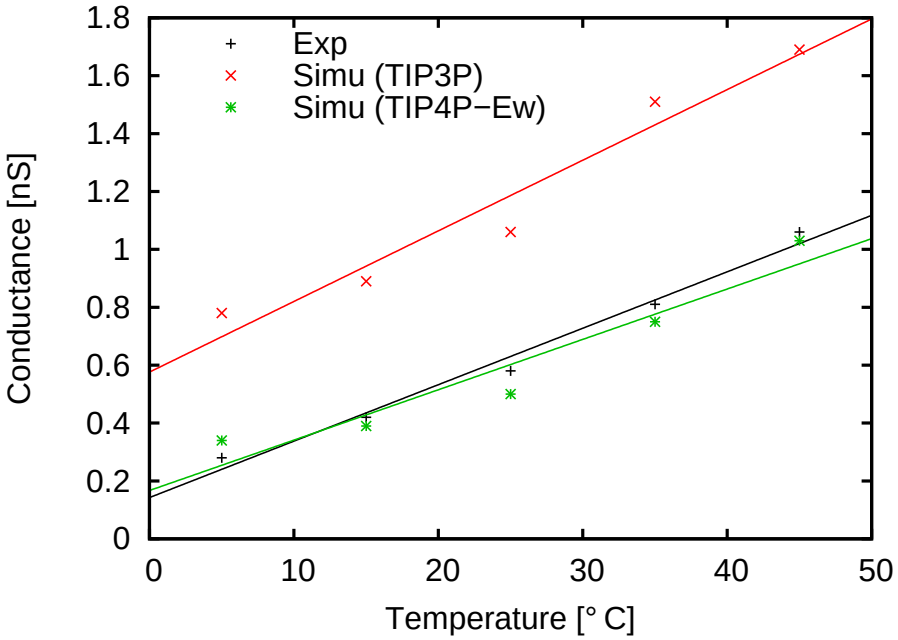

Figure 6.3.: Pore conductance versus temperature for experiment and simulation using two different water models together with linear fits of the datasets.

After the validation of the force fields and water models, the transport through OmpF was investigated. 30-ns simulations were performed for different temperatures and using the TIP3P and the TIP4P-Ew water models (see Appendix D for simulation details). The current was determined as described earlier [25, 27, 28]. The experimental results of the pore conductance of OmpF using 1 M BMIM-Cl solution at different temperatures show a linear dependence as shown in Fig. 6.3 (see Appendix D for experimental measurement details). Similar to the bulk conductivity calculations, the simulations using the TIP3P water model yield a considerably higher conductance, though also an almost linear increase with temperature. Results obtained with the TIP4P-Ew water model are in good quantitative agreement with the experimental results. These results further demonstrate

the dependence of such conductance measurements on the water model and their self-diffusion constant. The nice agreement between experimental and theoretical conductance can be further exploited to obtain atomic-level details of the transport process of BMIM-Cl through the OmpF pore.

Other than in experiment, the simulations immediately yield the contributions of the individual ion types to the current, i.e., $BMIM^+$ and Cl^- (see also supplementary movie). The ratio of the Cl^- to $BMIM^+$ currents is found to be in the range of 3-5 increasing with temperature in the range from 5 °C to 45 °C (data not shown). Analysis showed that the mobility of Cl^- ions is influenced more by the increasing temperature than the $BMIM^+$ ions. This leads to an increased ratio of Cl^- to $BMIM^+$ currents at higher temperatures. Furthermore, it is found that, at 25 °C, Cl^- ions have an approximately 4 times higher residence time in the constriction region compared to the $BMIM^+$ ions (see also below).

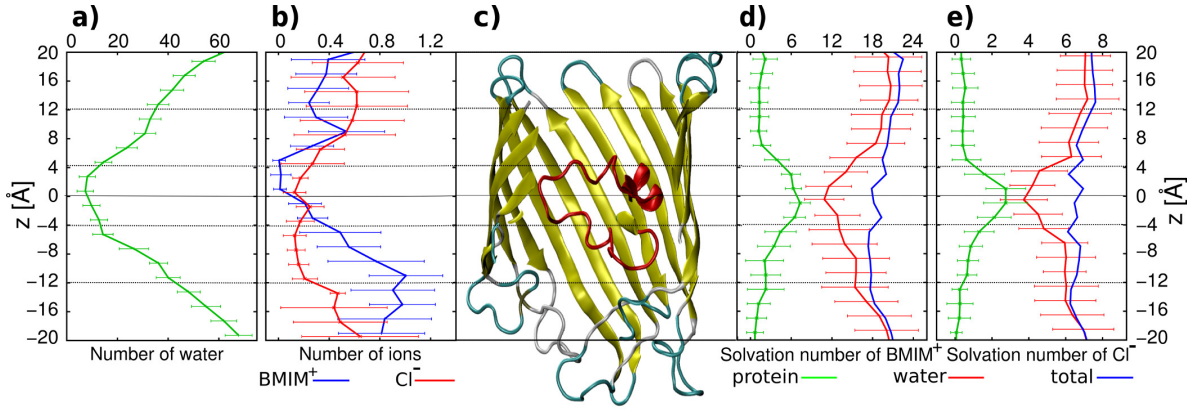

Figure 6.4.: Several ion quantities as a function of the channel coordinate z; (c) channel in the same scale as the ordinate; (a) number of water molecules; (b) number of ion molecules per species; (d) solvation number of the $BMIM^+$ ions; and (e) solvation number of the Cl^- ions (see main text). The dotted horizontal lines are given to help guiding the eye.

For further analysis of the MD data at 25 °C, the channel was divided into bins of 2 Å width along the channel coordinate z. If the center of mass of the molecule of interest was within the z range of this bin, the count of the individual quantities was increased. Subsequently, the number of molecules were averaged over the trajectory and are displayed in Fig. 6.4. In fact, the number of water molecules can be used as an estimate for the channel size. As can be clearly seen, the constriction zone extends from roughly -4 Å to +4 Å (Fig. 6.4a). For the analysis of the average ion occupation in the channel, note that the applied positive voltage forces the Cl^- ions down toward negative values of the channel coordinate z (from the periplasmic side of the membrane to the extracellular side) while the $BMIM^+$ are dragged up toward positive values. Compared to

the average water occupation in the channel, the Cl^- ions have a slightly higher average number above the constriction zone and a slightly depleted occupation at negative z values (Fig. 6.4b). This is due to the hindrance caused by the constriction region. Once the narrow part of the pore is passed, the ions are easily dragged away by the external field. As can also be seen in the supplementary movie, the effect is much more enhanced for the bulky $BMIM^+$ ions which are crowded below the constriction zone.

For the present non-specific channel, we examined the solvation characteristics of permeating $BMIM^+$ and Cl^- ions along the channel coordinate z. In general, ion channels regulate the flow of ions across the membrane via substituting the loss of hydration with favorable protein interactions [248]. To be able to quantify these, solvation shell definitions of the $BMIM^+$ and Cl^- ions were determined by calculating radial distribution function (RDF) for the previously described simulation of 1 M BMIM-Cl aqueous bulk solution and 4 ns long trajectories. For the $BMIM^+$ molecule, the center of charge was considered and a first minimum was found at 4.1 Å which was subsequently used as radius of the first hydration shell. Similarly for Cl^-, the radius of the first hydration shell was obtained as 3.2 Å. With regard to the protein contacts, only oxygen atoms were considered for the contribution of the protein to the solvation number of $BMIM^+$ ions and nitrogen atoms for that of Cl^- ions. For the ion-protein contacts, the same distance criteria as for the ion-water contacts were applied. The hydration number of the ions progressively alter in response to the changing environment as they move through the OmpF pore (Fig. 6.4d and e). The hydration number appears to be minimal in the constriction zone with approximately 10-11 water molecules around each $BMIM^+$ ion and 4 water molecules around each Cl^- ion. Interestingly, loss in hydration is compensated by protein contacts in the constriction region. Apparently, the contribution of water and protein contacts complement each other in order to keep the total solvation number per ion roughly constant throughout the channel. For KCl ions in OmpF, a similar phenomenon was observed earlier by Im and Roux [240]. In addition, both $BMIM^+$ and Cl^- follow separate pathways over the length of the pore in a screw-like fashion (see Appendix D, Fig. D2).

Compared to the simple potassium and chloride ions, an important feature of the more bulky $BMIM^+$ ions is their orientation with respect to the channel. This is a key feature not accessible by experiment but by MD simulations. As described above for the other calculations, the channel was divided into bins of 2 Å width along the channel coordinate z and the quantities were averaged over the full length of a 30-ns-trajectory. The orientation angle was measured between the dipole of each $BMIM^+$ ion residing in

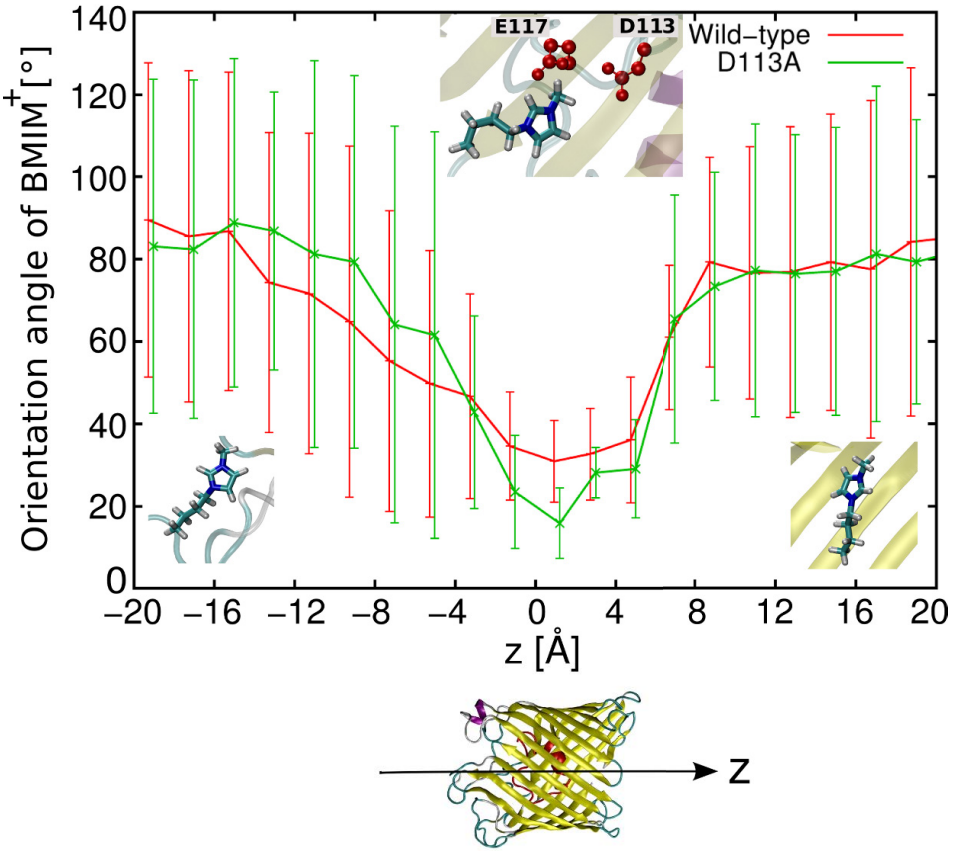

Figure 6.5.: Average orientation of the $BMIM^+$ dipole with respect to the channel coordinate z with error bars showing the standard deviation per bin. Representative orientations of $BMIM^+$ ions are shown in the insets for three particular regions of OmpF (center inset includes two important negatively charged residues in constriction region, see main text).

a particular bin and the z axis. As shown in Fig. 6.5, the orientation of the $BMIM^+$ ions changes gradually as it passes through the pore. Toward the extracellular (-20 Å $\leq$ z $\leq$ -12 Å) and the periplasmic side (12 Å $\leq$ z $\leq$ 20 Å) of the pore, $BMIM^+$ has an average orientation perpendicular to the channel axis with very large values of the standard deviation. This perpendicular direction is due to the charged residues lining the pore walls (see Appendix D, Fig. D2). These charges create local electric field components perpendicular to the channel axis and the $BMIM^+$ ions partially align to them. At the same time, the large standard deviation of the orientation angle toward the extracellular and periplasmic side of the pore shows that the ions have a large flexibility in their movement. The situation is different near the constriction region. The pore diameter is not large enough for $BMIM^+$ ions to pass in a perpendicular orientation. Therefore, they progressively start to change their orientation as they approach the constriction region. There, the $BMIM^+$ ions align almost parallel to the channel axis. In terms of the angle between dipole moment and channel axis, this leads to values around 30°. As shown in

the middle inset of Fig. 6.5, the positively charged head group, i.e., imidazole ring, of the $BMIM^+$ ion tends to tilt toward negatively charged residues in the constriction region, namely D113 and E117. This leads to an average angle of the $BMIM^+$ dipole away from the expected 0°. Probably more important than the average angle is the relatively small standard deviation in the constriction zone. Although not directly visible in Fig. 6.5 (but e.g., in the supplementary movie), the $BMIM^+$ ions have to pass the constriction zone with a certain directionality, i.e., the imidazole ring first. This shows that the ions first have to acquire a certain orientation before they can actually pass this region. On average, this leads to a prolongation of the passage time or a decrease in the current produced by the $BMIM^+$ ions. Fig. 6.5 shows a second curve, the orientation of the $BMIM^+$ ions through the OmpF mutant D113A, where a negatively charged aspartate residue in the constriction zone was mutated into a neutral alanine. The same system setup as for the wild-type OmpF simulations was used with the TIP4P-Ew water model and then the D113 residue was mutated. Subsequently, the system was equilibrated for 5 ns followed by a applied-field simulations for 10 ns. Due to the removal of a negative charge in the constriction zone, one may expect a change in the average orientation of the $BMIM^+$ dipole in this region. This can be attributed to the reduced electrostatic force experienced by the positively charged imidazole ring leading to a less pronounced tilting of the $BMIM^+$ head. Indeed, the average angle in the mutant is found to be around 15° compared to roughly 30° in wild-type. Farther away from the constriction zone, the average orientation and its standard deviation are rather similar to the wild-type data. This is reassuring since it shows that these two independent simulations yield very similar results away from the constriction zone as to be expected.

In Fig. 6.6, the temperature-dependent conductance of the D113A mutant from electrophysiology and MD simulations is displayed. At the lower considered temperatures, the agreement between both approaches is good, but it is obvious that the experimental and the theoretical curves have different slopes. The curve from the simulation is parallel shifted from the wild-type results to larger conductance values. In the case of the experiments, there is a considerable change in slope. Due to the very good agreement between theory and experiment for the wild-type OmpF, these data are somewhat surprising. Although the results are within the range of expected agreement between experiments it is obvious that some contribution is neglected in the mutant. The structure of the mutant was quite stable in the simulation and the modeling of simple ions provided an excellent agreement with the experiment [27, 28]. The ratio of Cl^- to $BMIM^+$ currents was found to be in the range of 5-8 increasing with temperature. Compared to the ratio of 3-5 for the wild-type, it was observed that mainly the Cl^- ions are responsible for the

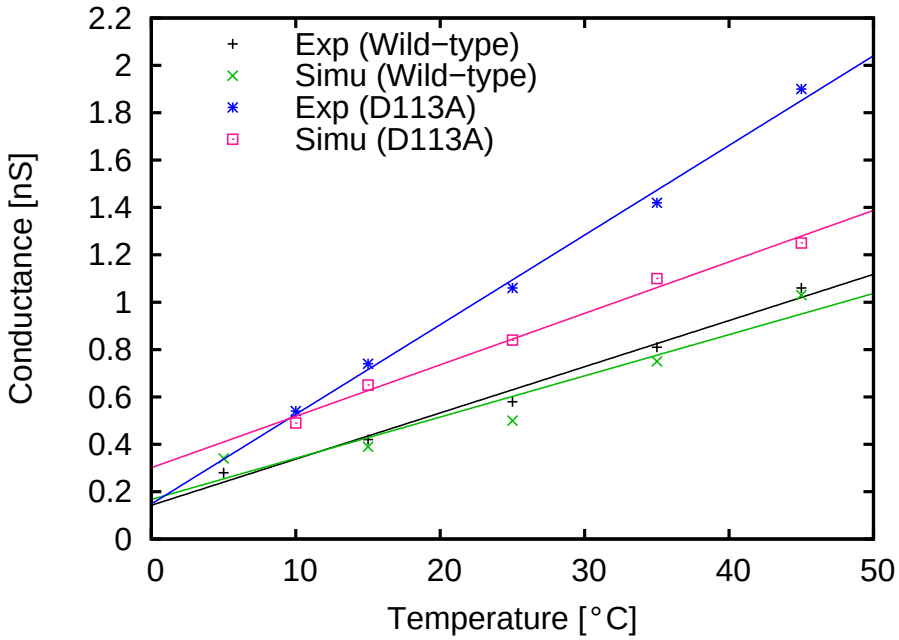

Figure 6.6.: Experimental and calculated pore conductance for the D113A mutant. For comparison, the conductance data for the wild-type are shown as well.

larger conductance of the D113A mutant since the contributions from the $BMIM^+$ ions were roughly the same as for the wild-type.

6.3. Conclusions

In conclusion, we have experimentally measured the temperature-dependent conductance of aqueous BMIM-Cl solution through OmpF trimer and also modeled it using MD simulations. An excellent agreement is obtained between electrophysiology and simulations of wild-type OmpF and a reasonable agreement for the D113A mutant. In addition to the experimental findings, the simulations yield a molecular-level picture of the ion transport. In particular, the kinetic simulations reveal the rate limiting interactions of the ions with the channel wall. As an important issue of the transport process, we have calculated the orientation of the $BMIM^+$ ions. It is really astonishing that one can see the realignment of the bulky ions within the time scale of the applied-field MD simulations. The necessity for the correct orientation of $BMIM^+$ near the constriction region may serve as a rate-limiting step of the passage, thereby slowing down the kinetics of antibiotic translocation through OmpF. This probably allows to observe an increased residence time of ampicillin in OmpF with BMIM-Cl compared to KCl as shown in Ref. 235. For the translocation of substrates such as antibiotic molecules, the translocation time is too long to be observed directly in standard MD simulations. Hence, one needs to go to

more indirect schemes as the calculation of the potential of mean force or steered MD simulations to theoretically understand these processes. Nevertheless, insights from the present study can be further exploited to understand antibiotic translocation processes and to investigate other ionic liquids for similar electrophysiological measurements through nanopores.

Acknowledgments

This work has been supported by grants KL 1299/6-1 and WI 2278/18-1 of the Deutsche Forschungsgemeinschaft (DFG).

Suppporting information

Experimental and computational details are given in Appendix D.

7. Simulation of Ion Transport Through an NanC Channel

Abstract

N-acetylneuraminic acid-inducible channel (NanC) is an outer membrane channel of *Escherichia coli*. This porin folds as a 12-stranded β-barrel leading to a tubular shape. Electrophysiological experiments have revealed an asymmetric conductance with respect to the direction of the applied voltage and a weak anion selectivity of the channel. To this end, we performed all-atom molecular dynamics (MD) simulations to decipher the ion transport properties of the NanC channel. Concentration-dependent applied-field MD simulations recover the asymmetric conductance property and the anion selectivity of the channel in agreement with experiments. Further molecular analysis revealed the role of the asymmetric charge distribution inside the channel as the basis of the asymmetry in conductance. In addition, the particular distribution of charged residues at the inner channel walls leads to a faster permeation of Cl^- ions compared to K^+ ions resulting in the anion selectivity of NanC. These findings are well supported by position-dependent diffusion coefficients and potential of mean force profiles derived from unbiased MD simulations. Taking one step further, we were able to engineer the NanC channel *in silico* by mutations leading to enhanced asymmetric conductances and anion selectivities. The E186Q mutant, for example, changes NanC into a decent molecular diode with an ionic current ratio of about 3:1 for opposite bias voltages.

Reproduced with permission form the article by Lu, J; Modi, N.; and Kleinekathöfer, U., "Simulation of Ion Transport Through an *N*-acetylneuraminic Acid-inducible Membrane Channel: From Understanding to Engineering", *J. Phys. Chem. B*, **2013**, 117(50), pp 15966-15975 (DOI: 10.1021/jp408495v). Copyright [2013] American Chemical Society.

The work presented in this chapter was also part of the Master's thesis of J. Lu. N. Modi contributed in the initial setting of the simulation systems, interpretation of the results and writing of the manuscript.

7.1. Introduction

A membrane separates the cell from its environment and serves as a permeation barrier to protect the cell and to regulate the exchange of nutrients, signaling molecules and molecular waste. Such regulated transport of various substances across the cell membrane are facilitated by membrane proteins [133]. Porins are channel-forming, β-barrel membrane proteins present in the outer membrane of Gram-negative bacteria [132]. They act as molecular sieves that allow passive diffusion of various substrates into the periplasm of bacteria. From the functional point of view, porins can be classified as either non-specific porins or substrate-specific porins [133]. Non-specific porins, e.g., OmpF, OmpC, and PhoE of *E. coli*, allow passive diffusion of small solutes down their electrochemical gradient without having a marked preference for particular solutes. Specific porins, on the contrary, have a clear preference for the specific solutes. Such specificity is generally achieved by the presence of the defined affinity sites inside the pore. Examples of specific porins are the phosphate and poly-phosphate selective porins OprP and OprO from *P. aeruginosa*, the carbohydrates transporting porins LamB and ScrY of *E. coli*, as well as the nucleoside specific Tsx porin of *E. coli*.

The *N*-acetylneuraminic acid-inducible channel (NanC), a specific porin of *E. coli*, belongs to the KdgM family of outer membrane channels [249–251]. Different to the classical porins, such as OmpF and OmpC which have trimeric structures with 16 β-strands, proteins from the KdgM family are monomeric and form a barrel which contains 12 to 14 β-strands containing 205-220 amino acids on average [250, 251]. As the name suggests, NanC expression is induced by the presence of *N*-acetylneuraminic acid (Neu5Ac), the most abundant sialic acid [252]. Sialic acids are negatively charged nine-carbon sugar molecules that can be used by bacteria as a source of carbon and nitrogen [253, 254]. In many cases, the virulence of pathogenic bacteria may depend on their ability to use sialic acid as a carbon and a nitrogen source [253, 255]. Hence also from the clinical point of view, it may be important to understand the structure-function relationship of the NanC channel and its role in sialic acid uptake inside bacteria. In the absence of the expression of OmpF and OmpC in *E. coli*, NanC is the only porin that can be used for Neu5Ac uptake as the sole source of carbon [252].

The crystal structure of NanC [256] revealed its monomeric character with 12 antiparallel β-strands folded into a β-barrel. The height of the β-barrel is about 28 Å and the size of the ellipsoidal cross section is about 26 Å × 20 Å. As observed for OmpF, the β-strands are connected via long extracellular loops (L1-L6) and short periplasmic turns

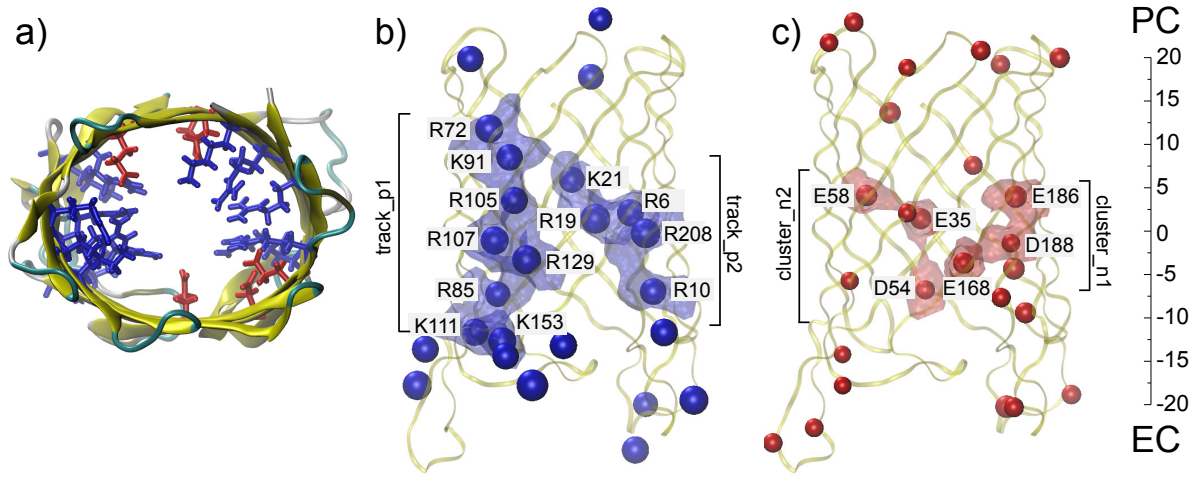

Figure 7.1.: Structure of NanC and its distribution of charged residues inside the channel. a) The charge quadrupole formed by the charged residues at the center of the channel is shown in a top view. The negatively and positively charged residues are shown as red and blue sticks, respectively. b) Positively charged residues in the channel shown as blue spheres. Two tracks of positively charged residues, track_p1 and track_p2, are highlighted by a blue surface. c) The negatively charged residues in the channel shown as red spheres. The two clusters of negatively charged residues, cluster_n1 and cluster_n2, are highlighted by red surfaces. Figures rendered using VMD [181].

(T1-T5). The shape of the NanC channel is tubular with an average radius of 3.3 Å. In the structures of OmpF [237] and OmpC [257], a loop (L3) is present at the central region of the pore and forms the constriction region. However, no such loop is found in NanC which could occlude the channel in the central region. The only theoretical studies so far are based on a simplified coarse grained model using an approximate model of the NanC channel [258].

A key feature of the NanC channel is the distribution of charged residues inside the pore [256]. Two tracks of positively charged residues (track_p1: R72, K91, R105, R129, R107, R85, K111 and K153; track_p2: K21, R19, R208, R6 and R10) are located at two poles on opposite sides of the channel (Figure 7.1b) [256]. One track of positively charged residues spans almost the entire channel (track_p1) while the other track is ranging from the center of the channel to the extracellular side (track_p2). Similarly aligned basic residues, also referred to as “ladder”, are reported in OprP [160, 172] and OprD [259]. However, contrary to NanC, only one line of electropositive residues are observed in these porins. Other than the positively charged tracks, NanC has two clusters of negatively charged residues (cluster_n1: E186, D188 and E168; cluster_n2: E58, E35 and D54) located at the two other poles of the channel as shown in Fig. 7.1c. Such a distribution of positively and negatively charged residue forms an electrostatic quadrupole (Figure 7.1a).

This feature is again different from the classical porins, like OmpF, OmpC or PhoE, where a dipolar rather than a quadrupolar arrangement of charged residues exist at the center of the pore [237, 257]. The amount of positively and negatively charged residues in the channel are almost equal. However, they are distributed differently along the channel wall. On one hand, the positively charged residues tend to form uninterrupted tracks, particularly track_p1, spanning almost the entire length of the pore and thereby generating a continuous electropositive sink throughout the length of the pore. On the other hand, the negatively charged residues in the channel are scattered and do not form such long tracks. Moreover, the distribution of charged residues in the channel is asymmetric, i.e., more charged residues are present at the extracellular than at the periplasmic side. Furthermore, more negatively charged residues are placed at the extracellular half of the channel compared to the periplasmic one.

Several electrophysiology studies characterized the ion transport properties of the NanC channel using planar lipid bilayer techniques. Condemine et al. [252] reported that NanC forms a channel with a conductance of 450pS at positive potentials and 300-400pS at negative potentials in a 800mM KCl solution. Giri et al. measured concentration-dependent conductance of KCl through NanC [260]. Voltage-dependent gating of the channel was also reported especially at higher voltages of about ±200 mV [260]. Such gating events are extremely demanding to study with MD simulations as they occur at the time scale range much larger than those usually used in MD simulations. In the present study, we report on the ion transport properties of NanC obtained using molecular dynamics (MD) simulations. Taking advantage of the atomic-level resolution provided by MD simulations, we can contribute to the molecular-level understanding of the observed channel properties in electrophysiological experiments, namely asymmetric conductance, anion selectivity and concentration-dependent conductance. Previous MD simulations of ion transport with porins, like OmpF [3, 27–29, 161, 232, 240, 261], OmpC [28], VDAC [32, 33], have complemented the electrophysiology experiments efficiently to aid the characterization of the channels. NanC - a 12 β-strand, tubular shaped porin with its particular arrangement of charged residues - is structurally unique when compared to other well-studied classical porins like OmpF and OmpC. This study also provides the opportunity to compare the ion transport properties of NanC to those well-characterized classical porins. To achieve the above objectives, both applied-field and unbiased MD simulations have been carried out.

7.2. Methods

7.2.1. Setup of the simulation systems

For the KCl bulk conductivity simulations, a cubic water box with a side length of 40 Å is generated using VMD [181]. The system contains ∼1900 water molecules and 8 to 282 Cl^- and K^+ ions were added according to the KCl concentration ranging from 0.1 M to 3.8 M. Concerning the channel simulation setup, the structure of the NanC monomer is available from the Protein Data Bank (PDB code: 2WJQ) [256]. Since coordinates of ten residues (residue number 43 to 52) are missing in the crystal structure, these are predicted using Modeller 9.10 [262]. The principal axis of the NanC channel is aligned parallel to the z axis and the channel is embedded into a pre-equilibrated POPE lipid bilayer. The membrane plane is chosen to be parallel to the $x-y$ plane. Moreover, the system is solvated with TIP3P water and varying numbers of ions are added to the system according to the salt concentration. In total, the system contains about 55,000 atoms.

7.2.2. Molecular dynamics parameters

The MD simulations have been performed using NAMD 2.9 [131] and the CHARMM27 force field [95] with modified Lennard-Jones parameters for the KCl ion pair[263]. The general method is described in previous studies [25, 27]. Periodic boundary conditions were employed and the short-range nonbonded interactions were calculated using a cutoff of 12 Å and a switching distance of 10 Å. The long-range electrostatic interactions are treated using the particle mesh Ewald method [183]. Using the r-RESPA multiple time step method [184], bonded interaction are evaluated every 1 fs while short-range nonbonded and long-range electrostatic interactions at every 2 fs and 4 fs, respectively. Bond constraints are applied to all water hydrogen atoms with the SHAKE algorithm [264]. The bulk conductivity simulations have been performed at a temperature of 310 K while the channel simulations at a temperature of 296 K controlled by a Langevin thermostat. For the applied field simulation, a homogeneous external field E is applied in the z direction proportional to the voltage V, $E = V/L_z$ with the system length L_z in z direction normal to the membrane [114].

For the bulk conductivity simulations, the systems have been equilibrated for 1 ns in NpT ensemble followed by a production run of 4 ns with an applied voltage of 0.4 V. For the channel conductance simulations, the whole system has been equilibrated for at least 6 ns. Two types of simulations, applied-field and unbiased, have been performed for the NanC system. The applied-field simulations have been carried out in an NVT

ensemble with an applied voltage of 1 V in z direction. In the present study, the direction of positive voltage is defined as the potential difference between the extracellular side and the periplasmic side of the NanC channel. All applied field simulations are at least 100 ns long for the smaller KCl concentrations up to 500mM and and at least 30 ns long for the larger concentrations above 500mM. Each data point is repeated at least three times to get an estimate of the statistical error and to avoid non-representative data points. For the unbiased simulation, no external field is applied and the production run is carried out for 80 ns with 500mM KCl concentration in NVT ensemble. The unbiased simulations have also been repeated three times.

7.2.3. Analysis

Current calculations

The instantaneous current at time t is calculated using [25]

$$I(t) = \frac{1}{L_z \Delta t} \sum_{i=1}^{N} q_i \Delta z_i \tag{7.1}$$

in which q_i denotes the charge and Δz_i the spatial displacement of atom i during the time interval $\Delta t = 10$ ps. The K^+ and Cl^- currents are determined separately and then combined to yield the net ionic currents. The cumulative currents can be obtained by adding up the instantaneous current at every sampling time [25, 27]. A linear fit of this cumulative current versus time leads to the average current. Subsequently, the conductance can be obtained as ratio of ionic current and applied voltage.

Position-dependent diffusion coefficient

The calculation of the position-dependent diffusion coefficient has to be performed with care as it is necessary to remove the effects of systematic forces (ion-protein interactions). Following Im and Roux [240], the diffusion coefficient D_z can be obtained using

$$D_z = \frac{\langle [\Delta z(t) - \langle \Delta z(t) \rangle]^2 \rangle}{2\tau} \tag{7.2}$$

where $\Delta z(t) = z(t+\tau) - z(t)$ with a short time interval τ and $\langle \Delta z(t) \rangle$ denoting the average z displacement during time τ under the influence of the systematic forces. In the present case, we choose $\tau = 5$ ps.

7.3. Results and Discussion

Bulk conductivity

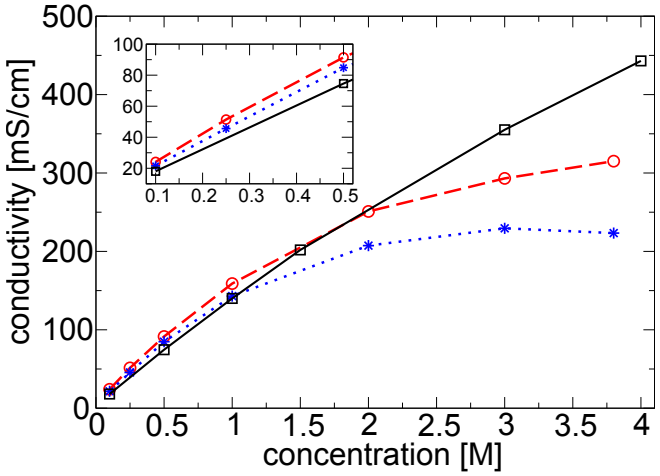

Figure 7.2.: Concentration-dependent KCl bulk conductivity from MD simulations compared to experimental results (black, solid) [27]. Two different sets of Lennard-Jones parameters have been used for the simulations, i.e., the standard CHARMM27 parameters [95] (blue, dotted) and modified ones [263] (red, dashed) which also have been used for the pore simulations.

Bulk conductivity simulations are used to benchmark the force fields which subsequently are employed in the ion transport simulations through membrane proteins. This procedure is advantageous since the bulk experiments are independent from the channel experiments and since the bulk simulations are easy to prepare and computationally not expensive. As we focus on the concentration-dependent KCl conductance through NanC in the present study, a force field set which is accurate at varying concentrations is desirable. To this end, we investigated two different types of KCl force fields, the standard CHARMM27 force field [95] and a force field with modified Lennard-Jones parameters [263], to simulate the concentration-dependent bulk conductivity of KCl electrolyte solutions. The force field with modified Lennard-Jones parameters for KCl was particularly developed to reproduce the osmotic pressure of KCl at higher salt concentrations [263]. The bulk conductivity results are shown in Fig. 7.2 and detailed in Table S. At low concentrations, both the standard and modified KCl force fields are in good agreement with the experimental bulk conductivity. However, at concentration above 1 M, the modified force field is in much better agreement with experiments especially up to the concentration of 2 M. Since in the nanoscale confinement of the channel the effective concentration of KCl might be much higher than in the bulk, the modified KCl force field set is chosen for the NanC channel simulations.

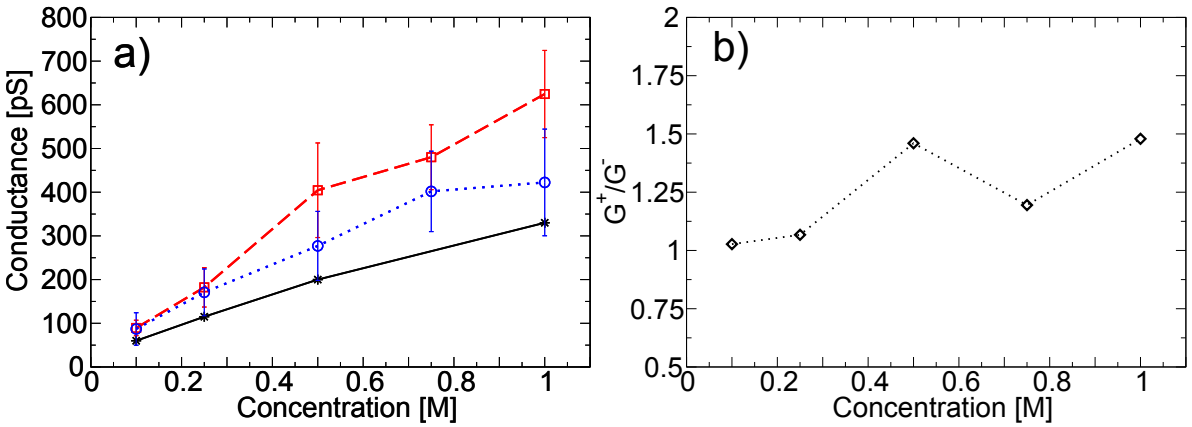

Figure 7.3.: a) Concentration-dependent NanC channel conductance calculated using applied-field MD simulations (+1V: red, dashed; -1V: blue, dotted). The experimental conductance data (black, solid) have been extracted from Ref. 260. The latter were determined over a 60 mV interval ranging from -30 to +30 mV. b) Ratio of calculated conductances for positive and negative applied voltages, G^+/G^-.

Pore conductance

The main goal of this study is to understand the concentration-dependent KCl channel conductance together with its asymmetric conductance property with respect to the direction of the applied voltage. To achieve this aim, applied-field MD simulations are carried out for five different KCl concentrations ranging from 0.1 M to 1 M and at two different voltages, a positive voltage of +1V and negative voltage of -1V. As shown in Fig. 7.3a, the calculated channel conductances resulting from the MD simulations are increasing for both, positive and negative voltage, with increasing KCl concentration in agreement with experiment. However, at both voltages the simulation results are higher than the experimental ones, particularly at larger concentrations. This is probably due to the large applied voltage and in part by the high diffusion coefficient of the TIP3P water model [161, 219]. The large variations in the simulated conductances for the simulations with the same parameters but varying initial velocities indicated by the error bars in Fig. 7.3a, can be attributed to the stochastic nature of the ion crossing events within the limited simulation times scale. This kind of effect tends to become more prominent in small channels like NanC.

At this point we would like to point out that the experimental conductances, extracted from Ref. 260 and presented in Fig. 7.3a, are average currents determined over a 60 mV interval ranging from -30 to +30 mV. In the electrophysiological experiments, this particular interval was chosen since at very low voltages of up to ±30 mV, their current-voltage (I-V) curve of the channel is linear [260]. However, at higher voltages the channel conductance tends to become asymmetric as reported by electrophysiological experiments[252, 260].

In the simulations we applied voltages of ±1V to overcome the problem of the limited time scale associated with MD simulations. These higher applied voltages help to obtain statistically meaningful numbers of ion permeation events within the available nanoseconds time scale. Due to the large applied voltage in our simulations, we also observed an asymmetry in the channel conductance with the larger conductance values at positive voltages (see Fig. 7.3a). The ratio of conductances at positive to negative voltage, G^+/G^-, is found to be in the range of 1.1 to 1.5 depending on the salt concentrations (see Fig. 7.3b). This value is in excellent agreement with different electrophysiological experiments in which similar ratios of 1.12 to 1.9 were reported depending on the KCl concentration [252, 260].

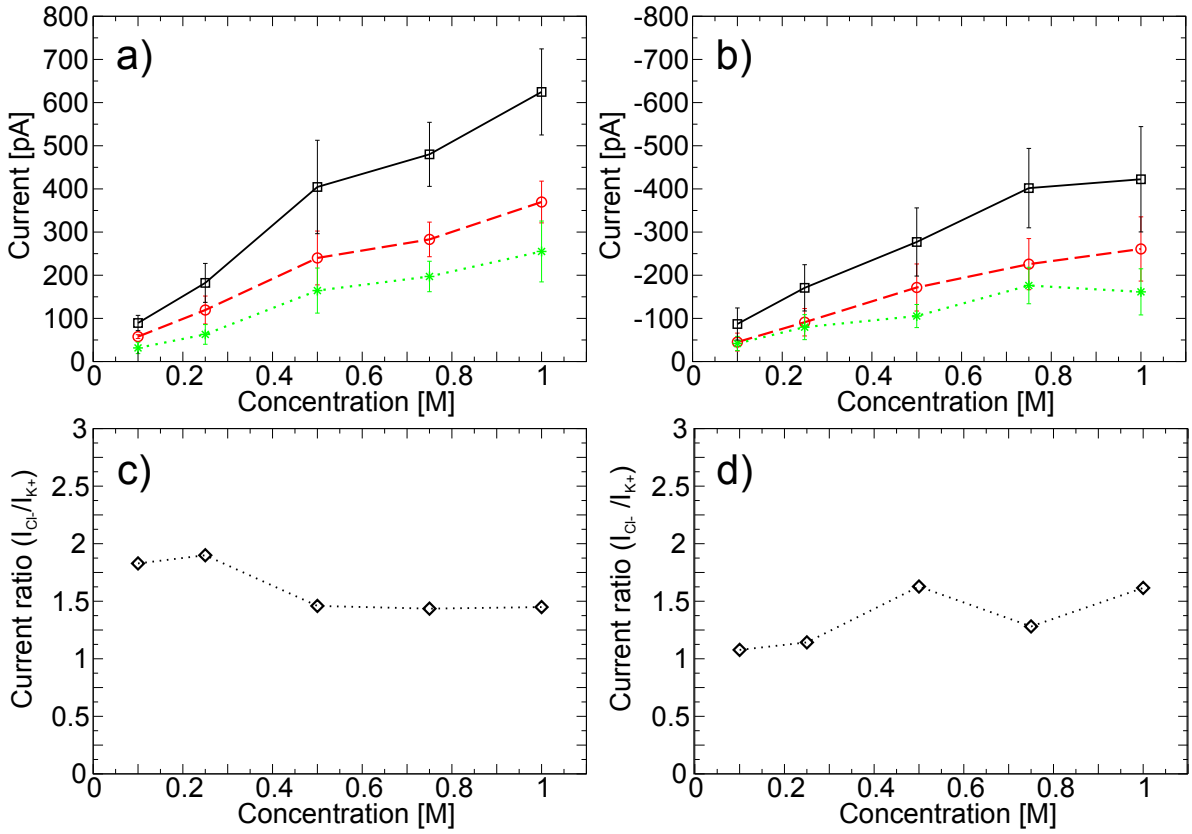

Figure 7.4.: Individual contributions of the K^+ (green, dotted) and Cl^- (red, dashed) currents towards the total current (black, solid) for applied voltages of a) +1V and b) -1V. Selectivity of the NanC channel, I_{Cl-}/I_{K+}, for applied voltages of c) +1V and d) -1V.

Ion selectivity

In the following, we concentrate on the ion selectivity of the NanC channel. For this purpose, the individual current contributions of K^+ and Cl^- ions towards to the total current are determined. For both, positive as well as negative voltages, Cl^- ions have a larger contribution to the total current compared to K^+ ions as shown in Figs. 7.4a

and b. Furthermore, both, the Cl^- and K^+ currents, show an asymmetric behavior with respect to the directionality of the applied bias. Moreover, we have calculated the ratio of Cl^- to K^+ current, I_{Cl-}/I_{K+}, for various KCl concentrations and both voltage directions (Fig 7.4c, d). The average ratio of Cl^- to K^+ currents is larger than one but smaller than two. This signals a weak anion selectivity of the NanC channel which is in accordance with the measured anion selectivities of 2.2 - 3.7 [252, 260]. This weak anion selectivity can be attributed to the two tracks (track_p1 and track_p2) of positively charged residues (Fig. 7.1) which provide a continuous electropositive sink throughout the length of the channel. Hence, the anions can easily pass through the channel by hoping from one positively charged residue to another throughout the length of the channel. However, the distribution of negatively charged residues is not as continuous as that of the positively charged residues. Therefore, the transport of K^+ ions through the channel may not be as fast as that of its negative counterparts. Thus, we propose a mechanism of anion selectivity of NanC in which the preference of anions by the channel is attributed to their higher transport efficiency through the channel as compared to their cationic counterparts based on the charge distribution in the channel (see the below section “Properties calculated from unbiased MD simulations”).

Although there is no drastic change in the ion selectivity depending on the concentration, the channel tends to be slightly more anion-selective, with a I_{Cl-}/I_{K+} ratio of about 1.9 at smaller KCl concentrations (250mM or below) and in the presence of positive transmembrane biases (Fig. 7.4c). In contrast, the channel is slightly less anion selective with a ratio I_{Cl-}/I_{K+} of about 1.1, at small KCl concentrations in the presence of a negative transmembrane bias (Fig. 7.4d). For porins like VDAC and OmpF, it was observed that the ion selectivity of the channel changes drastically at smaller concentrations [33, 57]. At higher KCl concentrations, effects exerted by charged residues inside the channel become less prominent due to the large electrostatic screening provided by the presence of a large number of ions inside the channel. Concentration-dependent changes in the ion selectivity can therefore be attributed to different screenings of charged residues at the interior channel wall depending on the salt concentration. Similarly, changes in the ion selectivity of the NanC channel depending on the direction of the applied voltage, particularly at the lower KCl concentrations (Fig. 7.4c and d), can be assigned to asymmetric distributions of charged residues inside the channel. At lower concentrations of KCl, i.e., in the absence of a strong electrostatic screening by ions, such asymmetric charge distribution can exert their largest effect.

Furthermore, we investigated the origin of the channel asymmetry and of the ion

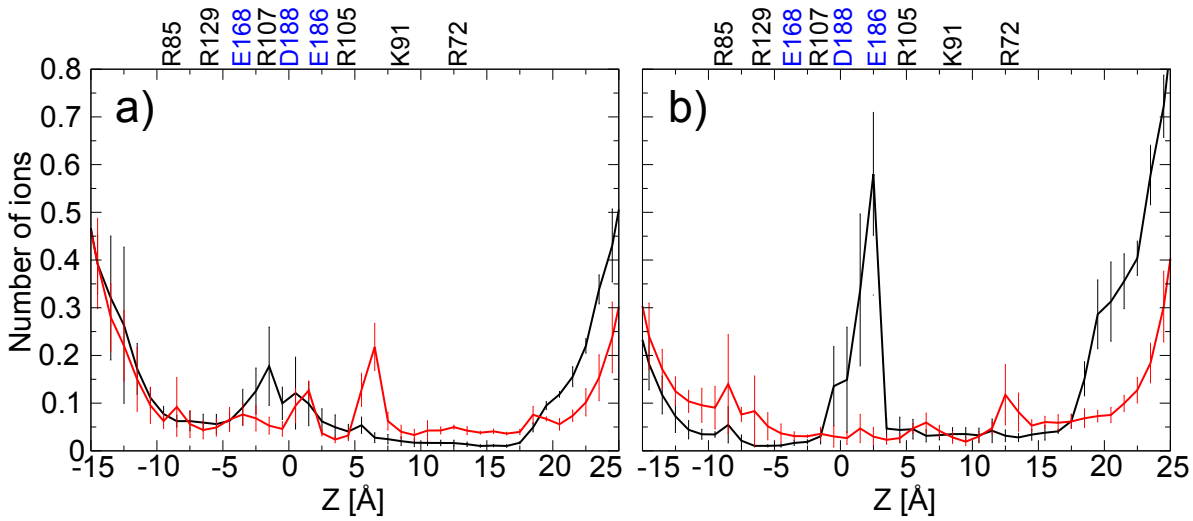

Figure 7.5.: Number of K^+ (black) and Cl^- (red) ions averaged over a 100 ns trajectory applying voltages of a) +1V and b) -1V. The important positively (black) and negatively charged (blue) residues are labeled at the top of the graphs at their approximate z position inside the channel. The direction of the z axis is defined as the direction from the extracellular towards the periplasmic side.

selectivity exploiting the atomic-level resolution provided by the MD simulations. On one hand, at very low salt concentrations, very few ion permeation events are observed within the limited simulation time which lead to a poor statistics in most of the calculated property. On the other hand, at high salt concentrations of 1 M, some of the channel property may become less pronounced due to the large electrostatic screening effects provided by the presence of a large number of ions. Hence we use the intermediate KCl concentration of 500 mM for the all the further analysis in this study.

Ion density

The average number of K^+ and Cl^- ions in the different regions of the pore along the z-axis have been calculated. For this purpose, the channel has been divided into bins of 1 Å width. One-dimensional K^+ and Cl^- ion density distributions along the channel z axis for both voltage directions are shown in Fig. 7.5. One of the most important features of these profiles is the change in the ion density depending on the direction of the applied voltage especially for the K^+ ions. Under the influence of a positive transmembrane bias, the K^+ ions have a tendency to accumulate in the region from -4 to 0 Å. However, applying a negative voltage, the K^+ ions have the highest tendency to stay in the region from 0 to 4 Å. For positive voltages a significant accumulation of Cl^- ions is found around 7 Å. Different ion distributions depending on the direction of the applied voltage are the outcome of the asymmetric charge distributions inside the channel (see Fig. 7.1) and also explain the asymmetric conductance properties of the NanC channel. Particular directional effects

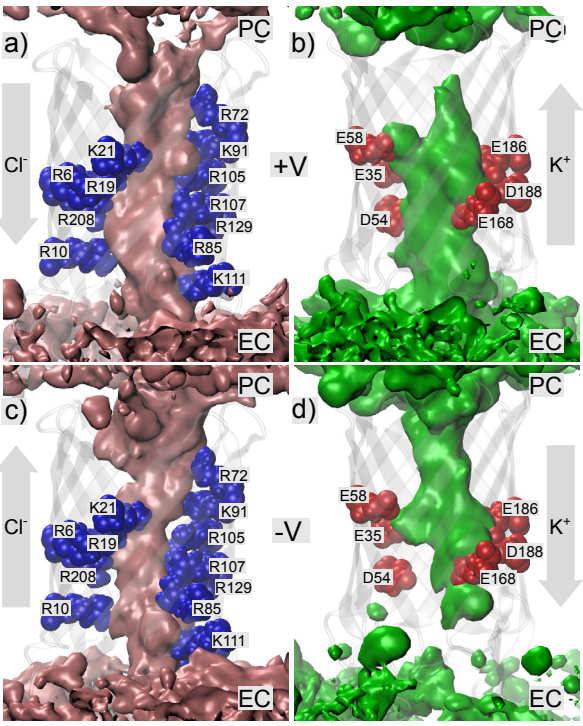

Figure 7.6.: Isosurfaces of Cl^- (left) and K^+ (right) densities averaged over a 100 ns trajectory for applied volages of +1V in panels a) and b) as well as -1 V in panels c) and d). The two tracks of positively charged residues (blue) and the two clusters of negatively charged residues (red) are highlighted. All figures have been plotted using the same iso-values. The arrows indicate the direction of the movement of the ions under the effect of the applied voltage (top row: positive voltage; bottom row: negative voltage).

on the ion densities are more prominent for K^+ than for Cl^- ions. Positively charged residues of track_p1 and track_p2 (Fig. 7.1) form continuous tracks throughout the length of the pore while the negatively charged residues are distributed in a scattered manner with more negative charges at the extracellular side of the channel. Due to the more asymmetric distribution of negatively charged residues inside the channel (Fig. 7.1), the K^+ distribution shows larger variations depending on the voltage direction. The relative large tendency of the K^+ ions to accumulate (see Fig. 7.5) indicates a slower permeation of the K^+ compared to the Cl^- ions. Similar findings were also observed in case of the anion-selective VDAC porin [32].

To obtain further insights, three-dimensional ion density profiles averaged over a 100 ns trajectory have been calculated using the VolMap plugin of VMD [181]. The isosurfaces of the K^+ and Cl^- densities using positive and negative voltages are displayed in Fig. 7.6. In OmpF, distinct separate pathways for K^+ and Cl^- ions can be observed along the length of the pore [240]. Furthermore, the ion density distributions inside VDAC revealed possible pathways for different ion species [32]. For NanC, however, no such

residue	residence time [ns] +1.0V	residence time [ns] -1.0V
E186	0.37 ±0.05	8.69 ±8.15
D188	0.94 ±0.14	10.55 ±3.58
E168	0.83 ±0.16	1.08 ±0.46
E35	0.34 ±0.10	0.83 ±0.74
D54	0.31 ±0.05	0.55 ±0.61
E58	0.39 ±0.37	0.19 ±0.18

Table 7.1.: Average residence times of K^+ ions at the most important negatively charged residues.

clearly separate ions tracks are obvious. One of the main reasons for this observation is the presence of two tracks of positively charges residues (also see Fig. 7.1) on both sides of the channel which prevent simple preferential pathways for cations or anions on either side of the pore. The ion density along the channel applying negative voltage is slightly smaller than for the opposite voltage direction for both ion types. This finding is in agreement with the calculated conductances in which higher conductance values are obtained applying positive rather than negative voltages. Furthermore, the Cl^- density is continuous throughout the length of the pore which is in agreement with the continuous distribution of positively charged residues throughout the length of the pore (Fig. 7.1b). The K^+ ion density, on the other hand, is sparse on either side of the channel depending on the direction of the applied voltage. The ion densities of both ion types are consistent with the distributions of positively and negatively charged residues inside the channel.

Residence time of K^+ and Cl^- ions

In a further step of our analysis, we quantified the contribution of the most important negatively and positively charged residues of NanC towards the binding of K^+ and Cl^- ions, respectively. We use the notion of "binding" here in a loose sense since we are in fact looking at residence times close to certain residues rather than real binding events. If any of the residues is within the first hydration shell radius distance of the K^+ or Cl^- ions (3.3 Å and 3.6 Å for K^+ and Cl^- ions, respectively [172]), then that particular residue is considered to be bound to the ion and the residence time is calculated as the time duration for which the ion remains bound to this residue. Only contact times larger than 100 ps are counted as residence times. Average residence times of K^+ and Cl^- ions for different residues are shown in Table 7.1 and Table 7.2. In particular, for some negatively charged residues, namely E186, D188 and E168, large residence times for K^+ ions are observed (Table 7.1). Especially at negative applied voltages, very large residence times of K^+ ions to the residues E186 and D188 are found. This finding explains the observed high density of K^+ ions in the region from 0 to 4 Å in Fig. 7.5b. For Cl^- ions, we do not

residue	residence time [ns] +1.0V	residence time [ns] -1.0V
R72	0.28 ±0.07	0.73 ±0.34
K91	0.56 ±0.03	0.87 ±0.35
R105	0.77 ±0.24	0.34 ±0.15
R107	0.28 ±0.04	0.34 ±0.07
R129	0.41 ±0.15	1.15 ±0.73
R85	0.37 ±0.08	0.75 ±0.47
K111	0.67 ±0.08	0.47 ±0.19
K153	0.47 ±0.15	0.46 ±0.13
R158	0.34 ±0.03	0.33 ±0.05
R6	0.26 ±0.09	0.21 ±0.21
R10	0.07 ±0.12	0.38 ±0.20
R19	0.31 ±0.06	0.23 ±0.06
K21	0.31 ±0.08	0.40 ±0.04
R208	0.46 ±0.24	0.38 ±0.19

Table 7.2.: Average residence times of Cl^- ions at the most important positively charged residues.

observe such large residence times to any of the positively charged residues. This analysis further supports our proposed mechanism of anion selectivity of the channel. Due to the faster permeation of Cl^- ions compared to the K^+ ions, Cl^- ions do not have a such large residence times as observed for the cations.

Properties calculated from unbiased MD simulations

Up to this point, our analysis of NanC channel is based on applied-field MD simulations. However, unbiased simulations can also be useful to further analyze the equilibrium properties of NanC channel in the absence of any external forces. Equilibrium simulations are carried out at a 500 mM KCl concentration. From the unbiased simulations, ion density profiles of the individual ion types have been extracted and the one-dimensional potentials of mean force (PMFs) for the K^+ and Cl^- ions along the z direction of the channel have been calculated using [28, 57]

$$W_\alpha(z) = -k_B T \ln(\rho_\alpha(z)/\rho_\alpha^{bulk}) \,. \tag{7.3}$$

In this expression, $\rho_\alpha(z)$ and ρ_α^{bulk} denote the ion densities of ion type α at position z along the channel and in bulk, respectively, T the temperature used in the simulations and k_B the Boltzmann constant. For simplicity, we determined the ion density in the channel as number of ions of type α divided by the total number of ions and water molecules in a bin. The bulk density is defined likewise. As shown in Fig. 7.7a, the free energy profile

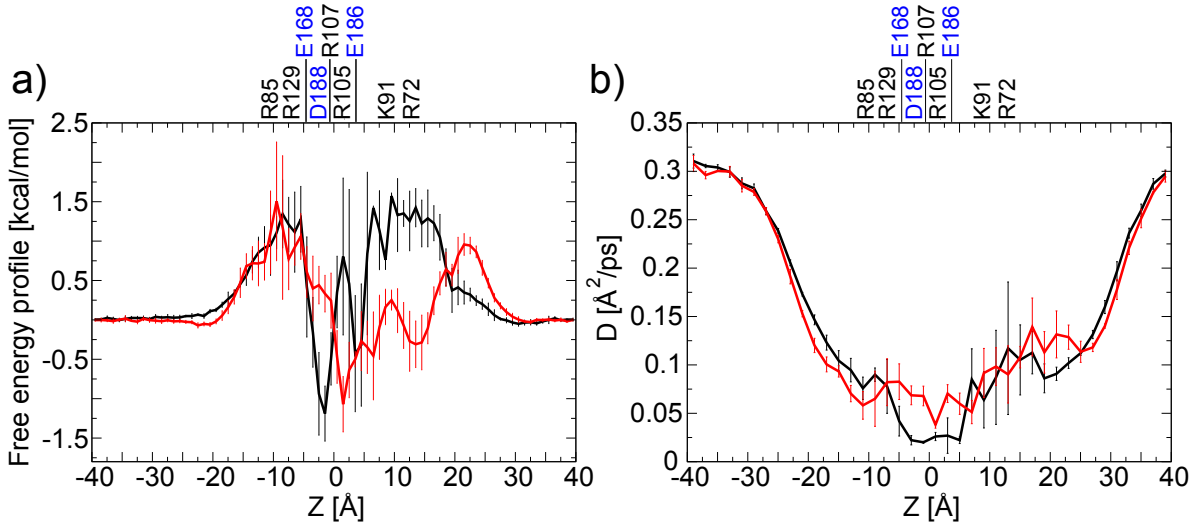

Figure 7.7.: Properties calculated from the unbiased MD simulations. a) One-dimensional free energy profiles [57] for K^+ (black) and Cl^- ions (red). b) Position-dependent diffusion coefficients for K^+ (black) and Cl^- (red) ions along the channel z axis. The important positively (black) and negatively charged (blue) residues are labeled at the top of the graphs at their approximate z position inside the channel.

for the K^+ ions have a very deep and narrow attracting well at the center of the channel together with two high energy barriers located at both sides which make the transport of K^+ ions through the channel rather slow. The deep binding site is due to the presence of negatively charged residues in that region, i.e., mainly E186, D188 and E168, while the large barriers on both sides originate from the positively charged arginine and lysine residues of track_p1 and track_p2 (see Fig. 7.1). In contrast to the K^+ profile, the Cl^- ions are subject to a more attractive PMF with wider binding regions which make the passage of Cl^- ions more efficient than that of the K^+ ions. These PMFs are in agreement with the dominant anion conductance and our proposed anion selectivity mechanism of the channel. If we compare the PMFs with those of OmpF, the PMFs of K^+ and Cl^- ions in OmpF are comparatively flat [28]. Due to the small size of the NanC channel, the ions form strong and stable electrostatic interactions with the charged residues of the NanC channel.

Another property which can be calculated from unbiased simulations is the position-dependent ion diffusion coefficient (see Methods). It is an important property to characterize the electrophysiological properties of the channel and also acts as input parameter for Brownian dynamics simulations [57, 87]. Figure 7.7b shows the position dependent diffusion coefficient for K^+ and Cl^- ions inside the NanC channel. Diffusion coefficients for both Cl^- and K^+ ions are decreased by about 60% to 80% inside the channel compared to the bulk region. A region of particular interest is from -5 to 5 Å where the K^+ ions diffuse

very slowly compared to Cl^- ions. This slow diffusion of K^+ ions in this region is due to the long residence times of these ions to the negatively charged residues (E186, D188 and E168) and the lack of a continuous distribution of negatively charged residues throughout the channel.

7.3.1. NanC mutants with modified transport characteristics

Mutations or chemical modifications can have important effects on the ion transport properties of porins. The general diffusion porin OmpF has been modified to be Ca^{2+} selective [60], to be a molecular diode [229] or to have other modified transport properties [27]. The porin OmpG has been altered to become a quiet pore for biosensing [137] and individual residues in OprP have been shown to be crucial in ion selectivity [193]. The latter porin has also been studied as a template for artificial channels [173]. Inspired by these studies we have studied mutations of NanC.

In our simulations of the WT channel, three negatively charged residues, namely E168, D188 and E186, have been demonstrated to be important in determining the overall conductance properties of the channel especially for the K^+ conductance. These residues have a large residence time concerning K^+ ions which in turn leads to important properties of the channel like asymmetric conductance and anion selectivity. To further decode the importance of these three residues, we performed applied-field ion transport studies for those mutants of the NanC channel. In total four mutants of NanC are generated *in silico*: the triple mutant E186Q D188N E168Q denoted as “tri_mut” and three single point mutants, namely, E186Q, D188N, and E168Q. E, D, Q and N denote the amino acids glutamate, aspartate, glutamine and aspargine, respectively. Simulations have been carried out using 500 mM KCl concentration and applied voltages of +1V and -1V.

In Fig. 7.8a and b, the total ion currents are displayed together with the separate Cl^- and K^+ currents for the WT and the four mutants for both voltage directions. For the positive voltage (Fig. 7.8a), the total current shows only small changes for the mutants compared to the WT. However, the contributions of the individual K^+ and Cl^- currents leading to the total current vary considerably for some of the mutants. For example, the mutant “tri_mut” has high Cl^- and low K^+ currents compared to the WT. As we have neutralized three negatively charged residues in this case, it is electrostatically not favorable for K^+ ions to pass while at the same time Cl^- ions can pass easier. At negative voltages (Fig. 7.8b), one prominent change is the drastic reduction of the total current for the mutant E186Q compared to the other channel variants including the WT. This drastic reduction in the total current is due to the simultaneous decrease of K^+ and Cl^-

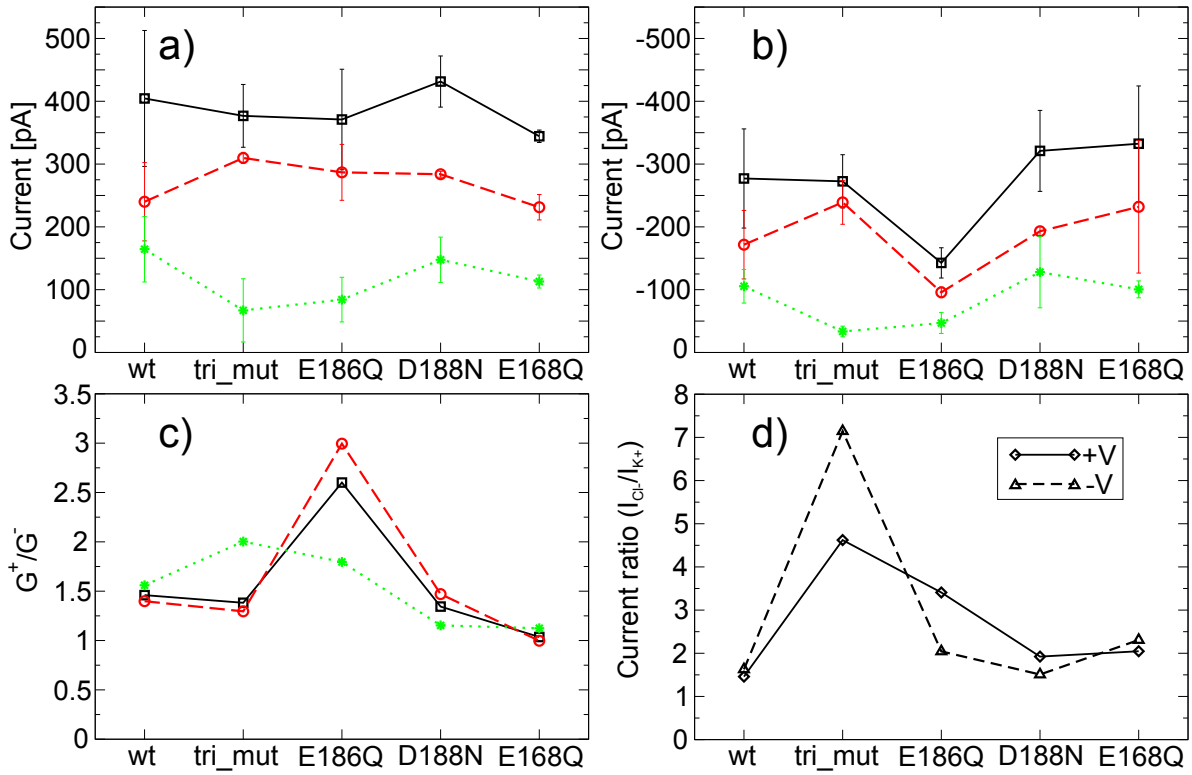

Figure 7.8.: Comparison of the total (black, solid), Cl^- (red, dashed), and K^+ (green, dotted) currents of the WT and the different mutants for applied voltages of a) +1V and b) -1V. c) Comparison of the channel asymmetries, G^+/G^-. d) Comparison of anion selectivities. The label "tri_mut" denotes the triple mutant E186Q D188N E168Q.

currents with a larger contribution from the later one. The reduction of the K^+ current is not very surprising as the negatively charged residue are neutralized. However, the large reduction in the Cl^- current may be attributed to a smaller electrostatic screening of the negatively charged residues inside the channel. Due to the smaller number of K^+ ions inside the channel of the E186Q mutant, the net negative charge of the mutant channel may increase. This is not favorable for the Cl^- conductance and may lead to a reduced Cl^- current. Applying a positive voltage, the absence of such a drastic reduction of the E186Q current can be attributed to the asymmetric distribution of negatively charged residues since more negatively charged residues are located between the center of the channel and the extracellular side (see Fig. 7.1). Hence Cl^- ions have to cross a large energetic barrier while entering from the extracellular side compared to entering from the periplasmic side especially in the absence of a large number of K^+ ions which would otherwise provide an electrostatic screening effect. We would like to point out that in our simulations, Cl^- ions have to enter from the extracellular side of the channel when applying a negative voltage. The presence of a slightly larger barrier for Cl^- ions from the extracellular side compared to periplasmic side is also confirmed by the PMF profile (Fig. 7.7a).

The asymmetric conductance and ion selectivity properties of the mutants are of particular interest. Fig. 7.8c shows the asymmetry properties of the mutants compared to the WT. Out of the four mutants, the mutant E186Q shows a significant increase in the asymmetry with the ratio G^+/G^- increasing from 1.5 for WT to 2.6 for the mutant. A large part of the asymmetry can be attributed to the Cl^- ions. So this mutant shows already a reasonable rectifying ability and might be, possibly with one or two additional point mutations, used as a molecular diode similar to the modification of OmpF [229]. Except for the E186Q mutant, the other mutants do not lead to any significant change in the asymmetry properties. In terms of ion selectivity of the channel (Fig. 7.8d), all mutants retained the anion selectivity. However, a drastic increase in anion selectivity is observed for the mutant "tri_mut" for both voltage directions. Applying a positive voltage, the anion selectivity of channel is increased with the ratio I_{Cl-}/I_{K+} reaching a value close to 5. The ratio is even higher, approximately 7, for negative voltages which is due to the fact that the neutralization of the negatively charged residues at the extracellular side reduces the energetic barrier for the Cl^- ions to enter from that side as discussed above. In summary, we are able to engineer the NanC channel with respect to two important properties. The mutant E186Q displays an increased asymmetry in the conductance while the mutant "tri_mut" (E186Q D188N E168Q) leads to a significant increase in the anion selectivity of the channel. The simulations of the mutants also indicate the particular importance of residue E186 involved in both most significant mutants in regulating the ion selectivity and the rectification property of the channel.

7.4. Conclusions

Applied-field and unbiased MD simulations have been carried out to probe the ion transport properties of the channel NanC. NanC is a porin present in the outer membrane of Gram-negative bacteria *E. coli*. One of its most important structural features, apart from being a porin with 12 β-strands and a tubular shape, is the distribution of its charged residues.

To understand the concentration-dependent ion transport through NanC, MD simulations with KCl concentrations ranging from 0.1 M to 1 M have been carried out for the both voltage directions. Earlier electrophysiological experiments showed an asymmetric behavior of the conductance and the anion selectivity of NanC [252, 260]. Our simulation results are found to be in good agreement with these experiments. Furthermore, we investigated the molecular basis for these channel properties. Averaged one-dimensional and three-dimensional ion distributions have been determined. This analysis revealed

the influence of the direction of the applied voltage on the distribution of ions inside the channel. The asymmetric distribution of charged residues inside the channel are found to be responsible for the asymmetric conductance property of the channel.

Moreover, we analyzed the residence times of K^+ and Cl^- ions to several important negatively and positively charged residues. For the K^+ ions we observed large residence times to a few negatively charged residues, namely E186, D188 and E168, while for the Cl^- ions we did not observe such large residence times to any of the positively charged residues. Based on the simulation results, we proposed a possible mechanism for the weak anion selectivity. The determining factor for this property is the favorable transport of Cl^- compared to their counterions. From unbiased MD simulations, PMFs and position-dependent diffusion coefficients are extracted for the transport of the K^+ and Cl^- ions. In the central region of the pore, the position-dependent diffusion coefficients are larger for the Cl^- ions compared to the K^+ ions. These results reinforce the suggested mechanism for the anion selectivity of the channel. Moreover, we observed a slight change in the ion selectivity of the channel depending on the KCl concentration. This may be attributed to the differential electrostatic screening of charged residues in the presence of a varying number of ions inside the channel depending on the KCl concentration.

Finally, we are able to engineer the NanC channel by modifying its rectifying behavior and the anion selectivity by designing mutant channels *in silico*. The point mutant, E186Q, shows an increased rectifying ratio of 2.6:1 while the triple mutant, E186Q D188N E168Q, leads to an increased anion selectivity. In particular, the residue E186 is found to be an important residue in governing the ion transport properties of the NanC channel since it involved in both significant mutants. Our study demonstrates the abilities of MD simulations to understand the structure-function relationships of porins such as NanC. The molecular details revealed from such an atomic-resolution method can be exploited to engineer channels with respect to various properties as has already been proven experimentally for OmpF [27, 61, 229] and OmpG [137]. For the NanC channel the proposed mutants would have to be manufactured and their transport properties to be measured experimentally.

An additional interesting point would be to study the ion transport behavior of porins and especially NanC within its natural membrane environment, i.e., an asymmetric membrane that incorporates lipopolysaccharide (LPS) molecules. Both the experimental [260] as well as computational studies reported here, used a simpler symmetric bilayer. It is an open question how some of the loops of porins interact with the LPS membrane. First attempts for modeling porins in LPS membranes have been performed [265, 266]

but this issue needs to be analyzed in more detail for the biological function of membrane proteins.

Acknowledgments

This work has been supported by grant KL 1299/6-1 of the Deutsche Forschungsgemeinschaft (DFG). Furthermore, the research leading to these results was conducted as part of the Translocation consortium (www.translocation.eu) and has received support from the Innovative Medicines Joint Undertaking under Grant Agreement n°115525, resources which are composed of financial contribution from the European Union's seventh framework programme (FP7/2007-2013) and EFPIA companies in kind contribution.

8. Summary and Outlook

The aim of this thesis is to understand ion transport processes through bacterial outer membrane porins and underlying structure-function relationships. Porins are membrane proteins present in the outer membrane of Gram-negative bacteria and some Gram-positive bacteria of the Mycolata group, the mitochondria and the chloroplast. They are channel-forming, β-barrel proteins and are responsible for the passage of diverse substrates into the periplasm of bacteria. Porins can be classified into two groups depending on their selectivity. Some porins are relatively non-specific (e.g., OmpF, OmpC, PhoE) while others are specific for substrates like sugars (LamB, ScrY), phosphate (OprP) and poly-phosphate (OprO). Porins exhibit a diverse range of the substrate and ion selectivity as well as the ion conductance properties and such properties can be engineered *via* generating the mutant channels. These characteristics along with the availability of the crystal structures of different porins make them the suitable candidates to probe the ion transport processes through nanopores using molecular dynamics simulations. A detailed understanding of the ion transport processes through porins have implications which are not limited to biological processes but extend to applications in the field of nanoanalytics and biosensing, e.g., DNA sequencing.

In this thesis, we have investigated different porins, namely, OprP and OprO from *Pseudomonas aeruginosa* and as well as OmpF and NanC from *Escherichia coli* for their ion selectivity and/or ion conductance properties. OprP is a phosphate-selective porin and is induced under conditions of phosphate starvation in the outer membrane of *P. aeruginosa* . Structurally it has a trimeric organization and each monomer consists of 16 β-strands. The ability of OprP to discriminate not only between anions and cations but also within anions is intriguing. To this end, free-energy molecular dynamics simulations were carried out using the adaptive biasing force (ABF) method to obtain the energetics of the phosphate, sulfate, chloride and potassium ions transport through OprP. For all four ions we observed characteristically different PMF profiles with the generalization that anions had energetically favorable bindings site regions while a cation had a barrier to permeate through the pore. Phosphate ions experienced two central binding sites whereas

only one central binding site was observed in case of the chloride ions. The overall electrostatic environment of the channel leads to the anion selectivity of the channel whereas a fine-tuned balance of interactions between the permeating ions and water as well as channel residues is responsible for the selectivity between different anions. The study provided the molecular factors leading to the phosphate selectivity of OprP and such findings were discussed in the context of the selectivity of the well-studied ion channels.

To further understand the structure-function relationships and the phosphate selectivity of OprP, important central binding sites residues were mutated to probe their individual contribution towards the selectivity of OprP. One such residue which was investigated concerning its role in the phosphate selectivity of OprP, is the arginine R133. R133 forms interactions with the phosphate ions in both central phosphate binding sites in OprP and is evolutionary conserved among the orthologs of OprP in different Pseudomonas species. Electrophysiological measurements indicated a roughly 30-40 times reduction in the binding affinity of phosphate for the R133 mutant channels compared to the wildtype OprP. Free-energy calculations for the permeation of phosphate through R133 mutant channels realized that the PMF profile changed from the energetically favorable binding site regions for the wildtype OprP to the energetically unfavorable barrier regions for the R133E/Q/A mutants of OprP. Molecular analysis revealed that the R133 residue of OprP, in addition to its positive charge, has an ability to desolvate the permeating ion along with the network of other residues of the channel. Hence the permeating ion becomes more vulnerable to the channel environment and thereby the R133 residue may control the interactions of the ion with the channel.

The other residue of OprP which was probed in detail for its significance in the phosphate binding and permeation is the aspartate D94. The presence of a negatively charged aspartate in a binding site of a negatively charged phosphate ion is intriguing if the complementary nature of the electrostatic interactions is considered. Electrophysiological measurements realized a roughly 20 times stronger binding of phosphate in the D94K mutant of OprP where a negatively charged aspartate residue is mutated to a positively charged lysine residue. PMF profiles also revealed a stronger binding of phosphate in the D94K mutant compared to the wildtype OprP. The possible role of the negatively charged D94 residue to impart the appropriate binding affinity to phosphate for OprP to enable an efficient and a unidirectional transport of phosphate across the outer membrane of *P. aeruginosa* was discussed. The presence and conservation of a similar negatively charged residue in the anion-binding sites of the anion-selective porins of the β-proteobacteria group of bacteria further confirmed the possible significance of a negatively charged

residue in the binding sites of such porins.

The investigation on the phosphate selectivity of OprP was further extended to unravel the diphosphate selectivity of OprO. OprO is a homologous porin of OprP from *P. aeruginosa* and they share 86% sequence similarity and 74% sequence identity. The important structural differences between OprP and OprO are the presence of two tyrosine residues Y62 and Y114 in OprP in the central narrowest region of the pore whereas the corresponding residues in OprO are F62 and D114. The presence of two bulky tyrosine residues in OprP leads to a smaller radius of the pore in the central region compared to OprO. PMF calculations revealed a deeper potential well for phosphate in OprP compared to OprO and in turn suggest a stronger binding of phosphate in OprP in qualitative agreement with electrophysiological experiments. OprO contained two central diphosphate binding sites while in case of OprP only one central binding site was observed and the second binding site was absent. The PMF calculations suggested a stronger binding of diphosphate in OprO than OprP in agreement with experiments. With the goal of swapping the phosphate and diphosphate selectivities of OprP and OprO respectively, *in silico* double mutant channels were generated, i.e., the Y62F Y114D double mutant of OprP and the F62Y D114Y double mutant of OprO. PMF profiles for the phosphate and diphosphate permeation through the double mutant channels realized a possible trend to swap the selectivities of OprP and OprO and suggested an importance of those two residues in assigning the different selectivities to each porin. Moreover, applied-field MD simulations for the KCl electrolyte through the wildtype OprP and OprO channels as well as the double mutant channels revealed a trend to interchange the KCl ion selectivity properties of OprP and OprO by their respective double mutant channels to a certain extent. The double mutant channels of OprP and OprO suggested based on the computational studies are going to be experimentally generated and will be investigated for their selectivities in electrophysiological measurements.

In addition, the non-specific porin OmpF was investigated concerning the temperature-dependent ion conductance of a special kind of ion type, i.e., the ionic liquid 1-butyl-3-methyl-imidazolium chloride (BMIM-Cl). OmpF is a 16 β-stranded porin with a trimeric structure. Aqueous solutions of the BMIM-Cl ions were reported to increase the translocation time of DNA and antibiotics through nanopores in electrophysiological measurements which can be exploited to enhance the time resolution of such measurements. The temperature-dependent transport of the ionic liquid BMIM-Cl through OmpF was probed utilizing applied-field MD simulations and compared with experimental electrophysiology measurements. An excellent agreement between theory and experiments was obtained.

Dependence of the BMIM-Cl conductance on different water models and their diffusion coefficients were discussed. It was observed that $BMIM^+$ ions had to realign themselves in a particular orientation to pass through the constriction region of OmpF. It was suggested that attaining a correct orientation of $BMIM^+$ near the constriction region may serve as a rate-limiting step and thereby enabling the slower kinetics of the substrates translocation through OmpF in the presence of such bulky ions.

Furthermore, the ion transport properties of the NanC porin were investigated by applied-field and unbiased MD simulations. NanC is a 12-stranded β-barrel porin with a tubular shape. An important feature of this porin is the asymmetric distribution of charged residues which imparts many of the observed properties of the porin in electrophysiological measurements, namely an asymmetric conductance with respect to the direction of the applied voltage and a weak anion selectivity of the channel. Applied-field MD simulations with the KCl electrolytes realized the asymmetric conductance property and weak anion selectivity of the porin in agreement with experiments. The ion density profiles for K^+ and Cl^- inside the pore were altered by the direction of the applied voltage in simulations and provided a clue about the asymmetric conductance property of the channel. The positively charged residues in NanC formed continuous tracks through out the length of the pore while the the negatively charged residues were more scattered. Hence a possible mechanism for the anion selectivity of the porin was suggested where Cl^- can be more efficiently transported through the pore due to the continuous electropositive sink provided by the tracks of the positively charged residue across the length of the porin. Indeed, position-dependent diffusion coefficients for K^+ and Cl^- indicated a faster permeation of Cl^- particularly at the central region of the pore. Going one step further, several *in silico* mutants of NanC were generated to modify the asymmetric conductance property and the weak anion selectivity of the porin. The triple mutant, E186Q D188N E168Q, led to an increased anion selectivity of the porin whereas the point mutant, E168Q, demonstrated a molecular diode kind of behavior with an increased asymmetric conductance property.

The findings presented in this thesis open several possibilities for future investigations. Although the atomic details provided by all-atom MD simulations are very valuable, they suffer the major drawback of limited time scales. Future investigations on the porins which are studied here can be focused on utilizing more abstract-level methods like brownian dynamics (BD) simulations and coarse-grained molecular dynamics simulations. Molecular details obtained from all-atom MD simulations can be utilized to improve the accuracy of the abstract-level methods. For example, diffusion coefficients of ion permeation can be

derived from MD simulations to use as an input parameter in BD simulations. The other line of investigation can be directed towards the simulations of porins studied in this thesis within its natural membrane environment, i.e., an asymmetric membrane that consists of lipopolysaccharide (LPS) molecules. It will be interesting to probe any altered dynamics of porins in such an asymmetric membrane environment and their possible effects on ion transport properties by comparing with results presented in this thesis.

Appendices

A. Supporting Information for Chapter 2

Modeling the Ion Selectivity of the Phosphate Specific Channel OprP

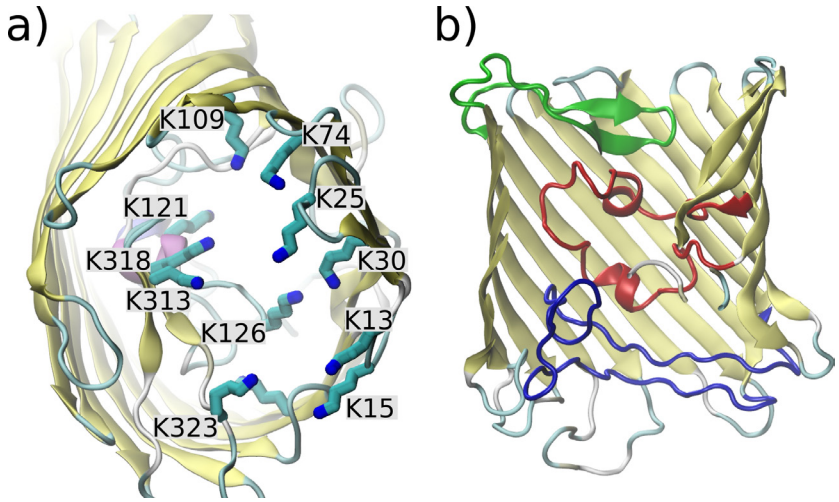

Figure A.1.: a) Residues of the lysine cluster on the periplasmic side of the pore. b) Loops L3 (red), L5 (blue) and T7 (green). Loop L3 is responsible for the formation of the constriction regions in the middle of the pore. Loop L5 and T7 contain some of the residues of the arginine ladder and the lysine cluster, respectively.

Molecular dynamics simulation details

A trimer of OprP (PDB 2O4v) [160] was embedded into a palmitoyloleoyl-glycero-phosphathidyl ethanolamine (POPE) lipid bilayer, which was constructed from pre-equilibrated patches using VMD [181]. Channel embedded in lipid bilayer is solvated using TIP3P water molecules. One of the four ions (phosphate, sulfate, chloride and potassium), was subsequently placed at the mouth of the one of the monomers on the extracellular side leading to four different systems. Phosphate ions are predominantly monobasic at around physiological pH of pH 7. Hence the monovalent form of the phosphate ion, $H_2PO_4^-$, was chosen in this study (different from the one in Ref. 121). The sulfate ion is taken in its divalent form (SO_4^2-) as it is the most preferable protonation state for physiological pH values. All four systems have been neutralized by addition of potassium ions and each system has ∼120,000 atoms. The system was subject to 2000 steps of energy minimization to remove unfavorable sterical contacts followed by a ∼5 ns of equilibration run to ensure proper packing of lipid bilayer around the channel.

All simulations were performed in the NPT ensemble with the program NAMD 2.8 [131] and the CHARMM27 force field [95] along with additional force field parameters for $H_2PO_4^-$ [182] and SO_4^{2-} [267]. Langevin dynamics along with a Langevin piston algorithm were utilized to maintain the temperature of 310 K and the pressure of 1 atm in all simulations. Periodic boundary conditions have been employed and short-range nonbonded interactions were calculated using a cutoff of 12 Å and a switching distance of 10 Å while the long-range electrostatic interactions were treated using the particle

mesh Ewald method [183]. Employing the r-RESPA multiple time step method [184], bonded interaction were evaluated every 1 fs while short-range nonbonded and long-range electrostatic interactions at every 2 fs and 4 fs, respectively. Bond constraints using the SHAKE algorithm [185] were applied to all water hydrogen atoms.

Within the ABF method, a reaction coordinate is defined as a position of an ion along the z axis (parallel to channel principal axis). The change in free energy is calculated with respect to the bulk value. To improve the sampling efficiency, the full reaction coordinate (length of ∼84 Å along the z) axis was subdivided into 21 windows with a length of 4 Å each. This range also includes extended bulk regions on both sides of the channel. Initial starting confirmations of the system for each window were obtained by performing constant velocity steered molecular dynamics (SMD) simulations in which each ion under investigation was dragged through the channel along the z axis. The average force acting on the respective ion was accumulated in 0.1 Å sized bins within each window. Moreover, the application of the adaptive bias was initiated only after 800 samples were accumulated in individual bins to overcome the fluctuations of the instantaneous forces and to obtain a reasonable starting estimation of the biasing forces. Subsequently, the resulting data were combined to generate the potential of mean force (PMF) profiles. Production runs in each window continued for at least 6 ns with considerably extended runs for about 15-20 ns in the central binding site windows (-10 to 10 Å). This lead to production runs of ∼160 ns for each ion and a total simulation time of 0.65 μs for all the four ions in total. A coarse upper-bound limit of the standard error in ABF calculation, $SD[\Delta A^{(ABF)}]$, for the free energy difference, $\Delta A^{(ABF)}$, between the points ξ_a and ξ_b along a reaction coordinate, ξ, can be calculated using [163]

$$SD[\Delta A^{(ABF)}] \approx (\xi_b - \xi_a)\frac{\sigma}{K^{1/2}}(1+2\kappa)^{1/2}\,. \tag{A.1}$$

In this equation σ denotes the standard deviation of thermodynamic force along ξ, K the total number of force values and κ the correlation length for the series of calculated forces. Errors are calculated for each bin having the width of 0.1 Å (i.e., ξ_b - $\xi_a = 0.1$ Å).

During the analysis the interaction energies were calculated using the NAMDEnergy plugin with the a cutoff distance of 12 Å with respect to the permeating ion.

Calculation of the dissociation constant

The standard free energy of binding ΔG° has been calculated using the method developed by Henchman and coworkers [268]. The dissociation constant K_d and ΔG° are

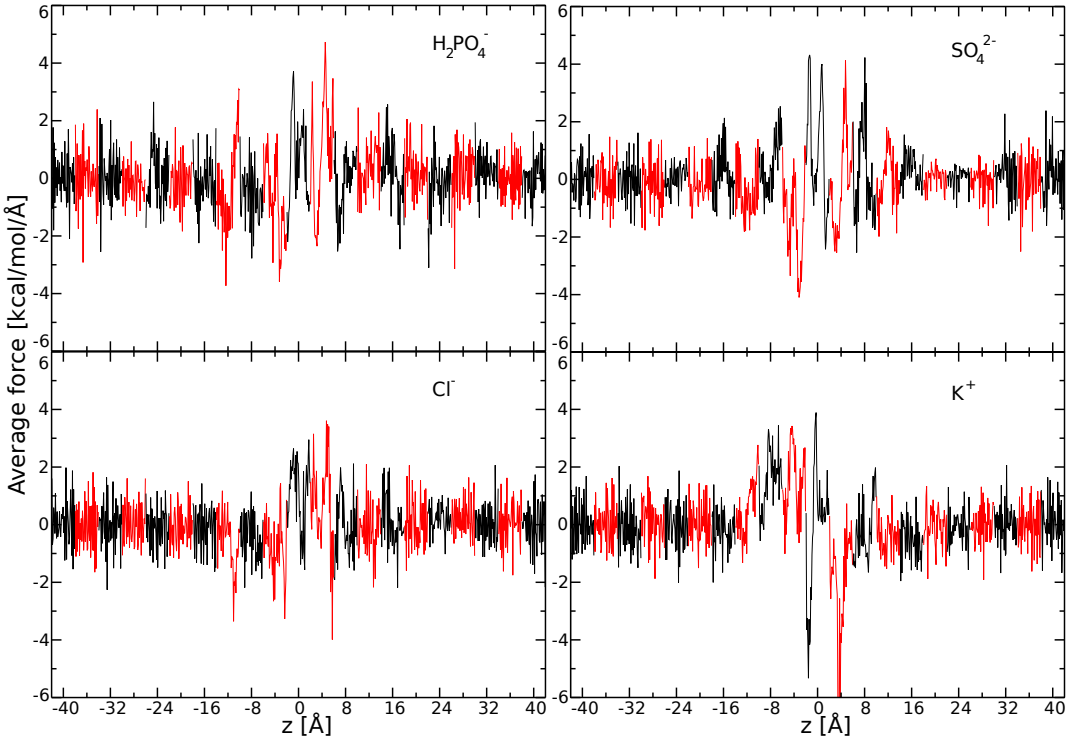

Figure A.2.: Convergence of the ABF simulations. The average forces across the 21 windows are continuously connected. Too guide the eye, alternating windows are shown in black and red, respectively.)

related via

$$K_d^{-1} = N_A V^\circ \exp(-\Delta G^\circ / RT) \tag{A.2}$$

where N_A is Avogadro's number, $V^\circ = 1661$ Å^3 is the standard volume which corresponds to a standard concentration of 1 M, R denotes the molar gas constant and T the temperature. In the present study the confinement provided by the periodic boundary conditions can be considered comparable to applying harmonic confinement potentials as described in Ref. 268 which allows to evaluate the involved integrals. A similar method has been used in Ref. 121. The free energy of binding ΔG° can be written as

$$\Delta G^\circ = \Delta G_{PMF} + \Delta G_V \tag{A.3}$$

where ΔG_{PMF} is the change in free energy of binding between the ligand-bound and unbound states whereas ΔG_V is the free energy change from unbound to standard-state volume. As there is no change in free energy due to the introduction of confinement restraints, the term ΔG_R present in Eq. 6 in Ref. 268 is not required here. The final form

of the standard binding free energy is given by

$$\Delta G^{\circ} = \Delta W - RTln\frac{l_b Au}{vV^{\circ}} \tag{A.4}$$

where ΔW denotes the depth of the binding site, l_b the bound length, Au the average cross sectional area of the simulation box perpendicular to the membrane normal, and v the number of ions sampled in the simulations.

The depth of the binding site ΔW is defined as the exponential average of the PMF, i.e., $W(z)$, over the entire unbound region

$$\Delta W = RTln\left[\int_{unbound} \exp\left(\frac{-[W(z) - minW(z)]}{RT}\right)dz \Big/ \int_{unbound} dz\right] . \tag{A.5}$$

The bound length l_b is a configurational integral of the PMF over the bound regions

$$l_b = \int_{bound} \exp\left(\frac{-[W(z) - minW(z)]}{RT}\right)dz \ . \tag{A.6}$$

Coordination number analysis

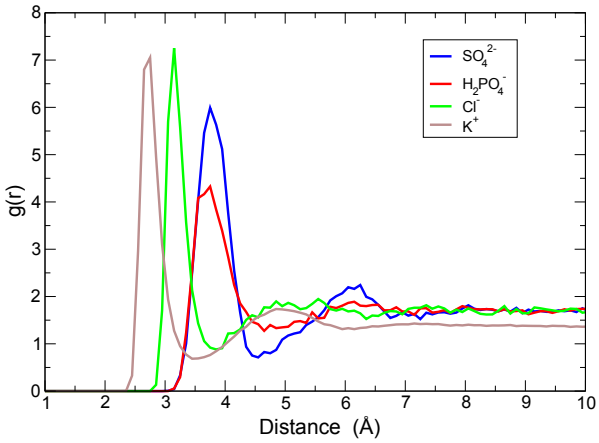

Figure A.3.: Radial distribution function (RDF) profile for all four ions in bulk water based on a water oxygen to ion center of mass distance.

Radial distribution function (RDF), $g(r)$, calculations were carried out considering a water oxygen to ion center of mass distance in bulk water to characterize the hydration shells of the various ions (Fig. A.3). The first minima of each RDF profile for the corresponding ion is considered as a first hydration shell distance. The first hydration shells for the $H_2PO_4^-$, SO_4^{2-}, Cl^-, and K^+ have been determined to be 4.6 Å , 4.4 Å , 3.6 Å , and 3.3 Å , respectively. The average number of water oxygen atoms or protein atoms within

the above specified distance in the different regions (bin width of 1Å along z axis) of the channel is defined as the "coordination number". Nitrogen atoms and oxygen atoms of the membrane protein were considered as contact atoms for the anions and cations, respectively.

Correlation coefficient calculations

To quantify the correlated movements between the permeating $H_2PO_4^-/SO_4^{2-}$ ions and the D94/K121 residues of the channel, correlation coefficients were determined. The Pearson correlation coefficient (denoted as r) between the z positions of the center of mass of the anions (denoted as A_i) and the C_γ atom of D94 or N_ε of K121 (denoted as R_i) in the different regions of the pore (bin width of 1 Å along z axis) have been calculated as

$$r = \frac{n(\sum_i A_i R_i) - (\sum_i A_i)(\sum_i R_i)}{\sqrt{n\sum_i A_i^2 - (\sum_i A_i)^2}\sqrt{n\sum_i R_i^2 - (\sum_i R_i)^2}} \tag{A.7}$$

where n denotes the number of the samples in each bin.

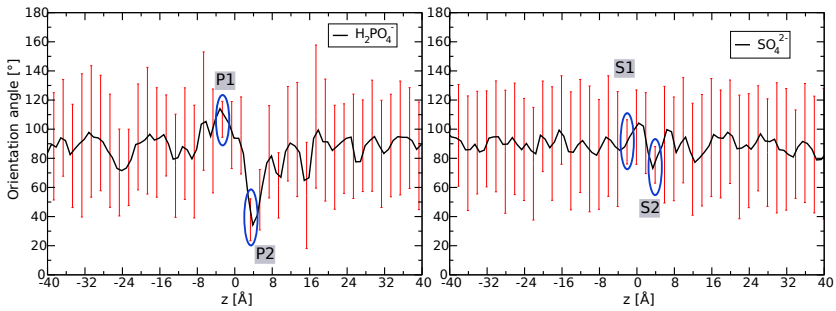

Figure A.4.: Average orientation angle of $H_2PO_4^-$ (selecting phosphate and one of the oxygen atoms to define the reference direction) and SO_4^{2-} (similarly selecting sulfur and one of the oxygen atoms to define the reference direction) w.r.t. the z axis. Average angles have been measured in the bin of width 1 Å and the standard deviation in each bin indicates the rotational degree of freedom ion encounters in a particular region. Both ions types have comparatively small standard deviation in binding sites (about 15° as highlighted by the blue circles compared to about 40-50° in the other regions). This indicates more restricted movements of the ions and may lead to higher entropic penalties in the binding sites.

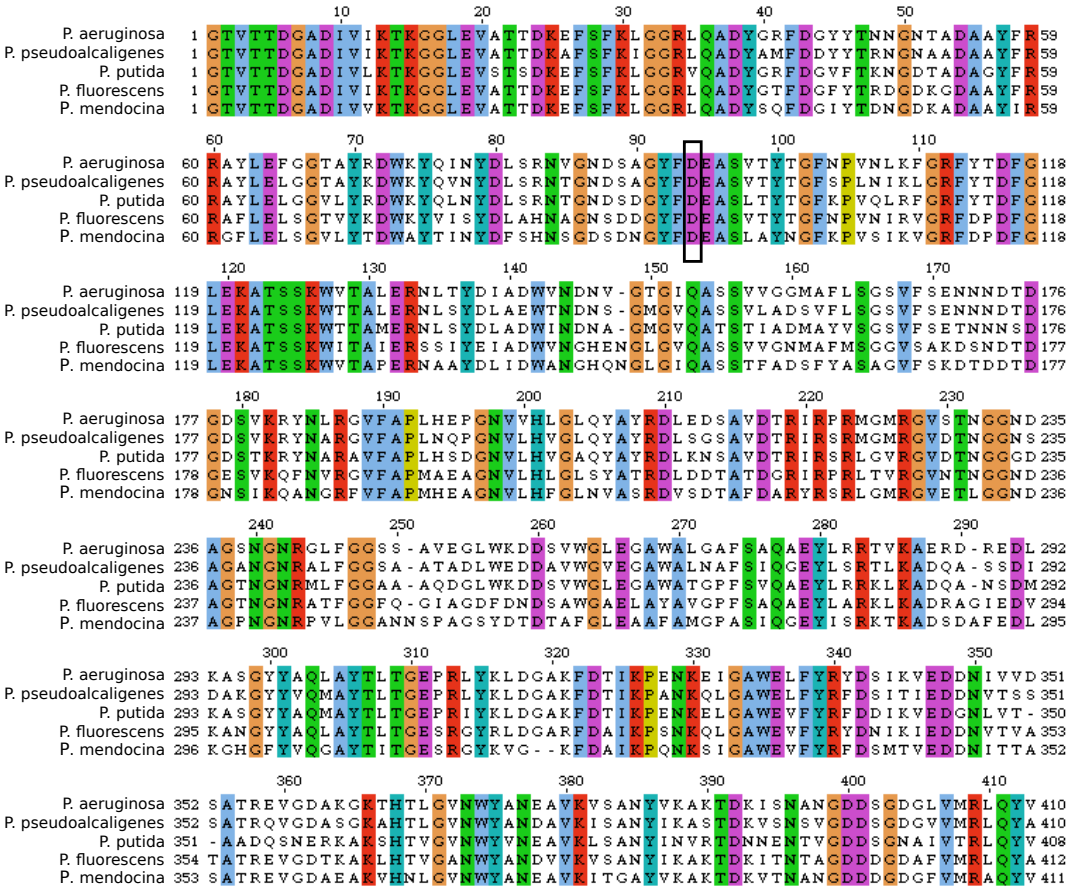

Figure A.5.: Multiple sequence alignment among OprP orthologs in different Pseudomonas species. D94 is conserved in all species as shown by the black box. The sequence alignment was generated using ClustalW [269].

B. Supporting Information for Chapter 3

Role of the Central Arginine R133 of OprP: Effects of Charge and Solvation

Reproduced with permission from the article by Modi, N.; Bárcena-Uribarri, I.; Bains, M; Benz, R; Hancock, R. E. W; and Kleinekathöfer, U., "Role of the Central Arginine R133 toward the Ion Selectivity of the Phosphate Specific Channel OprP: Effects of Charge and Solvation", *Biochemistry*, **2013**, 52(33), pp 5522-5532 (DOI: 10.1021/bi400522b). Copyright [2013] American Chemical Society.

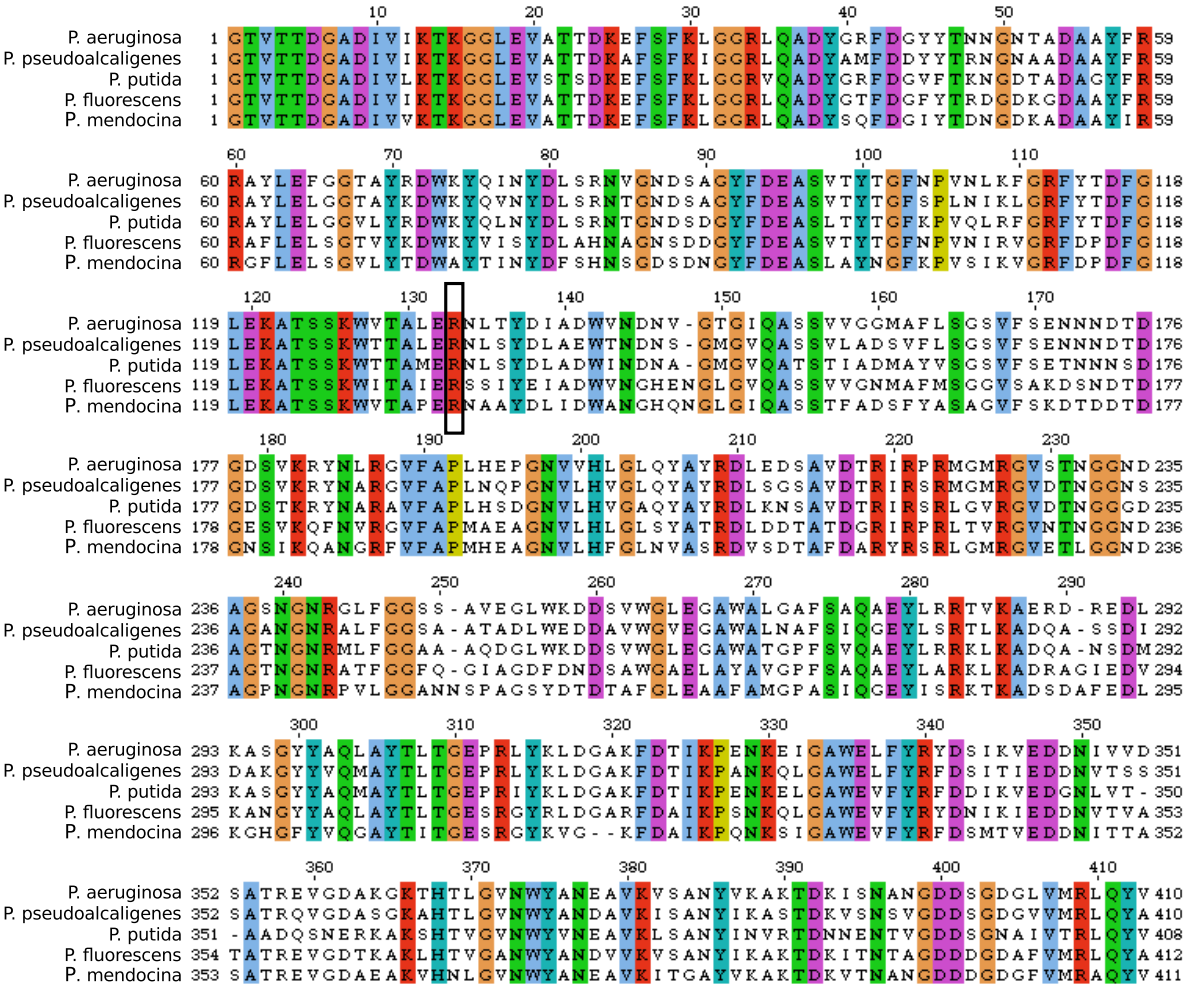

Figure B.1.: Multiple sequence alignment among OprP orthologs in different Pseudomonas species. R133 is conserved in all species as shown by the black box. The sequence alignment was generated using ClustalW [269]

Coordination number analysis

Radial distribution function (RDF), $g(r)$, calculations were carried out considering a water oxygen to ion center of mass distance in bulk water to characterize the hydration shells of the various ions (Fig. B.2) [172]. The first minima of each RDF profile for the corresponding ion is considered as a first hydration shell distance. The first hydration shells for the $H_2PO_4^-$, Cl^-, and K^+ have been determined to be 4.6 Å, 3.6 Å, and 3.3 Å, respectively. The average number of water oxygen atoms or protein atoms within the above specified distance in the different regions (bin width of 1Å along z axis) of the channel is defined as the "coordination number". Nitrogen atoms and oxygen atoms of the membrane protein were considered as contact atoms for the anions and cations, respectively.

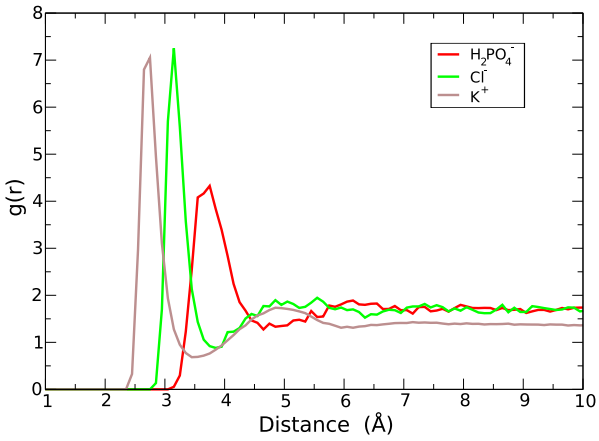

Figure B.2.: Radial distribution function (RDF) profile for all four ions in bulk water based on a water oxygen to ion center of mass distance [172].

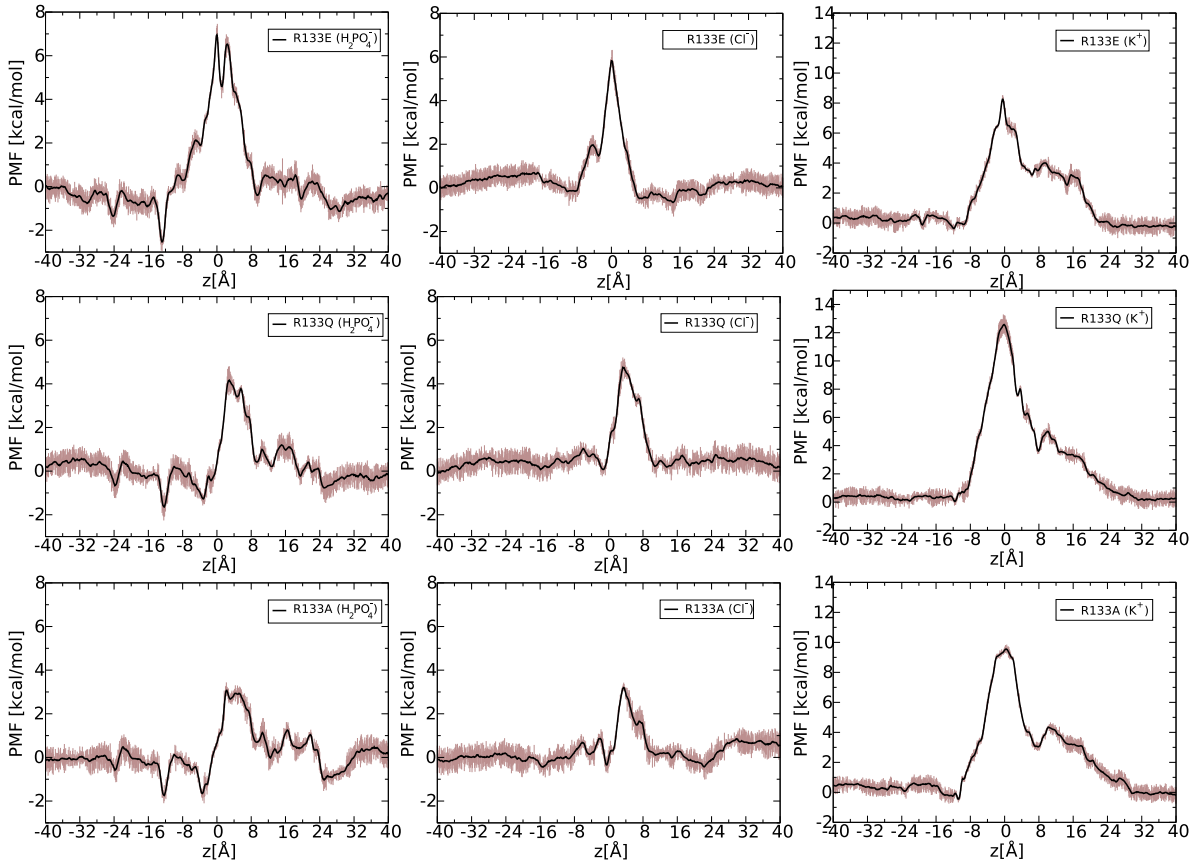

Figure B.3.: PMF profiles with error bars for the transport $H_2PO_4^-$, Cl^-, and K^+ ions through different R133 mutants.

C. Supporting Information for Chapter 4

Significance of a Negatively Charged Residue D94 of OprP in the Phosphate Binding and Permeation

```
1    GTVTTDGADIVIKTKGGLEVATTDKEFSFKLGGRLQADYGRFDGYYTNNGNTADAAYFRR   60  P.aeruginosa
1    GTVTTDGADIVIKTKGGLEVATTDKEFSFKLGGRLQADYGTFDGFYTRDGDKGDAAYFRR   60  P.pseudoalcaligenes
1    GTVTTDGADIVLKTKGGLEVSTSDKEFSFKLGGRVQADYGRFDGVFTKNGDTADAGYFRR   60  P.putida
1    GTVTTDGADIVVKTKGGLEVATTDKEFSFKVGGRLQADYSRFDGFYTVNGNNADAGYFRR   60  P.fulva
1    GTVTTDGADIVIKTKGGLEVATTDKAFSFKIGGRLQADYAMFDDYYTRNGNAADAAYFRR   60  P.mendocina
1    GTVTTDGADIVVKTKGGLEVATTDKEFSFKLGGRLQADYSRFDGVYTKNGDTADAAYFRR   60  P.chlororaphis
1    GTVTTDGADIVIKTKGGLEVGTTDKEFSFKLGGRLQADYSRFDGFYTKNGNDADAAYFRR   60  P.denitrificans
     **********:********.*:** ****:***:****. **  :* :*: .**.****
                                          D94
61   AYLEFGGTAYRDWKYQINYDLSRNVGN---DSAGYFDEASVTYTGFNPVNLKFGRFYTDF  117  P.aeruginosa
61   AFLELSGTVYKDWKYVISYDLAHNAGN---SDDGYFDEASVTYTGFNPVNIRVGRFDPDF  117  P.pseudoalcaligenes
61   AYLELGGVLYRDWKYQLNYDLSRNTGN---DSDGYFDEASLTYTGFKPVQLRFGRFYTDF  117  P.putida
61   AFLEIGGVLYTDWAYQLNYDFSHNSGGDNRSEDGYFDEASLAYNGFKPLSIKVGRFDPEF  120  P.fulva
61   AYLELGGTAYKDWKYQVNYDLSRNTGN---DSAGYFDEASVTYTGFSPLNIKLGRFYTDF  117  P.mendocina
61   AFLELSGVLYTDWAYTINYDFSHNTGD---SDNGYFDEASLAYNGFKPVSIKVGRFDPDF  117  P.chlororaphis
61   AYLELGGTMYRDWKYQISYDMAHNSGN---SDNGYFDEASFSYIGFSPVTLKFGRFDPDF  117  P.denitrificans
     *:**:.*. * ** * :.**:::* *    .. *******.:* **.*: ::.***  :*

118  GLEKATSSKWVTALERNLTYDIADWVND-NVGTGIQASSVVGGMAFLSGSVFSENNN--D  174  P.aeruginosa
118  GLEKATSSKWITAIERSSIYEIADWVNGHENGLGVQASSVVGNMAFMSGGVSAKDSN--D  175  P.pseudoalcaligenes
118  GLEKATSSKWTTAMERNLSYDLADWIND-NAGMGVQATSTIADMAYVSGSVFSETNN--N  174  P.putida
121  GLEKATSSKWVTAPERTAAYDLVDWANSHNGGMGIQVSGTAGDSLYGSAGFFAKDATNAD  180  P.fulva
118  GLEKATSSKWTTALERNLSYDLAEWTND-NSGMGVQASSVLADSVFLSGSVFSENNN--D  174  P.mendocina
118  GLEKATSSKWVTAPERNIAYDMVDWANTHQNGMGLQASSTFADSFYASAGVFSKDTD--D  175  P.chlororaphis
118  GLEKATSSKWVTATERNSAYELADWINTHQDGMGAQVGGVVANMAYLDAGVYAKDAD--D  175  P.denitrificans
     ********** ** **.  *::.:* *  : * * *. .. .   : .... ::     :

175  TDGDSVKRYNLRGVFAPLHEPGNVVHLGLQYAYRDLEDSAVDTRIRPRMGMRGVSTNGGN  234  P.aeruginosa
176  TDGESVKQFNVRGVFAPMAEAGNVLHLGLSYATRDLDDTATDGRIRPRLTVRGVNTNGGN  235  P.pseudoalcaligenes
175  SDGDSTKRYNVRGVFAPLHSDGNVLHVGAQYAYRDLKNSAVDTRIRSRLGVRGVDTNGGG  234  P.putida
181  KDGDSTKQFNLRGVFAPLHETGNVLHLGLNFAQRDLSDTAFDGRIRSRLGMRGVSTDGGQ  240  P.fulva
175  TDGDSVKRYNARGVFAPLNQPGNVLHVGLQYAYRDLSGSAVDTRIRSRMGMRGVDTNGGN  234  P.mendocina
176  TDGDSVKQVNGRFVFAPMHDAGNVLHFGVNVASRDVSDTAFDSRYRTRMGMRGVETLGGN  235  P.chlororaphis
176  TDGDSVKQFNFRGVFAPMNTDGNVLHLGVDYAYRDLDDTAFDSRIRPRLGMRGVSTNGGN  235  P.denitrificans
     .**:*.*: * * ****:   ***:*.* . * **:. :* * * * *: :***.* **

235  DAGSNGNRGLFGGSS-AVEGLWKDDSVWGLEGAWALGAFSAQAEYLRRTVKAERD-REDL  292  P.aeruginosa
236  DAGTNGNRATFGGFQ-GIAGDFDNDSAWGAELAYAVGPFSAQAEYLARKLKADRAGIEDV  294  P.pseudoalcaligenes
235  DAGTNGNRMLFGGAA-AQDGLWKDDSVWGLEGAWATGPFSVQAEYLRRKLKADQA-NNDM  292  P.putida
241  DAGTNGNRLLLGGANNLPVGSYDTDRAMGLEAAWAMGPLSIQGEYITRKMKADADTREDI  300  P.fulva
235  SAGANGNRALFGGSA-ATADLWEDDAVWGVEGAWALNAFSIQGEYLSRTLKADQA-SSDI  292  P.mendocina
236  DAGTNGNRPVLGGSSSSPAGSYDRDTAFGLEAAFAMGPASIQGEYITRKTKADSNAYEDI  295  P.chlororaphis
236  DAGENGNRATFGGATLSPAGSYKDDSTWGAEFAYAFGPFSAQAEYLKRKLKADADAYQDI  295  P.denitrificans
     .** ****  :**        :. * . * * *:*    * *.**: *. **:    .*:

293  KASGYYAQLAYTLTGEPRLYKLDGAKFDTIKPENKEIGAWELFYRYDSIKVEDDNIVVDS  352  P.aeruginosa
295  KANGYYAQLAYTLTGESRGYRLDGARFDAIKPSNKQLGAWEVFYRYDNIKIEDDNVTVAT  354  P.pseudoalcaligenes
293  KASGYYAQMAYTLTGEPRIYKLDGAKFDTIKPENKELGAWEVFYRFDDIKVEDGNLVTAA  352  P.putida
301  KAKGYYGQVAYTLTGEARAYKL--GKFDAIKPANKSIGAWELFYRYDHIAVEDDTVGIDP  358  P.fulva
293  DAKGYYVQMAYTLTGEPRLYKLDGAKFDTIKPANKQLGAWELFYRFDSITIEDDNVTSSS  352  P.mendocina
296  KGHGFYVQGAYTLTGESRGYKV--GKFDAIKPANKAFGAWELFYRYDSMTVEDDNITTAS  353  P.chlororaphis
296  KADGYYGQLAYTITGESRVYKLDGAKFDTIKPADKQLGAWEVFYRYDHIKVDDPNVTVAT  355  P.denitrificans
     .. *:* * ***:*** * *::  .:**:*** :* :****:***:* : ::* .:

353  ATREVGDAKGKTHTLGVNWYANEAVKVSANYVKAKTDKISNA----------NGDDSGD  401  P.aeruginosa
355  ATREVGDTKAKLHTVGANWYANDVVKVSANYIKAKTDKITNT----------AGDDDGD  403  P.pseudoalcaligenes
353  --DQSNERKAKSHTVGVNWYVNEAVKVSANYINVRTDNNENT----------VGDDSGN  399  P.putida
359  ----TDDVTGKVHNLGVNWYANEAVKVSATYIKAKVDNQVNSVA---------ADDDSGD  405  P.fulva
353  ATRQVGDASGKAHTLGVNWYANDAVKISANYIKASTDKVSNS----------VGDDSGD  401  P.mendocina
354  LTRDVGDAEVKVHNLGVNWYANEAVKISATYVKAKTDKVTNATAASGGTPAKRTGDDDGD  413  P.chlororaphis
356  ATRDVGDTKASTNTIGVNWYANEAVKVSLDYVHVTTDGIRNA----------NGDDDGN  404  P.denitrificans
          :   . ..:*.***.*:.**:*  *:.. .*   *:            **.*:

402  GLVMRLQYVF  411  P.aeruginosa
404  AFVMRLQYAF  413  P.pseudoalcaligenes
400  AIVTRLQYVF  409  P.putida
406  GVVLRAQYVF  415  P.fulva
402  GVVMRLQYAF  411  P.mendocina
414  GFIVRAQYVF  423  P.chlororaphis
405  GVVTRLQYVF  414  P.denitrificans
     ..: * **.*
```

Figure C.1.: Multiple sequence alignment among OprP orthologs in different Pseudomonas species. D94 is conserved in all species as shown by the red box. The sequence alignment was generated using ClustalW [269]

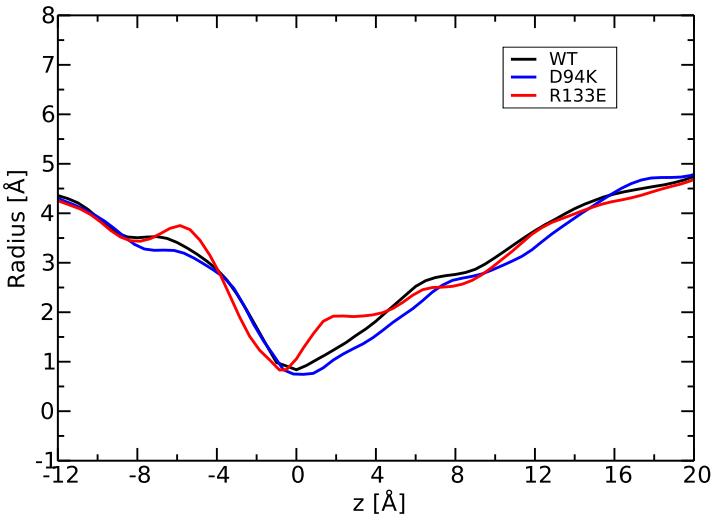

Figure C.2.: Average radius of OprP and mutants, D94K and R133E, in equilibrium MD simulations. Pore radius are determined using HOLE program[216].

```
1    ESSVTLFGIVDTNVAYVNKDAA-------------GDSRYGLGTSGASTSRLGLRGTEDL   47  D.acidovorans
1    ETSVTLYGIIDTGIGYNDVDFKVKGANADDSDFKYNHSRFGMINGVQNGSRWGLRGTEDL   60  B.pertussis
1    MADVTLYGTIKAGVETYRFVAHN-GAQAS--------GVETATEIADLGSKIGFKGQEDL   51  N.gonorrhoeae
1    MADVTLYGTIKAGVETSRSVEHN-GGQVV--------SVETGTGIVDLGSKIGFKGQEDL   51  N.meningitidis
1    QSSVTLYGRVNTTVERQKV----------------GDVS--TTGLFNNSSRFGFKGTEDL   42  A.delafieldii
      :.***:* :.: :                                  *: *::* ***
                 E58
48   GGGLKAGFWLEGEIFGDDGNAS--GFNFKRRSTVSLS-GNFGEVRLGRDLVPTSQKLTSY  104  D.acidovorans
61   GDGLQAVFQLEGSFNSGNGNSAQDGRLFGRQATIGLQSESWGRLDFGRQTNIASKYFGSI  120  B.pertussis
52   GNGLKAIWQLEQKAYVSGTN----TGWGDRQSFIGLK-GGFGKVRVGRLNSV-LKDTGGF  105  N.gonorrhoeae
52   GNGLKAIWQVEQKASIAGTD----SGWGNRQSFIGLK-GGFGKLRVGRLNSV-LKDTGDI  105  N.meningitidis
43   GGGLKAGFQLEGSFNSDTGASA--STFFGRQSEVNLS-GNFGMVRLGNFFAESYYATADY   99  A.delafieldii
     * **:* : :*                 *:: : *.   :* : .*.

105  DLFSATGIGPFMGFRNWAAGQGAD---DNGIRANNLISYYTPNFGGFNAGFGYAFDEKQT  161  D.acidovorans
121  DPFGA-------GFGQANIGMGMS--AMNTVRYDNMVMYQTPSYSGFQFGIGYSFSANDK  171  B.pertussis
106  NPWEGK--SEYLSLSNI---------A-RPEERPISVRYDSPEFAGFSGSVQYVPNDNSG  153  N.gonorrhoeae
106  NPWDSK--SDYLGVNKI---------A-EPEARLISVRYDSPEFAGLSGSVQYALNDNAG  153  N.meningitidis
100  VS-----------LHNHNTGSSSDALYAYVMQNANKVAYRTPSFGGFTVEGAVGLHEQTV  148  A.delafieldii
                . :                    : * :*.:.*:          :

162  IGTA-D-------SVGRYIGGYVAYDNGPLSASLGLAQQKTA----VGGLATD-RDEITL  208  D.acidovorans
172  DADAVNRVGFATADNVRAITTGLRYVNGPLNVALSYDQLNASNNQAQGEVDAT-PRSYGL  230  B.pertussis
154  ENKS------------ESYHAGFNYKNSGFFVQYAGSYKRHN--Y-----TTEKHQIHRL  194  N.gonorrhoeae
154  KYNS------------ESYHAGFNYKNGGFFVQYGGAYKRHV--RVDENVNIEKYQIHRL  199  N.meningitidis
149  -GGK-N-------AY----DLAANYAAGPLALGAGYSKQ------------GD-VNQFGL  182  A.delafieldii
                           *  . :    .                        *

209  GASYNFGVAKLSGLLQQT--KFKRDIGGDI-------------------KTNS-----YM  242  D.acidovorans
231  GGSYDFEVVKLALAYART--TDGWFGGQGYPVAVTLPSGDKFGGFGVNTFADGFKANSYM  288  B.pertussis
195  VGGYDHDALYASVAVQQQDAKLAWPDDNSH-----------------NSQTEVATTVAYR  237  N.gonorrhoeae
200  VSGYDNDALHASVAVQQQDAKLV-EDNYSH-----------------NSQTEVAATLAYR  241  N.meningitidis
183  RALYTYGAFTVGGYYQRD--KNAYVLNGGA-------------------RNNIRLAGAYT  221  A.delafieldii
      . *   .   .    :   .                            :     *

243  LGASAPVGGVGEVKLQYALYDQK--AIDSKAHQITLGYVHNLSKRTALYGNLAFLKNKDA  300  D.acidovorans
289  VGLSAPIGGASNVFGSWQMVDPKLTGGDEKMNVFSLGYTYDLSKRTNLYAYGSYAKNFAF  348  B.pertussis
238  FGNVTPRVSYAHGF--KGSVYEA--NHDNTYDQVVVGAEYDFSKRTSALVSAGWLQEGKG  293  N.gonorrhoeae
242  FGNVTPRVSYAHGF--KGSFDDA--DLSNDYDQVVVGAEYDFSKRTSALVSAGWLQEGKG  297  N.meningitidis
222  MGASEFHVNVG-----RANSYKN--VSDSAATQYTLGYNYNLSKRTKLYGYYTHINNDRN  274  A.delafieldii
     .*        .                ..      :*  :::****         ::

301  STLGLQAKGVYAGGVQAGESQTGVQVGIRHAF  332  D.acidovorans
349  L---------------EDAKSTAVGVGIRHRF  365  B.pertussis
294  ---------------AEKFVSTAGGVGLRHKF  310  N.gonorrhoeae
298  ---------------ENKFVSTAGGVGLRHKF  314  N.meningitidis
275  ASYGVGAAG---------ADFSSVAVGVRHNF  297  A.delafieldii
                      :.  **:** *
```

Figure C.3.: Multiple sequence alignment among anion-selective porins of β-proteobacteria group. Conserved E58 reidue is highlighted in red color box. The sequence alignment was generated using ClustalW [269]

D. Supporting Information for Chapter 6

Transport of Ionic Liquids in Aqueous Solutions Through OmpF

Reproduced with permission from the article by Modi, N.; Singh, P. R.; Mahendran, K. R.; Schulz, R; Winterhalter, M; and Kleinekathöfer, U., "Probing the transport of ionic liquids in aqueous solution through nanopores", *J. Phys. Chem. Lett.*, **2011**, 2(18), pp 2331-2336 (DOI: 10.1021/jz201006b).

Experimental details

The conductance was measured using the lipid bilayer technique. Solvent-free black lipid bilayers were formed according to the classical Montal-Mueller technique [233, 235]. For membrane formation we used 1, 2-Diphytanoyl-sn-Glycero-3-Phosphatidylcholine (DPhPC) (Avanti Polar Lipids, Alabaster, AL). A Teflon cell with an approximately 60-μm diameter aperture in the 25-μm-thick Teflon partition was placed between the two chambers of the cuvette. 1 M 1-butyl-3-methyl-imidazolium chloride (BMIM-Cl), 10 mM MES, pH 6 was used as an electrolyte and added to both sides of the chamber. For single channel measurement, small amount of porins from a diluted stock solution of 1 mg/ml, was added to the cis-side of the chamber. Spontaneous channel insertion was usually obtained while mixing the contents of the chamber under applied voltage. Membrane current was measured through commercially available Ag/AgCl electrodes (World Precision Instruments, Sarasota, FL). One electrode was used as ground (cis) and the other connected to the headstage of an Axopatch 200B amplifier (Axon Instruments, Foster City, CA), allowing the application of adjustable potentials across the membrane. Conductance measurements were performed using an Axopatch 200B amplifier in the voltage clamp mode. The ion current was digitized by an Axon Digidata 1440A digitizer and, controlled by the Clampex 10.0 software. The data was analyzed using the Clampfit 10.0 software (Molecular Devices, Sunnyvale, CA).

Simulation details

Bulk simulations

As in previous simulations for the KCl bulk conductivity [25, 27], a cubic water box with a side length of 42 Å was used (see Figure 1b). To obtain a 1 M BMIM-Cl solution with roughly 2,200 water molecules, 41 $BMIM^+$, and 41 Cl^- ions were inserted. Furthermore, periodic boundary conditions were employed and the electrostatics were determined using the particle-mesh Ewald method. Furthermore, the van der Waals potential was evaluated with a cutoff of 12 Å and a switching distance of 10 Å. The time step was set to 1 fs. While the non-bonded forces were evaluated every 2 fs, the electrostatic forces were determined every 4 fs. Bond constraints using the SHAKE algorithm were applied to all hydrogen atoms of water as all the tested water models were parametrized for a rigid geometry of the water molecules. Temperature control was gained by a Langevin thermostat which acts only on a selection of atoms. For the bulk simulations, this selection contained only the oxygen atoms of the water molecules with a damping constant of 0.4 ps^{-1} [25, 27]. Simulations were performed at different temperatures ranging form 10 °C to 60 °C, i.e.,

the same temperature range as in the experiments. Unlike equilibrium MD simulations, simulations for ion conductance calculations require the application of an external electric field. In the present work, a homogeneous external field E was applied in the z direction proportional to the voltage V, $E = V/L_z$ with the system length L_z in z direction normal to the membrane.

For the bulk simulations, the system was equilibrated for 1 ns in the NpT ensemble, followed by a 1 ns NVT ensemble equilibration run with an electric field corresponding to an applied voltage of 0.4 V. The ions leaving the simulation box due the applied field re-enter from the opposite side of the simulation box due to the periodic nature of the system setup. The length of the production runs was 4 ns. In first test simulations, we analyzed the $BMIM^+$ CHARMM force field [241]. The imidazole ring maintained its planar ring structure, major structural fluctuations were observed only in the butyl side chain and otherwise the molecular structure and fluctuations seem reasonable.

Pore simulations

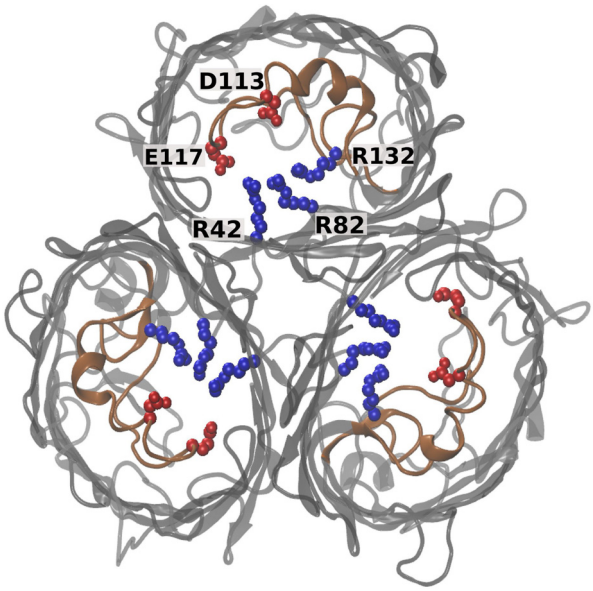

Figure D.1.: Top view of OmpF trimer with highlighted constriction zone (red: negatively charged residues D113 and E117; blue: positively charged residues R42, R82 and R132; orange: loop L3) The figure was generated using VMD [181].

A trimer of the OmpF channel protein [236] (protein data bank code: 2OMF)was embedded into a palmitoyloleoyl-glycero-phosphathidylethanolamine (POPE) lipid bilayer, which was constructed from pre-equilibrated patches using VMD [181]. The protonation states of the residues in the channel were chosen according to Im and Roux [240]. In the membrane plane, the simulation box had a hexagonal shape. The sizes of the two systems

with the different water models varied marginally. Both have a maximal breadth of 65 Å within the membrane plane. In the direction normal to the membrane the height is 86 Å for the TIP3P system and 83 Å for the TIP4P-Ew system. While the TIP3P system contains about 89,000 atoms, the latter system contains about 97,000 atoms, since the TIP4P-Ew water model includes an extra dummy atom. Both systems contain 1 M BMIM-Cl and were neutralized by adding 30 $BMIM^+$ counter ions to compensate for the extra charges of the protein. Similar system sizes were previously probed and used to study the transport of KCl through the same membrane pore [27, 28]. The simulation parameters are as described above for the bulk calculation except for the Langevin damping with a constant of 1.0 ps^{-1} which was applied to the heavy atoms of the lipids only. The system was equilibrated for 1 ns in a NpT ensemble, followed by a 1 ns equilibration run in a NVT ensemble. Production runs with a voltage of 1 V across the simulation box had lengths of 30 ns. These Simulations have been performed at different temperatures ranging from 5 °C to 45 °C in accordance with the temperature range used in the experimental measurements.

Computation of the current

The ionic current $I(t)$ in a system of length L_z can be determined by summing up the movement of all charges i projected on z axis via

$$I(t) = \frac{1}{L_z} \sum_{i=1}^{N} q_i \frac{z_i(t + \Delta t) - z_i(t)}{\Delta t} \tag{D.1}$$

The drift of the center of mass is taken into account in the determination of the current. The conductance is calculated as the ratio of current and applied voltage.

Ion specific pathways

We analyzed the average pathways followed by the ions in the course of one 30 ns long simulation with the applied external field at 25 °C. Average pathways for individual ion types were deduced by averaging out the positions of ions. A similar kind of study has been performed on a KCl solution which showed separate pathways for K^+ and Cl^- through a monomer of OmpF [27, 240]. For the same system, Roux and coworkers recently showed the existence of such selective cationic and anionic pathways near the constriction zone via anomalous X-ray diffraction technique [270]. As shown in Fig. D.2, the ions move in a screw-like fashion through the β barrel of OmpF with clearly separated pathways in the BMIM-Cl system as well. In the constriction zone, the separation is caused

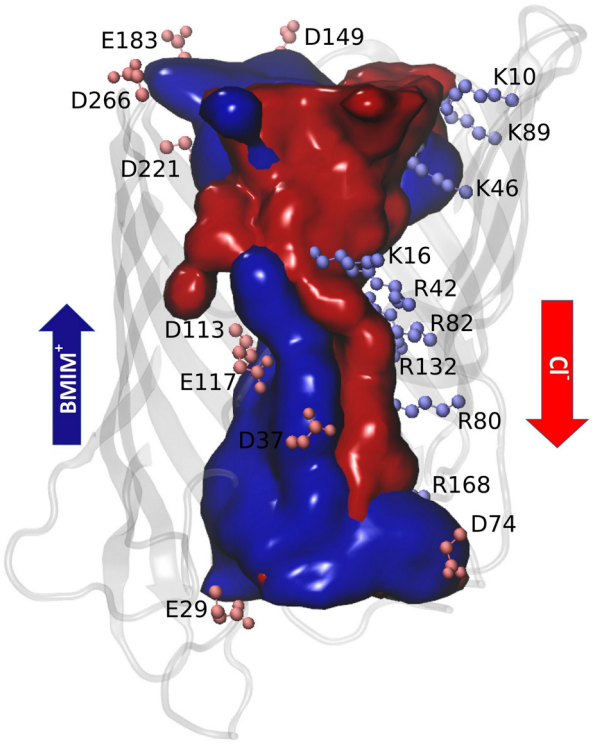

Figure D.2.: Average pathways followed by ions in the course of one simulation. Blue surface: $BMIM^+$, Red surface: Cl^-, Charged residues along the channel surface responsible for such distinguished pathways for the ions are shown. Positively charged and negatively charged residues are shown in blue and red ball-stick model, respectively. Arrows on both sides of the pore indicate the direction of the individual ion flow in the simulation.

by the strong transversal electric field generated between two acidic residues (D113 and E117) on the L3 loop and the arginine cluster (R42, R82 and R132) on the opposite wall of the β sheets. On the extracellular side of the constriction zone, some of the negatively charged residues like E29, D37 and D74 influence the pathway of $BMIM^+$ additionally. Similarly, positively charged residues like R167 and R168 play an important role for the local Cl^- pathway. On the periplasmic side of the constriction zone, negatively charged residues like D149, D221, D266, E181 and E183 along with positively charged residues like K10, K16, K46 and K89 lead the respective ions in a screw-like fashion, Hence, not only the charges in the constriction region play an important part of the ion pathways but many charged residues lining the inner pore walls.

E. Feature article

Computational modeling of ion transport through nanopores

Partly included in the introductory Chapter 1.

Reproduced from the feature article by Modi, N.; Winterhalter, M; and Kleinekathöfer, U., "Computational modeling of ion transport through nanopores", *Nanoscale*, **2012**, 4(20), pp 6166-6180 (DOI: 10.1039/C2NR31024D) - by permission of The Royal Society of Chemistry.

Nanoscale

Dynamic Article Links

Cite this: *Nanoscale*, 2012, **4**, 6166

www.rsc.org/nanoscale

FEATURE ARTICLE

Computational modeling of ion transport through nanopores

Niraj Modi, Mathias Winterhalter and Ulrich Kleinekathöfer*

Received 27th April 2012, Accepted 30th May 2012
DOI: 10.1039/c2nr31024d

Nanoscale pores are ubiquitous in biological systems while artificial nanopores are being fabricated for an increasing number of applications. Biological pores are responsible for the transport of various ions and substrates between the different compartments of biological systems separated by membranes while artificial pores are aimed at emulating such transport properties. As an experimental method, electrophysiology has proven to be an important nano-analytical tool for the study of substrate transport through nanopores utilizing ion current measurements as a probe for the detection. Independent of the pore type, *i.e.*, biological or synthetic, and objective of the study, *i.e.*, to model cellular processes of ion transport or electrophysiological experiments, it has become increasingly important to understand the dynamics of ions in nanoscale confinements. To this end, numerical simulations have established themselves as an indispensable tool to decipher ion transport processes through biological as well as artificial nanopores. This article provides an overview of different theoretical and computational methods to study ion transport in general and to calculate ion conductance in particular. Potential new improvements in the existing methods and their applications are highlighted wherever applicable. Moreover, representative examples are given describing the ion transport through biological and synthetic nanopores as well as the high selectivity of ion channels. Special emphasis is placed on the usage of molecular dynamics simulations which already have demonstrated their potential to unravel ion transport properties at an atomic level.

1 Introduction

Nanopores, both biological as well as synthetic, are pores with a diameter in the range of nanometer or often even below.[1] Channels of this size are ubiquitous in nature but these days they can also be manufactured artificially. The scientific interest in

School of Engineering and Science, Jacobs University Bremen, Campus Ring 1, 28759 Bremen, Germany. E-mail: u.kleinekathoefer@jacobs-university.de; Fax: +49 421 200 49 3523; Tel: +49 421 200 3523

Niraj Modi

Niraj Modi is currently doing his PhD in the field of computational biophysics at Jacobs University Bremen, Germany, since 2010. He studied Pharmaceutical Sciences and graduated in B.Pharm. from North Gujarat University, India (2006) and M.S. (Pharm.) from National Institute of Pharmaceutical Education and Research, Mohali, India (2008). His research interests include transport of ions through membrane proteins, protein modeling and structure-based drug design.

Mathias Winterhalter

Mathias Winterhalter is Professor of Biophysics at Jacobs University Bremen. He received his PhD in theoretical physics from the Free University of Berlin in 1988. After post-doctoral training at National Institutes of Health in Bethesda, at the Centre de Recherche Paul Pascal in Bordeaux and the Biozentrum in Würzburg and Basel, he became Professor of Biophysics in Toulouse. In 2003 he joined the faculty in Bremen. His research interests include molecular transport in particular antibiotic translocation across porins from the outer membrane of bacteria.

both types of nanopores has been enormous in the last few years due to their importance and possible applications.[1,2] In biological systems different compartments are separated by membranes and various substances need to be exchanged between them in a rather controlled manner. This is achieved by passive channels or active pumps working against certain gradients. Due to the large variety of ions and substances to be transported, many different biological nanopores exist.[2–4] Understanding the functional role and mechanism of biological pores and ion channels is of crucial physiological importance to develop new diagnostic tests for diseases and to discover novel drug molecules. Using man-made nanopores one wants to mimic some of the functions of their biological counterparts but also go beyond[5,6] including interesting applications in the field of nanofluidics.[7] Among the envisioned applications are desalination, very specific ion sieves,[2] sensors for biological agents[8] as well as sequencing of DNA or RNA.[9,10] Especially the later application has driven the field of nanopores considerably in the last few years.[11,12]

Despite the obvious differences between biological and artificial nanopores, there are several important common features which define their function to a large degree.[2] Due to the small diameter, the ratio of interior surface to volume is very high, *i.e.*, the smaller the radius the larger the ratio. This makes artificial channels ideal candidates for nanofluidic devices and biological channels can be viewed as such in many features.[7] Looking at the interactions between nanopores and ions/substrates, it is necessary to identify the characteristic length scales of various intermolecular forces. The length scales of electrostatic as well as steric and van der Waals interactions are often within the range of the nanoscale confinements provided by the pores. Hence all these interactions together can perturb the collective behavior of substrates and ions in the pore. Analysis of this behavior of ions and other molecules in nanoscale confinements is crucial to understand the functioning of biological pores and channels and to engineer synthetic pores for various applications.

Recently with the development of the patch-clamp technique,[13] electrophysiological measurements have been established as a standard tool in the field of nanopore analytics where ion currents are used as a probe to sense the transport of molecules. Fig. 1 depicts one such schematic experimental setup along with an all-atom model of the corresponding molecular dynamics (MD) system. Time resolution and sensitivity of such measurements have been drastically improved, *e.g.*, by miniaturization of the experimental setup.[4] Individual biological pores can be reconstituted into artificial membranes leading to very clear measurements compared to those involving a large number of channels at the same time.[14] Solid-state nanopores are, *e.g.*, manufactured using highly focused ion beams in different materials such as silicon-based insulators or metal-oxide semiconductors.[5]

The theoretical modeling of ion transport through nanopores dates back to the seminal works by Nernst[15] and Planck.[16] The Poisson–Nernst–Planck (PNP)[17–19] theory is a drift and diffusion continuum theory. It can be used to determine ionic currents though its applicability can be problematic in constricted volumes such as the interior of nanopores. Going one step ahead in the hierarchy of detailed descriptions of the system, the Brownian Dynamics (BD) approach treats the ions as particles while protein and water are usually still assumed to be continuous and rigid.[20,21] With the advancement of computer power, fully atomistic representations of molecular systems were realized in MD simulations.[22,23] This approach is based on the classical force field approximation and describes the movement of all individual ions but also water, protein and membrane atoms. This article will focus on the theoretical and computational approaches widely used to study ion transport through nanopores together with possible implications and limitations associated with the various methods. A series of examples will be discussed demonstrating several ion transport properties through biological and solid-state nanopores as well as ion channels with a special focus on MD simulations.

2 Computational approaches to ion transport through nanopores

Various theories have been developed to determine the ion transport through nanopores. In general there is a trade-off between the computational resources needed and the details as well as the accuracy which can be extracted from the respective

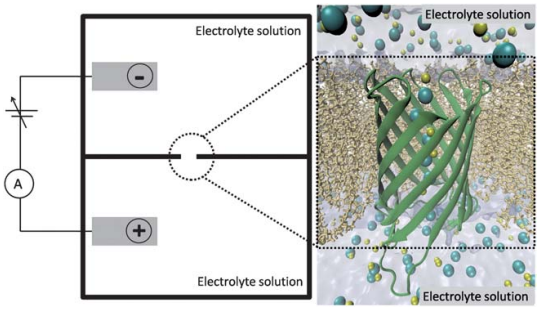

Fig. 1 Experimental setup of ion transport measurements through nanopores together with a corresponding all-atom model being used in molecular dynamics simulations.

Ulrich Kleinekathöfer

Ulrich Kleinekathöfer is Professor of Theoretical Physics at Jacobs University Bremen since 2006. He received his PhD in physics from the University of Göttingen after doing his research on atomic interactions at the Max-Planck-Institute for Fluid Dynamics. Following a postdoctoral training at the Weizmann Institute of Science in Israel, he moved to Chemnitz University of Technology where he obtained his habilitation degree in 2002. His research interest includes classical as well as quantum dynamical studies of large molecular complexes especially of biological macromolecules with applications ranging from ion transport to photosynthesis.

method. With the theoretical modeling of ion transport one attempts, among others, to tackle the following questions:

- What is the detailed mechanism of ion passage?
- Where are binding sites located in the pore?
- Is there any ion selectivity of the nanopore?
- Which are the rate-limiting steps for the transport?

The methods discussed below can be used individually or, to some extent, in a combination with each other. Such a combination of methods can help to portray a better picture of ion transport by overcoming the limitations associated with a particular method. Especially one has to keep in mind the large space and time scales over which the calculations need to be performed in a converged manner.[24]

2.1 Continuum models

The main idea in continuum models is to approximate all components of the simulated system, *i.e.*, water, ions, proteins, *etc. via* a continuum. Instead of a large number of individual atoms, a system with a few continuous elements is achieved. The most well-known continuum theory for ion transport is certainly the Poisson–Nernst–Planck (PNP) scheme[17–19,25,26] which combines the Nernst–Planck and the Poisson equations. The Nernst–Planck continuum electro-diffusion theory describes the flux density $\boldsymbol{J}_\alpha$ of ion type α at position $\boldsymbol{R}$ in terms of its concentration C_α and the corresponding potential gradients[15,16,27,28]

$$\boldsymbol{J}_\alpha(\boldsymbol{R}) = -D_\alpha(\boldsymbol{R})\left(\nabla C_\alpha(\boldsymbol{R}) + \frac{C_\alpha(\boldsymbol{R})}{k_\mathrm{B}T}\nabla V_\alpha^{\mathrm{eff}}(\boldsymbol{R})\right) \quad (1)$$

with the diffusion coefficient $D_\alpha(\boldsymbol{R})$ and the effective potential V_α^{eff}. The potential, $V_\alpha^{\mathrm{eff}}(\boldsymbol{R})$, at each position $\boldsymbol{R}$ is the sum of potentials excluding ions from the interior of the pore or membrane and an electrostatic potential $\phi(\boldsymbol{R})$. The later one is determined by solving the Poisson equation

$$\nabla\left[\varepsilon(\boldsymbol{R})\nabla\phi(\boldsymbol{R})\right] = -4\pi\left(\rho_\mathrm{P}(\boldsymbol{R}) + \sum_\alpha C_\alpha(\boldsymbol{R})\right) \quad (2)$$

where $\varepsilon(\boldsymbol{R})$ denotes the position-dependent dielectric constant and $\rho_\mathrm{P}(\boldsymbol{R})$, the charge density of the pore. Solving these two coupled differential equations, the Nernst–Planck equation, eqn (1), and the Poisson equation, eqn (2), in a self-consistent manner yields the electrostatic potential, the concentration, and the flux of the ions. The parameters for the PNP calculations are often obtained empirically but in some cases have been, at least partially, extracted from atomistic simulations.[27,29] While ions and water molecules are always treated as a continuum, the channel is sometimes approximated to various extents in its form and charge distribution. To give some examples, the PNP method was applied to study the ion transport through the outer membrane protein F (OmpF),[27,30–32] the voltage-dependent anion channel (VDAC),[29] a calcium channel,[33] the gramicidin channel,[18,34] the protegrin transmembrane pore[35] and also synthetic nanopores.[36–39]

However, a simplistic representation as in the PNP approach has several limitations and various questions regarding the applicability of the continuum based method in the nanoscale systems have already been raised.[19,40] The PNP theory works best for wide aqueous pores and may cause problems for regions of constricted volume. Furthermore, the finite volume of the ions which becomes important for narrow nanopores is neglected.[41] Additionally, exclusion of non-electrostatic interactions between ions, overestimation of the shielding effect by counterions inside a pore[42,43] and lack of the description of dielectric boundary effects are a few shortcomings associated with the method. Nevertheless, the PNP method has shown its usefulness to study ion transport at a relatively small computational cost.[44]

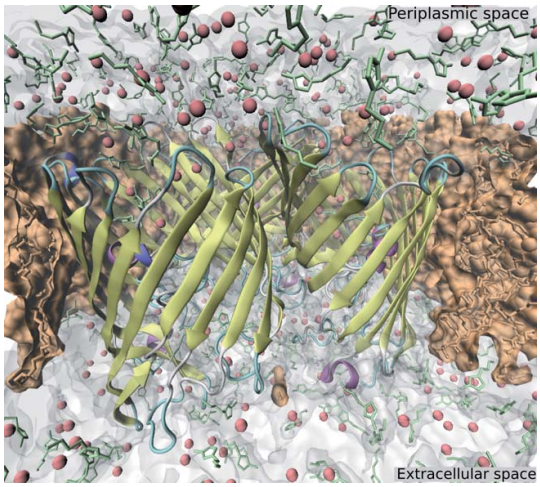

Fig. 2 Typical MD simulation setup for ion transport through nanopores. The OmpF nanopore is shown in a yellow cartoon representation and water as a gray surface. Moreover, the $BMIM^+$ ions are displayed using a green stick delineation and the Cl^- ions as pink spheres. The figure has been generated using VMD.[65]

In addition, a large number of extensions of the PNP approach has been developed over the years. One of them is the density functional theory-PNP method in which the ions are described as charged hard spheres with excess chemical potentials computed from equilibrium density functional theory.[33,45,46] Its efficiency has been tested especially for the ryanodine receptor calcium channel to study the energetics of Ca^{2+}-binding selectivity over the monovalent cations.[33] Another theory, the Energetic Variational Analysis (EnVarA), has been developed by Eisenberg and co-workers.[47] This variational model was developed to deal with complex fluids including flowing interacting sub-elements which can be more complex than hard sphere ions. Furthermore, in yet another complementary approach one aims at determining structural features of nanopores from measurements of its function, namely current voltage curves in different solutions. From a mathematical point of view, this is an inverse problem.[48,49] At the same time one can employ this approach to design channels with desirable properties such as a particular selectivity.[49]

2.2 Brownian dynamics

The Brownian dynamics (BD) method lies in between the dichotomy of detailed all-atom MD simulations and continuum-based approaches. In the BD scheme, the ions and nanopores are treated explicitly while the solvent molecules are described

implicitly. The interactions of the solvent molecules with the rest of the system are modeled *via* frictional and stochastic forces. These two latter forces are not independent from each other but interrelated *via* the fluctuation–dissipation theorem.[50] The equation of motion is given by a Langevin equation[20,21,25,26]

$$m_i \frac{\mathrm{d}^2}{\mathrm{d}t^2} \boldsymbol{R}_i(t) = \boldsymbol{F}_i(t, \boldsymbol{R}) - m_i \gamma_i \dot{\boldsymbol{R}}_i(t) - \xi_i(t) \quad (3)$$

where ξ_i denotes the stochastic forces and $\boldsymbol{F}_i$ the systematic forces. The term $m_i\gamma_i\dot{\boldsymbol{R}}_i$ denotes the frictional forces with m_i being the mass, γ_i being the reciprocal of the relaxation time and $\dot{\boldsymbol{R}}_i$ the velocity of the i^{th} particle. The systematic force $\boldsymbol{F}_i$ accounts for electrostatic forces due to the interactions between the charged particles and with a possible external potential.

Several biological pores such as OmpF,[27,51,52] potassium channels,[53,54] α-hemolysin,[55] the VDAC,[56] and synthetic nanopores[57] have been investigated utilizing BD simulations. Using this method, one can obtain current–voltage and conductance–concentration curves at a reasonable computational cost. Furthermore, these results can be directly compared to experimental measurements which provide the basis for the validation of this kind of simulations. On the other hand, limitations associated with the representation of the rigid protein–water interface and the continuum solvent should be considered carefully. Generally, constant dielectric fields are used throughout the system to represent the water implicitly. In reality, the local dielectric constant of water may vary considerably depending on the environment. For example, water molecules present in the pore may have altered dielectric constants due to charges and confinements. In such cases, environment-dependent dielectric constants can correctly account for electrostatic screening effects. As a possible extension, one might extract local dielectric constants from MD simulations and subsequently employ them in BD calculations.[27,56]

As a promising augmentation, an atomic-resolution BD method has recently been developed.[58,59] For this scheme one needs to determine the three-dimensional potential of mean force (PMF) maps at high resolution from all-atom MD simulations. This approach has been applied to measure ion currents during DNA translocation.[59] It has been shown that the atomic-resolution BD method produces results with orders of magnitude less computational effort than all-atom MD. At the same time, the ion distributions and ion currents predicted by both methods are in agreement.[59] Though the numerical effort for the 3D PMF maps is very large, the speedup is tremendous if viewed in connection with the obtained accuracy. This approach seems to be very promising and will most likely be applied to other systems in the near future as well.

As an alternative to the BD approach one might view the dynamic Monte Carlo scheme,[60] an extension of the equilibrium Monte Carlo theory. In this approach a randomly chosen ion from the ionic solution is moved to a new random position within a maximum displacement of its previous position. The paths followed by the ions constructed in such a manner resemble those of MD or BD ion trajectories.[60]

2.3 Molecular dynamics

Molecular Dynamics (MD) simulations have become a very valuable tool for biophysical and biochemical analysis as well as prediction over the last few years. In this approach, all atoms in the system are treated as classical particles moving under the influence of the Newton's classical equations of motion[22]

$$m_i \frac{\mathrm{d}^2}{\mathrm{d}t^2} \boldsymbol{R}_i(t) = \boldsymbol{F}_i(t) = -\nabla V\big(\boldsymbol{R}_i(t), \ldots, \ \boldsymbol{R}_N(t)\big) \quad (4)$$

where $\boldsymbol{R}_i$ and m_i denote the position and the mass of the atom i, respectively, and N the total number of atoms in the system. The force $\boldsymbol{F}_i$ acts on atom i and is determined as the gradient of the potential energy, $V(\boldsymbol{R}(t))$, of the system. The empirical force fields describe the potential energy of the system in terms of the interactions between the atoms. In its functional form, the potential energy function has two kinds of parameters, bonded and non-bonded ones. The former class consists of potentials for bond lengths, bond angles, improper dihedral angles as well as torsional angles. The later class contains the non-bonding terms, *i.e.*, the electrostatic as well as the van der Waals interactions. The parameters for the force fields are obtained *via* quantum-mechanical calculations which can be further improved by fitting to experimental data. Among the force fields commonly used in MD simulation of biomolecules are CHARMM,[61] AMBER,[62] GROMOS,[63] and OPLS.[64] The various force fields may differ in the functional form of individual terms and especially in the parametrization procedures for the large number of parameters involved.

A typical MD simulation setup to study ion transport through nanopores is depicted in Fig. 2. One of the biggest advantages of the MD technique is the readily available time-dependent atomic detail of the molecular system making an analysis of the structure–function relationship feasible. Unfortunately this advantage comes at a large computational cost. Moreover, one has to keep in mind that various biological processes occur at time scales ranging from femtoseconds over milliseconds to seconds with, *e.g.*, protein folding, being on the slower side of this spectrum. This has to be seen in connection to the usual MD time step in the femtoseconds range to account for fast vibrational modes such as hydrogen bond vibrations. With the present computational resources, simulations in the range of a few hundreds of nanoseconds are the common practice[66] which may be extended up to several microseconds.[67]

Although MD simulations have been very successful providing microscopic details of biological processes, several limitations associated with the method have to be taken into account. Standard force fields used in biomolecular simulations account for electrostatic interactions in terms of fixed, usually atom-centered, charges and the corresponding interactions are often based on a simple pairwise-additive models. However, real physical systems undergo substantial polarization when placed into a medium with a high dielectric constant such as water or in the presence of an external applied electric field. Polarizable force fields are available to explicitly account for many-body induced polarization effects but they are computationally more expensive.[68,69] Modeling a pH value is another challenge in MD simulations. Regularly, the effect of a certain pH value is indirectly incorporated into the system setup by calculating the pK_a of ionizable residues.[70] The protonation states of these residues are fixed according to the pK_a results and usually not changed during a MD simulation. Recent extensions address this issue such as the λ dynamics in which the titration coordinate λ is

driven by generalized forces between the protonated and deprotonated states.[71,72]

Ion transport through nanopores is normally driven by a potential difference across the membrane. In living cells, such potential differences across membranes are generated by ionic concentration gradients maintained by ion channels and transporters. In electrophysiological measurements, artificial potential gradients are generated using an electrode-based experimental setup. Therefore the question arises on how to apply an electrostatic potential difference across the membrane in MD simulations. The generation of an ionic concentration gradient across the membrane and in turn a potential difference is not a straightforward task considering the periodic boundary conditions used in the simulation. These boundary conditions are regularly applied to avoid finite-size effects. One method to address this problem is to build a system comprising of two parallel lipid membranes, the so-called twin-bilayer approach, to generate two separate bulk phases.[73,74] An electrostatic potential difference in such a system setup can be generated by different ionic concentrations in the two separate bulk phases. This kind of approach increases the system size considerably and hence the computational cost. Alternatively, a slightly less expensive approach can be used in which the second membrane is replaced by a vacuum slab separating the two bulk phases.[75] In both above approaches, it is troublesome to maintain a uniform transmembrane potential over a finite simulation time as even one permeating ion can change the electrostatic potential considerably.[75] In practice, one has to continuously monitor the potential difference across the membrane and adjust charge imbalances to avoid any large deviations in the transmembrane potential. Recently this problem has been tackled by a new scheme in MD simulations[76] which has been applied in BD simulations earlier.[77] In this approach, the ion concentration in each compartment and thus the electrostatic potential is regulated by exchange of ions and water molecules between different compartments.[76]

An alternative approach is to apply a homogeneous electric field E throughout the entire system sometimes called the tinfoil approach.[78,79] In this scheme one effectively applies an additional force $q_i \cdot E$ to all charged atoms with charge q_i as if they would be subject to a homogeneous electric field E. This field E is usually applied perpendicular to the membrane plane (z direction) and is proportional to the applied voltage V, *i.e.*, $E = V/L_z$, with the system length L_z in z direction. In the field of MD simulations for membrane proteins, this approach was first used by Aksimentiev and Schulten[23] to quantitatively study the ion transport through an α-hemolysin nanopore. Subsequently, this scheme has been successfully employed to study ion transport in diverse systems.[67,80–88] Furthermore, the validity of this approach has recently been tested for several examples.[89,90] Moreover, also the transport of charged substrate molecules can be accelerated using an applied electrical field.[11,91,92] Since ion currents through nanopores are usually in the sub-nA to nA range only a limited number of charges permeate through the nanopore in a simulation time of a nanosecond. To obtain statistically meaningful numbers of ion permeation events, the applied voltage in simulations is often in the range of 1 V and therefore a few times larger than the usually applied 50–150 mV in biological nanopore experiments.

A completely different approach especially to obtain ion currents through very narrow nanopores is to employ rate theories using simulated PMFs (see ref. 93 and references therein). Various schemes for the calculation of the PMFs using MD simulations exist[94] and have been applied to the ion transport through nanopores.[95–103] The PMF incorporates all governing forces for the ion passage and the mechanisms of ion permeation can be studied with respect to important reaction coordinates, *viz.*, the position of ions inside the pore, ion hydration, *etc.* Approaches based on probability distributions and histogram analysis[104,105] using umbrella sampling[106] and more recently developed methods like Adaptive Biasing Force (ABF)[107,108] and metadynamics[109,110] are used to calculate PMF profiles and to understand the energetics of ion transport through nanopores.

3 Bulk conductivity of ionic solutions

In the following the opportunities and challenges of MD simulations for determining ion currents are detailed and discussed. To get started we first focus on the ion conductivity in the bulk phase. At the same time these bulk simulations provide an important test ground for the MD simulations of ions in water. As has been shown,[23] using periodic boundary conditions a cubic water box of a side length of ~4 to 5 nm is large enough for bulk simulations of ion conductivity. Applying a homogeneous electric field E in z direction, one can subsequently determine the ionic current by summing up the movement of the charges projected onto the z direction *via*[23,78]

$$I(t) = \frac{1}{L_z} \sum_{i=1}^{N} q_i \frac{z_i(t + \Delta t) - z_i(t)}{\Delta t}. \quad (5)$$

The bulk conductivity is then defined as the ratio of computed current and applied voltage.

Of critical importance for the bulk conductivity are the force fields for the ions, for the water molecules and their interplay. These force fields can be benchmarked by comparing the calculated values for the bulk conductivity with the experimental ones. Ionic force fields usually contain two adjustable parameters, namely the Lennard-Jones diameter and the interaction strength. One can find a plethora of parameters in the literature for various ion types including recent improvements.[68,111–119] In principle these empirical force field parameters could further be benchmarked using *ab initio* MD simulations though these are computationally expensive and do have some problems on their own.[120] Moreover, the inclusion of polarization is still costly in terms of the computation for large systems. Corresponding force fields and schemes are still under development.[68,69] Care has to be taken when mixing parameters from different standard force fields in simulations. Standard combinations of ionic and water force fields have recently been benchmarked with respect to the excess electrochemical potential differences of single ions at finite ionic strength.[121] It was shown that certain combinations do yield accurate results while others do not.[121]

As the main focus here is on the movement of ions under the influence of an electric field, the bulk conductivity serves as an important test bed for the force fields before studying the transport through nanopores. Moreover, the direct comparisons of experimental and simulated bulk conductivities can provide a temperature and concentration-dependent correction factor. If

appropriate, this can subsequently be used to correct pore conductance simulations for inaccuracies already rising for bulk calculations.[83,86] Results for the bulk conductivity calculations as shown in Fig. 3 using the CHARMM force field clearly show a dependence on the ion concentration,[86] temperature,[86–88] as well as on the water model.[88] Up to KCl concentrations of 1 M, the bulk conductivities are in excellent agreement with experiments (Fig. 3b).[86] Above this concentration, the theoretical conductivities using the standard CHARMM force fields for the ions and TIP3P water get saturated. This saturation indicates a possible problem of correctly representing ion pairing effects at very high concentrations in the simulations. With respect to the temperature dependence, the best agreement has been obtained at around 25 °C which is not very surprising considering the fact that most of the force field parameters are optimized in this temperature range.[86] The choice of the water model is also a critical issue in conductivity simulations. Presently, none of the existing water model is reliable enough to reasonably reproduce all experimental measurements. Various water models have been developed which are optimized with respect to certain properties. As one studies the transport properties of ions in this case, the (self-) diffusion properties of the different water models do play a significant role in the conductivity calculations as can be seen in Fig. 3c and d. Data for different ion types also suggest that the choice of the appropriate water model depends on the considered ion type.[86,88] In addition, the use of flexible or rigid bonds in water models such as the TIP3P variant likewise influences the conductivity.[85]

4 Biological nanopores

Amongst the various studied biological nanopores, α-hemolysin is the most widely used one in nanopore analytics.[5] It has been employed in nanopore-based DNA sequencing and as a tool to study the transport of various substrates including peptides, proteins as well as small molecules.[5] Another class of membrane proteins, the so-called porins, has been investigated thoroughly concerning the transport of various substrates. These porins can be either non-specific or solute specific, *e.g.*, for sugar and phosphate.[3] One of these porins, OmpF, has been studied to understand its role in transport of antibiotics through the outer membrane of bacteria both experimentally as well as computationally.[122–125] Another porin that has shown a great potential in molecular sensing and especially in DNA sequencing is MspA.[10]

All the above-mentioned nanopores as well as various other ones have very stable pore forming structures. In addition, the transport properties of this kind of pores can be engineered *via* mutating individual charged residues while still maintaining the overall stability and pore-forming capability. These structural features make them ideal candidates in the field of nano-analytics and to be investigated by electrophysiological experiments. In such experiments, ion conductance measurements are used as a probe to detect the transport of substrates through nanopores. During the passage of a substrate molecule, the nanopore gets blocked completely or to a (large) fraction altering the ion transport process compared to the open pore. This can be seen in time-dependent electrophysiological measurements in the form

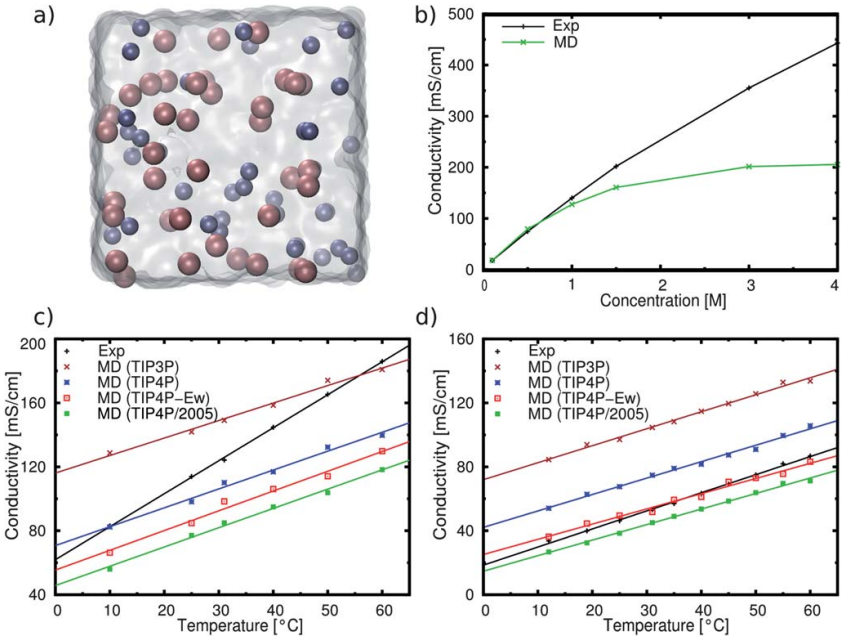

Fig. 3 Simulations for bulk conductivity. (a) A typical system setup for bulk conductivity simulations. The ions are shown as spheres and the water is indicated by the surface. (b) Concentration dependence of the KCl bulk conductivity.[86] (c) Temperature and water model dependence of the bulk conductivity for 1 M KCl. (d) Temperature and water model dependence of bulk conductivity for 1 M BMIM-Cl.[88]

of current blockages.[4] From the theoretical point of view, one can split the description of this process into two separate problems: the ion transport through the pores without substrates and the translocation of a substrate molecule. In the present article we focus only on the first step, *i.e.*, the ion transport dynamics. To this end, one aims at a reasonable agreement between experimental and simulated conductance values by modeling the interactions of the ions with the nanopores as accurately as possible. Below it is shown how fully atomistic simulations can help to unravel molecular details and to provide a comprehensive picture of the ion transport dynamics through nanopores such as ion specific pathways and ion pairing.

4.1 Transport of mono-atomic ions

The first biological nanopore for which the ion conductivity was determined using applied field MD simulations was α-hemolysin.[23] Simulations at different applied voltage biases revealed an asymmetric current–voltage curve indicating an ion current rectification (ICR).[23] This feature arises due to the dependence of the current value on the polarity of the applied bias. It was recently shown that the magnitude of the rectification also depends on the type of the cation by investigating different alkali chloride solutions for current–voltage relationships.[126] This kind of cation-dependence was attributed to different affinities of the respective cations to charged residues positioned at the ends of the nanopore. Furthermore, the ion selectivity of the pore was found to be dependent on the polarity of the applied voltages. At positive applied biases, the channel was found to be cation selective while anion selectivity was observed for negative bias voltages.[23] In addition, it was reported that the ion conductance was severely affected by the protonation state of an individual residue suggesting its possible role in pH assisted gating of the pore.[23]

Among other biological pores, a wealth of experimental data is available for OmpF which was also studied theoretically as shown below. Having a total length of about 5 nm, OmpF is a slightly cation selective trimer facilitating three nanopores for the transport of ions or substrate molecules.[127] Structurally it consists of sixteen β-strands forming a β-barrel. The most important structural feature is the so-called L3 loop which is folded into the pore and narrows the diameter of the pore at the constriction zone leading to an hourglass shape (see Fig. 4 inset). The interior of the pore is lined with charges and especially those in the constriction zone do have a major influence on the transport behavior. Mutations of individual amino acids have been reported to strongly influence the ion flux and selectivity.[30,51,128] In such a manner OmpF can even be made, *e.g.*, Ca^{2+} selective.[30]

Fig. 4 shows an example of the temperature-dependent conductance through OmpF. As is clearly visible MD simulations do yield results in close agreement with the experimental data though one has to note that the electrostatic potential of 1 V applied in simulations is larger than those in the experiment which are around 10–150 mV. Furthermore, one should keep in mind that at a calculated current of 1 nA in a simulation of 1 ns, only about 3 ions cross the membrane. Hence at the very least 10 ns of simulation time are necessary to obtain reasonable statistics. Having obtained a good agreement between the experimental and calculated macroscopic pore conductance, one

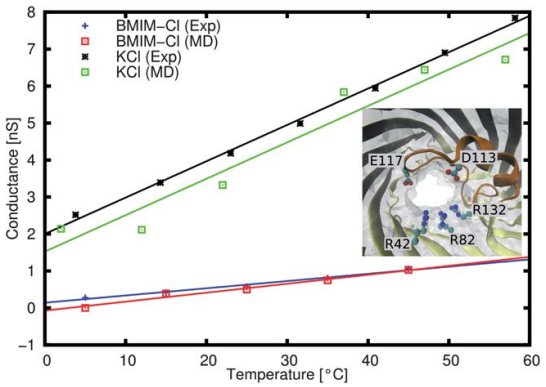

Fig. 4 Comparison between the experimental and theoretical OmpF conductance as a function of temperature for 1 M concentrations of two different electrolyte solutions, KCl and BMIM-Cl.[86,88] The inset shows the constriction zone of OmpF highlighting some charged residues.

can analyze the MD data in much more detail than the experimental data since the positions of all atoms are known during the simulations. Therefore one can attempt to understand the microscopic reasons for the macroscopic properties such as conductance. One such analysis is the determination of ion pathways as already discussed by Im and Roux using MD simulations without external fields (see Fig. 5).[27,129] The positive ions tend to be located close to negative charges at the interior of the channel walls while the negative ions are found near the positive charges of the channel walls indicating the influence of the charge distribution inside the pore on the ion-transport. Furthermore one can study, *e.g.*, the number of ion pairs within the channel compared to the bulk and its dependence on the temperature.[85]

In biological pores the internal charge distribution can rather easily be changed by single or multiple point mutations. Such engineered nanopores can have significantly different transport properties which can be explored for their enhanced applicability in stochastic sensing. For channels with an hourglass-like form such as OmpF, charges at the narrowest part of the channel, *i.e.*, the constriction zone are of most important. Table 1 shows the conductances and the corresponding ion selectivities for wildtype OmpF and two mutants in which either all positive or all negative charges (inset in Fig. 4) in the constriction zone were neutralized.[86] Furthermore, ion selectivities for mutants are depicted in Fig. 5 using averaged ion-density profiles which show the dependence of the ionic densities in the constriction region on the number and type of charged residues. It is interesting to point out that the simulations were performed before the experiments and were only later confirmed to be in good agreement with the measurements. This shows the predictive power of MD simulations which is expected to be further improved by the availability of new techniques and more computer power in the years to come.

Another biological channel similar to OmpF but slightly smaller in dimensions is the outer membrane protein C (OmpC). The same methods can be applied to this system as well and the results for smaller concentrations are surprisingly accurate as

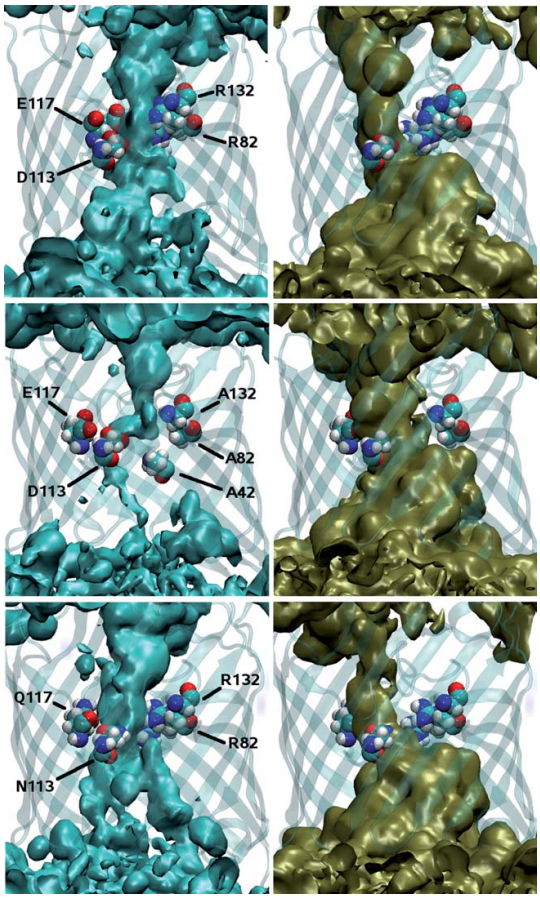

Fig. 5 Iso-density surfaces of the Cl^- (left) and K^+ densities (right) averaged over a trajectory. The top row displays the wildtype, the middle row the protein with all bases in the constriction zone mutated to neutral ones, and the bottom row with all acidic residues to neutral ones. The iso-surfaces in all subfigures do have the same iso-values. In addition, the charged or mutated residues in the constriction zone are highlighted. Figure reprinted from ref. 86 with permission from Elsevier.

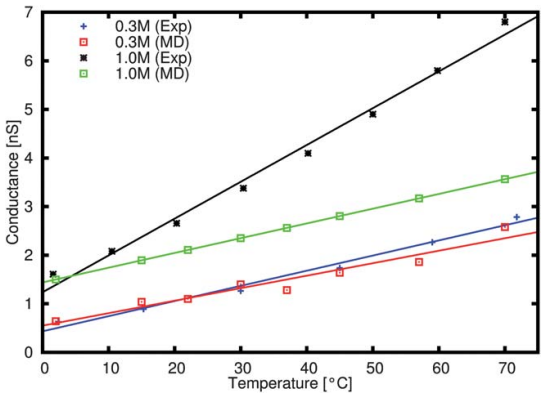

Fig. 6 Comparison between experimental and computed temperature-dependent OmpC conductances for different concentrations of KCl.[87]

shown in Fig. 6. At larger concentrations agreement is not as good as for smaller concentration especially at the higher temperatures.[87] Similar problems related to large concentrations and high temperatures were discussed in the bulk conductivity simulations above. Likewise VDAC, a mitochondrial porin, was investigated for anion selectivity and its dependence on the concentration of electrolytes, ion selective pathways, *etc.* using MD[130,131] and BD[56] simulations.

The transport of multivalent ions, especially divalent ions, *e.g.*, Mg^{2+}, Ca^{2+}, through OmpF has surprisingly found an anion selectivity while the pore is slightly cation selective for KCl.[132,133] This phenomenon is known as charge inversion (CI) which is defined as the reversal of the effective surface charge when charges at an interface attract counterions in excess of their own nominal charges. Corresponding simulations with Mg^{2+} ions observed a strong positional correlation between divalent ions and acidic groups of the nanopore.[134] This indicates a strong binding of Mg^{2+} ions to negative residues in the channel leading to the reversal of the effective surface charge and making the channel anion selective. Recent experiments with the trivalent La^{3+} ions[135] also showed a very remarkable behavior which still needs corresponding simulations.

4.2 Transport of multi-atomic ions

Recent experiments have shown an increased interest in the transport of multi-atomic ions through membrane pores. Some of those ions belong to the class of ionic liquids which have gained considerable attention in recent years due to their interesting physicochemical properties. The ionic liquid 1-butyl-3-methyl-imidazolium chloride (BMIM-Cl) has shown to drastically slowdown the transport of the substrate through nanopores such as α-hemolysin and OmpF.[14,136] This reduction in kinetics is quite interesting from an experimental point of view

Table 1 Comparison of the calculated and measured conductances G as well as selectivities S for a 1 M KCl solution at 22 °C for OmpF and its mutants. Either all positive or negatively charged residues in the constriction zone have been mutated to neutral residues. In addition, the ratio of the partial currents I_{K^+}/I_{Cl^-} obtained in the MD simulation is given. Concerning the theoretical selectivity estimates, the experimental wildtype results were used to determine a proportionality constant as described in ref. 86

	G_{MD} [nS]	G_{exp} [nS]	I_{K^+}/I_{Cl^-}	S_{exp}	S_{est}
Wildtype	3.0	4.0	1.2	3.5 ± 0.2	3.5
Negative residues neutralized	1.9	1.8	0.7	2.9 ± 0.2	2.0
Positive residues neutralized	4.7	4.2	4.5	14.1 ± 1.4	13.1

due to the limited time-resolution of the experimental setups and hence yields a useful improvement in the field of nanopore analytics. Molecular details of the transport of these bulky ions through OmpF were investigated using MD simulations to understand the experimental observations.[88] Chemically the electrostatic interactions of such multi-atomic ions with the pore can be quite different due to the delocalized charges spread over all atoms compared to the single point charges of the mono-atomic ions. In addition, van der Waals interactions and hydrogen bond interactions can play a significant role in determining the overall transport process thorough nanopores. The temperature-dependent conductance of BMIM-Cl showed a quite good agreement between experiments and simulations (Fig. 4). Further atomic level analysis was aimed at characterizing the ion transport in general and to specifically address the question of altered kinetics in the pore. For example, the behavior of the hydration shell around the ions during the transport through the pore was investigated. It has been shown that for both ion types, $BMIM^+$ as well as Cl^-, the removal of water molecules from the hydration shell is compensated by the corresponding protein contacts so that the more generally defined solvation number (number of water molecules within the first hydration shell plus corresponding protein contacts) remains almost constant throughout the length of the pore. This avoids the need of extra dehydration energy for the passage through the pore.[88]

Probably the most interesting quantity for the transport of BMIM-Cl through the OmpF is the orientation of the $BMIM^+$ ions with respect to the channel axis during the transport process (Fig. 7). At both ends of the channel, the ions do have a favorable orientation due to the charges within the interior of the pore but fluctuate rather severely around these values by about $\pm 20°$. Within the constriction region, on the other hand, the ions tend to adopt a certain angle with respect to the channel axis before they are likely to move through the narrowest part of the channel. In addition, this angle has to be adapted rather accurately with a deviation of about $\pm 5°$. The accurate orientation in the narrowest part of the pore comprises a possible rate-limiting step leading to a reduced kinetics inside the pore.[88] These orientation dependencies are a feature of bulky ions which distinguishes them from simple mono-atomic ions. Nevertheless, the computational MD simulations are able to capture the conductance of these ions through nanopores rather accurately yielding useful atomic details.

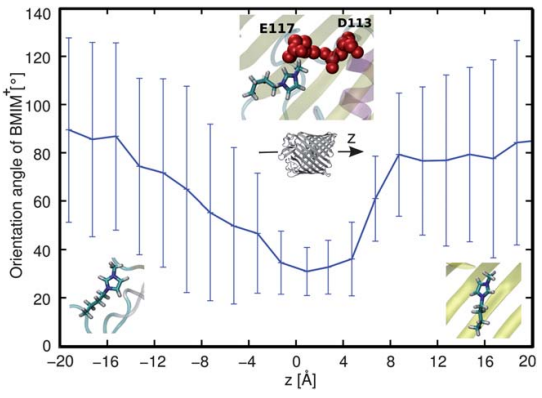

Fig. 7 Average orientation of the $BMIM^+$ dipole moment with respect to the channel coordinate z with error bars showing the standard deviation per bin. Representative orientations of $BMIM^+$ ions are shown in the insets for three particular regions of OmpF (the center inset includes two important negatively charged residues in the constriction region).[88]

5 Solid-state nanopores

Solid-state nanopores are pores composed of synthetic materials and have radii in the nanometer range. Robust and mechanically very stable solid-state nanopores offer an attractive alternative to biological pores. These man-made pores allow recordings over wide ranges of external conditions such as temperature, pH, ionic strength and applied electric field.[5] For biological pores such as α-hemolysin and OmpF, one needs tedious procedures to incorporate them into membranes and they are usually mechanically more fragile than their solid-state counterparts. On the other hand, the biological pores have the advantage of reproducibility in terms of geometry and chemical structure with atomic level precision. This is actually one of the drawbacks of solid-state nanopores. Even though manufactured using the same procedure, all these pores tend to have slightly different shapes and surface charges affecting the transport properties of the individual pores.[11] Nevertheless, solid-state nanopores have been used to examine the feasibility of a fast sequencing DNA techniques[139,140] and to study in detail the interactions between proteins and DNA.[141] Ion-transport properties of such nanopores can be engineered with respect to different external stimuli like pH, temperature, light, electric potential, ions and molecules.[142,143] Apart from this wide range of potential applications, artificial nanopores can be used as model systems to test fundamental theories of ion transport in nanoscale confinements.[144] Moreover, ion-selective solid-state nanopores can be used to unravel structure–function relationships of biological ion-channels *via* bottom-up engineering strategies whereby constituents responsible for selectivity can be studied outside of a complex cellular environment.[145]

The current design and preparation of solid-state nanopores can be summarized as follows (see ref. 5 and 142 as well as references therein):

(1) Selection of the material to build nanopores. Materials used include silica, silicon nitride, silicon dioxide, glass and polymer based materials like polyethylene terephthalate (PET), polycarbonate (PC) and polyimide (PI).

(2) Design and synthesis of various shapes and structures of nanopores using fabrication techniques such as electrochemical etching, anodic oxidation methods, electron beam schemes, laser approaches and ion-track-etching technologies.

(3) Subsequently the interior surface of the nanopore can be modified, if needed, using functional molecules. Such chemical modifications can assign tailor-made properties to solid-state nanopores for various purposes, *viz.*, to emulate ion selectivity, to recognize specific substrates or to remove undesired properties. For example, the deposition of Al_2O_3 on silicon nitride nanopores has been reported to reduce the noise level in channel recordings.[146] Similarly, attaching diamines to PET[147] or PI[148] may reverse the pore selectivity from cation selective to anion selective.

As most applications of nanopore-sensing are based on measuring changes in the ionic current, understanding the ion dynamics through these nanopores is essential. Several interesting and surprising experimental findings regarding the behavior of ions in synthetic nanoscale confinements have been observed. These effects include surface charge inversion due to divalent cations,[149] ion selectivity,[28,150] enhanced ionic currents due to DNA translocation and low salt concentrations[151] and nanoprecipitation by addition of divalent cations to monovalent ionic solutions.[152] Thus a broad range of topics and open questions can and need to be addressed *via* computational modeling.

Among the first solid-state nanopores used as molecular sensors were those based on silicon material, in particular silicon nitride.[153] MD simulations have been successfully applied to dissect the ion dynamics and several interesting phenomena like ion current rectification (ICR) and selectivity inversion in silica nanopores.[137,154] Initial observations based on Si_3N_4 nanopores coated with SiO_2 led to the assumption that the physical characteristics of the nanopore surface play a major role for ICR.[146] It was observed that current rectification can be abolished by lowering the pH[146] or by coating the surface with Al_2O_3.[155] To understand the role of surface features in such ionic rectifications, silica nanopores with three different surface properties were investigated in detail by Schulten and co-workers using MD simulation (Fig. 8).[137] Silica pores differ in their content of so-called dangling atoms at the surface. Crystalline pores, amorphous pores and annealed amorphous pores have comparatively high, medium and none/very few dangling atoms, respectively. Dangling atoms correspond to the atomic-scale roughness originating from silicon and oxygen atoms which are not fully coordinated to other atoms. These atoms then form potential ion-binding spots, *i.e.*, have the ability to dehydrate the ions and to temporarily bind to them. A detailed atomic analysis revealed that asymmetric distribution of dangling atoms affects the ion-distribution inside the pore depending on the polarity of the applied voltage. In turn, it generates an asymmetric electrostatic potential leading to an altered electrostatic profiles resulting in current rectification. Contrarily, nanopores that lack dangling atoms will have similar ion distributions and symmetric electrostatic potentials independent of the polarity of the applied voltage which produces a symmetric current–voltage behavior.[137] This example shows how computer simulations can help to understand macroscopic ion transport properties.

Another interesting phenomenon which was investigated using MD simulations following experimental observations[149] is the charge inversion (CI). To decipher atomic level details of such phenomena *via* MD simulations, regions near the silica interface have been divided into three layers based on the distance between silica oxygen atoms and the ions.[154] Each layer was analyzed for the relative charge population of the cation Ca^{2+} and the anion Cl^-. The first layer (distance <3 Å from silica oxygen) has a net positive charge and while the third layer (distance within 7 to 12 Å from silica oxygen) has a net negative charge indicating a relatively high population of Ca^{2+} and Cl^- ions in the respective layer. The middle layer has both cationic and anionic charge populations in reasonable amounts with slightly higher cationic charges. Furthermore, Ca^{2+} ions have a very high residence time of ~2 ns in the first layer. This indicates the presence of tightly bound Ca^{2+} ions in the first layer leading to a charge inversion of the silica surface. In addition, a net negative charge in the third layer is a signature of CI as the large population of Cl^- ions in this diffuse layer indicates an anion selective channel. Recent simulations with trivalent and quadrivalent ions to examine DNA transport through silica nanopores revealed a reverse direction of the DNA electrophoretic motion upon increasing the concentration of the electrolytes.[156] This behavior arises due to the inversion of the effective DNA charge upon binding of cations. In electrophysiological experiments, a dependence of transport properties on the type and concentration of electrolytes can further be exploited for nanotechnological applications.

In another study, the structural and transport properties of NaCl and $CaCl_2$ were characterized in silica nanopores of different diameters.[157] Small amounts of CI occurred for 0.5 M $CaCl_2$ but was absent for 0.5 M NaCl. Transport properties of monovalent and divalent ions are significantly different and also strongly dependent on the pore diameter. The average current increases with the pore diameter for both electrolyte solutions. A correlated movement of the cations and anions in the same direction was observed in $CaCl_2$ but was absent in NaCl. This leads to higher current values for the monovalent system compared to the divalent one.

Similarly PET nanopores were investigated concerning the effect of different pH conditions on the ion selectivity.[158] Different pH values correspond to different surface charges in the nanopore. All carboxylate groups of the PET pore are neutral at pH 4 and negatively charged at pH 7. MD simulations with 1 M KCl indicated the absence of charge selectivity at pH 4 and a cation selectivity at pH 7. Moreover, an incremental addition of $CaCl_2$ to KCl showed a reversal of the electrostatic potential of the system compared to KCl. This is a possible indication for CI. However, reversal of the ion selectivity could not be observed in current measurements which was attributed to the high ionic concentration used during the study. An additional interesting phenomenon which was investigated using long MD simulations is the nanoprecipitation effect for calcium phosphate electrolyte solutions in PET nanopores.[159] Such effects are characterized by transient formations of precipitates in the nanopore lumen, producing a sequence of low and high conductance states in the ionic current through the pore. Simulations revealed the influence of the surface carboxylic groups on the transient formation of precipitates and a subsequent detachment depending on the protonation states of these groups leading to a series of low and high conduction states.

Further synthetic pores which have recently received considerable attention, especially in DNA sequencing, are graphene based nanopores.[160,161] This material has extraordinary mechanical and chemical properties which assure the manufacturability and durability of graphene nanopore in electrophysiological measurements.[162] It is the thinnest known material with a thickness similar to the distance between two successive bases in DNA which makes a single-base sensitivity in DNA sequencing attainable. Recently applied-field MD simulations were employed to investigate the transport of DNA through graphene nanopores.[138] As a first step to model such electrophysiological experiments with the new material, transport of KCl was characterized with respect to different pore diameters (2 nm to 7 nm) of graphene sheets. The analysis of the pore resistance (R) as a function of the pore diameter (d) showed a

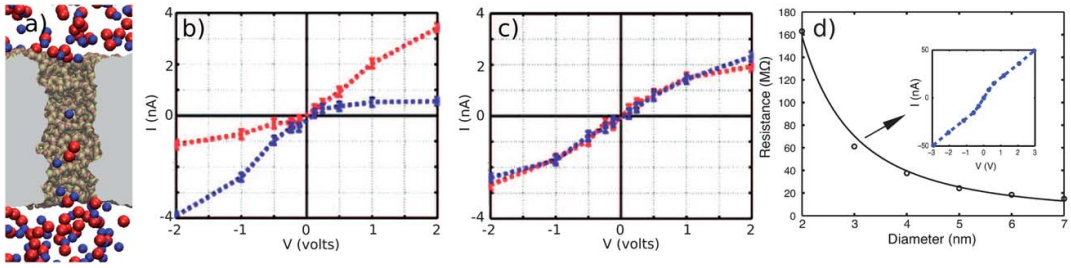

Fig. 8 (a) The atomic model of a silica nanopore. The nanopore is shown sliced in the middle. The gray surface covers the bulk silica region to permit the view on the pore interior. The K^+ and Cl^- ions are shown as spheres while water is not shown. (b) The current–voltage curve for a crystalline (red) and an amorphous (blue) silica nanopore for 1 M KCl. Both pores show rectification due to the presence of the dangling atoms. (c) Similar current–voltages curve for two different annealed amorphous silica pores (red and blue) at 1 M KCl. The curves are symmetric and hence no rectification due to the absence of dangling atoms. (d) For a different system, a graphene nanopore, the dependence of the pore resistance on the nanopore diameter d for the transport at 1 M KCl is shown. The solid line represents a $1/d^2$ fit to the circles. The inset shows the current–voltage curve for a pore diameter of 3 nm. (a)–(c) are adapted from ref. 137 and (d) from ref. 138 with permission from the American Chemical Society.

relationship $R \approx 1/d^2$ which is in qualitative accordance with the experiment (Fig. 8d). The resistance values obtained *via* simulation are 3–4 times smaller than in the corresponding experiments. This was attributed to the high voltage of 3 V applied in the simulations, the discrepancies between the exact shape and charge distribution of the pore in experiments and simulations or a possible inaccuracy of the force fields. The above-discussed series of examples shows that nanopore simulations can achieve macroscopic ion currents close to experimental data while at the same time provide the opportunity for a detailed molecular analysis.

6 Ion channels

Biological channels with high selectivities towards specific ions generally belong to the class of "ion channels". Their diameter is usually below the nanometer scale in the narrowest part of the channel. These channels are in many cases so narrow that water and ions can only pass in a single file. Many of them may assume different conformations dependent on external stimuli. The high selectivity of ion channels helps them to discriminate not only between cations and anions but also among the ions with the same charge. The requirement of such a high-level ion selectivity is due to the fact that many physiological processes of living cells are governed by proper ionic gradients across their membranes. The computational modeling of ion transport through these channels and in particular of the selectivity is challenging as one has to precisely account for electrostatics and other interactions between the ions, protein surfaces and solvent molecules. At the same time applied-field MD simulations or MD simulations with an ion gradient across the membrane are computationally very demanding due to the low values of the corresponding ion current which is considerably lower than, for example, in the case of the much wider OmpF channel. Therefore it has been employed only in exceptional cases.[67,163]

As an example for an ion channel some computational studies on the potassium channel KcsA are briefly summarized. The structure of KcsA[164,165] revealed that the extracellular side of the pore is very narrow and exclusively lined by backbone carbonylic oxygen atoms (Fig. 9).[164] This region of the pore acts as

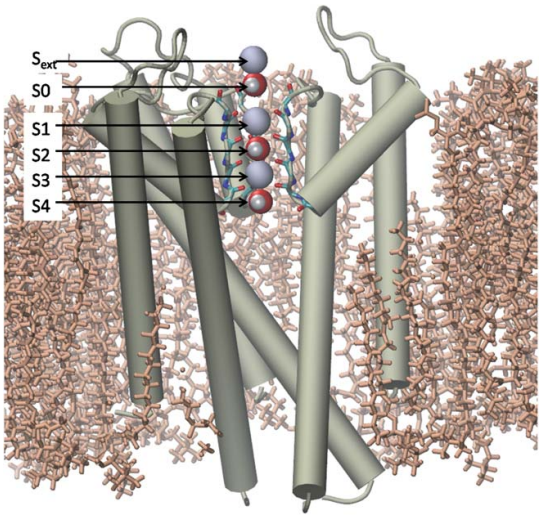

Fig. 9 A KcsA channel embedded in a lipid membrane. The binding sites S0 to S4 and S_{ext} are shown to be occupied by K^+ ions (blue spheres) and water (red and white spheres) in an alternative manner. Backbone residues of 'selectivity filter' region are shown in stick representation. One of the four monomers of KcsA is not shown for the sake of clear visualization of the binding sites. The figure has been generated using VMD.[65]

"selectivity filter". The intracellular part of the pore is wider with a cavity radius of around 8 Å.[164] Calculations of the PMF using MD simulation played a significant role in understanding the potassium transport through the channel. It was shown that K^+ ions can be located at five energetically favorable binding sites (S0 to S4)[166] which was also supported by high-resolution crystal structures.[165] Moreover, it was suggested that configurations with two or three K^+ ions alternatively occupying the binding sites and separated by one water molecule are the favorable ones (the so-called S1–S3 and S0–S2–S4 configurations).[165,167] The transition between the two configurations is to a large extent given by a channel-specific energy barrier.[168] Recently

applied-field MD simulation on the microsecond time scale for the Kv1.2 channel has verified the above-mentioned mechanism of ion permeation which was obtained from PMF-based strategies.[67]

The issue of ion selectivity in potassium channels is still a matter of debate with three different working hypotheses. The "snug-fit hypothesis", attributes the selectivity to the slightly different atomic size of the K^+ and Na^+ ions.[164,169] Due to atomic fluctuation in the binding site which is larger than the difference in ionic radii, this hypothesis is questionable.[170] The "field-strength hypothesis" suggests that the number and/or physical properties of the ligands coordinating the bound ions determine the ion selectivity.[170,171] The third variant, the "over-coordination hypotheses", proposes that it is the number of coordinating ligands to the bound ion and not their physical properties which largely decide the selectivity.[172,173] Sansom and co-workers compared all three hypotheses for the selective K^+ channel KcsA and the non-selective NaK channel using MD simulations.[174] According to this study, using the snug-fit hypothesis one could not differentiate between the selectivity of the KcsA channel and the non-selectivity of the NaK channel while the over-coordination hypothesis was able to justify the selectivity. Results regarding the field-strength hypothesis were inconclusive in the above study while some other recent studies supported the hypothesis.[171,175] In addition, quantum mechanics/molecular mechanics (QM/MM) Car–Parrinello simulations were performed to shed light on the processes underlying the selectivity filter[176] though also this method has its own problems.[177]

The opening and closing of ion channels, *i.e.*, their gating, under the effect of external stimuli is another important property. However, it is computationally challenging to model such gating processes due to the long time scales involved. Crystal structures of KcsA in low and high salt concentrations revealed different structural arrangements in the selectivity filter region.[178] This suggests a possible role of the filter region in the gating mechanism, the so-called C-type inactivation, which was also explored by several computational studies.[179–181] Targeted MD study suggested the transition between closed and open states to occur in a 'zipper-like' fashion.[182] Recent studies with a series of KcsA crystal structures in fully open and partially open forms investigated the structural mechanism of C-type inactivation and proposed a possible contribution of allosteric couplings between different regions of the channel in the inactivation process.[183] Moreover, the movement of the inner gate on the intracellular side of channel and its influence on the inactivation process by inducing conformational changes in the filter region was investigated by a combined experimental and computational study.[184]

Similarly other channels such as the anion-selective ClC channel and the cation-selective nicotinic acetylcholine receptor (nAchR) were computationally investigated concerning their ion-permeation and selectivity mechanisms.[101,102,185] However, a detailed discussion about all of them is outside the purview of this article. Nevertheless it should become clear that nature has designed rather complex and delicate processes to achieve very high ion selectivities. Attempts have been made to emulate such selectivities for synthetic channels but one probably has to understand more of the sophisticated details to achieve the same degree of selectivity in the synthetic counterparts.

7 Discussion and outlook

Ion transport through nanopores is an important process in biological systems and extensive applications of synthetic solid-state nanopores are realized as should have become apparent by many of the examples above. This article focused on presenting an (certainly not complete) overview of the progress in theoretical and computational approaches to decipher ion dynamics through such pores. Roughly three different levels of modeling exist: continuum models, BD, and MD approaches. Continuum models often discard quite a bit of the molecular details of the problem including the discreteness of the ions but on the other hand enjoy the advantage of superior computational efficiency and thus making the calculations for long time scales quite feasible. Ions are treated as discrete particles in BD but usually the rest of the system is still assumed to be a rigid continuum though there are several variants and improvements of the approach. The atomistic details and flexibility of the underlying system are retained in MD simulations but at the price of a large computational cost. With the advent of increasing computer power, it has now become possible to vigorously test the existing force fields by long simulation runs and to improve them. Since the computational effort is large and many details of the system do not influence the ion dynamics, a combination of the above methods in multi-scale schemes needs to be further explored in the years to come. For example, diffusion constants for BD calculations have been extracted from MD simulations.[27,56] A rather promising approach seems to be the atomic-resolution BD[58,59] though the initial calculation of the 3D PMFs from MD simulations for all constituents is computationally very expensive. Nevertheless, this scheme opens the possibilities to determine long-time trajectories with a high level of details once the initial parametrization has been performed. More methodological advancements in the multi-scale direction are certainly to be expected in the future to overcome some of the limitations of the present approaches.

One of the limitations of the present force fields is their non-polarizability. In ionic systems polarization certainly plays an important role especially in confined geometries. Standard force fields like CHARMM and AMBER include polarizability implicitly in an average way in their parameterization procedure. Extensions are being developed[68,69] although it will certainly take some time until polarizable force fields can be as widely used as the non-polarizable versions right now. As an alternative quantum mechanics/molecular mechanics (QM/MM) Car–Parrinello simulations can be performed but are computationally very expensive and do have some limitations as well.[176]

Artificial nanopores which have not been discussed in this overview are nanopores consisting of synthetic nanotubes. Various computational efforts[186,187] have been made to determine the sizes and properties of carbon nanotubes to gain a high selectivity for certain ions or water only. This might become a very important field of nanopore research due to the potential application, *e.g.*, for water purification. Another step towards an advanced design level of synthetic systems might be achieved by taking Brownian ratchet effects into account. This type of effects might play an interesting role in ion transport.[135,188] It is sometime speculated if nature uses similar effects for the transport and/or selectivity of certain ion or molecule types through

biological channels however further investigations in this direction are needed.

Many of the biological and solid-state nanopores are designed not only to let ions pass but also certain classes of macromolecules. As already discussed above, the goal of sequencing DNA by threading it through nanopores has driven the whole nanopore research considerably.[10,12] Simulations have played an important role in understanding and designing some of these experiments.[11] Another example is the translocation of antibiotics through OmpF. Also in this field the computational studies are helping to understand and design experiments on ion current blockage by the substrate molecules.[123–125] In future calculations it would also be interesting to model substrate and ion transport simultaneously over longer time scales to be able to understand the interplay between the two of them. Ions might alter binding spots for the substrates and *vice versa* leading to a quite different transport dynamics. At the same time ions also play an important role in active membrane pumps, such as the channel parts in tripartite pumps like TolC.[80]

In conclusion it is clearly evident that computer simulations have established themselves as quite versatile tools to comprehend transport processes at the nanometer scale. A larger number and more fruitful collaborations between theory and experiments are to be expected in the (near) future if not already established. An increasing number of fully atomistic structures of biological pores/channels and new fabrication techniques for synthetic pores will provide a platform for a further expansion of the existing knowledge. Theoretical and computational methods development and increase in computational power are believed to fuel great progress in the field over the next years to come.

Acknowledgements

The authors would like to thank Roland Benz, Soroosh Pezeshki, Robert Schulz, Kozhinjampara R. Mahendran, Pratik Raj Singh, and Catalin Chimerel for fruitful and enjoyable collaborations. This work has been supported by grants KL 1299/6-1 and WI 2278/18-1 of the Deutsche Forschungsgemeinschaft (DFG) and by Jacobs University Bremen.

References

1 *Nature Nanotechnology Focus on Nanopores*, http://www.nature.com/nnano/focus/nanopores.
2 S. Majd, E. C. Yusko, Y. N. Billeh, M. X. Macrae, J. Yang and M. Mayer, *Curr. Opin. Biotechnol.*, 2010, **21**, 439–476.
3 *Bacterial and Eukaryotic Porins*, ed. R. Benz, Wiley-VCH, Weinheim, 2004.
4 T. Albrecht, J. B. Edel and M. Winterhalter, *J. Phys.: Condens. Matter*, 2010, **22**, 450301.
5 S. Howorka and Z. Siwy, *Chem. Soc. Rev.*, 2009, **38**, 2360–2384.
6 Z. S. Siwy and S. Howorka, *Chem. Soc. Rev.*, 2010, **39**, 1115–1132.
7 H. Daiguji, *Chem. Soc. Rev.*, 2010, **39**, 901–911.
8 V. Krishnamurthy and B. Cornell, *Protoplasma*, 2012, **249**, 3–9.
9 A. Singer, S. Rapireddy, D. H. Ly and A. Meller, *Nano Lett.*, 2012, **12**, 1722–1728.
10 E. A. Manrao, I. M. Derrington, A. H. Laszlo, K. W. Langford, M. K. Hopper, N. Gillgren, M. Pavlenok, M. Niederweis and J. H. Gundlach, *Nat. Biotechnol.*, 2012, **30**, 349–353.
11 A. Aksimentiev, *Nanoscale*, 2010, **2**, 468–473.
12 B. Luan, G. Stolovitzky and G. Martyna, *Nanoscale*, 2012, **4**, 1068–1077.
13 E. Neher and B. Sakmann, *Nature*, 1976, **260**, 799–802.
14 K. R. Mahendran, P. R. Singh, J. Arning, S. Stolte, U. Kleinekathöfer and M. Winterhalter, *J. Phys.: Condens. Matter*, 2010, **22**, 454131.
15 W. Nernst, *Z. Phys. Chem.*, 1888, **2**, 613–637.
16 M. Planck, *Ann. Phys. Chem.*, 1890, **39**, 161–186.
17 B. Eisenberg, *Contemp. Phys.*, 1998, **39**, 447–466.
18 M. Kurnikova, R. Coalson, P. Graf and A. Nitzan, *Biophys. J.*, 1999, **76**, 642–656.
19 Z. Schuss, B. Nadler and R. S. Eisenberg, *Phys. Rev. E: Stat. Phys., Plasmas, Fluids, Relat. Interdiscip. Top.*, 2001, **64**, 036116.
20 W. Van Gunsteren, H. Berendsen and J. Rullmann, *Mol. Phys.*, 1981, **44**, 69–95.
21 S. Li, M. Hoyles, S. Kuyucak and S. Chung, *Biophys. J.*, 1998, **74**, 37–47.
22 D. C. Rapaport, *The Art of Molecular Dynamics Simulation*, Cambridge University Press, 2nd edn, 2004.
23 A. Aksimentiev and K. Schulten, *Biophys. J.*, 2005, **88**, 3745–3751.
24 B. Eisenberg, *J. Phys. Chem. C*, 2010, **114**, 20719–20733.
25 S. Kuyucak, O. S. Andersen and S.-H. Chung, *Rep. Prog. Phys.*, 2001, **64**, 1427–1472.
26 *Biological Membrane Ion Channels*, ed. S.-H. Chung, O. S. Anderson and V. V. Krishnamurthy, Springer, 2007.
27 W. Im and B. Roux, *J. Mol. Biol.*, 2002, **322**, 851–869.
28 J. Cervera, B. Schiedt, R. Neumann, S. Mafé and P. Ramírez, *J. Chem. Phys.*, 2006, **124**, 104706.
29 O. Choudhary, R. Ujwal, W. Kowallis, R. Coalson, J. Abramson and M. Grabe, *J. Mol. Biol.*, 2010, **396**, 580–592.
30 H. Miedema, M. Vrouenraets, J. Wierenga, D. Gillespie, B. Eisenberg, W. Meijberg and W. Nonner, *Biophys. J.*, 2006, **91**, 4392–4400.
31 H. Miedema, A. Meter-Arkema, J. Wierenga, J. Tang, B. Eisenberg, W. Nonner, H. Hektor, D. Gillespie and W. Meijberg, *Biophys. J.*, 2004, **87**, 3137.
32 E. García-Giménez, M. L. López, V. M. Aguilella and A. Alcaraz, *Biochem. Biophys. Res. Commun.*, 2011, **404**, 330–334.
33 D. Gillespie, *Biophys. J.*, 2008, **94**, 1169–1184.
34 A. Mamonov, M. Kurnikova and R. Coalson, *Biophys. Chem.*, 2006, **124**, 268–278.
35 D. Bolintineanu, A. Sayyed-Ahmad, H. Davis and Y. Kaznessis, *PLoS Comput. Biol.*, 2009, **5**, e1000277.
36 C. Ho, R. Qiao, J. Heng, A. Chatterjee, R. Timp, N. Aluru and G. Timp, *Proc. Natl. Acad. Sci. U. S. A.*, 2005, **102**, 10445.
37 M. Ali, S. Nasir, P. Ramirez, I. Ahmed, Q. H. Nguyen, L. Fruk, S. Mafe and W. Ensinger, *Adv. Funct. Mater.*, 2012, **22**, 390–396.
38 J. Cervera, B. Schiedt and P. Ramirez, *Europhys. Lett.*, 2005, **71**, 35.
39 I. Kosińska, I. Goychuk, M. Kostur, G. Schmid and P. Hänggi, *Phys. Rev. E: Stat., Nonlinear, Soft Matter Phys.*, 2008, **77**, 031131.
40 D. Krapf, B. Quinn, M. Wu, H. Zandbergen, C. Dekker and S. Lemay, *Nano Lett.*, 2006, **6**, 2531–2535.
41 Y. Jung, B. Lu and M. Mascagni, *J. Chem. Phys.*, 2009, **131**, 215101.
42 B. Corry, S. Kuyucak and S. Chung, *Biophys. J.*, 2000, **78**, 2364–2381.
43 G. Moy, B. Corry, S. Kuyucak and S. Chung, *Biophys. J.*, 2000, **78**, 2349–2363.
44 C. Song and B. Corry, *PLoS One*, 2011, **6**, e21204.
45 D. Gillespie, W. Nonner and R. S. Eisenberg, *J. Phys.: Condens. Matter*, 2002, **14**, 12129.
46 R. Roth and D. Gillespie, *Phys. Rev. Lett.*, 2005, **95**, 247801.
47 B. Eisenberg, Y. Hyon and C. Liu, *J. Chem. Phys.*, 2010, **133**, 104104.
48 M. Burger, R. S. Eisenberg and H. W. Engl, *SIAM Journal on Applied Mathematics*, 2007, **67**, 960–989.
49 M. Burger, *Inverse Probl.*, 2011, **27**, 083001.
50 F. Reif, *Fundamentals of Statistical and Thermal Physics*, McGraw-Hill Book Company, 1967.
51 P. S. Phale, A. Philippsen, C. Widmer, V. P. Phale, J. P. Rosenbusch and T. Schirmer, *Biochemistry*, 2001, **40**, 6319–6325.
52 T. Schirmer and P. S. Phale, *J. Mol. Biol.*, 1999, **294**, 1159–1167.
53 T. Allen, M. Hoyles, S. Kuyucak and S. Chung, *Chem. Phys. Lett.*, 1999, **313**, 358–365.
54 S. Chung, T. Allen and S. Kuyucak, *Biophys. J.*, 2002, **83**, 263–277.
55 S. Noskov, W. Im and B. Roux, *Biophys. J.*, 2004, **87**, 2299–2309.
56 K. Lee, H. Rui, R. Pastor and W. Im, *Biophys. J.*, 2011, **100**, 611–619.

57 T. Hilder, D. Gordon and S. Chung, *Biophys. J.*, 2010, **99**, 1734–1742.
58 R. Carr, J. Comer, M. D. Ginsberg and A. Aksimentiev, *Lab Chip*, 2011, **11**, 3766–3773.
59 J. Comer and A. Aksimentiev, *J. Phys. Chem. C*, 2012, **116**, 3376–3393.
60 E. Csanyi, D. Boda, D. Gillespie and T. Kristof, *Biochim. Biophys. Acta, Biomembr.*, 2012, **1818**, 592–600.
61 A. MacKerell, D. Bashford, M. Bellott, R. Dunbrack, J. Evanseck, M. Field, S. Fischer, J. Gao, H. Guo, S. Ha, D. Joseph-McCarthy, L. Kuchnir, K. Kuczera, F. Lau, C. Mattos, S. Michnick, T. Ngo, D. Nguyen, B. Prodhom, W. Reiher, B. Roux, M. Schlenkrich, J. Smith, R. Stote, J. Straub, M. Watanabe, J. Wiorkiewicz-Kuczera, D. Yin and M. Karplus, *J. Phys. Chem. B*, 1998, **102**, 3586–3616.
62 J. W. Ponder and D. A. Case, *Adv. Protein Chem.*, 2003, **66**, 27–85.
63 W. Scott, P. Hünenberger, I. Tironi, A. Mark, S. Billeter, J. Fennen, A. Torda, T. Huber, P. Krüger and W. V. Gunsteren, *J. Phys. Chem. A.*, 1999, **103**, 3596–3607.
64 W. Jorgensen, D. Maxwell and J. Tirado-Rives, *J. Am. Chem. Soc.*, 1996, **118**, 11225–11236.
65 W. F. Humphrey, A. Dalke and K. Schulten, *J. Mol. Graphics*, 1996, **14**, 33–38.
66 F. Khalili-Araghi, J. Gumbart, P. C. Wen, M. Sotomayor, E. Tajkhorshid and K. Schulten, *Curr. Opin. Struct. Biol.*, 2009, **19**, 128–137.
67 M. Jensen, D. Borhani, K. Lindorff-Larsen, P. Maragakis, V. Jogini, M. Eastwood, R. Dror and D. Shaw, *Proc. Natl. Acad. Sci. U. S. A.*, 2010, **107**, 5833.
68 H. Yu, T. Whitfield, E. Harder, G. Lamoureux, I. Vorobyov, V. Anisimov, A. MacKerell Jr and B. Roux, *J. Chem. Theory Comput.*, 2010, **6**, 774–786.
69 W. Jiang, D. J. Hardy, J. C. Phillips, A. D. MacKerell, K. Schulten and B. Roux, *J. Phys. Chem. Lett.*, 2010, **2**, 87–92.
70 A. Alcaraz, E. M. Nestorovich, M. Aguilella-Arzo, V. M. Aguilella and S. M. Bezrukov, *Biophys. J.*, 2004, **87**, 943–947.
71 S. Donnini, F. Tegeler, G. Groenhof and H. Grubmüller, *J. Chem. Theory Comput.*, 2011, **7**, 1962–1978.
72 G. B. Goh, J. L. Knight and C. L. Brooks, *J. Chem. Theory Comput.*, 2011, **8**, 36–46.
73 A. Gurtovenko and I. Vattulainen, *J. Am. Chem. Soc.*, 2005, **127**, 17570–17571.
74 J. N. Sachs, P. S. Crozier and T. B. Woolf, *J. Chem. Phys.*, 2004, **121**, 10847–10851.
75 L. Delemotte, F. Dehez, W. Treptow and M. Tarek, *J. Phys. Chem. B*, 2008, **112**, 5547–5550.
76 C. Kutzner, H. Grubmüller, B. L. de Groot and U. Zachariae, *Biophys. J.*, 2011, **101**, 809–817.
77 B. Corry, M. Hoyles, T. W. Allen, M. Walker, S. Kuyucak and S.-H. Chung, *Biophys. J.*, 2002, **82**, 1975–1984.
78 P. S. Crozier, D. Henderson, R. L. Rowley and D. D. Busath, *Biophys. J.*, 2001, **81**, 3077–3079.
79 A. Suenaga, Y. Komeiji, M. Uebayasi, T. Meguro, M. Saito and I. Yamato, *Biosci. Rep.*, 1998, **18**, 39–48.
80 R. Schulz and U. Kleinekathöfer, *Biophys. J.*, 2009, **96**, 3116–3125.
81 C. Maffeo and A. Aksimentiev, *Biophys. J.*, 2009, **96**, 4853–4865.
82 S. Siu and R. Böckmann, *J. Struct. Biol.*, 2007, **157**, 545–556.
83 M. Sotomayor, V. Vasquez, E. Perozo and K. Schulten, *Biophys. J.*, 2007, **92**, 886–902.
84 F. Khalili-Araghi, E. Tajkhorshid and K. Schulten, *Biophys. J.*, 2006, **91**, L72–L74.
85 C. Chimerel, L. Movileanu, S. Pezeshki, M. Winterhalter and U. Kleinekathöfer, *Eur. Biophys. J.*, 2008, **38**, 121–125.
86 S. Pezeshki, C. Chimerel, A. Bessenov, M. Winterhalter and U. Kleinekathöfer, *Biophys. J.*, 2009, **97**, 1898–1906.
87 I. Biro, S. Pezeshki, H. Weingart, M. Winterhalter and U. Kleinekathöfer, *Biophys. J.*, 2010, **98**, 1830–1839.
88 N. Modi, P. R. Singh, K. R. Mahendran, R. Schulz, M. Winterhalter and U. Kleinekathöfer, *J. Phys. Chem. Lett.*, 2011, **2**, 2331–2336.
89 D. P. Tieleman, *BMC Biochem.*, 2004, **5**, 10.
90 J. Gumbart, F. Khalili-Araghi, M. Sotomayor and B. Roux, *Biochim. Biophys. Acta, Biomembr.*, 2012, **1818**, 294–302.
91 Y. Xie, Y. Kong, A. Soh and H. Gao, *J. Chem. Phys.*, 2007, **127**, 225101.
92 P. Vernier, M. Ziegler, Y. Sun, M. Gundersen and D. Tieleman, *Phys. Biol.*, 2006, **3**, 233.
93 E. Abad, J. Reingruber and M. S. P. Sansom, *J. Chem. Phys.*, 2009, **130**, 085101-18.
94 A. Pohorille, C. Jarzynski and C. Chipot, *J. Phys. Chem. B*, 2010, **114**, 10235–10253.
95 P. Pongprayoon, O. Beckstein, C. L. Wee and M. S. Sansom, *Proc. Natl. Acad. Sci. U. S. A.*, 2009, 21614–21618.
96 S. Patel, J. Davis and B. Bauer, *J. Am. Chem. Soc.*, 2009, **131**, 13890–13891.
97 Y. Zhang and G. A. Voth, *J. Chem. Theory Comput.*, 2011, **7**, 2277–2283.
98 B. Corry and M. Thomas, *J. Am. Chem. Soc.*, 2012, **134**, 1840–1846.
99 T. Bastug and S. Kuyucak, *Biophys. J.*, 2006, **90**, 3941–3950.
100 J. Yu, A. Yool, K. Schulten and E. Tajkhorshid, *Structure*, 2006, **14**, 1411–1423.
101 J. Cohen and K. Schulten, *Biophys. J.*, 2004, **86**, 836–845.
102 I. Ivanov, X. Cheng, M. Steven and J. McCammon, *J. Am. Chem. Soc.*, 2007, **129**, 8217–8224.
103 T. W. Allen, O. S. Andersen and B. Roux, *Biophys. J.*, 2006, **90**, 3447–3448.
104 S. Kumar, J. Rosenberg, D. Bouzida, R. Swendsen and P. Kollman, *J. Comput. Chem.*, 1992, **13**, 1011–1021.
105 M. Souaille and B. Roux, *Comput. Phys. Commun.*, 2001, **135**, 40–57.
106 G. Torrie and J. Valleau, *Chem. Phys. Lett.*, 1974, **28**, 578–581.
107 E. Darve and A. Pohorille, *J. Chem. Phys.*, 2001, **115**, 9169.
108 J. Hénin and C. Chipot, *J. Chem. Phys.*, 2004, **121**, 2904.
109 A. Laio and M. Parrinello, *Proc. Natl. Acad. Sci. U. S. A.*, 2002, **99**, 12562.
110 C. Micheletti, A. Laio and M. Parrinello, *Phys. Rev. Lett.*, 2004, **92**, 170601.
111 T. Straatsma and H. Berendsen, *J. Chem. Phys.*, 1988, **89**, 5876.
112 J. Aaqvist, *J. Phys. Chem.*, 1990, **94**, 8021–8024.
113 L. Dang, *J. Am. Chem. Soc.*, 1995, **117**, 6954–6960.
114 K. Jensen and W. Jorgensen, *J. Chem. Theory Comput.*, 2006, **2**, 1499–1509.
115 I. Joung and T. Cheatham III, *J. Phys. Chem. B*, 2008, **112**, 9020–9041.
116 D. Horinek, S. Mamatkulov and R. Netz, *J. Chem. Phys.*, 2009, **130**, 124507.
117 M. Fyta and R. R. Netz, *J. Chem. Phys.*, 2012, **136**, 124103–124111.
118 Y. Luo and B. Roux, *J. Phys. Chem. Lett.*, 2009, **1**, 183–189.
119 J. Yoo and A. Aksimentiev, *J. Phys. Chem. Lett.*, 2011, **3**, 45–50.
120 J. Timko, D. Bucher and S. Kuyucak, *J. Chem. Phys.*, 2010, **132**, 114510–114518.
121 C. Zhang, S. Raugei, B. Eisenberg and P. Carloni, *J. Chem. Theory Comput.*, 2010, **6**, 2167–2175.
122 J. M. Pages, C. E. James and M. Winterhalter, *Nat. Rev. Microbiol.*, 2008, **6**, 893–903.
123 M. Ceccarelli and P. Ruggerone, *Curr. Drug Targets*, 2008, **9**, 779–788.
124 K. R. Mahendran, E. Hajjar, T. Mach, M. Lovelle, A. Kumar, I. Sousa, E. Spiga, H. Weingart, P. Gameiro, M. Winterhalter and M. Ceccarelli, *J. Phys. Chem. B*, 2010, **114**, 5170–5179.
125 E. Hajjar, K. R. Mahendran, A. Kumar, A. Bessonov, M. Petrescu, H. Weingart, P. Ruggerone, M. Winterhalter and M. Ceccarelli, *Biophys. J.*, 2010, **98**, 569–575.
126 S. Bhattacharya, L. Muzard, L. Payet, J. Mathé, U. Bockelmann, A. Aksimentiev and V. Viasnoff, *J. Phys. Chem. C*, 2011, **115**, 4255.
127 S. W. Cowan, T. Schirmer, G. Rummel, M. Steiert, R. Ghosh, R. A. Pauptit, J. N. Jansonius and J. P. Rosenbusch, *Nature*, 1992, **358**, 727–733.
128 P. S. Phale, T. Schirmer, A. Prilipov, K. L. Lou, A. Hardmeyer and J. P. Rosenbusch, *Proc. Natl. Acad. Sci. U. S. A.*, 1997, **94**, 6741–6745.
129 W. Im and B. Roux, *J. Mol. Biol.*, 2002, **319**, 1177–1197.
130 H. Rui, K. I. Lee, R. W. Pastor and W. Im, *Biophys. J.*, 2011, **100**, 602–610.
131 E.-M. Krammer, F. Homble and M. Prevost, *PLoS One*, 2011, **6**, e27994.
132 A. Alcaraz, E. Nestorovich, M. López, E. García-Giménez, S. Bezrukov and V. Aguilella, *Biophys. J.*, 2009, **96**, 56–66.
133 V. M. Aguilella, M. Queralt-Martin, M. Aguilella-Arzo and A. Alcaraz, *Integr. Biol.*, 2011, **3**, 159–172.

134 M. Aguilella-Arzo, C. Calero and J. Faraudo, *Soft Matter*, 2010, **6**, 6079–6082.
135 C. Verdia-Baguena, M. Queralt-Martin, V. M. Aguilella and A. Alcaraz, *J. Phys. Chem. C*, 2012, **116**, 6537–6542.
136 R. de Zoysa, D. Jayawardhana, Q. Zhao, D. Wang, D. Armstrong and X. Guan, *J. Phys. Chem. B*, 2009, **113**, 13332–13336.
137 E. R. Cruz-Chu, A. Aksimentiev and K. Schulten, *J. Phys. Chem. C*, 2009, **113**, 1850–1862.
138 C. Sathe, X. Zou, J.-P. Leburton and K. Schulten, *ACS Nano*, 2011, **5**, 8842–8851.
139 G. Sigalov, J. Comer, G. Timp and A. Aksimentiev, *Nano Lett.*, 2008, **8**, 56–63.
140 D. Branton, D. Deamer, A. Marziali, H. Bayley, S. Benner, T. Butler, M. Di Ventra, S. Garaj, A. Hibbs and X. Huang, *et al.*, *Nat. Biotechnol.*, 2008, **26**, 1146–1153.
141 Q. Zhao, G. Sigalov, V. Dimitrov, B. Dorvel, U. Mirsaidov, S. Sligar, A. Aksimentiev and G. Timp, *Nano Lett.*, 2007, **7**, 1680–1685.
142 X. Hou, W. Guo and L. Jiang, *Chem. Soc. Rev.*, 2011, **40**, 2385–2401.
143 Z. Sun, C. Han, L. Wen, D. Tian, H. Li and L. Jiang, *Chem. Commun.*, 2012, **48**, 3282–3284.
144 D. Gillespie, D. Boda, Y. He, P. Apel and Z. Siwy, *Biophys. J.*, 2008, **95**, 609–619.
145 S. W. Kowalczyk, T. R. Blosser and C. Dekker, *Trends Biotechnol.*, 2011, **29**, 607–614.
146 P. Chen, T. Mitsui, D. Farmer, J. Golovchenko, R. Gordon and D. Branton, *Nano Lett.*, 2004, **4**, 1333–1337.
147 I. Vlassiouk and Z. Siwy, *Nano Lett.*, 2007, **7**, 552–556.
148 M. Ali, B. Schiedt, K. Healy, R. Neumann and W. Ensinger, *Nanotechnology*, 2008, **19**, 085713.
149 F. Van der Heyden, D. Stein, K. Besteman, S. Lemay and C. Dekker, *Phys. Rev. Lett.*, 2006, **96**, 224502.
150 Z. Siwy, Y. Gu, H. Spohr, D. Baur, A. Wolf-Reber, R. Spohr, P. Apel and Y. Korchev, *Europhys. Lett.*, 2002, **60**, 349.
151 R. Smeets, U. Keyser, D. Krapf, M. Wu, H. Nynke and C. Dekker, *Nano Lett.*, 2006, **6**, 89–95.
152 M. R. Powell, M. Sullivan, I. Vlassiouk, D. Constantin, O. Sudre, C. C. Martens, R. S. Eisenberg and Z. S. Siwy, *Nat. Nanotechnol.*, 2008, **3**, 51–57.
153 M. Aziz, J. Golovchenko, D. Branton, C. McMullan, D. Stein and J. Li, *Nature*, 2001, **412**, 166–169.
154 C. D. Lorenz and A. Travesset, *Phys. Rev. E: Stat., Nonlinear, Soft Matter Phys.*, 2007, **75**, 061202.
155 C. Wei, A. Bard and S. Feldberg, *Anal. Chem.*, 1997, **69**, 4627–4633.
156 B. Luan and A. Aksimentiev, *Soft Matter*, 2010, **6**, 243–246.
157 N. R. Haria and C. D. Lorenz, *Phys. Chem. Chem. Phys.*, 2012, **14**, 5935–5944.
158 E. R. Cruz-Chu, T. Ritz, Z. S. Siwy and K. Schulten, *Faraday Discuss.*, 2009, **143**, 47–62.
159 E. Cruz-Chu and K. Schulten, *ACS Nano*, 2010, **4**, 4463–4474.
160 C. A. Merchant, K. Healy, M. Wanunu, V. Ray, N. Peterman, J. Bartel, M. D. Fischbein, K. Venta, Z. Luo, A. T. C. Johnson and M. Drndic, *Nano Lett.*, 2010, **10**, 2915–2921.
161 G. Schneider, S. Kowalczyk, V. Calado, G. Pandraud, H. Zandbergen, L. Vandersypen and C. Dekker, *Nano Lett.*, 2010, **10**, 3163–3167.
162 Y. Liu, X. Dong and P. Chen, *Chem. Soc. Rev.*, 2012, **41**, 2283–2307.
163 L. Delemotte, M. Tarek, M. L. Klein, C. Amaral and W. Treptow, *Proc. Natl. Acad. Sci. U. S. A.*, 2011, **108**, 6109–6114.
164 D. Doyle, J. Cabral, R. Pfuetzner, A. Kuo, J. Gulbis, S. Cohen, B. Chait and R. MacKinnon, *Science*, 1998, **280**, 69–77.
165 M. Zhou and R. MacKinnon, *J. Mol. Biol.*, 2004, **338**, 839–846.
166 S. Berneche and B. Roux, *et al.*, *Nature*, 2001, **414**, 73–76.
167 S. Bernèche and B. Roux, *Proc. Natl. Acad. Sci. U. S. A.*, 2003, **100**, 8644.
168 W. Treptow and M. Tarek, *Biophys. J.*, 2006, **91**, L81–L83.
169 F. Bezanilla and C. Armstrong, *J. Gen. Physiol.*, 1972, **60**, 588–608.
170 S. Noskov, S. Berneche and B. Roux, *Nature*, 2004, **431**, 830–834.
171 B. Egwolf and B. Roux, *J. Mol. Biol.*, 2010, **401**, 831–842.
172 M. Thomas, D. Jayatilaka and B. Corry, *Biophys. J.*, 2007, **93**, 2635–2643.
173 S. Varma and S. Rempe, *Biophys. J.*, 2007, **93**, 1093–1099.
174 P. W. Fowler, K. Tai and M. S. Sansom, *Biophys. J.*, 2008, **95**, 5062–5072.
175 B. Roux, *Biophys. J.*, 2010, **98**, 2877.
176 D. Bucher, L. Guidoni, P. Carloni and U. Rothlisberger, *Biophys. J.*, 2010, **98**, L47–L49.
177 T. Whitfield, S. Varma, E. Harder, G. Lamoureux, S. Rempe and B. Roux, *J. Chem. Theory Comput.*, 2007, **3**, 2068–2082.
178 Y. Zhou, J. Morais-Cabral, A. Kaufman and R. MacKinnon, *Nature*, 2001, **414**, 43–48.
179 S. Bernèche and B. Roux, *Structure*, 2005, **13**, 591–600.
180 J. Cordero-Morales, L. Cuello, Y. Zhao, V. Jogini, D. Cortes, B. Roux and E. Perozo, *Nat. Struct. Mol. Biol.*, 2006, **13**, 311–318.
181 C. Domene, S. Vemparala, S. Furini, K. Sharp and M. L. Klein, *J. Am. Chem. Soc.*, 2008, **130**, 3389–3398.
182 M. Compoint, F. Picaud, C. Ramseyer and C. Girardet, *J. Chem. Phys.*, 2005, **122**, 134707.
183 L. Cuello, V. Jogini, D. Cortes and E. Perozo, *Nature*, 2010, **466**, 203–208.
184 L. Cuello, V. Jogini, D. Cortes, A. Pan, D. Gagnon, O. Dalmas, J. Cordero-Morales, S. Chakrapani, B. Roux and E. Perozo, *Nature*, 2010, **466**, 272–275.
185 H. Wang, X. Cheng, P. Taylor, J. McCammon and S. Sine, *PLoS Comput. Biol.*, 2008, **4**, e41.
186 B. Corry, *Energy Environ. Sci.*, 2011, **4**, 751–759.
187 T. A. Hilder, D. Gordon and S.-H. Chung, *Nanomed.: Nanotechnol., Biol. Med.*, 2011, **7**, 702–709.
188 P. Hänggi and F. Marchesoni, *Rev. Mod. Phys.*, 2009, **81**, 387–442.

F. Publication on a channel from *Nocardia farcinica*

Pulling Peptides across Nanochannels: Resolving Peptide Binding and Translocation through the Hetero-oligomeric Channel from *Nocardia farcinica*

ARTICLE

Pulling Peptides across Nanochannels: Resolving Peptide Binding and Translocation through the Hetero-oligomeric Channel from *Nocardia farcinica*

Pratik Raj Singh, Iván Bárcena-Uribarri, Niraj Modi, Ulrich Kleinekathöfer, Roland Benz, Mathias Winterhalter,* and Kozhinjampara R Mahendran*

Jacobs University Bremen, Campus Ring 1, D-28759 Bremen, Germany

ABSTRACT We investigated translocation of cationic peptides through nanochannels derived from the Gram-positive bacterium *Nocardia farcinica* at the single-molecule level. The two subunits NfpA and NfpB form a hetero-oligomeric cation selective channel. On the basis of amino acid comparison we performed homology modeling and obtained a channel structurally related to MspA of *Mycobacterium smegmatis*. The quantitative single-molecule measurements provide an insight into transport processes of solutes through nanochannels. High-resolution ion conductance measurements in the presence of peptides of different charge and length revealed the kinetics of peptide binding. The observed asymmetry in peptide binding kinetics indicated a unidirectional channel insertion in the lipid bilayer. In the case of cationic peptides, the external voltage acts as a driving force that promotes the interaction of the peptide with the channel surface. At low voltage, the peptide just binds to the channel, whereas at higher voltage, the force is strong enough to pull the peptide across the channel. This allows distinguishing quantitatively between peptide binding and translocation through the channel.

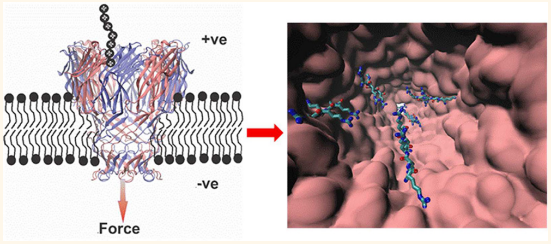

KEYWORDS: *Nocardia* · cationic peptides · applied voltage · binding kinetics · affinity

Bacterial cells continuously need to exchange small molecules, nutrients, and proteins with the exterior environment, simultaneously keeping toxic substances out. Selective transport of molecules through the cell wall is a fundamental process in bacterial life. Many of these processes involve channels made by aggregation of peptides, membrane proteins, or receptors.[1−6] For example, the cell walls of Gram-positive bacteria contain a thick peptidoglycan layer, which allows the permeation of hydrophilic substances up to a molecular mass of 100 kDa.[7] From this follows that unlike Gram-negative bacteria, Gram-positive bacteria do not require pore-forming proteins in their cell wall to transport hydrophilic molecules.[5,7] However, among this group of bacteria, a subgroup belonging to the order actinomycetales contains an even thicker cell wall with a large amount of lipid covalently linked *via* arabinogalactan to the peptidoglycan layer, termed mycolic acid.[7] This thick lipid layer is called the mycolic acid layer because of the presence of long-chain mycolic acids. It represents a second permeability barrier besides the cytoplasmic membrane. In recent years, water-filled pores have been identified in the mycolic acid layer of certain bacteria that allow the permeation of hydrophilic molecules into the space between the inner membrane and the mycolic acid layer. A well-studied channel belonging to this class of membrane channels includes MspA, a major porin of *Mycobacterium smegmatis*, mediating the exchange of hydrophilic solutes across the outer membrane.[7−9]

* Address correspondence to k.mahendran@jacobs-university.de, m.winterhalter@jacobs-university.de.

Received for review August 25, 2012 and accepted November 2, 2012.

Published online November 02, 2012
10.1021/nn303900y

This porin has an octameric goblet-like conformation. The constriction zone of the octameric MspA channel consists of 16 aspartate residues (D90/D91) creating a high density of negative charges, which likely explains the high cation selectivity of this porin.[8] Similar to *M. smegmatis*, the cell wall of the Gram-positive bacterium *Nocardia farcinica* contains also a cation-selective channel composed of two subunits, *N. farcinica porin A* (NfpA) *and N. farcinica porin B* (NfpB), that form together a channel in artificial lipid bilayers.[10−12] The *N. farcinica* channel (NfpA−NfpB) is a hetero-oligomer and structurally related to MspA of *M. smegmatis* based on amino acid comparison. The amino acid sequence alignment suggests an overall amino acid sequence identity of 11% between NfpA, NfpB, and MspA, whereas the identity between NfpA and NfpB is about 52%.[10−12]

The complexity of biological systems makes it important to study specific functions of membrane proteins *in vitro*. Techniques such as electrophysiology, computer simulations, and X-ray crystallography are used to investigate the translocation pathways of antibiotics, nutrients, genetic material (DNA), polyelectrolytes, and peptides across protein channels.[13−19] The purification from the native membrane and reconstitution of the purified protein into an artificial biomimetic membrane is the primary method by which the characterization of membrane proteins can be studied isolated from other components.[20] To obtain initial information on the function of membrane channels, the method of choice is to record the ion currents across the channel.[13,14,17] The underlying measuring principle is the huge difference in ion conductance between the insulating lipid membrane and ion conducting channel, allowing readily a first characterization of single channels with respect to pore size or ion selectivity.[2,16,17,22] Porins reconstituted into liposomes and planar lipid bilayers were recently used for measurements of substrate translocation.[20−22] As the energy barriers for influx of several substrates are asymmetric with channel orientation, it becomes interesting to investigate the orientation of reconstituted porins relative to their directionality *in vivo*.[22,23]

The interaction of polypeptides with transmembrane protein pores is of fundamental importance in biology.[24] Today most studies on the mechanism of protein and peptide translocation across lipid membranes used the ion channels alpha-hemolysin and aerolysin reconstituted into planar lipid bilayers as model translocation systems.[25−31] Here in this work, we express and purify outer membrane porin subunits from *N. farcinica*, NfpA and NfpB, that form hetero-oligomeric channels when reconstituted into planar lipid bilayers. The single-channel properties such as ion conductance, selectivity, and channel gating were investigated. We analyzed also the interaction pathways of the peptides by reconstituting single porins into artificial planar lipid bilayers and measuring the binding of peptides by time-resolved ion current blockages. Homology modeling of the *N. farcinica* channel with respect to MspA indicated that the channel is highly asymmetric in shape, and we probed the orientation of the channel in the lipid bilayers by adding peptides asymmetrically to either the cis or the trans side. Furthermore, we have shown that the entry and exit dynamics of charged peptides of different lengths with respect to the pore can be substantially altered by applying an external electric field. Therefore this effect can change the balance between the forces driving polymers into the pore and the forces driving them out.

RESULTS

Homology Modeling. The structural model of the *N. farcinica* channel was built based upon the Modeler suite of programs.[8,12] Initially, several iterations of the PSI-BLAST protein sequence search program in the PDB database were performed to allow detection of remote homologues of the *N. farcinica* channel. Only the templates with nonredundant structures were kept and further used for building the homology model. These templates included the MspA protein from *M. smegmatis*. The three-dimensional structure of MspA is known (PDB code: 1UUN) and therefore was used as a template to model the *N. farcinica* channel (NfpA−NfpB) structure.[8] From the modeled structure, it can be concluded that the *N. farcinica* channel forms a highly asymmetrically shaped channel similar to MspA, and in its heteroligomeric architecture, two subunits, NfpA and NfpB, are most likely to be arranged in an alternating fashion (Figure 1). In addition, the channel is cation selective with a cluster of negatively charged amino acids distributed through the channel lining and an electrostatic potential surface indicating a highly negative potential inside the lumen of the channel (Figure 1). Moreover, the periplasmic side (stem) of the channel consists of negatively charged residues clustered like a ring, yielding a high charge density, whereas, in the extracellular side (cap), negatively charged residues are scattered rather randomly along the channel surface.

Structural Asymmetry Causes Asymmetric Transport Properties. To test the structural prediction, single *N. farcinica* channels (NfpA and NfpB) were reconstituted into planar lipid bilayers. The single channel conductance was measured to be 3.0 $\pm$ 0.2 nS at 1 M KCl (Figure 2). The channel showed a slight asymmetry of conductance with respect to the polarity of the applied transmembrane potential, supporting the view of an asymmetrical channel reconstituted in lipid bilayers. In addition, the channels showed asymmetric closure with respect to the polarity of the applied voltage. At positive voltages, we observed that the threshold potential for channel closure was around 30 mV, whereas at negative voltage the threshold potential

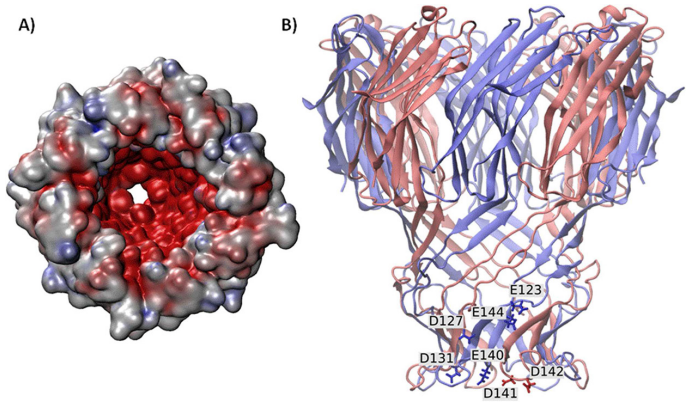

Figure 1. The modeled structure of the *N. farcinica porin A* (NfpA) and *N. farcinica* porin B (NfpB) subunits based on multiple templates of MspA from *M. smegmatis*. Negatively charged amino acid residues are clustered in the channel, resulting in high charge density. (A) Electrostatic potential surface of the modeled structure showing highly negative potential (red color surface) inside the lumen of the channel. (B) Four NfpA and four NfpB subunits are shown in red- and blue-colored secondary structures, respectively, where they are arranged in an alternating fashion. Negatively charged amino acid residues shown as sticks are clustered in the channel stem region, resulting in a high charge density.

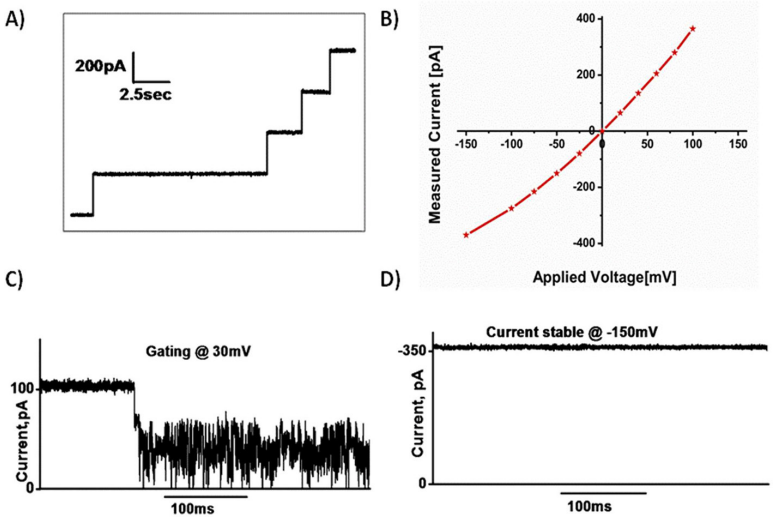

Figure 2. (A) Stepwise insertion of four *N. farcinica* channels reconstituted into planar lipid bilayers at −100 mV. (B) *I*−*V* curve of single-channel *N. farcinica* channel. Ionic currents through single *N. farcinica* channel at (C) +30 and (D) −150 mV. At 30 mV, the channel fluctuates between open and closed conductance state with random gating, whereas at −150 mV the channel exists in one open state. Experimental conditions are 1 M KCl, 10 mM HEPES, pH 7.4.

for channel closure was above 200 mV (Figure 2). The mechanism of this voltage-dependent closure of the channel is so far unclear. Moreover, ion selectivity measurements indicated that the channel is cation selective.[12]

Our model (Figure 1) is used for the interpretation of possible binding sites and their effect on the ion current. To elucidate the effect of the asymmetric structure on the transport properties, we characterized the translocation of differently sized polyarginines (tri, penta, and hepta) using ion current fluctuation analysis. Addition of triarginine to the cis side of the channel hardly induced any ion current blockages, showing negligible interaction of the peptide with the channel surface (Figure 3A). Titrating the channel with penta-arginine caused short, unresolved ion current flickering (Figure 3B). As expected, ion current flickering increased with increasing peptide concentration. Addition of the hepta-arginine causes fluctuations in a concentration- and voltage-dependent manner. However compared to penta-arginine, the number of events is higher (Figure 3C). Under negative potentials

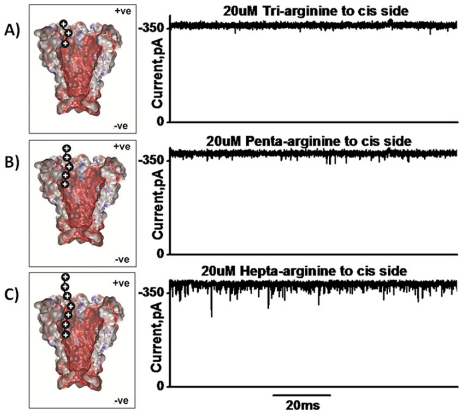

Figure 3. Typical ion current recordings through a single *N. farcinica* channel in the presence of 20 μM (A) triarginine, (B) penta-arginine, and (C) hepta-arginine added to the cis side of the lipid membrane with applied voltage of −150 mV. Experimental conditions are 1 M KCl, 10 mM HEPES, pH 7.4. Corresponding schematic representation showing peptide translocation through the channel driven by applied voltage.

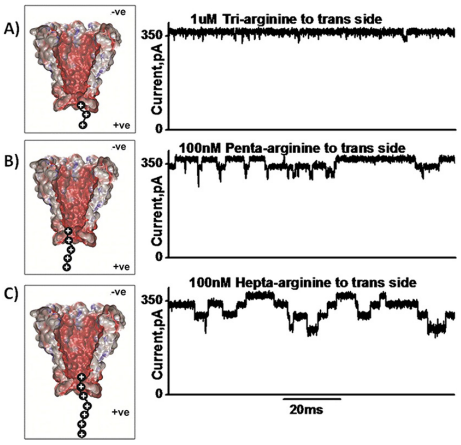

Figure 4. Typical ion current recordings through a single *N. farcinica* channel in the presence of (A) 1 μM triarginine, (B) 100 nM penta-arginine, and (C) 100 nM hepta-arginine added to the trans side of the lipid membrane with applied voltage of +100 mV. Experimental conditions are 1 M KCl, 10 mM HEPES, pH 7.4. Corresponding schematic representation showing peptide translocation through the channel driven by applied voltage.

the addition of peptides on the cis side of the chamber increased the number of events, whereas positive voltages had no effect (*i.e.*, created no blockage events). We hypothesize that when peptide enters the channel through the extracellular side, there is enough space for the ions to pass through, which means cis side addition of the peptide does not produce pronounced blocking.

Reversing the external voltage and the side of peptide addition revealed the asymmetry of the channel. Addition of peptides to the trans side induced pronounced blocking of the channel, indicating strong interaction with the channel surface but with reversed voltage dependence: positive voltages induced ion current blockages, whereas at negative voltages no ion current blockages were produced. As mentioned above, the frequency of channel closure (gating) in the absence of the peptide drastically increased at positive voltages. To distinguish between spontaneous and peptide-induced gating of the channel, we selected the time interval that showed only little intrinsic gating. Triarginine (1 μM) added to the trans side of the membrane produced short but visible ion current blockage events (Figure 4A). In contrast, penta-arginine and hepta-arginine strongly interacted with the channel, resulting in ion current blockages in different steps with reduction in the ion conductance (Figure 4B and C). The corresponding amplitude histogram showing the different conductance states is shown in supplementary Figure 1. This indicated that longer peptides have multiple binding sites in the channel. It is important to note that a concentration in the low nanomolar range of these peptides added to the trans side is strong enough to block the channel as compared to addition of peptide to the cis side. The strength of the channel−peptide interaction is in the order hepta-arginine > penta-arginine > triarginine. The channel blockades caused by the peptides penta-arginine and hepta-arginine are greater in amplitude and duration than those for a short peptide, triarginine. We hypothesize that in the case of trans side addition of the peptide, the negative charges clustered in rings on the periplasmic entry strongly interact with the peptide and there is only limited space for the ions to pass through. As a result, we observed strong blocking of the channel by the peptide. From the asymmetrical addition of the peptide, we concluded that the channel is oriented in the bilayers with the extracellular part at the cis side and the periplasmic part inserted into lipid bilayers that can easily be accessed from the trans side.

Previously it has been shown that noise analysis of the single-channel level revealed asymmetries in channel transport.[14,22] Such asymmetries are often hidden in membrane preparations with multiple insertions, in which the channel orientation appeared to be equally distributed. Previous analysis of the ion current fluctuations under asymmetric conditions revealed that the kinetics of sugar entry depends on the side of addition for maltoporin reconstituted into artificial lipid bilayers.[22] Moreover, chemical modifications of the sugar allowed only the entry of the sugar on one side but no permeation. This enabled us to distinguish translocation from entry and bouncing back to the same side. It has been shown that maltoporin catalyzes the transport more efficiently from the outside to the inside than under reversed asymmetric conditions.[14,22,23,34]

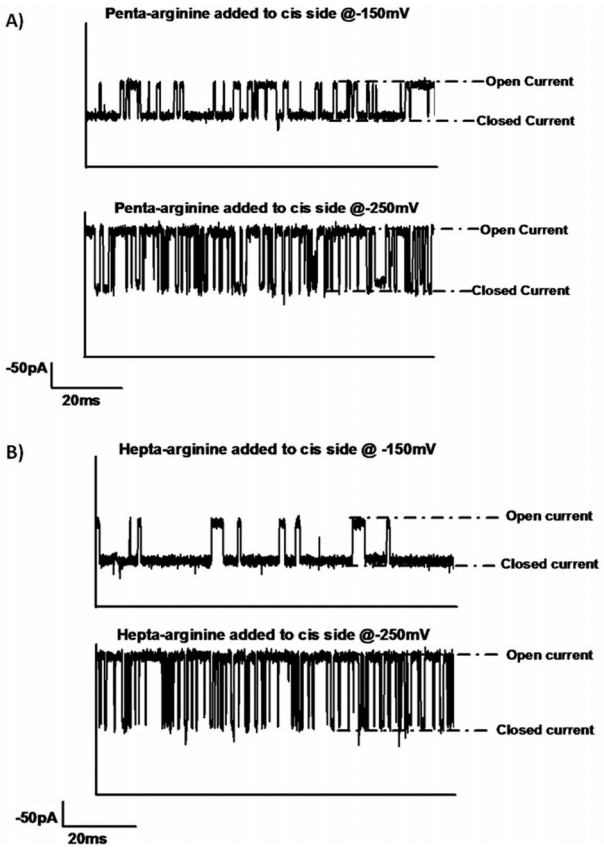

Figure 5. Typical ion current recordings through a single *N. farcinica* channel in the presence of (A) penta-arginine added to the cis side at −150 and −250 mV and (B) hepta-arginine added to the *cis* side at −150 and −250 mV. The closed current represents the time spent by the peptide in the channel or the residence time of the peptide. Experimental conditions are 150 mM KCl, 10 mM HEPES, pH 7.4.

Here we extended our study toward interaction of peptides with the hetero-oligomeric channel from *N. farcinica*. As shown in Figure 1, the channel consists of an extracellular part of large diameter, whereas the periplasmic side consists of a rather narrow opening. The addition of cationic peptides of different charge and length produced an asymmetry in the peptide binding kinetics that can be used to distinguish the orientation of the channel reconstituted into lipid bilayers.

Resolving Binding and Translocation. To elucidate the electrostatic contributions of peptide interaction with the channel surface, we reduced the salt concentration from 1 M to 150 mM KCl and investigated the peptide binding kinetics by single-channel analysis. Addition of penta-arginine and hepta-arginine to the cis side of the channel produced well-defined ion current blockage events. The channel fluctuated between the fully open conductance state and the closed conductance state (Figure 5). The frequency and duration of the ion current fluctuations depended strongly on the applied voltage and peptide concentration. The number of peptide blocking events and the average residence time of the peptide blockage increased at low salt concentration, which indicated charge effects on the peptide−channel interaction. The peptide binding kinetics was derived from the two factors τ_c (blockage time) and τ_o (open time or time between successful blockage) fitted with an exponential fit of the open and closed time histogram. We found that the reciprocal of τ_o (the mean interevent interval) is linearly dependent on the polypeptide concentration, whereas τ_c (the mean dwell time) is independent of the polypeptide concentration. The applied voltage serves as the main driving force to pull the cationic peptides from the aqueous bath to the channel surface. We plotted τ_c and τ_o as a function of the applied voltage from −100 mV to −250 mV for the cis side addition of the peptide (Figure 6). The plot of average residence time as a function of the applied voltage allows distinguishing peptide binding from the translocation. The τ_c is higher for hepta-arginine as compared to penta-arginine (supplementary

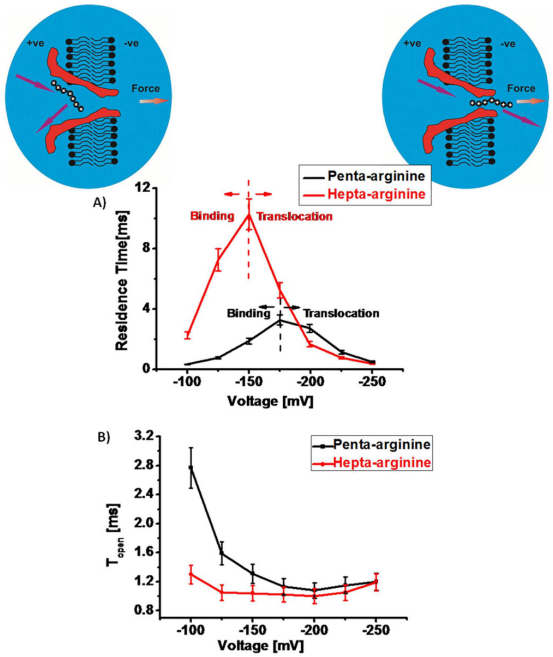

Figure 6. (A) The residence time and (B) the open channel time as a function of the applied voltage (−100 to −250 mV) for penta-arginine and hepta-arginine. Experimental conditions are 150 mM KCl, 10 mM HEPES, pH 7.4. Peptide is added to the cis side of the channel.

TABLE 1. Rate Constants of Peptide Association (k_{on}) and Dissociation (k_{off}) and Equilibrium Binding Constant K of the Interaction between Peptide and *Nocardia farcinica* Channel

penta-arginine				hepta-arginine			
voltage [mV]	K_{on} [M^{-1} s^{-1}] × 10^9	K_{off} [s^{-1}] × 10^3	K [M^{-1}] × 10^7	voltage [mV]	K_{on} [M^{-1} s^{-1}] × 10^9	K_{off} [s^{-1}] × 10^3	K [M^{-1}] × 10^7
−100	2.5 ± 0.2	2.4 ± 0.24	0.11 ± 0.01	−100	7.7 ± 0.8	0.4 ± 0.04	1.74 ± 0.02
−150	5.8 ± 0.5	0.6 ± 0.05	1.06 ± 0.1	−150	9.6 ± 0.9	0.09 ± 0.01	9.88 ± 0.04
−250	7.6 ± 0.7	1.9 ± 0.20	0.39 ± 0.04	−250	8.4 ± 0.8	2.7 ± 0.3	0.31 ± 0.02

Figure 2). In case of hepta-arginine τ_c increased with increasing voltage from −100 mV to −150 mV, which indicated that hepta-arginine just binds to the channel without effective translocation. Surprisingly, when the voltage was increased above −150 mV, we observed a decrease in the average residence time with increasing voltage, suggesting successful translocation of the peptide through the channel. The threshold potential for pulling hepta-arginine through the channel was calculated to be ∼−150 mV, where force is strong enough to drag the peptide from the binding site of the channel. In the case of penta-arginine, we observed a similar behavior of increase in the residence time at lower voltages and a decrease in residence time at higher voltage. However, the threshold potential for effective translocation to pull the peptide out of the channel was calculated to be ∼−175 mV. The τ_o decreased with increasing concentration of peptide and increasing applied voltage. Addition of the peptide to the trans side completely closed the channel due to strong binding at low salt concentration caused by charge effects. Subsequently τ_o and τ_c could not be obtained. The results suggested a simple bimolecular interaction between the polypeptide and the pore. The rate constants of association k_{on} can be derived from the slopes of plots of $1/\tau_o$ *vs* [pept], where [pept] is the peptide concentration in the aqueous phase. The rate constants of dissociation (k_{off}) were determined by averaging the $1/\tau_c$ values recorded over the whole concentration range. The equilibrium association constant was then calculated by using $K = k_{on}/k_{off}$, which gives the affinity of the peptide to the channel. Peptide binding kinetics for penta-arginine and hepta-arginine are summarized in Table 1.

Most approaches investigate the modulation of the ion current through channels in the presence of permeating solutes caused by slight size differences.[13,17,33] However, the translocation of macromolecules through nanopores is not only determined by the size but to a large extent also influenced by electrostatic,

hydrodynamic, hydrophobic, and van der Waals interactions with the nanopore walls.[13−19] The quantification of transported uncharged molecules across a few nanometer long channels remains experimentally a challenge. Ensemble measurements on liposomes (liposome swelling) have only a limited time resolution.[20] The above-described method of noise analysis of the ion current has a number of unique advantages, among others, the use of very little material with single-molecule resolution, the potential for parallelization, and the relatively good time resolution. However, with respect to the translocation of uncharged molecules, a direct conclusion from binding on transport is not possible.[32] In contrast for charged compounds, the applied transmembrane voltage is the driving force to pull the molecule out of the channel.

In particular pulling DNA through nanopores for next-generation sequencing remains a very prominent research area.[6,19,36] Despite the rapid development of single-molecule techniques, the underlying mechanisms and forces in this molecular transport are poorly characterized and not fully understood. Previously it has been shown that solid-state nanopores and biological nanopores have been used to study the coupling between protein translocation and folding.[7,24,28−31,33] This allows for detection and analysis in real-time protein translocation events. For example, alpha hemolysin was used to study the partitioning of synthetic cationic alanine-based peptides.[25−27] The kinetics of association and dissociation rate constants obtained from a single alpha hemolysin channel in the presence of micromolar concentrations of peptide are strongly dependent on the transmembrane voltage and peptide length.[31]

CONCLUSION

Here in this work, we introduced a new type of channel, a novel hetero-oligomeric nanochannel derived from *N. farcinica*. In the present contribution, we showed an experimental strategy to illuminate various kinetic contributions to polypeptide translocation through the *N. farcinica* channel reconstituted into lipid bilayers. We have been able to measure time-resolved single-molecule events of peptide entry into the pore and obtain detailed kinetic information. Moreover, it has been discussed that *N. farcinica* channels reconstituted into planar lipid bilayers have asymmetric properties in both ion conductance and peptide binding. This asymmetry in the peptide binding reveals that channel insertion is unidirectional. The applied transmembrane voltage acts as a possible driving force for diffusion of cationic macromolecules through the channel. We hypothesize that the binding is enhanced at low voltages and that with increasing applied voltage the peptide is pulled out of the channel, resulting in successful translocation. The kinetic data obtained from our single-channel measurements can be used to distinguish the peptide binding events from the translocation events. In conclusion this work demonstrates that a biological nanopore can represent a versatile single-molecule tool for exploring protein interactions.

METHOD

Purification of Two Subunits of Porins from *Nocardia farcinica*. The purification of the two subunits NfpA and NfpB expressed in *E. coli* BL21 (DE3) Omp8 was performed as described previously.[12,37] In brief, the genes flanked with 10 histidine residues were cloned into the expression plasmid pARAJS2 containing an arabinose-induced promoter sequence.[38] This plasmid had been prepared, and the porin-deficient *E.coli* Omp8 cells containing the plasmid were grown in an LB-ampicillin media at 37 °C until it reached the OD_{600} of 0.5−0.9. The cells were then induced with 0.02% of arabinose for overexpression and were grown at 16 °C for 16 h. The cell broth was centrifuged at 5000*g* for 10 min at 4 °C, and the pellet was resuspended in 10 mM Tris pH 8. The resuspended pellet was later broken down by French press, and the cell debris was obtained by centrifugation at 5000*g* for 10 min at 4 °C. The supernatant was ultracentrifuged at 48000*g* for 1 h at 4 °C to obtain a supernatant containing the cytosolic proteins and the pellet containing membrane proteins. Our proteins of interest were found to be present in both the supernatant and pellet fractions. The protein present in the supernatant fraction was obtained as inclusion bodies that were not large enough to pellet down during ultracentrifugation. The temperature of 16 °C used for cell growth after induction with arabinose facilitated the smaller aggregation of proteins as inclusion bodies. Nevertheless, the His-Tag protein purification from the supernatant fraction had to be performed under denaturating conditions using urea buffer. The purification under denaturating conditions was performed by suspending 1 mL of the supernatant in 4 mL of 8 M urea/10 mM Tris/200 μL Ni-Sepharose High Performance/20 mM imidazole pH 8 buffer for 6 h at room temperature. The beads were then extensively washed with 8 M urea/10 mM Tris/100 mM imidazole pH 8 to remove impurities. Later the NfpA/NfpB proteins were eluted with the solution containing 8 M urea/10 mM Tris/500 mM imidazole pH 8. The expression and purification of proteins were monitored by SDS page and Western blot in every step. The two subunits, purified separately, were refolded together to form a hetero-oligomeric channel by ammonium sulfate precipitation. The two purified subunits were mixed together in a 1:1 ratio and precipitated using saturated ammonium sulfate solution. The solution was incubated overnight and was centrifuged at 18000*g* for 30 min to remove the supernatant. The precipitated protein pellet was refolded to native state by incubating for 12 h in 10 mM Tris-HCl with 1% Triton X-100 and 150 mM NaCl.[12]

Solvent-Free Lipid Bilayer Technique. Reconstitution experiments and noise analysis have been performed as described in detail previously.[32,35] The phospholipid bilayer was formed with DPhPC (1,2-diphytanoyl-*sn*-glycero-3-phosphocholine) by employing the classic Montal and Muller technique.[35] A Teflon cell with an approximately 50 μm diameter aperture in the 25 μm thick Teflon partition was placed between the two chambers of the cuvette. The aperture was small enough to form a stable bilayer with the possibility of protein insertion. As the electrolyte, 1 M KCl, 10 mM HEPES, pH 7.4 was used and added to both sides of the chamber unless otherwise indicated. Standard silver−silver chloride electrodes from WPI (World Precision Instruments) were placed in each chamber to measure the ion current. For single-channel measurement, small amounts of porin were added to the cis-side of the chamber

(side connected to the ground electrode). Spontaneous channel insertion was usually obtained while stirring under applied voltage. In order to prevent insertion of more than one porin, the cis side of the chamber was carefully diluted with the same buffer to remove the remaining channels. Conductance measurements were performed using an Axopatch 200B amplifier (Axon Instruments) in the voltage clamp mode. Signals were filtered by an on board low pass Bessel filter at 10 kHz and recorded onto a computer hard drive with a sampling frequency of 50 kHz. Amplitude, probability, and noise analyses were performed using Origin (Microcal Software Inc.) and Clampfit (Axon Instruments) software. Single channel analysis was used to determine the peptide binding kinetics. To obtain good statistics for the results, the experiments were repeated five times with different *N. farcinica* channels. We determined the association and dissociation rate constants and the partitioning data from single-channel recordings of the *N. farcinica* channel. In a single-channel measurement the usual measured quantities as illustrated in Figure 6 are the duration of closed levels residence time (τ_c) and open channel time (τ_o), or for short blockages the average residence time (τ_c) and the number of blockage events per second.

Conflict of Interest: The authors declare no competing financial interest.

Acknowledgment. The authors are grateful for financial support through the Deutsche Forschungsgemeinschaft (DFG WI 2278/18-1) and from Jacobs University Bremen.

Supporting Information Available: Amplitude histogram showing fluctuation of the channel between different conductance steps in the presence of penta-arginine and hepta-arginine; dwell time histogram for closed time and open time in the presence of penta-arginine and hepta-arginine; concentration dependence of peptide interaction with the channel; hepta-arginine added to trans side of the chamber at low salt concentration. This information is available free of charge *via* the Internet at http://pubs.acs.org.

REFERENCES AND NOTES

1. Benz, R.; Janko, K.; Boos, W.; Läuger, P. Formation of Large, Ion-Permeable Membrane Channels by the Matrix Protein (porin) of *Escherichia coli*. *Biochim. Biophys. Acta* **1978**, *511*, 305–319.
2. Mueller, P.; Rudin, D. O. Induced Excitability in Reconstituted Cell Membrane Structure. *J. Theor. Biol.* **1963**, *4*, 268–280.
3. Benz, R.; Schmid, A.; Hancock, R. E. Ion Selectivity of Gram-Negative Bacterial Porins. *J. Bacteriol.* **1985**, *162*, 722–727.
4. Luckey, M.; Nikaido, H. Diffusion of Solutes Through Channels Produced by Phage Lambda Receptor Protein of *Escherichia coli*: Inhibition by Higher Oligosaccharides of Maltose Series. *Biochem. Biophys. Res. Commun.* **1980**, *93*, 166–171.
5. Nikaido, H. Porins and Specific Channels of Bacterial Outer Membranes. *Mol. Microbiol.* **1992**, *6*, 435–442.
6. Hall, A. R.; Scott, A.; Rotem, D.; Mehta, K. K.; Bayley, H.; Dekker, C. Hybrid Pore Formation by Directed Insertion of Alpha-Hemolysin into Solid-State Nanopores. *Nat. Nanotechnol.* **2011**, *5*, 874–877.
7. Brennan, P. J.; Nikaido, H. The Envelope of Mycobacteria. *Annu. Rev. Biochem.* **1995**, *64*, 29–63.
8. Faller, M.; Niederweis, M.; Schulz, G. E. The structure of a Mycobacterial Outer-Membrane Channel. *Science* **2004**, *303*, 1189–1192.
9. Stahl, C.; Kubetzko, S.; Kaps, I.; Seeber, S.; Engelhardt, H; Niederweis, M. MspA Provides the Main Hydrophilic Pathway through the Cell Wall of *Mycobacterium smegmatis*. *Mol. Microbiol.* **2001**, *40*, 451–464.
10. Riess, F. G.; Lichtinger, T.; Yassin, A. F.; Schaal, K. P.; Benz, R. The Cell Wall Porin of The Gram-Positive Bacterium *Nocardia asteroides* forms Cation-Selective Channels that Exhibit Asymmetric Voltage Dependence. *Arch. Microbiol.* **1999**, *171*, 173–182.
11. Riess, F. G.; Lichtinger, T.; Cseh, R.; Yassin, A. F.; Schaal, K. P.; Benz, R. The Cell Wall Porin of *Nocardia farcinica*: Biochemical Identification of The Channel-Forming Protein and Biophysical Characterization of The Channel Properties. *Mol. Microbiol.* **1998**, *29*, 139–150.
12. Kläckta, C.; Knörzer, P.; Riess, F.; Benz, R. Hetero-Oligomeric Cell Wall Channels (porins) of *Nocardia farcinica*. *Biochim. Biophys. Acta, Biomembr.* **2011**, *1808*, 1601–1610.
13. Bezrukov, S. M.; Vodyanoy, I.; Parsegian, V. A. Counting Polymers Moving Through a Single Ion Channel. *Nature* **1994**, *370*, 279–281.
14. Nekolla, S.; Andersen, C.; Benz, R. Noise Analysis of Ion Current Through The Open and The Sugar-Induced Closed State of the LamB Channel of *Escherichia coli* Outer Membrane: Evaluation of the Sugar Binding Kinetics to the Channel Interior. *Biophys. J.* **1994**, *66*, 1388–1397.
15. Aksimentiev, A.; Schulten, K. Imaging Alpha-Hemolysin with Molecular Dynamics: Ionic Conductance, Osmotic Permeability, and the Electrostatic Potential Map. *Biophys. J.* **2005**, *88*, 3745–3761.
16. Merzlyak, P. G.; Yuldasheva, L. N.; Rodrigues, C. G.; Carneiro, C. M.; Krasilnikov, O. V.; Bezrukov, S. M. Polymeric Nonelectrolytes to Probe Pore Geometry: Application to the Alpha-Toxin Transmembrane Channel. *Biophys. J.* **1999**, *77*, 3023–3033.
17. Bezrukov, S. M. Ion Channels as Molecular Coulter Counters to Probe Metabolite Transport. *J. Membr. Biol.* **2000**, *174*, 1–13.
18. Wong, C. T.; Muthukumar, M. Polymer Translocation through Alpha-Hemolysin Pore with Tunable Polymers-Pore Electrostatic Interactions. *J. Chem. Phys.* **2010**, *133*, 045101.
19. Muthukumar, M. Mechanism of DNA Transport through Pores. *Annu. Rev. Biophys. Biomol. Struct.* **2007**, *36*, 435–450.
20. Nikaido, H.; Rosenberg, E. Y. Porin Channels in *Escherichia coli*: Studies with Liposomes Reconstituted from Purified Proteins. *J. Bacteriol.* **1983**, *153*, 241–252.
21. Eren, E.; Vijayaraghavan, J.; Liu, J.; Cheneke, B. R.; Touw, D. S.; Lepore, B. W.; Indic, M.; Movileanu, L.; Van den Berg, B. Substrate Specificity within a Family of Outer Membrane Carboxylate Channels. *PLoS Biol.* **2012**, *10*, e1001242.
22. Danelon, C.; Brando, T.; Winterhalter, M. Probing the Orientation of Reconstituted Maltoporin Channels at the Single-Protein Level. *J. Biol. Chem.* **2003**, *278*, 35542–35551.
23. Kullman, L.; Gurnev, P. A.; Winterhalter, M.; Bezrukov, S. M. Functional Subconformations in Protein Folding: Evidence from Single-Channel Experiments. *Phys. Rev. Lett.* **2006**, *96*, 038101.
24. Dobson, C. M. Protein Folding and Misfolding. *Nature* **2003**, *426*, 884–890.
25. Mohammad, M. M.; Movileanu, L. Excursion of a Single Polypeptide into a Protein Pore: Simple Physics, but Complicated Biology. *Eur. Biophys. J.* **2008**, *37*, 913–925.
26. Movileanu, L.; Schmittschmitt, J. P.; Scholtz, J. M.; Bayley, H. Interactions of Peptides with a Protein Pore. *Biophys. J.* **2005**, *89*, 1030–1045.
27. Wolfe, A. J.; Mohammad, M. M.; Cheley, S.; Bayley, H.; Movileanu, L. Catalyzing The Translocation of Polypeptides through Attractive Interactions. *J. Am. Chem. Soc.* **2007**, *129*, 14034–14041.
28. Oukhaled, G.; Mathé, J.; Biance, A. L.; Bacari, L.; Betton, J. M.; Lairez, D.; Pelta, J.; Auvray, L. Unfolding of Proteins and Long Transient Conformations Detected by Single Nanopore Recording. *Phys. Rev. Lett.* **2007**, *98*, 158101–158104.
29. Pastoriza-Gallego, M.; Rabah, L.; Gibrat, G.; Thiebot, B.; Van der Goot, F. G.; Auvray, L.; Betton, J. M.; Pelta, J. Dynamics of Unfolded Protein Transport through an Aerolysin Pore. *J. Am. Chem. Soc.* **2010**, *133*, 2923–2931.
30. Bikwemu, R.; Wolfe, A. J.; Xing, X.; Movileanu, L. Facilitated Translocation of Polypeptides through a Single Nanopore. *J. Phys.: Condens. Matter* **2010**, *22*, 454117.
31. Meng, H.; Detillieux, D.; Baran, C.; Krasniqi, B.; Christensen, C.; Madampage, C.; Stefureac, R. I.; Lee, J. S. Nanopore Analysis of Tethered Peptides. *J. Pept. Sci.* **2010**, *16*, 701–708.

32. Mahendran, K.; Hajjar, E.; Mach, T.; Lovelle, M.; Sousa, I.; Kumar, A.; Spiga, E.; Weingart, H.; Gameiro, P.; Winterhalter, M.; *et al*. Molecular Basis of Enrofloxacin Translocation through a Bacterial Porin —When Binding does not Imply Translocation. *J. Phys. Chem. B* **2010**, *114*, 5170–5179.
33. Cressiot, B.; Oukhaled, A.; Patriarche, G.; Pastoriza-Gallego, M.; Betton, J. M.; Auvray, L.; Muthukumar, M.; Bacri, L.; Pelta, J. Protein Transport through a Narrow Solid-State Nanopore at High Voltage: Experiments and Theory. *ACS Nano* **2012**, *6*, 6236–6243.
34. Berezhkovskii, A. M.; Bezrukov, S. M. Optimizing Transport of Metabolites through Large Channels: Molecular Sieves with and without Binding. *Biophys. J.* **2005**, *88*, L17–L19.
35. Montal, M.; Müller, P. Formation of Bimolecular Membranes from Lipid Monolayers and a Study of their Electrical Properties. *Proc. Natl. Acad. Sci. U. S. A.* **1972**, *69*, 3561–3566.
36. Wallace, E. V.; Stoddart, D.; Heron, A. J.; Mikhailova, E.; Maglia, G.; Donohoe, T. J.; Bayley, H. Identification of Epigenetic DNA Modifications with a Protein Nanopore. *Chem. Commun. (Cambridge, U.K.)* **2010**, *46*, 8195–8197.
37. Prilipov, A.; Phale, P. S.; Van Gelder, P.; Rosenbusch, J.; Koebnik, R. Coupling Site-Directed Mutagenesis with High-Level Expression: Large Scale Production of Mutant Porins from *E. coli*. *FEMS Microbiol. Lett.* **1998**, *163*, 65–72.
38. Polleichtner, G.; Andersen, C. The Channel-Tunnel HI1462 of *Haemophilus influenzae* reveals Differences to *Escherichia coli* TolC. *Microbiology* **2006**, *152*, 1639–1647.

Bibliography

[1] Bertil Hille. *Ion Channels of Excitable Membranes* (Sinauer, Sunderland, MA, 2001), 3rd edition.

[2] E. Gouaux and R. MacKinnon. *Principles of selective ion transport in channels and pumps*. Science **310** (2005) 1461.

[3] N. Modi, M. Winterhalter and U. Kleinekathöfer. *Computational modeling of ion transport through nanopores*. Nanoscale **4** (2012) 6166.

[4] D. C. Camerino, J.-F. Desaphy, D. Tricarico, S. Pierno and A. Liantonio. *Therapeutic approaches to ion channel diseases*. Adv. Genet. **64** (2008) 81.

[5] J. Overington, B. Al Lazikani and A. Hopkins. *How many drug targets are there?* Nat. Rev. Drug Discovery **5** (2006) 993.

[6] X. Hou, W. Guo and L. Jiang. *Biomimetic smart nanopores and nanochannels*. Chem. Soc. Rev. **40** (2011) 2385.

[7] A. Aksimentiev. *Deciphering ionic current signatures of DNA transport through a nanopore*. Nanoscale **2** (2010) 468.

[8] S. Howorka and Z. Siwy. *Nanopore analytics: sensing of single molecules*. Chem. Soc. Rev. **38** (2009) 2360.

[9] P. J. Bond, A. T. Guy, A. J. Heron, H. Bayley and S. Khalid. *Molecular dynamics simulations of DNA within a nanopore: Arginine- phosphate tethering and a binding/sliding mechanism for translocationde*. Biochemistry **50** (2011) 3777.

[10] A. T. Guy, T. J. Piggot and S. Khalid. *Single-stranded dna within nanopores: conformational dynamics and implications for sequencing; a molecular dynamics simulation study*. Biophys. J. **103** (2012) 1028.

[11] D. Doyle, J. Cabral, R. Pfuetzner, A. Kuo, J. Gulbis, S. Cohen, B. Chait and R. MacKinnon. *The structure of the potassium channel: molecular basis of K^+ conduction and selectivity*. Science **280** (1998) 69.

[12] M. Zhou and R. MacKinnon. *A mutant KcsA K^+ channel with altered conduction properties and selectivity filter ion distribution*. J. Mol. Biol. **338** (2004) 839.

[13] F. Bezanilla and C. Armstrong. *Negative conductance caused by entry of sodium and cesium ions into the potassium channels of squid axons*. J. Gen. Physiol. **60** (1972) 588.

[14] S. Noskov, S. Bernéche and B. Roux. *Control of ion selectivity in potassium channels by electrostatic and dynamic properties of carbonyl ligands*. Nature **431** (2004) 830.

[15] B. Egwolf and B. Roux. *Ion selectivity of the KcsA channel: a perspective from multi-ion free energy landscapes*. J. Mol. Biol. **401** (2010) 831.

[16] M. Thomas, D. Jayatilaka and B. Corry. *The predominant role of coordination number in potassium channel selectivity*. Biophys. J. **93** (2007) 2635.

[17] S. Varma and S. Rempe. *Tuning ion coordination architectures to enable selective partitioning*. Biophys. J. **93** (2007) 1093.

[18] P. W. Fowler, K. Tai and M. S. Sansom. *The selectivity of K^+ ion channels: testing the hypotheses*. Biophys. J. **95** (2008) 5062.

[19] B. Roux. *Exploring the ion selectivity properties of a large number of simplified binding site models*. Biophys. J. **98** (2010) 2877.

[20] D. Bucher, L. Guidoni, P. Carloni and U. Rothlisberger. *Coordination numbers of K^+ and Na^+ ions inside the selectivity filter of the KcsA potassium channel: insights from first principles molecular dynamics*. Biophys. J. **98** (2010) L47.

[21] T. Whitfield, S. Varma, E. Harder, G. Lamoureux, S. Rempe and B. Roux. *Theoretical study of aqueous solvation of K+ comparing ab initio, polarizable, and fixed-charge models*. J. Chem. Theory Comput. **3** (2007) 2068.

[22] J. Cohen and K. Schulten. *Mechanism of anionic conduction across ClC*. Biophys. J. **86** (2004) 836.

[23] I. Ivanov, X. Cheng, M. Steven and J. McCammon. *Barriers to ion translocation in cationic and anionic receptors from the Cys-loop family*. J. Am. Chem. Soc. **129** (2007) 8217.

[24] H. Wang, X. Cheng, P. Taylor, J. McCammon and S. Sine. *Control of cation permeation through the nicotinic receptor channel*. PLoS Comput. Biol. **4** (2008) e41.

[25] A. Aksimentiev and K. Schulten. *Imaging alpha-hemolysin with molecular dynamics: ionic conductance, osmotic permeability, and the electrostatic potential map*. Biophys. J. **88** (2005) 3745.

[26] S. Bhattacharya, L. Muzard, L. Payet, J. Mathé, U. Bockelmann, A. Aksimentiev and V. Viasnoff. *Rectification of the current in alpha-hemolysin pore depends on the cation type: the alkali series probed by MD simulations and experiments*. J. Phys. Chem. C **115** (2011) 4255.

[27] S. Pezeshki, C. Chimerel, A. Bessenov, M. Winterhalter and U. Kleinekathöfer. *Understanding ion conductance on a molecular level: An all-atom modeling of the bacterial porin OmpF*. Biophys. J. **97** (2009) 1898.

[28] I. Biro, S. Pezeshki, H. Weingart, M. Winterhalter and U. Kleinekathöfer. *Comparing the temperature-dependentependent conductance of the two structurally similar E. coli porins OmpC and OmpF*. Biophys. J. **98** (2010) 1830.

[29] C. Chimerel, L. Movileanu, S. Pezeshki, M. Winterhalter and U. Kleinekathöfer. *Transport at the nanoscale: temperature dependence of ion conductance*. Eur. Biophys. J. **38** (2008) 121.

[30] A. Alcaraz, E. Nestorovich, M. López, E. García Giménez, S. Bezrukov and V. Aguilella. *Diffusion, exclusion, and specific binding in a large channel: a study of OmpF selectivity inversion*. Biophys. J. **96** (2009) 56.

[31] V. M. Aguilella, M. Queralt Martin, M. Aguilella Arzo and A. Alcaraz. *Insights on the permeability of wide protein channels: measurement and interpretation of ion selectivity*. Integr. Biol. **3** (2011) 159.

[32] H. Rui, K. I. Lee, R. W. Pastor and W. Im. *Molecular dynamics studies of ion permeation in VDAC*. Biophys. J. **100** (2011) 602.

[33] E.-M. Krammer, F. Homble and M. Prevost. *Concentration dependent ion selectivity in VDAC: a molecular dynamics simulation study*. PLoS ONE **6** (2011) e27994.

[34] K. I. Lee, H. Rui, R. W. Pastor and W. Im. *Brownian dynamics simulations of ion transport through the VDAC*. Biophys. J. **100** (2011) 611.

[35] M. Jensen, D. Borhani, K. Lindorff Larsen, P. Maragakis, V. Jogini, M. Eastwood, R. Dror and D. Shaw. *Principles of conduction and hydrophobic gating in K+ channels*. Proc. Natl. Acad. Sci. USA **107** (2010) 5833.

[36] S. Bernèche and B. Roux. *A microscopic view of ion conduction through the K^+ channel*. Proc. Natl. Acad. Sci. USA **100** (2003) 8644.

[37] Y. Zhou, J. Morais Cabral, A. Kaufman and R. MacKinnon. *Chemistry of ion coordination and hydration revealed by a K^+ channel-Fab complex at 2 Å resolution*. Nature **414** (2001) 43.

[38] S. Bernéche and B. Roux. *A gate in the selectivity filter of potassium channels.* Structure **13** (2005) 591.

[39] J. Cordero Morales, L. Cuello, Y. Zhao, V. Jogini, D. Cortes, B. Roux and E. Perozo. *Molecular determinants of gating at the potassium-channel selectivity filter*. Nat. Struct. Mol. Biol. **13** (2006) 311.

[40] C. Domene, S. Vemparala, S. Furini, K. Sharp and M. L. Klein. *The role of conformation in ion permeation in a K^+ channel*. J. Am. Chem. Soc. **130** (2008) 3389.

[41] M. Compoint, F. Picaud, C. Ramseyer and C. Girardet. *Targeted molecular dynamics of an open-state KcsA channel*. J. Chem. Phys. **122** (2005) 134707.

[42] L. Cuello, V. Jogini, D. Cortes and E. Perozo. *Structural mechanism of C-type inactivation in K^+ channels*. Nature **466** (2010) 203.

[43] L. Cuello, V. Jogini, D. Cortes, A. Pan, D. Gagnon, O. Dalmas, J. Cordero Morales, S. Chakrapani, B. Roux and E. Perozo. *Structural basis for the coupling between activation and inactivation gates in K^+ channels*. Nature **466** (2010) 272.

[44] Y. Kong, Y. Shen, T. E. Warth and J. Ma. *Conformational pathways in the gating of Ekhscherichia coli mechanosensitive channel*. Proc. Natl. Acad. Sci. USA **99** (2002) 5999.

[45] J. Gullingsrud, D. Kosztin and K. Schulten. *Structural determinants of MscL gating studied by molecular dynamics simulations*. Biophys. J.s **80** (2001) 2074.

[46] S. Khalid, P. J. Bond, T. Carpenter and M. S. Sansom. *OmpA: gating and dynamics via molecular dynamics simulations*. BBA-Biomembranes **1778** (2008) 1871.

[47] S. Khalid, P. J. Bond, S. S. Deol and M. S. Sansom. *Modeling and simulations of a bacterial outer membrane protein: OprF from Pseudomonas aeruginosa*. Proteins: Struct., Funct., Bioinf. **63** (2006) 6.

[48] J. Liu, E. Eren, J. Vijayaraghavan, B. R. Cheneke, M. Indic, B. van den Berg and L. Movileanu. *OccK channels from Pseudomonas aeruginosa exhibit diverse single-channel electrical signatures but conserved anion selectivity*. Biochemistry **51** (2012) 2319.

[49] B. Eisenberg. *Multiple scales in the simulation of ion channels and proteins*. J. Phys. Chem. C **114** (2010) 20719.

[50] B. Eisenberg. *Ionic channels in biological membranes. Electrostatic analysis of a natural nanotube*. Contemp. Phys. **39** (1998) 447.

[51] M. Kurnikova, R. Coalson, P. Graf and A. Nitzan. *A lattice relaxation algorithm for three-dimensional Poisson-Nernst-Planck theory with application to ion transport through the gramicidin A channel*. Biophys. J. **76** (1999) 642.

[52] Z. Schuss, B. Nadler and R. S. Eisenberg. *Derivation of Poisson and Nernst-Planck equations in a bath and channel from a molecular model*. Phys. Rev. E **64** (2001) 036116.

[53] Serdar Kuyucak, Olaf Sparre Andersen and Shin-Ho Chung. *Models of permeation in ion channels*. Rep. Prog. Phys. **64** (2001) 1427.

[54] S.-H. Chung, O. S. Anderson and V. V. Krishnamurthy (Eds.). *Biological membrane ion channels*. Biological and Medical Physics, Biomedical Engineering (Springer, 2007).

[55] W. Nernst. *Zur Kinetik der in Lösung befindlichen Körper*. Z. Phys. Chem. **2** (1888) 613.

[56] M. Planck. *Über die Erregung von Elektrizität und Wärme in Elektrolyten*. Ann. Phys. Chem. **39** (1890) 161.

[57] W. Im and B. Roux. *Ion permeation and selectivity of OmpF porin: a theoretical study based on molecular dynamics, brownian dynamics, and continuum electrodiffusion theory*. J. Mol. Biol. **322** (2002) 851.

[58] J. Cervera, B. Schiedt, R. Neumann, S. Mafé and P. Ramírez. *Ionic conduction, rectification, and selectivity in single conical nanopores*. J. Chem. Phys. **124** (2006) 104706.

[59] O. Choudhary, R. Ujwal, W. Kowallis, R. Coalson, J. Abramson and M. Grabe. *The electrostatics of VDAC: implications for selectivity and gating*. J. Mol. Biol. **396** (2010) 580.

[60] H. Miedema, M. Vrouenraets, J. Wierenga, D. Gillespie, B. Eisenberg, W. Meijberg and W. Nonner. *Ca^{2+} selectivity of a chemically modified OmpF with reduced pore volume*. Biophys. J. **91** (2006) 4392.

[61] H. Miedema, A. Meter Arkema, J. Wierenga, J. Tang, B. Eisenberg, W. Nonner, H. Hektor, D. Gillespie and W. Meijberg. *Permeation properties of an engineered bacterial OmpF porin containing the EEEE-locus of Ca^{2+} channels*. Biophys. J. **87** (2004) 3137.

[62] E. García Giménez, M. L. López, V. M. Aguilella and A. Alcaraz. *Linearity, saturation and blocking in a large multiionic channel: divalent cation modulation of the OmpF porin conductance.* Biochem. Biophys. Res. Commun. **404** (2011) 330.

[63] D. Gillespie. *Energetics of divalent selectivity in a calcium channel: the ryanodine receptor case study*. Biophys. J. **94** (2008) 1169.

[64] A. Mamonov, M. Kurnikova and R. Coalson. *Diffusion constant of K^+ inside Gramicidin A: A comparative study of four computational methods*. Biophys. Chem **124** (2006) 268.

[65] D. Bolintineanu, A. Sayyed Ahmad, H. Davis and Y. Kaznessis. *Poisson-Nernst-Planck models of nonequilibrium ion electrodiffusion through a protegrin transmembrane pore*. PLoS Comput. Biol. **5** (2009) e1000277.

[66] C. Ho, R. Qiao, J. Heng, A. Chatterjee, R. Timp, N. Aluru and G. Timp. *Electrolytic transport through a synthetic nanometer-diameter pore*. Proc. Natl. Acad. Sci. USA **102** (2005) 10445.

[67] M. Ali, S. Nasir, P. Ramirez, I. Ahmed, Q. H. Nguyen, L. Fruk, S. Mafe and W. Ensinger. *Optical gating of photosensitive synthetic ion channels*. Adv. Funct. Mater. **22** (2012) 390.

[68] J. Cervera, B. Schiedt and P. Ramirez. *A Poisson/Nernst-Planck model for ionic transport through synthetic conical nanopores*. Europhys. Lett. **71** (2005) 35.

[69] I. Kosińska, I. Goychuk, M. Kostur, G. Schmid and P. Hänggi. *Rectification in synthetic conical nanopores: A one-dimensional Poisson-Nernst-Planck model*. Phys. Rev. E **77** (2008) 031131.

[70] D. Krapf, B. Quinn, M. Wu, H. Zandbergen, C. Dekker and S. Lemay. *Experimental observation of nonlinear ionic transport at the nanometer scale*. Nano Lett. **6** (2006) 2531.

[71] Y. Jung, B. Lu and M. Mascagni. *A computational study of ion conductance in the KcsA K^+ channel using a Nernst–Planck model with explicit resident ions*. J. Chem. Phys. **131** (2009) 215101.

[72] B. Corry, S. Kuyucak and S. Chung. *Tests of continuum theories as models of ion channels. II. Poisson-Nernst-Planck theory versus Brownian dynamics*. Biophys. J. **78** (2000) 2364.

[73] G. Moy, B. Corry, S. Kuyucak and S. Chung. *Tests of continuum theories as models of ion channels. I. Poisson-Boltzmann theory versus Brownian dynamics*. Biophys. J. **78** (2000) 2349.

[74] C. Song and B. Corry. *Testing the Applicability of Nernst-Planck Theory in Ion Channels: Comparisons with Brownian Dynamics Simulations*. PLoS ONE **6** (2011) e21204.

[75] Dirk Gillespie, Wolfgang Nonner and Robert S Eisenberg. *Coupling Poisson-Nernst-Planck and density functional theory to calculate ion flux*. J. Phys.: Condens. Matter **14** (2002) 12129.

[76] R. Roth and D. Gillespie. *Physics of size selectivity*. Phys. Rev. Lett. **95** (2005) 247801.

[77] Bob Eisenberg, YunKyong Hyon and Chun Liu. *Energy variational analysis of ions in water and channels: Field theory for primitive models of complex ionic fluids*. J. Chem. Phys. **133** (2010) 104104.

[78] Martin Burger, Robert S. Eisenberg and Heinz W. Engl. *Inverse problems related to ion channel selectivity*. SIAM J. Appl. Math. **67** (2007) 960.

[79] Martin Burger. *Inverse problems in ion channel modelling*. Inverse Problems **27** (2011) 083001.

[80] F. Reif. *Fundamentals of statistical and thermal physics* (McGraw-Hill Book Company, 1967).

[81] W. Van Gunsteren, H. Berendsen and J. Rullmann. *Stochastic dynamics for molecules with constraints*. Mol. Phys. **44** (1981) 69.

[82] S. Li, M. Hoyles, S. Kuyucak and S. Chung. *Brownian dynamics study of ion transport in the vestibule of membrane channels*. Biophys. J. **74** (1998) 37.

[83] P. S. Phale, A. Philippsen, C. Widmer, V. P. Phale, J. P. Rosenbusch and T. Schirmer. *Role of charged residues at the OmpF porin channel constriction probed by mutagenesis and simulation*. Biochemistry **40** (2001) 6319.

[84] T. Schirmer and P. S. Phale. *Brownian dynamics simulation of ion flow through porin channels*. J. Mol. Biol. **294** (1999) 1159.

[85] T. Allen, M. Hoyles, S. Kuyucak and S. Chung. *Molecular and Brownian dynamics study of ion selectivity and conductivity in the potassium channel*. Chem. Phys. Lett. **313** (1999) 358.

[86] S. Chung, T. Allen and S. Kuyucak. *Modeling diverse range of potassium channels with Brownian dynamics*. Biophys. J. **83** (2002) 263.

[87] S. Noskov, W. Im and B. Roux. *Ion permeation through the α-hemolysin channel: theoretical studies based on Brownian dynamics and Poisson-Nernst-Plank electrodiffusion theory*. Biophys. J. **87** (2004) 2299.

[88] T. Hilder, D. Gordon and S. Chung. *Synthetic chloride-selective carbon nanotubes examined by using molecular and stochastic dynamics*. Biophys. J. **99** (2010) 1734.

[89] R. Carr, J. Comer, M. D. Ginsberg and A. Aksimentiev. *Atoms-to-microns model for small solute transport through sticky nanochannels*. Lab Chip **11** (2011) 3766.

[90] J. Comer and A. Aksimentiev. *Predicting the DNA sequence dependence of nanopore ion current using atomic-resolution brownian dynamics*. J. Phys. Chem. C **116** (2012) 3376.

[91] E. Csanyi, D. Boda, D. Gillespie and T. Kristof. *Current and selectivity in a model sodium channel under physiological conditions: Dynamic Monte Carlo simulations*. Biochim. Biophys. Acta, Biomembr. **1818** (2012) 592.

[92] A. R. Leach and D. Schomburg. *Molecular modelling: principles and applications* (Longman London, 1996).

[93] D. C. Rapaport. *The art of molecular dynamics simulation* (Cambridge University Press, 2004), 2nd edition.

[94] S. A. Adcock and J. A. McCammon. *Molecular dynamics: survey of methods for simulating the activity of proteins*. Chem. Rev. **106** (2006) 1589.

[95] A. MacKerell, D. Bashford, M. Bellott, R. Dunbrack, J. Evanseck, M. Field, S. Fischer, J. Gao, H. Guo, S. Ha, D. Joseph McCarthy, L. Kuchnir, K. Kuczera, F. Lau, C. Mattos, S. Michnick, T. Ngo, D. Nguyen, B. Prodhom, W. Reiher, B. Roux, M. Schlenkrich, J. Smith, R. Stote, J. Straub, M. Watanabe, J. Wiorkiewicz Kuczera, D. Yin and M. Karplus. *All-Atom Empirical Potential for Molecular Modeling and Dynamics Studies of Proteins*. J. Phys. Chem. B **102** (1998) 3586.

[96] Jay W Ponder and David A Case. *Force fields for protein simulations.* Adv. Protein Chem. **66** (2003) 27.

[97] W. Scott, P. Hünenberger, I. Tironi, A. Mark, S. Billeter, J. Fennen, A. Torda, T. Huber, P. Krüger and W. Van Gunsteren. *The GROMOS biomolecular simulation program package*. J. Phys. Chem. A **103** (1999) 3596.

[98] W. Jorgensen, D. Maxwell and J. Tirado Rives. *Development and testing of the OPLS all-atom force field on conformational energetics and properties of organic liquids*. J. Am. Chem. Soc. **118** (1996) 11225.

[99] F. Khalili Araghi, J. Gumbart, P. C. Wen, M. Sotomayor, E. Tajkhorshid and K. Schulten. *Molecular dynamics simulations of membrane channels and transporters*. Curr. Opin. Struct. Biol. **19** (2009) 128.

[100] R. O. Dror, R. M. Dirks, J. Grossman, H. Xu and D. E. Shaw. *Biomolecular simulation: a computational microscope for molecular biology*. Annu. Rev. Biophys. **41** (2012) 429.

[101] H. Yu, T. Whitfield, E. Harder, G. Lamoureux, I. Vorobyov, V. Anisimov, A. MacKerell Jr and B. Roux. *Simulating monovalent and divalent ions in aqueous solution using a Drude polarizable force field*. J. Chem. Theory Comput. **6** (2010) 774.

[102] W. Jiang, D. J. Hardy, J. C. Phillips, A. D. MacKerell, K. Schulten and B. Roux. *High-performance scalable molecular dynamics simulations of a polarizable force field based on classical drude oscillators in NAMD*. J. Phys. Chem. Lett. **2** (2010) 87.

[103] A. Alcaraz, E. M. Nestorovich, M. Aguilella Arzo, V. M. Aguilella and S. M. Bezrukov. *Salting out the ionic selectivity of a wide channel: the asymmetry of OmpF*. Biophys. J. **87** (2004) 943.

[104] S. Donnini, F. Tegeler, G. Groenhof and H. Grubmüller. *Constant pH molecular dynamics in explicit solvent with λ-dynamics*. J. Chem. Theory Comput. **7** (2011) 1962.

[105] G. B. Goh, J. L. Knight and C. L. Brooks. *Constant pH molecular dynamics simulations of nucleic acids in explicit solvent*. J. Chem. Theory Comput. **8** (2011) 36.

[106] A. Gurtovenko and I. Vattulainen. *Pore formation coupled to ion transport through lipid membranes as induced by transmembrane ionic charge imbalance: atomistic molecular dynamics study*. J. Am. Chem. Soc. **127** (2005) 17570.

[107] J. N. Sachs, P. S. Crozier and T. B. Woolf. *Atomistic simulations of biologically realistic transmembrane potential gradients*. J. Chem. Phys. **121** (2004) 10847.

[108] L. Delemotte, F. Dehez, W. Treptow and M. Tarek. *Modeling membranes under a transmembrane potential*. J. Phys. Chem. B **112** (2008) 5547.

[109] C. Kutzner, H. Grubmüller, B. L. de Groot and U. Zachariae. *Computational electrophysiology: the molecular dynamics of ion channel permeation and selectivity in atomistic detail*. Biophys. J. **101** (2011) 809.

[110] B. Corry, M. Hoyles, T. W. Allen, M. Walker, S. Kuyucak and S.-H. Chung. *Reservoir boundaries in brownian dynamics simulations of ion channels*. Biophys. J. **82** (2002) 1975.

[111] F. Khalili-Araghi, B. Ziervogel, J. C. Gumbart and B. Roux. *Molecular dynamics simulations of membrane proteins under asymmetric ionic concentrations*. J. Gen. Physiol. **142** (2013) 465.

[112] P. S. Crozier, D. Henderson, R. L. Rowley and D. D. Busath. *Model channel ion currents in NaCl-extended simple point charge water solution with applied-field molecular dynamics*. Biophys. J. **81** (2001) 3077.

[113] A. Suenaga, Y. Komeiji, M. Uebayasi, T. Meguro, M. Saito and I. Yamato. *Computational observation of an ion permeation through a channel protein*. Biosci. Rep. **18** (1998) 39.

[114] J. Gumbart, F. Khalili Araghi, M. Sotomayor and B. Roux. *Constant electric field simulations of the membrane potential illustrated with simple systems.* Biochim. Biophys. Acta, Biomembr. **1818** (2012) 294.

[115] R. Schulz and U. Kleinekathöfer. *Transitions between closed and open conformations of TolC: the effects of ions in simulations*. Biophys. J. **96** (2009) 3116.

[116] C. Maffeo and A. Aksimentiev. *Structure, dynamics, and ion conductance of the phospholamban pentamer*. Biophys. J. **96** (2009) 4853.

[117] S. Siu and R. Böckmann. *Electric field effects on membranes: Gramicidin A as a test ground*. J. Struct. Biol. **157** (2007) 545.

[118] M. Sotomayor, V. Vasquez, E. Perozo and K. Schulten. *Ion Conduction through MscS as Determined by Electrophysiology and Simulation*. Biophys. J. **92** (2007) 886.

[119] F. Khalili Araghi, E. Tajkhorshid and K. Schulten. *Dynamics of K^+ ion conduction through Kv1.2*. Biophys. J. **91** (2006) L72.

[120] D. P. Tieleman. *The molecular basis of electroporation*. BMC Biochemistry **5** (2004) 10.

[121] P. Pongprayoon, O. Beckstein, C. L. Wee and M. S. Sansom. *Simulations of anion transport through OprP reveal the molecular basis for high affinity and selectivity for phosphate*. Proc. Natl. Acad. Sci. U.S.A. **106** (2009) 21614.

[122] S. Patel, J. Davis and B. Bauer. *Exploring ion permeation energetics in gramicidin A using polarizable charge equilibration force fields*. J. Am. Chem. Soc. **131** (2009) 13890.

[123] Y. Zhang and G. A. Voth. *Combined metadynamics and umbrella sampling method for the calculation of ion permeation free energy profiles*. J. Chem. Theory Comput. **7** (2011) 2277.

[124] B. Corry and M. Thomas. *Mechanism of ion permeation and selectivity in a voltage gated sodium channel.* J. Am. Chem. Soc. **134** (2012) 1840.

[125] T. Bastug and S. Kuyucak. *Energetics of ion permeation, rejection, binding, and block in gramicidin A from free energy simulations*. Biophys. J. **90** (2006) 3941.

[126] J. Yu, A. Yool, K. Schulten and E. Tajkhorshid. *Mechanism of gating and ion conductivity of a possible tetrameric pore in aquaporin-1*. Structure **14** (2006) 1411.

[127] T. W. Allen, O. S. Andersen and B. Roux. *Ion permeation through a narrow channel: using gramicidin to ascertain all-atom molecular dynamics potential of mean force methodology and biomolecular force fields*. Biophys. J. **90** (2006) 3447.

[128] C. Chipot and A. Pohorille. *Free energy calculations* (Springer, New York, 2007).

[129] A. Laio and M. Parrinello. *Escaping free-energy minima*. Proc. Natl. Acad. Sci. USA **99** (2002) 12562.

[130] A. Barducci, M. Bonomi and M. Parrinello. *Metadynamics*. Wiley Interdiscip. Rev. Comput. Mol. Sci. **1** (2011) 826.

[131] J. C. Phillips, R. Braun, W. Wang, J. Gumbart, E. Tajkhorshid, E. Villa, C. Chipot, R. D. Skeel, L. Kale and K. Schulten. *Scalable molecular dynamics with NAMD*. J. Comput. Chem. **26** (2005) 1781.

[132] H. Nikaido. *Molecular basis of bacterial outer membrane permeability revisited*. Microbiol. Mol. Biol. Rev. **67** (2003) 593.

[133] R. Benz (Ed.). *Bacterial and Eukaryotic Porins* (Wiley-VCH, Weinheim, 2004).

[134] S. Khalid and M. Baaden. *Molecular dynamics studies of outer membrane proteins: a story of barrels*. Mol. Simulations Biomembr. Biophys. Funct. **20** (2010) 225.

[135] W. Im, S. Seefeld and B. Roux. *A Grand Canonical Monte Carlo-Brownian dynamics algorithm for simulating ion channels*. Biophys. J. **79** (2000) 788.

[136] W. Im and B. Roux. *Brownian dynamics simulations of ions channels: a general treatment of electrostatic reaction fields for molecular pores of arbitrary geometry*. J. Chem. Phys. **115** (2001) 4850.

[137] M. Chen, S. Khalid, M. S. P. Sansom and H. Bayley. *Outer membrane protein G: engineering a quiet pore for biosensing*. Proc. Natl. Acad. Sci. U.S.A. **105** (2008) 6272.

[138] H. Miedema, M. Vrouenraets, J. Wierenga, B. Eisenberg, T. Schirmer, A. Basle and W. Meijberg. *Conductance and selectivity fluctuations in D127 mutants of the bacterial porin OmpF*. Eur. Biophys. J. **36** (2006) 13.

[139] J. M. Pages, C. E. James and M. Winterhalter. *The porin and the permeating antibiotic: a selective diffusion barrier in Gram-negative bacteria*. Nature Rev. Microbiol. **6** (2008) 893.

[140] E. M. Nestorovich, C. Danelon, M. Winterhalter and S. M. Bezrukov. *Designed to penetrate: Time-resolved interaction of single antibiotic molecules with bacterial pores*. Proc. Natl. Acad. Sci. USA **99** (2002) 9789.

[141] H. Weingart, M. Petrescu and M. Winterhalter. *Biophysical characterization of in- and efflux in Gram-negative bacteria*. Curr. Drug Targets **9** (2008) 789.

[142] M. Ceccarelli and P. Ruggerone. *Physical insights into permeation of and resistance to antibiotics in bacteria*. Curr. Drug Targets **9** (2008) 779.

[143] K. R. Mahendran, E. Hajjar, T. Mach, M. Lovelle, A. Kumar, I. Sousa, E. Spiga, H. Weingart, P. Gameiro, M. Winterhalter and M. Ceccarelli. *Molecular basis of enrofloxacin translocation through OmpF, an outer membrane channel of Escherichia coli–when binding does not imply translocation*. J. Phys. Chem. B **114** (2010) 5170.

[144] E. Hajjar, K. R. Mahendran, A. Kumar, A. Bessonov, M. Petrescu, H. Weingart, P. Ruggerone, M. Winterhalter and M. Ceccarelli. *Bridging timescales and length scales: from macroscopic flux to the molecular mechanism of antibiotic diffusion through porins*. Biophys. J. **98** (2010) 569.

[145] C. Danelon, E. M. Nestorovich, M. Winterhalter, M. Ceccarelli and S. M. Bezrukov. *Interaction of zwitterionic penicillins with the OmpF channel facilitates their translocation*. Biophys. J. **90** (2006) 1617.

[146] T. Mach, P. Neves, E. Spiga, H. Weingart, M. Winterhalter, P. Ruggerone, M. Ceccarelli and P. Gameiro. *Facilitated permeation of antibiotics across membrane channels–interaction of the quinolone moxifloxacin with the OmpF channel*. J. Am. Chem. Soc. **130** (2008) 13301.

[147] P. Raj Singh, M. Ceccarelli, M. Lovelle, M. Winterhalter and K. R. Mahendran. *Antibiotic permeation across the OmpF channel: modulation of the affinity site in the presence of magnesium*. J. Phys. Chem. B **116** (2012) 4433.

[148] C. E. James, K. R. Mahendran, A. Molitor, J. M. Bolla, A. N. Bessonov, M. Winterhalter and J. M. Pages. *How beta-lactam antibiotics enter bacteria: a dialogue with the porins*. PLoS One **4** (2009) e5453.

[149] B. K. Ziervogel and B. Roux. *The binding of antibiotics in OmpF porin*. Structure **21** (2013) 76.

[150] M. Page and E. Di Cera. *Role of Na^+ and K^+ in enzyme function*. Physiol. Rev. **86** (2006) 1049.

[151] M. Shannon, P. Bohn, M. Elimelech, J. Georgiadis, B. Marinas and A. Mayes. *Science and technology for water purification in the coming decades*. Nature **452** (2008) 301.

[152] I. Shrivastava and M. Sansom. *Simulations of ion permeation through a potassium channel: molecular dynamics of KcsA in a phospholipid bilayer*. Biophys. J. **78** (2000) 557.

[153] S. Bernèche and B. Roux. *Energetics of ion conduction through the K^+ channel*. Nature **414** (2001) 73.

[154] J. Cohen and K. Schulten. *Mechanism of anionic conduction across ClC*. Biophys. J. **86** (2004) 836.

[155] S. Noskov and B. Roux. *Importance of hydration and dynamics on the selectivity of the KcsA and NaK channels*. J. Gen. Physiol. **129** (2007) 135.

[156] R. E. W. Hancock, K. Poole and R. Benz. *Outer membrane protein P of Pseudomonas aeruginosa: regulation by phosphate deficiency and formation of small anion-specific channels in lipid bilayer membranes.* J. Bacteriol. **150** (1982) 730.

[157] R. Benz, C. Egli and R. E. W. Hancock. *Anion transport through the phosphate-specific OprP-channel of the Pseudomonas aeruginosa outer membrane: effects of phosphate, di-and tribasic anions and of negatively-charged lipids*. Biochim. Biophys. Acta, Biomembr. **1149** (1993) 224.

[158] R. Benz and R. E. W. Hancock. *Mechanism of ion transport through the anion-selective channel of the Pseudomonas aeruginosa outer membrane.* J. Gen. Physiol. **89** (1987) 275.

[159] R. E. W. Hancock and R. Benz. *Demonstration and chemical modification of a specific phosphate binding site in the phosphate-starvation-inducible outer membrane porin protein P of Pseudomonas aeruginosa*. Biochim. Biophys. Acta, Biomembr. **860** (1986) 699.

[160] T. Moraes, M. Bains, R. E. W. Hancock and N. Strynadka. *An arginine ladder in OprP mediates phosphate-specific transfer across the outer membrane*. Nat. Struct. Mol. Biol. **14** (2006) 85.

[161] N. Modi, P. R. Singh, K. R. Mahendran, R. Schulz, M. Winterhalter and U. Kleinekathöfer. *Probing the transport of ionic liquids in aqueous solution through nanopores*. J. Phys. Chem. Lett. **2** (2011) 2331.

[162] E. Darve and A. Pohorille. *Calculating free energies using average force*. J. Chem. Phys. **115** (2001) 9169.

[163] J. Hénin and C. Chipot. *Overcoming free energy barriers using unconstrained molecular dynamics simulations*. J. Chem. Phys. **121** (2004) 2904.

[164] C. Chang, W. Chen and M. Gilson. *Ligand configurational entropy and protein binding*. Proc. Natl. Acad. Sci. USA **104** (2007) 1534.

[165] J. Bormann, O. Hamill and B. Sakmann. *Mechanism of anion permeation through channels gated by glycine and gamma-aminobutyric acid in mouse cultured spinal neurones.* J. Physiol. (Lond.) **385** (1987) 243.

[166] B. Verdon, J. Winpenny, K. Whitfield, B. Argent and M. Gray. *Volume-activated chloride currents in pancreatic duct cells*. J. Membr. Biol. **147** (1995) 173.

[167] P. Linsdell and J. Hanrahan. *Adenosine triphosphate–dependent asymmetry of anion permeation in the cystic fibrosis transmembrane conductance regulator chloride channel*. J. Gen. Physiol. **111** (1998) 601.

[168] J. Zhang, A. Kamenev and B. I. Shklovskii. *Ion exchange phase transitions in water-filled channels with charged walls*. Phys. Rev. E **73** (2006) 051205.

[169] G. Hummer, L. Pratt and A. García. *Free energy of ionic hydration*. J. Phys. Chem. **100** (1996) 1206.

[170] Z. S. Siwy and S. Howorka. *Engineered voltage-responsive nanopores*. Chem. Soc. Rev. **39** (2010) 1115.

[171] C. Maffeo, S. Bhattacharya, J. Yoo, D. Wells and A. Aksimentiev. *Modeling and simulation of ion channels*. Chem. Rev. **112** (2012) 6250.

[172] N. Modi, R. Benz, R. E. W. Hancock and U. Kleinekathöfer. *Modeling the ion selectivity of the phosphate specific channel OprP*. J. Phys. Chem. Lett. **3** (2012) 3639.

[173] P. Pongprayoon, O. Beckstein and M. S. P. Sansom. *Biomimetic design of a brush-like nanopore: simulation studies*. J. Phys. Chem. B **116** (2011) 462.

[174] A. Sukhan and R. E. W. Hancock. *Insertion mutagenesis of the Pseudomonas aeruginosa phosphate-specific porin OprP.* J. Bacteriol. **177** (1995) 4914.

[175] K. Bauer, M. Struyve, D. Bosch, R. Benz and J. Tommassen. *One single lysine residue is responsible for the special interaction between polyphosphate and the outer membrane porin PhoE of Escherichia coli*. J Biol Chem. **264** (1989) 16393.

[176] R. Benz, K. Janko and P. Lauger. *Ionic selectivity of pores formed by the matrix protein (porin) of Escherichia coli*. Biochim. Biophys. Acta, Biomembr. **551** (1979) 238.

[177] R. Benz, A. Schmid and G. H. Vos Scheperkeuter. *Mechanism of sugar transport through the sugar-specific LamB channel of Escherichia coli outer membrane*. J. Membr. Biol. **100** (1987) 21.

[178] R. Benz, A. Schmid, T. Nakae and G. Vos Scheperkeuter. *Pore formation by LamB of Escherichia coli in lipid bilayer membranes*. J. Bacteriol. **165** (1986) 978.

[179] M. Thein, M. Bonde, I. Bunikis, K. Denker, A. Sickmann, S. Bergström and R. Benz. *DipA, a pore-forming protein in the outer membrane of lyme disease spirochetes exhibits specificity for the permeation of dicarboxylates*. PLoS one **7** (2012) e36523.

[180] O. Ludwig, V. De Pinto, F. Palmieri and R. Benz. *Pore formation by the mitochondrial porin of rat brain in lipid bilayer membranes.* Biochim. Biophys. Acta, Biomembr. **860** (1986) 268.

[181] W. F. Humphrey, A. Dalke and K. Schulten. *VMD – Visual Molecular Dynamics*. J. Mol. Graph. **14** (1996) 33.

[182] U. Kleinekathöfer, Barry Isralewitz, Markus Dittrich and Klaus Schulten. *Domain motion of individual F_1-ATPase β-subunits during unbiased molecular dynamics simulations*. J. Phys. Chem. A **115** (2011) 7267.

[183] T. Darden, D. York and L. Pedersen. *Particle mesh Ewald: An N log (N) method for Ewald sums in large systems*. J. Chem. Phys. **98** (1993) 10089.

[184] M. Tuckerman, B. Berne and G. Martyna. *Reversible multiple time scale molecular dynamics*. J. Chem. Phys. **97** (1992) 1990.

[185] J.-P. Ryckaert, G. Ciccotti and H. J. Berendsen. *Numerical integration of the cartesian equations of motion of a system with constraints: molecular dynamics of n-alkanes*. J. Comput. Phys. **23** (1977) 327.

[186] J. Hénin, G. Fiorin, C. Chipot and M. L. Klein. *Exploring multidimensional free energy landscapes using time-dependent biases on collective variables*. J. Chem. Theory Comput. **6** (2010) 35.

[187] L. A. Richards, A. I. Schäfer, B. S. Richards and B. Corry. *The importance of dehydration in determining ion transport in narrow pores*. Small **8** (2012) 1701.

[188] R. Benz, K. Poole and R. E. W. Hancock. *Characterization and chemical modification of small anion specific channels formed in lipid bilayer membranes by outer membrane protein P of Pseudomonas aeruginosa*. Biophys. J. **45** (1984) 81.

[189] J. Kuriyan, B. Konforti and D. Wemmer. *The Molecules of Life: Physical and Chemical Principles* (Garland Science, Taylor & Francis Group, 2013).

[190] E. Fischer. *Einfluss der Configuration auf die Wirkung der Enzyme*. Ber. Dtsch. Chem. Ges. **27** (1894) 2985.

[191] L. Pauling and M. Delbrück. *The nature of the intermolecular forces operative in biological processes*. Science **92** (1940) 77.

[192] E. A. Worobec, R. J. Siehnel, P. Gladman and R. E. W. Hancock. *Gene cloning and expression of the Pseudomonas aeruginosa periplasmic phosphate-binding protein*. FEMS Microbiol. Lett. **52** (1988) 235.

[193] N. Modi, I. Bárcena-Uribarri, M. Bains, R. Benz, R. E. W. Hancock and U. Kleinekathöfer. *Role of the central arginine R133 towards the ion selectivity of the phosphate specific channel OprP: effects of charge and solvation*. Biochemistry **52** (2013) 5522.

[194] R. Oliva, G. Calamita, J. M. Thornton and M. Pellegrini Calace. *Electrostatics of aquaporin and aquaglyceroporin channels correlates with their transport selectivity*. Proc. Natl. Acad. Sci. USA. **107** (2010) 4135.

[195] A.-M. Lacoste, A. Cassaigne and E. Neuzil. *Transport of inorganic phosphate in Pseudomonas aeruginosa*. Curr. Microbiol. **6** (1981) 115.

[196] K. Poole and R. E. W. Hancock. *Phosphate transport in Pseudomonas aeruginosa*. Eur. J. Biochem. **144** (1984) 607.

[197] P. Bavoil and H. Nikaido. *Physical interaction between the phage lambda receptor protein and the carrier-immobilized maltose-binding protein of Escherichia coli.* J. Biol. Chem. **256** (1981) 11385.

[198] T. Ferenci and W. Boos. *The role of the Escherichia coli λ receptor in the transport of maltose and maltodextrins*. J. Supramol. Struct. **13** (1980) 101.

[199] H. Luecke and F. A. Quiocho. *High specificity of a phosphate transport protein determined by hydrogen bonds*. Nature **347** (1990) 402.

[200] J. W. Pflugrath and F. A. Quiocho. *The 2 Å resolution structure of the sulfate-binding protein involved in active transport in Salmonella typhimurium*. J. Mol. Biol. **200** (1988) 163.

[201] J. Pflugrath and F. Quiocho. *Sulphate sequestered in the sulphate-binding protein of Salmonella typhimurium is bound solely by hydrogen bonds*. Nature **314** (1985) 257.

[202] F. A. Quiocho. *Atomic basis of the exquisite specificity of phosphate and sulfate transport receptors.* Kidney Int. **49** (1996) 943.

[203] A. Karshikoff, V. Spassov, S. W. Cowan, R. Ladenstein and T. Schirmer. *Electrostatic properties of two porin channels from Escherichia coli*. J. Mol. Biol. **240** (1994) 372.

[204] U. Zachariae, A. Koumanov, H. Engelhardt and A. Karshikoff. *Electrostatic properties of the anion selective porin Omp32 from Delftia acidovorans and of the arginine cluster of bacterial porins*. Protein Sci. **11** (2002) 1309.

[205] A. Mathes and H. Engelhardt. *Nonlinear and asymmetric open channel characteristics of an ion-selective porin in planar membranes*. Biophys. J. **75** (1998) 1255.

[206] U. Zachariae, V. Helms and H. Engelhardt. *Multistep mechanism of chloride translocation in a strongly anion-selective porin channel*. Biophys. J. **85** (2003) 954.

[207] H. Nikaido. *Molecular basis of bacterial outer membrane permeability revisited*. Microbiol. Mol. Biol. Rev. **67** (2003) 593.

[208] S. Armstrong, T. Parr, C. Parker and R. E. W. Hancock. *Bordetella pertussis major outer membrane porin protein forms small, anion-selective channels in lipid bilayer membranes.* J. Bacteriol. **166** (1986) 212.

[209] A. Mauro, M. Blake and P. Labarca. *Voltage gating of conductance in lipid bilayers induced by porin from outer membrane of Neisseria gonorrhoeae*. Proc. Natl. Acad. Sci. USA. **85** (1988) 1071.

[210] J. Song, C. A. Minetti, M. Blake and M. Colombini. *Successful recovery of the normal electrophysiological properties of PorB (Class 3) porin from Neisseria meningitidis after expression in Escherichia coli and renaturation*. BBA-Biomembranes **1370** (1998) 289.

[211] M. Brunen and H. Engelhardt. *Asymmetry of orientation and voltage gating of the Acidovorax delafieldii porin Omp34 in lipid bilayers*. Eur. J. Biochem. **212** (1993) 129.

[212] R. J. Siehnel, C. Egli and R. E. W. Hancock. *Polyphosphate-selective porin OprO of Pseudomonas aeruginosa: expression, purification and sequence*. Mol. Microbiol. **6** (1992) 2319.

[213] R. E. W. Hancock, C. Egli, R. Benz and R. J. Siehnel. *Overexpression in Escherichia coli and functional analysis of a novel PPi-selective porin, OprO, from Pseudomonas aeruginosa.z*. J. Bacteriol. **174** (1992) 471.

[214] A. Labarga, F. Valentin, M. Anderson and R. Lopez. *Web services at the european bioinformatics institute*. Nucleic Acids Res. **35** (2007) W6.

[215] A. M. Waterhouse, J. B. Procter, D. M. Martin, M. Clamp and G. J. Barton. *Jalview version 2-a multiple sequence alignment editor and analysis workbench*. Bioinformatics **25** (2009) 1189.

[216] O. S. Smart, J. G. Neduvelil, X. Wang, B. Wallace and M. S. Sansom. *Hole: a program for the analysis of the pore dimensions of ion channel structural models*. J. Mol. Graph. **14** (1996) 354.

[217] K. Vanommeslaeghe and A. MacKerell Jr. *Automation of the charmm general force field (cgenff) I: bond perception and atom typing*. J. Chem. Inf. Model. **52** (2012) 3144.

[218] K. Vanommeslaeghe, E. P. Raman and A. MacKerell Jr. *Automation of the charmm general force field (cgenff) II: assignment of bonded parameters and partial atomic charges*. J. Chem. Inf. Model. **52** (2012) 3155.

[219] S. E. Feller, R. W. Pastor, A. Rojnuckarin, S. Bogusz and B. R. Brooks. *Effect of electrostatic force truncation on interfacial and transport properties of water*. J. Phys. Chem. **100** (1996) 17011.

[220] T. Welton. *Room-temperature ionic liquids: solvents for synthesis and catalysis*. Chem. Rev. **99** (1999) 2071.

[221] R. Rogers and K. Seddon. *Ionic liquids - solvents of the future?* Science **302** (2003) 792.

[222] E. I. Izgorodina. *Towards large-scale, fully ab initio calculations of ionic liquids*. Phys. Chem. Chem. Phys. **13** (2011) 4189.

[223] M. Galinski, A. Lewandowski and I. Stepniak. *Ionic liquids as electrolytes*. Electrochim. Acta **51** (2006) 5567.

[224] J. Anderson, D. Armstrong and G. Wei. *Ionic liquids in analytical chemistry*. Anal. Chem. **78** (2006) 2892.

[225] A. Heintz, R. Ludwig and E. Schmidt. *Limiting diffusion coefficients of ionic liquids in water and methanol: a combined experimental and molecular dynamics study*. Phys. Chem. Chem. Phys. **13** (2011) 3268.

[226] T. Mendez Morales, J. Carrete, O. Cabeza, L. J. Gallego and L. M. Varela. *Molecular dynamics simulation of the structure and dynamics of water-1-alkyl-3-methylimidazolium ionic liquid mixtures*. J. Phys. Chem. B **115** (2011) 6995.

[227] T. Albrecht, J. B. Edel and M. Winterhalter. *New developments in nanopore research–from fundamentals to applications*. J. Phys.: Condens. Matter **22** (2010) 450301.

[228] B. Roux, T. Allen, S. Bernéche and W. Im. *Theoretical and computational models of biological ion channels*. Q. Rev. Biophys. **37** (2004) 15.

[229] H. Miedema, M. Vrouenraets, J. Wierenga, W. Meijberg, G. Robillard and B. Eisenberg. *A biological porin engineered into a molecular, nanofluidic diode*. Nano Lett. **7** (2007) 2886.

[230] M. L. Lopez, M. Aguilella Arzo, V. M. Aguilella and A. Alcaraz. *Ion selectivity of a biological channel at high concentration ratio: insights on small ion diffusion and binding*. J. Phys. Chem. B **113** (2009) 8745.

[231] Eduardo R. Cruz Chu, Aleksei Aksimentiev and Klaus Schulten. *Ionic current rectification through silica nanopores*. J. Phys. Chem. C **113** (2009) 1850.

[232] J. Faraudo, C. Calero and M. Aguilella Arzo. *Ionic partition and transport in multi-ionic channels: a molecular dynamics simulation study of the OmpF bacterial porin*. Biophys. J. **99** (2010) 2107.

[233] M. Romero Ruiz, K. R. Mahendran, R. Eckert, M. Winterhalter and S. Nussberger. *Interactions of mitochondrial presequence peptides with the mitochondrial outer membrane preprotein translocase TOM*. Biophys. J. **99** (2010) 774.

[234] R. de Zoysa, D. Jayawardhana, Q. Zhao, D. Wang, D. Armstrong and X. Guan. *Slowing DNA translocation through nanopores using a solution containing organic salts*. J. Phys. Chem. B **113** (2009) 13332.

[235] K. R. Mahendran, P. R. Singh, J. Arning, S. Stolte, U. Kleinekathöfer and M. Winterhalter. *Permeation through nanochannels: Revealing fast kinetics*. J. Phys.: Condens. Matter **22** (2010) 454131.

[236] S. W. Cowan, T. Schirmer, G. Rummel, M. Steiert, R. Ghosh, R. A. Pauptit, J. N. Jansonius and J. P. Rosenbusch. *Crystal structures explain functional properties of two E. coli porins*. Nature **358** (1992) 727.

[237] S. W. Cowan, R. M. Garavito, J. N. Jansonius, J. A. Jenkins, R. Karlsson, N. Konig, E. F. Pai, R. A. Pauptit, P. J. Rizkallah and J. P. Rosenbusch. *The structure of OmpF porin in a tetragonal crystal form*. Structure **3** (1995) 1041.

[238] D. P. Tieleman and H. J. Berendsen. *A molecular dynamics study of the pores formed by Escherichia coli OmpF porin in a fully hydrated palmitoyloleoylphosphatidylcholine bilayer*. Biophys. J. **74** (1998) 2786.

[239] K. M. Robertson and D. P. Tieleman. *Orientation and interactions of dipolar molecules during transport through OmpF porin*. FEBS Lett. **528** (2002) 53.

[240] W. Im and B. Roux. *Ions and counterions in a biological channel: a molecular dynamics simulation of OmpF porin from Escherichia coli in an explicit membrane with 1 M KCl aqueous salt solution*. J. Mol. Biol. **319** (2002) 1177.

[241] T. Morrow and E. Maginn. *Molecular dynamics study of the ionic liquid 1-n-butyl-3-methylimidazolium hexafluorophosphate*. J. Phys. Chem. B **106** (2002) 12807.

[242] W. L. Jorgensen, J. Chandrasekhar, J. D. Madura, R. W. Impey and M. L. Klein. *Comparison of simple potential functions for simulating liquid water*. J. Chem. Phys. **79** (1983) 926.

[243] W. Jorgensen and J. Madura. *Temperature and size dependence for Monte-Carlo simulations of TIP4P water*. Mol. Phys. **56** (1985) 1381.

[244] H. Horn, W. Swope, J. Pitera, J. Madura, T. Dick, G. Hura and T. Head Gordon. *Development of an improved four-site water model for biomolecular simulations: TIP4P-Ew*. J. Chem. Phys. **120** (2004) 9665.

[245] J. Abascal and C. Vega. *A general purpose model for the condensed phases of water: TIP4P/2005*. J. Chem. Phys. **123** (2005) 234505.

[246] L. Longsworth. *The mutual diffusion of light and heavy water*. J. Phys. Chem. **64** (1960) 1914.

[247] M. Mahoney and W. Jorgensen. *Diffusion constant of the TIP5P model of liquid water*. J. Chem. Phys. **114** (2001) 363.

[248] B. Alberts, A. Johnson, J. Lewis, M. Raff, K. Roberts and P. Walter. *Molecular Biology of the Cell* (Garland Science, New York, 2002), 4th edition.

[249] G. Condemine and A. Ghazi. *Differential regulation of two oligogalacturonate outer membrane channels, KdgN and KdgM, of Dickeya dadantii (Erwinia chrysanthemi)*. J. Bacteriol. **189** (2007) 5955.

[250] T. Pellinen, H. Ahlfors, N. Blot and G. Condemine. *Topology of the Erwinia chrysanthemi oligogalacturonate porin KdgM.* Biochem. J. **372** (2003) 329.

[251] N. Blot, C. Berrier, N. Hugouvieux-Cotte Pattat, A. Ghazi and G. Condemine. *The oligogalacturonate-specific porin KdgM of Erwinia chrysanthemi belongs to a new porin family*. J. Biol. Chem. **277** (2002) 7936.

[252] G. Condemine, C. Berrier, J. Plumbridge and A. Ghazi. *Function and expression of an N-acetylneuraminic acid-inducible outer membrane channel in Escherichia coli*. J. Bacteriol. **187** (2005) 1959.

[253] E. Severi, D. W. Hood and G. H. Thomas. *Sialic acid utilization by bacterial pathogens*. Microbiology **153** (2007) 2817.

[254] T. Angata and A. Varki. *Chemical diversity in the sialic acids and related alpha-keto acids: an evolutionary perspective*. Chem. Rev. **102** (2002) 439.

[255] E. R. Vimr, K. A. Kalivoda, E. L. Deszo and S. M. Steenbergen. *Diversity of microbial sialic acid metabolism*. Microbiol. Mol. Biol. Rev. **68** (2004) 132.

[256] C. Wirth, G. Condemine, C. Boiteux, S. Bernèche, T. Schirmer and C. M. Peneff. *NanC crystal structure, a model for outer-membrane channels of the acidic sugar-specific KdgM porin family*. J. Mol. Biol. **394** (2009) 718.

[257] A. Baslé, G. Rummel, P. Storici, J. P. Rosenbusch and T. Schirmer. *Crystal structure of osmoporin OmpC from E. coli at 2.0 A*. J. Mol. Biol. **362** (2006) 933.

[258] J. J. Finnerty, R. Eisenberg and P. Carloni. *Localizing the charged side chains of ion channels within the crowded charge models*. J. Chem. Theory Comput. **9** (2012) 766.

[259] S. Biswas, M. M. Mohammad, D. R. Patel, L. Movileanu and B. van den Berg. *Structural insight into OprD substrate specificity*. Nat. Struct. Mol. Biol. **14** (2007) 1108.

[260] J. Giri, J. M. Tang, C. Wirth, C. M. Peneff and B. Eisenberg. *Single-channel measurements of an N-acetylneuraminic acid-inducible outer membrane channel in Escherichia coli*. Eur. Biophys. J. **41** (2012) 259.

[261] M. Aguilella Arzo, C. Calero and J. Faraudo. *Simulation of electrokinetics at the nanoscale: inversion of selectivity in a bio-nanochannel*. Soft Matter **6** (2010) 6079.

[262] N. Eswar, B. Webb, M. A. Marti Renom, M. Madhusudhan, D. Eramian, M.-y. Shen, U. Pieper and A. Sali. *Comparative protein structure modeling using Modeller*. Curr. Protoc. Bioinformatics (2006) 5.

[263] Y. Luo and B. Roux. *Simulation of osmotic pressure in concentrated aqueous salt solutions*. J. Phys. Chem. Lett. **1** (2009) 183.

[264] W. Van Gunsteren and H. Berendsen. *Algorithms for macromolecular dynamics and constraint dynamics*. Mol. Phys. **34** (1977) 1311.

[265] T. Straatsma and T. Soares. *Characterization of the outer membrane protein OprF of Pseudomonas aeruginosa in a lipopolysaccharide membrane by computer simulation*. Proteins: Struct., Funct., and Bioinf. **74** (2009) 475.

[266] T. J. Piggot, D. A. Holdbrook and S. Khalid. *Conformational dynamics and membrane interactions of the E. coli outer membrane protein FecA: A molecular dynamics simulation study*. Biochim. Biophys. Acta, Biomembr. **1828** (2013) 284.

[267] W. Cannon, B. Pettitt and J. McCammon. *Sulfate anion in water: model structural, thermodynamic, and dynamic properties*. J. Phys. Chem. **98** (1994) 6225.

[268] S. Doudou, N. Burton and R. Henchman. *Standard free energy of binding from a one-dimensional potential of mean force*. J. Chem. Theory Comput. **5** (2009) 909.

[269] M. Larkin, G. Blackshields, N. Brown, R. Chenna, P. McGettigan, H. McWilliam, F. Valentin, I. Wallace, A. Wilm, R. Lopez, J. hompson, T. Gibson and D. Higgins. *Clustal W and Clustal X version 2.0*. Bioinformatics **23** (2007) 2947.

[270] B. Dhakshnamoorthy, S. Raychaudhury, L. Blachowicz and B. Roux. *Cation-selective pathway of OmpF porin revealed by anomalous X-ray diffraction*. J. Mol. Biol. **396** (2010) 293.

List of Publications

Publications

1. Kaur, S., **Modi, N.**, Panda, D., Roy, N. (2010). Probing the binding site of curcumin in *Escherichia coli* and *Bacillus subtilis* FtsZ-A structural insight to unveil antibacterial activity of curcumin. *European Journal of Medicinal Chemistry*, 45, 4209-4214.
2. **Modi, N.**, Singh, P. R., Mahendran, K. R., Winterhalter, M., Kleinekathöfer, U. (2011). Probing the Transport of Ionic Liquids in Aqueous Solution Through Nanopores. *Journal of Physical Chemistry Letters*, 2, 2331-2336.
3. **Modi, N.**, Winterhalter, M., Kleinekathöfer, U. (2012). Computational modeling of ion transport through nanopores. *Nanoscale*, 4, 6166-6180.
4. Singh, P. R., Bárcena-Uribarri, I., **Modi, N.**, Kleinekathöfer, U., Benz, R., Winterhalter, M., Mahendran, K. R. (2012). Pulling Peptides across Nanochannels: Resolving Peptide Binding and Translocation through the Hetero-oligomeric Channel from Nocardia farcinica. *ACS Nano*, 6, 10699-10707.
5. **Modi, N.**, Benz, R., Hancock, R.E.W., Kleinekathöfer, U. (2012). Modeling the Ion Selectivity of the Phosphate Specific Channel OprP. *Journal of Physical Chemistry Letters*, 3, 3639-3645.
6. **Modi, N.**, Bárcena-Uribarri, I., Bains, M., Benz, R., Hancock, R.E.W., Kleinekathöfer, U. (2013). Role of the Central Arginine R133 toward the Ion Selectivity of the Phosphate Specific Channel OprP: Effects of Charge and Solvation. *Biochemistry*, 52, 5522-5532.
7. Lu, J., **Modi, N.**, Kleinekathöfer, U. (2013). Simulation of Ion Transport Through an N-acetylneuraminic Acid-inducible Membrane Channel: From Understanding to Engineering. *J. Phys. Chem. B*, 117, 15966-15975.
8. Benz, R., Jones, M., Maier, E., **Modi, N.**, Mentele, R., Lottspeich, F., Kleinekathöfer, U, Smit, J. (2013). OmpW of *Caulobacter crescentus* functions as an outer membrane channel. submitted.

Oral Presentations

1. **Modi, N.**, Singh, P. R., Mahendran, K. R., Winterhalter, M., Kleinekathöfer, U. "Transport of ionic liquids", NANOFUN Research Center Retreat, Clausthal- Zellerfeld, Germany (January 2011).

2. **Modi, N.**, Singh, P. R., Mahendran, K. R., Winterhalter, M., Kleinekathöfer, U. “Transport of ions through bacterial porins”, Workshop on "Computer simulation and theory of macromolecules 2012", Hünfeld, Germany (April, 2012).
3. **Modi, N.**, Singh, P. R., Mahendran, K. R., Winterhalter, M., Kleinekathöfer, U. “Probing the transport of ionic liquids through nanopores”, NANOFUN Research Center Retreat, Clausthal-Zellerfeld, Germany (June 2012).
4. **Modi, N.**, Bárcena-Uribarri, I., Singh, P. R., Mahendran, K. R., Bains, M., Benz, R., Hancock, R.E.W., Winterhalter, M., Kleinekathöfer, U. “Computational modeling of ion transport through porins”, 541th WE-Heraeus- Seminar on "Transport through nanopores: from understanding to engineering”, Jacobs University Bremen, Germany (July 2013).

Poster Presentations

1. **Modi, N.**, Singh, P. R., Mahendran, K. R., Winterhalter, M., Kleinekathöfer, U. “Transport of ionic liquids in aqueous solution through nanopores”, 4th North German biophysics meeting, Borstel, Germany (January 2011).
2. **Modi, N.**, Singh, P. R., Mahendran, K. R., Winterhalter, M., Kleinekathöfer, U. “Probing the transport of ionic liquids in aqueous solution through nanopores”, International WE-Heraeus Workshop on “Nanofluidics in Biology: Protein and Toxin Translocation through Nanopores”, Jacobs University Bremen, Germany (June 2011).
3. **Modi, N.**, Singh, P. R., Mahendran, K. R., Winterhalter, M., Kleinekathöfer, U. “Probing the transport of ionic liquids in aqueous solution through nanopores”, Conference on “Molecular simulations in biosystems and material science", University of Konstanz, Germany (September 2011).
4. **Modi, N.**, Singh, P. R., Mahendran, K. R., Winterhalter, M., Kleinekathöfer, U. “Transport through nanopores”, Conference on "Perspectives and challenges of simulations at bio-materials interfaces", University of Bremen, Germany (October 2011).
5. **Modi, N.**, Benz, R., Hancock, R.E.W., Kleinekathöfer, U. “Phosphate selectivity of OprP”, 6th North German biophysics meeting, Borstel, Germany (January 2013).
6. **Modi, N.**, Benz, R., Hancock, R.E.W., Kleinekathöfer, U. “Deciphering the Ion Selectivity of the Phosphate Specific Channel OprP from Pseudomonas Aeruginosa: A Free-Energy Molecular Dynamics Simulation Study ”, 57th Biophysical Society meeting, Philadelphia, USA (February 2013).
7. **Modi, N.**, Benz, R., Hancock, R.E.W., Kleinekathöfer, U. “Ion Selectivity of the Phosphate Specific Channel OprP from Pseudomonas Aeruginosa: A Free-Energy Molecular Dynamics Simulation Study”, 541th WE-Heraeus- Seminar on "Transport through nanopores: from understanding to engineering”, Jacobs University Bremen, Germany (July 2013).